PRECISION LATTICE PARAMETER MEASUREMENTS

ON SOME

SUPERCONDUCTING INDIUM ALLOYS

Thesis submitted for the degree of

Doctor of Philosophy

by

CHRISTOPHER JOHN GILLHAM

January 1971

Department of Metallurgy
Imperial College
London S.W.7.

"How now my metal of India"

- Sir Toby Belch (Twelfth Night)

ABSTRACT

A review of the literature on the electron theory of metals and alloys reveals that the problem of the relative stability of crystal structures cannot, in general, be treated in terms of fermi surface-Brillouin zone interactions. It is observed that the only basis for a true theory of alloy phases, is one in which the total energy, of the possible crystal structures, may be calculated. The theory of the pseudopotential is the most promising approach in this direction, and is accordingly examined in detail.

A critical examination of the fully focusing geometry applied to X-ray diffractometry, indicates that higher intensities in the back reflection region, may be attained without loss of resolution. Some errors, including axial divergence, which have not previously been considered for this geometry, have been analysed. A versatile fully-focusing diffractometer has been constructed and used, in conjunction with a liquid nitrogen cryostat, for the examination of various indium alloys. The apparatus has a variable specimen position and the upper angular limit of measurement is extended from $164^{\circ}2\theta$ to $172^{\circ}2\theta$. A factor which makes alignment possible is that the apparatus may readily be converted from fully-focusing to conventional geometry. Consideration of the errors has resulted in the tabulation of an appropriate extrapolation function.

In order to measure the superconducting transition temperatures, T_c, of a large number of specimens it was necessary to build a multi-specimen probe for a helium cryostat. To facilitate the measurements a system has been devised to simultaneously record the coil signal and the temperature.

Diffraction and superconducting measurements are used to fix the positions of phase boundaries in the indium alloys. The crystal

structures are established and for tetragonal phases, the axial ratio, $^{c}/_{a}$, is determined as a function of composition.

Energy calculations for the indium based solid solutions containing Pb, Sn, Bi, Hg and Cd, using the pseudopotential method, make good sense of most of the observed structures. Kinks, in plots of $^{c}/_{a}$ and T_c against composition, in various systems are explained in terms of fermi surface-Brillouin zone interactions in the light of recent band-structure calculations. The general trends in T_c are also shown to be consistent with the density of states resulting from these band-structure calculations.

ACKNOWLEDGEMENTS

Acknowledgements are due to Professor J.G. Ball for the provision of research facilities in the Department and to the R.R.E., Malvern for financial support.

I take great pleasure in thanking my supervisor, Dr. H.W. King, for much useful discussion and encouragement in the course of this project. I also feel fortunate to have belonged to a research group in which such a general spirit of amity has existed. I should also like to express my thanks to individual members of this group for particular services. Mr. D.W. Penfold, Mr. B.J. Gunnell and, particularly, Miss Karen Gott have acted for me on many occasions, as a telephone link with the computer and Mr. P.L. Ormiston (when he was not reading the Azerbaijani Journal of Physics) acted as a, much needed, second pair of hands on the X-ray cryostat. I am also grateful to Dr. D.C. Larbalestier whose competent experimental advice was very helpful in my salad days as a postgraduate.

I have had more than my fair share of workshop time and would like to thank Mr. G. Green especially, for excellent workmanship. I would also like to thank Mr. F.G. Huggins for making up my silver-zinc alloys and I am sensible of the numerous other services he has performed for me in the past. For very kind treatment from the photographic department, I am indebted to Miss P. Martins. I would like to thank my father for, amongst other things, translating some German papers, and Mr. M.J. Losty for valuable advice on computer programming.

Finally, I cannot adequately express my gratitude to Theresa. Discovering that 'though this be madness, yet there is method in it' she has deciphered my confused and much corrected scribblings and made a most excellent job of typing this thesis. She has also assisted with a number of other tasks associated with the production of a thesis but I am most thankful for her forbearance and the cheerful encouragement given to me during the writing of it.

TABLE OF CONTENTS

INTRODUCTION

The theory of metals and alloys is principally concerned with the relative stability of competing crystal structures. The problem set by Nature is exceedingly difficult, since it appears that the energy differences between structures are very small and the theory has to be correspondingly detailed. Of particular interest are the structures that are somewhat distorted from the close-packed arrangements, notably the tetragonal distortions of FCC observed in indium and its alloys. The interest in indium arises because a considerable amount of quantitative information on this metal is available, in particular in relation to its band structure. It is of theoretical importance since it is characterised as a simple metal surrounded, in the periodic table, by other simple metals which in most cases have moderate or large solubility in it. The crystal structure (in particular, the axial ratio in the tetragonal phases) and the superconducting transition temperature are both dependent on the electronic structure and one can look for relationships between them.

An unfortunate aspect of the low melting point indium alloys is their relative softness as a result of which each grain in a powder is a single crystal. This results in a considerable loss of intensity which, together with the fact that diffraction profiles of indium suffer very much from thermal broadening at room temperature means that the evaluation of lattice parameters is subject to large error. The thermal problem may be circumvented by means of cryogenic diffractometry but in order to get over the large grain size problem it is necessary to illuminate a larger volume of specimen. This may be achieved, on a conventional diffractometer, merely by increasing the width of the divergence slit, except that considerable loss of resolution is then entailed. The fully-focusing (Seemann-Bohlin) geometry overcomes this difficulty, but the only equipment of this type recorded, is limited in the range of Bragg

angles available. It has, therefore, been necessary to construct a special diffractometer. To investigate the feasibility of the method and to take full advantage of it, it is necessary to be fully aware of all the possible sources of error and in consequence a general survey has been made of the errors and also the experimental conditions.

Because of the volume of arithmetic the calculation of the energy of a crystal structure would not have been possible a few years ago, even had the theory been sufficiently advanced. The advent of the high speed computer, however, now makes it possible to test the modern theories without much difficulty. The computer has not been neglected in the present project and, in particular, has been used to make a number of pseudopotential calculations on the indium alloys. These have achieved a measure of success except in the alloys with high concentrations of Pb or Tl. This success in distinguishing between competing structures cannot be emulated by fermi surface-Brillouin zone arguments. Discussion of the latter sort do, however, appear to be useful in the qualitative analysis of small anomalies in the observed properties of the alloys. These would seem to be determined by the fine details of the energy pattern which the pseudopotential method is unable to resolve.

CHAPTER 1

CHAPTER 1

REVIEW OF THE LITERATURE

1.1 THE ELECTRON THEORY OF METALS

This review is primarily concerned with those aspects of electron theory which have led to the present theories of the crystal structure of metals and alloys.

The beginnings of an electron theory of metals are to be found in a suggestion of Drude (1900), that the electrical and thermal properties of metals might be explained by the presence of field-free electrons. Early calculations of bulk properties, using Maxwell-Boltzmann statistics, by Lorentz (1904) were revised by Sommerfeld (1928) when the Pauli principle had shown Fermi-Dirac statistics to be more realistic. The success of the free electron model, in calculating electrical and thermal conductivities and electrothermal effects, was remarkable.

If an electron theory is to be used in the calculation of atomic properties, such as the stability of crystal structures, it must generate the total energy of a system. The new quantum mechanics allowed the exact solution of the energy equation for the hydrogen atom (Schrödinger (1926), Dirac (1928) whilst variational solutions, using sets of one-electron functions, were made for the many-electron single atoms by Hartree (1928) and Fock (1930).

The extension to multiatomic systems began with the treatment of the hydrogen molecule by Heitler and London (1927), in which two single atom wave functions were linearly combined. Another approach to the same problem, by Hund (1928) and Mulliken (1928), involved using a single wave function for the molecule rather than a combination of single atom orbitals.

Quantum mechanics was applied to the bulk crystalline solid in the elegant group theoretical proof of the famous theorem of Bloch (1928). Bloch assumed the atoms to be far enough apart to have no overlap of the free atom wave functions. The crystal was then represented by a linear combination of atomic orbitals (LCAO or the tight-binding approximation).

Another approximation which goes to the opposite extreme is the nearly-free-electron model introduced by Peierls (1930), in which the ionic potential acts as a small perturbation on an otherwise free electron system. The process was developed generally, in two and three dimensions by Brillouin (1930), who found it necessary to divide wavenumber space up, according to the Bragg reflection conditions, into 'zones'.

In order to calculate the total energy of a particular crystal structure Wigner and Seitz (1933) made the approximation that each electron moves in the field of a singly charged ion. The approximation is valid for monovalent metals because it is unlikely that two electrons will be found at the same lattice site. The method involves approximating the ion-electron interaction in the Hartree equations, in crystals with a high rotational symmetry, by a spherically symmetric potential. Crystal space is divided up into unit cells, analogous to the Brillouin zones in reciprocal space, each cell centred on an ion and the Hartree equations are solved within each unit cell.

In order to obtain the correct potential for calculations of the Wigner-Seitz type, Kuhn and Van Vleck (1950) suggested the use of spectroscopic information. The potential outside the core is treated as coulombic and two independent solutions of Schrödinger's equation are determined. The two solutions are coupled together in a linear combination, the coupling constant being determined at specific energies using the term values obtained from spectroscopic data on the free atom. The energies in the solid state are determined by interpolation or extrapolation. This approach is known as the 'quantum defect' method.

The limiting factor with any cellular model is the complexity of the boundary conditions and resultant doubts concerning convergence (Callaway (1963). An approach which seeks to circumvent the boundary condition difficulty is the variational procedure of Kohn and Rostoker (1954) who used a Green's function solution to an integral form of Schrödinger's equation, adapted to the cellular model. The approach is only feasible as a result of modern machine computation and has been applied to the alkali metals by Ham (1960).

Alternative approaches to the band-structure problem involve the expansion of the wave function in suitably chosen basis functions. The only functions that satisfy the Bloch condition with any facility are plane wave combinations, whilst close to the nucleus only spherical wave combinations are sensible. These considerations led Slater (1937) to propose a hybrid expansion of plane waves and spherical harmonics which led to the so-called 'augmented plane wave' method (APW). This has been further pursued by such authors as Howarth (1955) and Leigh (1956) but again the complexity of the mathematics restricted its development until the advent of the electronic computer.

In the meantime alternative expansions of plane waves were being used. The ordinary Fourier expansion of plane waves, in all but the very simplest models, showed great reluctance to converge and the convergence was always directed to the state of lowest energy. Herring (1940) pointed out that the wave functions of the conduction electrons must be orthogonal to those of the core electrons and suggested an expansion of plane waves orthogonalised to known core functions (the so-called OPW method).

Although the various energy band calculations described have had considerable success in understanding and predicting many of the electronic properties of materials (transport properties, optical properties, etc.), they have, nevertheless, had little success with the problem of the stability of crystal structure. The most promising approach in this direction is that of the

pseudopotential theory. Since much of the discussion of the present work will be couched in terms of the pseudopotential it is thought advisable to give a more thorough review of the basic theory.

1.2 THE THEORY OF THE PSEUDOPOTENTIAL

The remarkable applicability of the free-electron model to metals has already been mentioned. The success of the model is remarkable because the potential inside a metal is very far from constant, changing violently in the regions close to the ions. Clearly the conduction electron-ion interaction is somehow replaced by an effective weak potential - the pseudopotential. It can be seen how this arises using the OPW method (Harrison (1966).

The conduction band states may be given by an expansion of orthogonalised plane waves OPW_k given by

$$OPW_{\underline{k}} = |\underline{k}\rangle - \sum_{\alpha} |\alpha\rangle\langle\alpha|\underline{k}\rangle \qquad \ldots (1.1)$$

where $|\underline{k}\rangle$ is the plane wave to be orthogonalised to the set of core states $|\alpha\rangle$. Now if P is the operator, $\sum_{\alpha} |\alpha\rangle\langle\alpha|$, that projects any function on to the core states, then the wave function may be given as the expansion

$$\psi_{\underline{k}} = \sum_{q} a_q(\underline{k}) (1 - P) |\underline{k} + \underline{q}\rangle \qquad \ldots (1.2)$$

and Schrodinger's equation becomes (in the usual notation),

$$\sum_{q} a_q(\underline{k}) H (1 - P) |\underline{k} + \underline{q}\rangle = E_{\underline{k}} \sum_{q} a_q(\underline{k}) (1 - P)|\underline{k} + \underline{q}\rangle$$

which may be arranged in the form

$$T \phi_{\underline{k}} + W \phi_{\underline{k}} = E_{\underline{k}} \phi_{\underline{k}} \qquad \ldots (1.3)$$

where the 'pseudopotential' W is given by

$$W = V(\underline{r}) + (E_{\underline{k}} - H) P \qquad \ldots (1.4)$$

and the pseudo-wave-function ϕ by

$$\phi_{\underline{k}} = \sum_{q} a_q(\underline{k}) \, | \, \underline{k} + \underline{q} > \qquad \ldots (1.5)$$

or $$\psi_{\underline{k}} = (1 - P) \phi_{\underline{k}}$$

The second term in (1.4) is repulsive, opposing the attractive potential V and leaving the weak pseudopotential, a fact first pointed out by Phillips and Kleinman (1959). Equation (1.3) does not uniquely define the wave function ϕ and as a result the pseudopotential can be more generally defined (Austin, Heine and Sham (1962), by its operation on plane waves, as

$$W \, | \, \underline{k} > = V | \underline{k} > + \sum_{\alpha} f(\underline{k}, \alpha) < \alpha \, | \underline{k} > \, | \, \alpha > \qquad \ldots (1.6)$$

where $f(\underline{k}, \alpha)$ is an arbitrary function.

In order to produce a first-principles pseudopotential which could be used in low order perturbation theory with the best convergence, Harrison (1966) uses the smoothness criterion of Cohen and Heine (1961) in which the quantity

$$\int | \nabla \phi |^2 \, d\tau \Big/ \int | \phi |^2 \, d\tau$$

is minimised for optimum smoothness of the wave function. The resulting pseudopotential is

$$W = V + \sum_{\alpha} | \alpha \rangle\langle \alpha | \left(- \frac{\hbar^2 \nabla^2}{2m} + \langle \underline{k} | W | \underline{k} \rangle - E_{\alpha}\right) \quad \ldots (1.7)$$

It is readily seen that W is an operator and its appearance on both sides of the equation implies a self-consistent calculation. If W is replaced by a simple (algebraic) potential it is termed 'local'.

One very important property of the pseudopotential is that it can be represented as a sum of individual ionic potentials

$$W = \sum_{j} w(\underline{r} - \underline{r}_j) \quad \ldots (1.8)$$

Furthermore these ionic pseudopotentials, being the sum of the coulomb potential and a sum over all core states, are spherically symmetric.

Application of the Pseudopotential

In order to calculate the total energy of a crystal the sums of contributions due to the interactions of ions will be needed. These may be divided into the direct interaction of ions which gives rise to the electrostatic energy and the indirect (ion-electron-ion) interaction which is responsible for the 'band-structure energy'. The latter can be represented by an effective two-body central field potential which is readily built into the pseudopotential formalism, suggesting the suitability of the pseudopotential method for calculating atomic properties. Furthermore, calculations of the effective ion interactions reveal 'Friedel' oscillations of quite long range

in the crystal. The APW and Kohn-Rostoker methods are implicitly short range and hence of little value in computation of atomic properties.

The relative simplicity of the pseudopotential method arises out of the ability to reduce all the interactions in a body (or a liquid) to an effective interaction between a pair of ions. This results in a set of 'form-factors' $v(q)$ being ascribable to each element. These form-factors are the matrix elements of the ionic pseudopotential which scatters an electron from $|\underline{k}\rangle$ to $|\underline{k} + \underline{q}\rangle$. They may also be thought of as the Fourier transform of the ionic pseudopotential. The complexity of any pseudopotential calculation lies in the determination of these form-factors.

The presently accepted form-factors have been derived by Animalu and Heine (1965) using a model potential (which although not a potential of the general kind (1.6), can still be thought of as a pseudopotential) proposed by Heine and Abarenkov (1964).

The Heine-Abarenkov (HA) model is essentially a quantum-defect method in which the region near the ion is treated as a black box, the details of the potential inside being unimportant. A simple model potential can replace the black box if it can reproduce the observed properties outside the box.

In the HA procedure an electron is added to a free ion of charge Z, the eigenstate of the electron being specified by quantum numbers ℓ and m. If a sphere of radius R_M is inscribed around the ion the eigenstate outside will be completely described by ℓ, m, the energy E and the logarithmic derivative of the wave function at R_M. If the potential inside the sphere is replaced by a constant $-A_\ell$ (E) (the potential outside being coulombic i.e. $-Ze^2/r$) such that the eigenstate $j_\ell(\kappa r)$ ($\kappa = (\frac{2m}{\hbar^2}(E + A_\ell(E)))$ has the same logarithmic derivative at R_M, then the energy eigen values for states outside this sphere will be the same as in the free ion.

In the bulk crystalline solid the HA method is to choose a sphere

radius R_M greater than the core and smaller than the unit cell. The potential $-A_\ell$ is adjusted until the lowest energy eigenstate belonging to ℓ has an energy equal to the observed term value (from spectroscopic data) for the bare ion plus one electron. The process is repeated for term values of higher energy and the value of $A_\ell(E)$ determined for energies other than the term values, by interpolation or extrapolation.

The HA method has one great advantage in that the core electron-valence electron exchange and all correlation effects within the core are accounted for automatically. All that is required is to allow for exchange and screening amongst the conduction electrons. If the HA pseudopotential, for the bare ion, is represented by a Fourier transform $v^b(g)$, then the conduction electron charge density is directly related to it by Poisson's equation. A self-consistent calculation reduces $v^b(g)$ to

$$v(g) = v^b(g) / \varepsilon(g) \qquad \ldots (1.9)$$

$\varepsilon(g)$ being the screening factor, in the Hartree approximation, and usually called the dielectric constant. The Hartree function is (Harrison 1966)

$$\varepsilon(g) = 1 + \frac{me^2}{2\pi k_F \hbar^2 \eta^2}\left[\frac{1-\eta^2}{2\eta}\ln\left|\frac{1+\eta}{1-\eta}\right| + 1\right] \qquad \ldots (1.10)$$

where k_F is the Fermi wavenumber and $\eta = g/2k_F$.

For a non-local pseudopotential, however, more complex treatments are necessary. Heine and Abarenkov employed the Hubbard (1957) approximation to obtain the dielectric function $\varepsilon_2(g)$

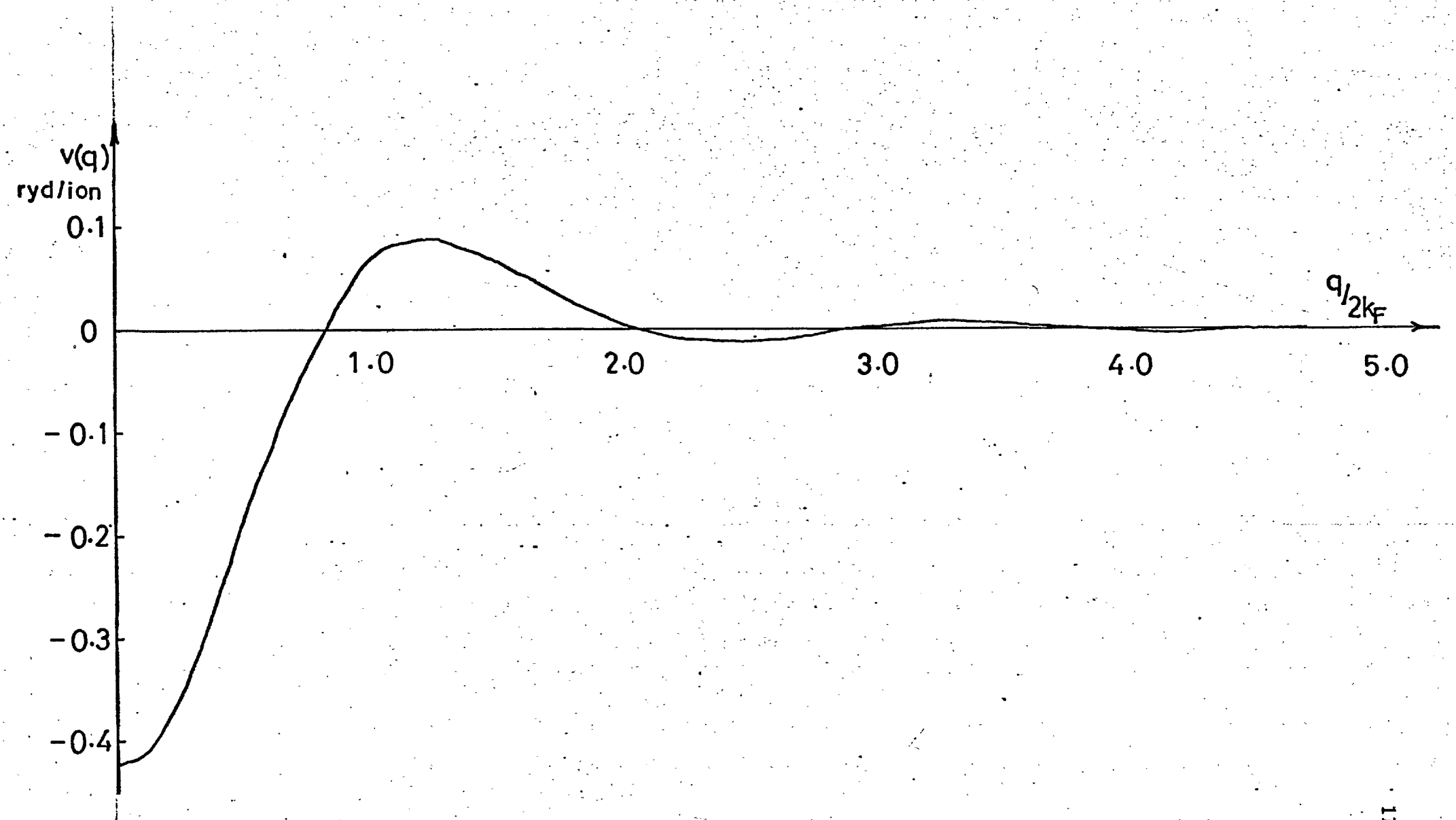

Figure 1.1 A plot of the Animalu and Heine form factors for indium.

$$\varepsilon_2(g) = 1 + (1 + \alpha)\ \frac{8\pi e^2}{\Omega_0 g^2}\left[1 - \frac{\frac{1}{2}g^2}{g^2 + k_F^2 + k_s^2}\right]\chi(g) \qquad \ldots (1.11)$$

where

$$\chi(g) = \frac{Z}{2}\left\{\frac{2}{3}E_{fo}\right\}^{-1}\left[\frac{1}{2} + \frac{1-\eta^2}{4\eta}\ln\left|\frac{1+\eta}{1-\eta}\right|\right]$$

and k_s^2 is half the square of the Thomas-Fermi screening length or $k_s^2 = \frac{2k_F}{\pi}$ atomic units. The charge distribution in the core is not uniform because of oscillations of the wave function in the core which leads to a reduced density there called the 'orthogonalisation hole'. A corresponding heaping-up of charge to $Z(1 + \alpha)$ ($\alpha \sim 0.1$) occurs outside the core which explains the appearance of this factor in (1.11).

The form-factors $v(q)$ have been calculated for twenty-nine simple elements by Animalu and Heine (1965) and Animalu (1966) using the Heine-Abarenkov model. The function for indium, which is rather typical, is shown in Fig. (1.1).

The Band-Structure Energy

The 'band-structure' energy arises from the indirect (ion-electron-ion) interaction and since it involves two ion-electron interactions is clearly proportional to $v(q)^2$. In second order perturbation theory the energy is given by

$$E(\underline{k}) = \frac{\hbar^2 k^2}{2m} + \langle \underline{k}|W|\underline{k}\rangle + \sum_{\underline{q}}{}' \frac{\langle \underline{k}+\underline{q}\ |W|\underline{k}\rangle\langle \underline{k}\ |W|\underline{k}+\underline{q}\rangle}{\hbar^2/_{2m}(k^2 - |\underline{k}+\underline{q}\ |^2)} \qquad \ldots (1.12)$$

The first two terms are the structure independent free-electron

terms and since the only concern is with structurally dependent energies, they will be ignored. Furthermore, the pseudopotential may be broken down into ionic pseudopotentials

$$\langle \underline{k} + \underline{q} \,|\, W(\underline{r}) \,|\, \underline{k} \rangle = S(\underline{q}) \langle \underline{k} + \underline{q} \,|\, w \,|\, \underline{k} \rangle \qquad \ldots (1.13)$$

where $S(\underline{q})$ is the crystallographic structure factor

$$S(\underline{q}) = \frac{1}{N} \sum_j e^{-i\underline{q} \cdot \underline{r}_j} \qquad \ldots (1.14)$$

for N ions. The third term in the HA formalism becomes

$$E(\underline{k}) = \sum_{\underline{q}}' \frac{|S(\underline{q})\, v(q)|^2}{\underline{k}^2 - (\underline{k} + \underline{q})^2}$$

(the prime on the sum indicating that the term with q = 0 is to be omitted)

If this is integrated over all $\underline{k}$ within the Fermi sphere (no error occurs to second order in the sphere approximation - see Heine (1969) for example) then the band structure energy is

$$E_{bs} = \sum_{\underline{q}}' |S(\underline{q})\, v(q)|^2 \chi(q)$$

where $\chi(q)$ is given in (1.11) and if exchange, correlation and screening are introduced, the final form of the band structure energy per ion (Heine (1969) is

$$E_{bs} = \sum_{\underline{q}}' |S(\underline{q})\, v(q)|^2 \chi(q)\, \epsilon_2(q) \qquad \ldots (1.15)$$

The direct electron-electron interaction energy is included

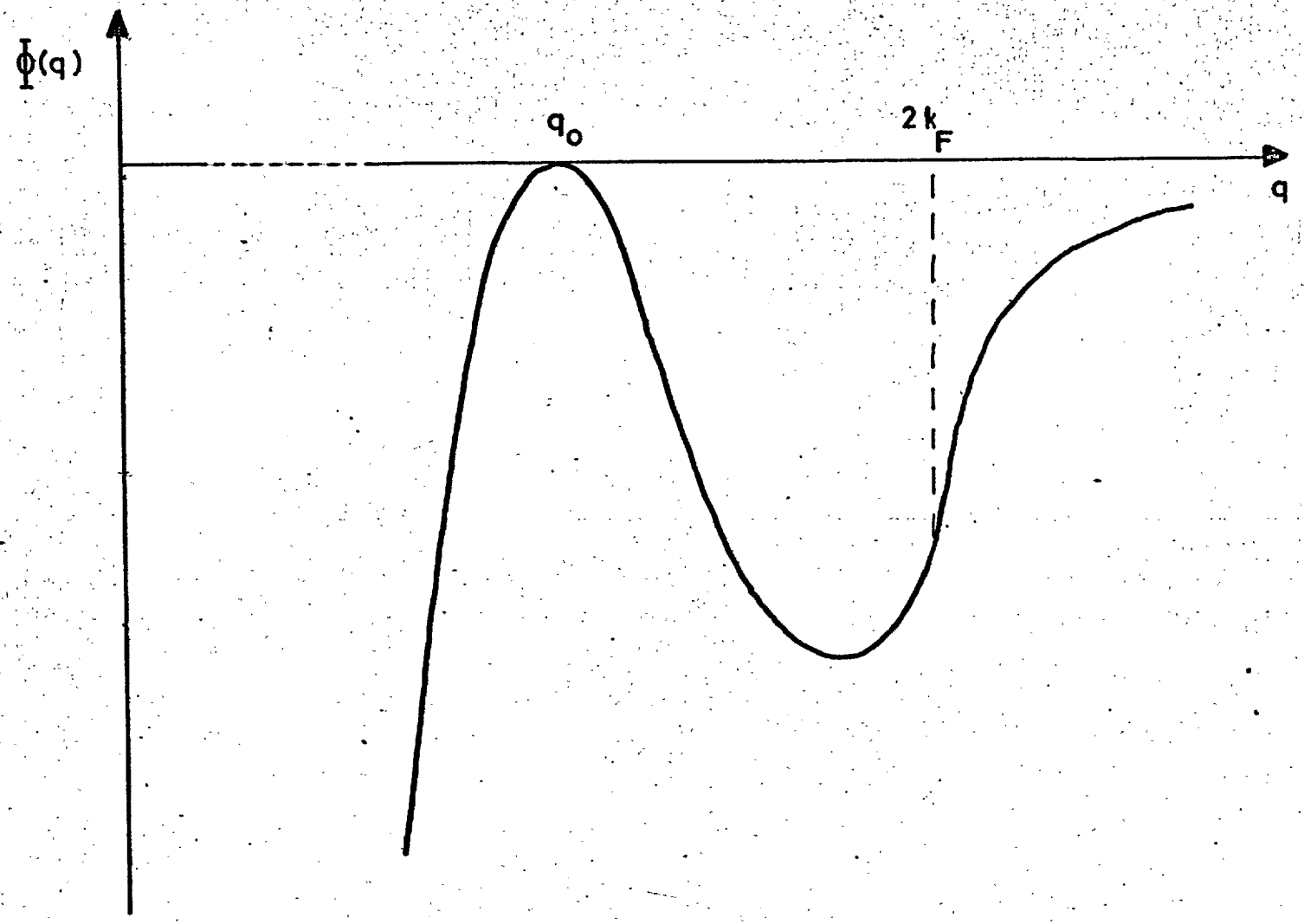

Figure 1.2 The energy-wavenumber characteristic of indium (from Heine, 1969).

in this expression. The direct ion-ion interaction (electrostatic) energy requires quite separate treatment and will be developed, for the particular structures under consideration, in a later section (Chapter 5).

The quantity $v(q)^2\ \chi(q)\ \varepsilon_2(q)$ in (1.15) is known as the 'energy-wavenumber characteristic' $\Phi(q)$ and this is shown for indium in Fig. (1.2). Heine and Weaire (1966) were able to qualitatively compare the stabilities of different structures for divalent and trivalent metals, by superimposing a spectrum of the structure factor on the characteristic $\Phi(q)$. The structure which appeared to have the greatest structural weight $(P(q)\,|\,S(\underline{q})\,|$ where $P(q)$ is the multiplicity factor) avoiding the maximum at q_o (Fig. 1.2) or lying close to the energy minimum, was considered to be the most stable.

Application to Alloys

From Harrison (1966) the pseudopotential may be written as the sum of the ionic potentials of type A at positions $\underline{r}_{iA}$ and type B at positions $\underline{r}_{iB}$:-

$$W(\underline{r}) = \sum_{iA} w_A(\underline{r} - \underline{r}_i) + \sum_{iB} w_B(\underline{r} - \underline{r}_i)$$

The matrix elements of W are now given by

$$\langle \underline{k}+\underline{q}\,|\,W\,|\,\underline{k}\rangle = \frac{1}{N}\sum_{iA} e^{-i\underline{q}\cdot\underline{r}_i}\langle \underline{k}+\underline{q}\,|\,w_A|\,\underline{k}\rangle + \frac{1}{N}\sum_{iB} e^{-i\underline{q}\cdot\underline{r}_i}\langle \underline{k}+\underline{q}\,|\,w_B\,|\,\underline{k}\rangle \quad \ldots (1.16)$$

or

$$\langle \underline{k}+\underline{q}\,|\,W\,|\,\underline{k}\rangle = \frac{1}{N}\sum_{i} e^{-i\underline{q}\cdot\underline{r}_i}\langle \underline{k}+\underline{q}\,|\,w_A|\,\underline{k}\rangle + \frac{1}{N}\sum_{iB} e^{-i\underline{q}\cdot\underline{r}_i}\langle \underline{k}+\underline{q}\,|\,w_A - w_B\,|\,\underline{k}\rangle \quad \ldots (1.17)$$

The first sum in (1.17) is over the average lattice generated by all the $\underline{r}_i$, ignoring the difference between atoms. The second sum is only over the B atoms. If $\underline{q}$ is a wavenumber, $\underline{q}_o$, of the average lattice then $e^{-i\underline{q}_o \cdot \underline{r}_i}$ is unity at each ion position so that from (1.16)

$$\langle \underline{k} + \underline{q}_o \,|\, W \,|\, \underline{k} \rangle = (1 - c) \langle \underline{k} + \underline{q}_o \,|\, w_A \,|\, \underline{k} \rangle + c \langle \underline{k} + \underline{q}_o \,|\, w_B \,|\, \underline{k} \rangle \qquad \ldots (1.18)$$

where c is the fractional composition of B atoms in the alloy. If q is not on the wavenumber lattice then $S(\underline{q})$ is zero and (1.17) gives

$$\langle \underline{k} + \underline{q} \,|\, W \,|\, \underline{k} \rangle = \frac{1}{N} \sum_{iB} e^{-i\underline{q} \cdot \underline{r}_i} \langle \underline{k} + \underline{q} \,|\, w_A - w_B \,|\, \underline{k} \rangle \qquad \ldots (1.19)$$

Effectively (1.18) is an 'average' term whilst (1.19) is a 'difference' term. When the equivalent of (1.15) for the band structure energy comes to be formulated these average and difference terms will appear again.

The average band structure energy is

$$E_{bs} = \sum_{\underline{q}_o}{}' \left| S(\underline{q}) \; \overline{v(q)} \right|^2 \overline{\chi(q)} \; \overline{\varepsilon_2(q)}, \qquad \ldots (1.20)$$

where $\overline{v(q)}$ is obtained by averaging as in (1.18) whilst $\overline{\chi(q)}$ and $\overline{\varepsilon_2(q)}$ are found using average values of the valence. The 'difference' band structure energy is given by

$$E_{bsa} = \sum_{q} \left| S_B(\underline{q}) \; v_a(q) \right|^2 \overline{\chi(q)} \; \overline{\varepsilon_2(q)} \qquad \ldots (1.21)$$

where the summation is over all $\underline{q}$ not on the wavenumber lattice and

$v_a(q)$ is the difference or 'alloying' pseudopotential. Harrison (1966) shows the structure factor S_B to be given by

$$| S_B(\underline{q}) |^2 = \frac{c\,(1-c)}{N}$$

for a disordered alloy (N being the number of ions). Since the summation in (1.21) is over all $\underline{q}$ it can be taken over into the integral (Inglesfield (1969):

$$E_{bsa}(\text{disordered}) = \frac{c\,(1-c)\,\Omega_o}{2\pi^2} \int q^2\, \Phi_a(q)\, dq \qquad \ldots (1.22)$$

where $\Phi_a(q)$ is the alloying energy-wavenumber characteristic

$$\Phi_a(q) = | v_a(q) |^2\, \overline{\varepsilon_2(q)}\; \overline{\chi(q)} \qquad \ldots (1.23)$$

Recent developments in the theory of the pseudopotential include the calculations by Shaw and Harrison (1967) of the orthogonality correction α for a number of elements. Shaw (1968) has evaluated new form factors, for a limited number of elements, using an optimised HA model. The alloy problem has been investigated further by Inglesfield (1969, 1970) in a study of ordering processes and intermediate compounds in various divalent metal alloy systems.

1.3 SUPERCONDUCTING TRANSITION TEMPERATURE

The complete disappearance of electrical resistance, in a number of metals, at a particular temperature, was first observed by Onnes (1911). The second manifestation of the phenomenon known as superconductivity, was noticed by Meissner and Ochsenfeld (1933). Prior to their experiments it had been observed that, below its transition temperature, a superconductor excluded (virtually) all magnetic field from its interior. The explanation of this had, naturally, been ascribed to eddy currents on the infinitely conducting surface of the specimen, but Meissner and Ochsenfeld, however, demonstrated that the field was actually expelled from the specimen when the transition to superconductivity occurred.

London (1935, 1937), recognising that the two phenomena (superconductivity and flux expulsion) were quite distinct manifestations of the same transition, and further noting that the usual relationship between flux density $\underline{B}$, and magnetisation $\underline{M}$ (usual, that is for all but ferromagnets) was not applicable, proposed a phenomenological formalism. In this $\underline{B}$ was related to a density of 'supercurrent' which led to a new relationship between $\underline{M}$ and $\underline{B}$, the solution of which, for a slab of material in a uniform field, showed a rapid exponential fall-off quite untypical of ordinary diamagnets and characterised by a penetration depth λ.

A superconductor equivalent of Ohm's Law relating electric field to the rate of change of the density of supercurrent was also formulated by London to allow for the phenomenon of persistent ring currents.

In an attempt to find some theoretical basis for the successful London equations, Ginzburg (1945) and later Ginzburg and Landau (1950) proposed a two-fluid model consisting of normal and 'super' electrons. Assigning the density of superelectrons to the square modulus of a 'wave function' for superelectrons and finding the expectation value

of the kinetic energy (including a term due to the vector potential A) these authors developed a free energy equation. Minimisation of the free energy gave rise to a set of self-consistent equations of the Hartree-Fock kind. The general equations required numerical solution but the weak field solution was analytic and resolved to an equation, for the supercurrent density, identical with that suggested by London. The theory also predicted a modification to the London penetration depth which fitted later measurements. A better fit was obtained using an effective charge, of the superelectrons, equal to twice the electronic charge. The success of the Ginzburg-Landau model was surprising and very interesting because the main assumption of the theory was that all the superelectrons were given by the same wave function. This could only mean that the 'superelectrons' were not fermions!

The theorists, who were looking for a 'microscopic' (fundamental quantum mechanical) theory for the superconductor, also noted three other features of interest. From surface energy considerations and observations on the sharpness of the transition, Pippard (1953) had proposed another characteristic length, several orders of magnitude greater than the London depth, and which he called 'coherence length'. Further, in order to make sense of the London equations the diamagnetic current rings must be considered to be of the same order of size as the bulk of the superconductor. The third property, demonstrated amongst other things by the frequency threshold of infra-red absorption, was the suggestion of a very small energy gap ($\sim 10^{-3}$ eV).

Preliminary considerations of the properties prompted theorists to look for correlations between electrons, the obvious correlation being the electron-electron coulomb interaction. Various attempts at developing a theory on the basis of this interaction were made (see Blatt (1964), p. 39 for references) but none were successful.

Frohlich (1950) paved the way to the present microscopic theory, by reminding physicists of the cause of electrical resistance, in particular that a perfect lattice has no resistance. The principal

imperfection involved is the thermal vibration - i.e. electrical resistivity is due to electron-phonon scattering. Frohlich suggested that an indirect electron-electron interaction (electron-phonon-electron) might be of importance in superconductors. Analogous theories exist in nuclear physics for the interaction of nucleons (by emission and absorption of a virtual meson). In the light of this suggestion sense could be made of the fact that only bad conductors become superconductors, since the good conductors have only a weak electron-phonon drag. Furthermore, since lattice dynamics is involved, the mass of the ions should be important. It was thus of great interest that, independently of Frohlich's theory, Reynolds et al (1950) and Maxwell (1950) discovered the isotope effect, where the superconducting transition temperature is found to be inversely proportional to the square root of the isotopic mass.

The next milestone in the development of a microscopic theory came when Ginzburg (1952, 1953) and Feynman (1953) independently demonstrated that the ideal Bose-Einstein gas in the condensed state exhibits a Meissner effect. Such a gas, however, shows a permanent magnetic moment above its condensation point, quite unlike the magnetisation behaviour of superconductors in the normal state. If a quasi-boson system exists then the particles must vanish in the normal state. It was clear then that the number of bosons had to become an additional variable to be dealt with by the methods of second quantisation. This factor was more obviously important when it was realised that the condensation temperature was considerably greater than the superconducting transition temperatures ($\sim 10^4\ ^{o}K$).

Phonons and excitons are obvious candidates for the required quasi-boson, but for their electrical neutrality. The first real suggestion of an electron pair was made by Schafroth (1954) and Cooper (1956) showed that an electron pair can form a stable bound state provided there is at least a weak electron-electron attraction. The now famous theory of Bardeen, Cooper and Schrieffer (BCS) (1957) did not, however, use a state of an electron pair but, rather, introduced the concept of paired single electron states. The creation of pairs

was not performed by a single operator but by a whole set of operators characterised by a given momentum $\underline{k}$. Furthermore the only pair creations considered were those which led to zero momentum singlet states, that is correlations of equal and opposite momenta and opposite spin. BCS used a reduced Hamiltonian in which only the matrix elements connecting these pairs were considered and the energy was minimised by a variational procedure.

The BCS theory was able to demonstrate the right order of magnitude for the critical field, $H_c(0)$, and also showed that the Pippard coherence length can be interpreted as the average distance between members of an electron pair. Furthermore, the theory readily produced an energy gap in good agreement with experiment for the type of excitation used.

A more detailed approach was made by Bogoliubov, Tolmachov and Shirkov (1958) in which the specific (virtual phonon) nature of the coupling was incorporated and perturbation calculations were made from the proper ground state, the condensed pair state, rather than from the Fermi-sea state. Both theories produced the same expression for the transition temperature T_c, i.e.

$$T_c = 0.344\ \theta_D \exp\left(-\tfrac{1}{\rho}\right) \qquad \ldots (1.24)$$

where θ_D is the Debye temperature and ρ is the 'coupling constant' which BCS gave as proportional to the density of states at the Fermi surface (at $0^{\circ}K$), $N(0)$, and the interaction potential V. The BCS theory also showed that the isotope effect is implicit in equation (1.24) since θ_D is directly related to a cut-off frequency ω_c, which is proportional to $M^{-\frac{1}{2}}$, M being the isotopic mass.

The Bogoliubov theory demonstrates an upper limit to the coupling constant (0.5) which was later shown by Zubarev (1960) to be equivalent to an upper limit to the transition temperature, precluding the possibility of room temperature superconductors.

The microscopic theory of superconductivity is sufficiently well developed to allow, at least in principle, the calculation of T_c from properties of the normal metal. In practice, however, these normal state properties (the electronic band structure near the Fermi surface, the phonon dispersion curves, the screened electron-phonon interaction and the screened electron-electron coulomb interaction) are not sufficiently well known. An important paper on the theory of the transition temperature has been written by McMillan (1967), who takes the opposite view that the T_c is an accurately known quantity and may thus be used for the determination of normal state properties. He devised the following equation for T_c in terms of an electron-phonon coupling constant (or mass enhancement) λ and the screened pseudopotential μ^* of Morel and Anderson (1962):

$$T_c = \frac{\Theta_D}{1.45} \exp\left[\frac{-1.04\ (1+\lambda)}{\lambda - \mu^*\ (1 + 0.62\ \lambda)}\right] \quad \ldots (1.25)$$

The pseudopotential term arises out of a treatment of the coulomb interaction between electrons and numerical values of μ^* are obtained from measurements of the isotope shift. Hence from a knowledge of T_c and Θ_D, λ can be extracted and since this quantity is directly proportional to the density of states at the Fermi surface, some insight into the band structure can be obtained.

Carbotte and Dynes (1968) set out to make a realistic assessment of λ. To do this they fitted phonon dispersion curves, obtained from inelastic neutron scattering experiments, to a Born-von Kármán model. The treatment of the electron-phonon interaction requires matrix elements of the electron-ion interaction potential which Carbotte and Dynes replaced with the Animalu-Heine pseudopotential form factors. With these calculations they were able to predict T_c for Al and Pb to within 10% of the experimental result.

Allen and Cohen (1969) developed a model to obtain λ, in which an undistorted Fermi surface was used and a Debye sphere replaced the phonon Brillouin zone (i.e. completely spherical symmetry was assumed). Phonon dispersion curves were taken from the neutron scattering data of Iyengar et al (1965). Recognising the non-uniqueness of the pseudopotential they tried fitting various empirical pseudopotentials as well as the Heine-Animalu form factors. These show reasonable agreement with experiment (especially for the divalent hexagonal metals) and introduce the interesting possibility of superconductivity in lithium and magnesium.

The corresponding theory for the prediction of T_c in alloys is much less advanced. Matthias (1957, 1960) has observed interesting regularities when T_c is related to such quantities as the total number of electrons outside the inert gas shell, the volume per atom and the mass of the average atom, but no theory has so far been developed to explain these correlations.

Chanin, Lynton and Serin (1958) observed a uniform depression of T_c for dilute (less than 1 at.%) solutions of impurity elements in indium (except in the case of gallium) and aluminium, while Lynton, Serin and Zucker (1957) have reported a similar effect in tin alloys. To explain these results Anderson (1959) has proposed a theory for 'dirty' superconductors based on the energy gap anisotropy. The electron interaction, being via phonons, must be dependent on the direction of the electronic momenta relative to the lattice. The addition of impurities rapidly smears the electron states over the Fermi surface and smooths out the anisotropy. Markowitz and Kadanoff (1963) have based calculations on the Anderson model, attributing the behaviour of T_c to two effects. One is a gradual change of the gross parameters of the system (e.g. ω_D and ρ) the other is an abrupt reduction in anisotropy. The first effect, the 'valence effect', causes a linear change in T_c of either sign whilst the second effect, called the 'mean-free-path effect', causes a sudden decrease of Tc. The anisotropy reduction is evaluated by a rather complex calculation and the two contributing (or competing) effects are combined. Adjusting parameters

representing the relative strengths of the two effects, Markowitz and Kadanoff were able to fit curves quite closely to the experimental results.

1.4 FERMI SURFACE-BRILLOUIN ZONE INTERACTIONS

Alloy theory will have reached one of its main goals when it is capable of justifying and even predicting the stable crystal structures in an alloy phase diagram. It has long been evident that the cohesion of metals is an electronic effect and that consequently the detailed nature of the electronic structure is very important. A vast amount of effort has been put into the investigation of the band structure of metals and, but for one or two exceptions, the prediction of the most stable crystal structure (of a number of possibilities) has remained elusive. The reason for this is that the difference in energy between any two of the three common metallic structures (FCC, BCC and HCP) is very small.

Most alloy theory has been only semi-quantitative and has made use of such parameters as the difference in atomic size (Hume-Rothery, Mabbott and Channel-Evans, 1937), electronegativity (Hume-Rothery et al, 1940) and the density of electron states at the fermi surface (Jones, 1934). The main consideration will be with the variation of structure across a single system in which case the first two factors are less important and the dominant factor is then the density of states.

Jones (1937) demonstrated the importance of the density of states by showing that primary solid solutions based on copper and silver suffer a breakdown in structure at the electron-to-atom ratio for which the FCC and BCC structures have the same density of states.

A basic assumption of the Jones model, however, was that of

the rigid band structure. Furthermore, the fermi surface was effectively assumed to be nearly spherical, not quite touching the zone boundaries in FCC copper when later measurements of the surface by Pippard (1957) showed that in reality it was already well in contact with the zone in pure copper.

Cohen and Heine (1958) salvaged the Jones model by rejecting the rigid band (no change in shape of the density of states curve on alloying) and making a rough estimate of the energy difference between the s and p states at the centre of the nearest zone faces. E_s and E_p were calculated, using the s-p excitation energy and the quantum defect method. Two effects of alloying were visualised, a change in E_p or a filling-up of the band structure. The former would have the effect of pulling the fermi surface away from the zone faces, whilst the latter would do the reverse. Cohen and Heine were unable to say which effect should predominate.

Deviations from Ideal Axial Ratio in HCP

One of the interesting factors requiring explanation by an alloy theory is the occurrence of the non-ideal axial ratio in HCP structures and the small tetragonal distortion from FCC such as those observed in indium alloys.

The electrostatic energy for HCP was shown by Harrison (1966) to be minimum at the ideal axial ratio (1.633) as had always been intuitively assumed. An explanation of the distorted HCP was attempted by Jones (1934) who proposed that electrons overlapped certain faces of a modified Brillouin zone for the structure, exerting a back pressure on those faces resulting in distortion. This model was successful in explaining the observed axial ratio trends in the ϵ and η phases in the Cu-Zn system.

Goodenough (1953) noted that the low temperature lithium structure was distorted HCP (Barrett and Trautz, 1948) yet a one-electron sphere

would imply no overlap of electrons into the second zone. Consideration of this and of the complex hexagonal ζ-phase in Ag-Zn led Goodenough to propose that, if the fermi surface is close to an energy discontinuity, then the total electron energy will be decreased by moving the discontinuity (zone face) towards the origin of k-space. The volume is kept constant by a compensating movement of other planes, with only small increases in electronic energy, resulting in a change of axial ratio. The movement of the planes was thought of as an effective interaction between the fermi surface and the Brillouin zone.

Although Goodenough describes detailed mechanisms for the effect of contact McClure (1955) has pointed out a detailed knowledge of the band structure would be necessary to decide whether the total energy is thereby increased or decreased. McClure derives an 'effective stress' operating on the zone faces using the Hartree-Fock approximation. This stress is divided up into a small electrostatic term, a roughly estimated exchange term and a term called 'kinetic' stress which is the stress of Jones and Goodenough. McClure's semi-quantitative discussion of the effects of alloying on axial ratios, although differing in spirit from the Jones argument, differs very little in its conclusions. The McClure procedure is to expand the energy of the structure in terms of an effective stress and a single elastic constant, the latter being obtained experimentally. In treating the alloy a similar process was adopted. The value of such calculations is somewhat doubtful since it seems to have replaced one problem by an equally intractable one. The elastic constant is a function of the band structure just as much as is the axial ratio.

1.5 INDIUM AND ITS ALLOYS

Theoretical Considerations

In the last decade or two, more and more attention, both experimental and theoretical, has been paid to the polyvalent simple metals (e.g. Pb, Sn, In, Cd). This has been due in part to the availability of high purity specimens (with long mean free paths) whilst the applicability of low order perturbation theory has also attracted the theoretician to these metals.

The metal indium has thus been investigated extensively. An unusual feature of this metal is its crystal structure, which is, strictly, body centred tetragonal but is more conveniently (and fundamentally) recognised as tetragonally distorted FCC with an axial ratio about 1.08, i.e. quite close to unity. Just why this distortion should occur has been the subject of much discussion, mostly in terms of the behaviour of the fermi surface at the boundaries of the Brillouin zone, using the model of Jones (1934) described earlier (section 1.4). The rigid band model used by Jones has achieved a measure of success in alloys based on Cu, Ag and Au but is less applicable to the polyvalent simple metals and consequently less success is to be expected in justifying the distortion in indium. It has already been seen (section 1.2) that the structurally important terms in the energy expansions for the simple metals (equation 1.12) are the second order terms in the perturbing potential. These are exactly the terms ignored in a rigid band approximation. Furthermore, the rigid band approximation becomes less valid the closer the fermi surface is to the zone boundaries (Raimes, 1962) and is, therefore, less valid for the polyvalent metals.

In the various models for indium, the density of states at the fermi surface, $N(E_F)$, is assumed to play a dominant role in determining the relative energy changes on alloying. Many electronic properties, notably the thermoelectric power and the superconducting transition temperature T_c, depend upon $N(E_F)$ and the models have been used to

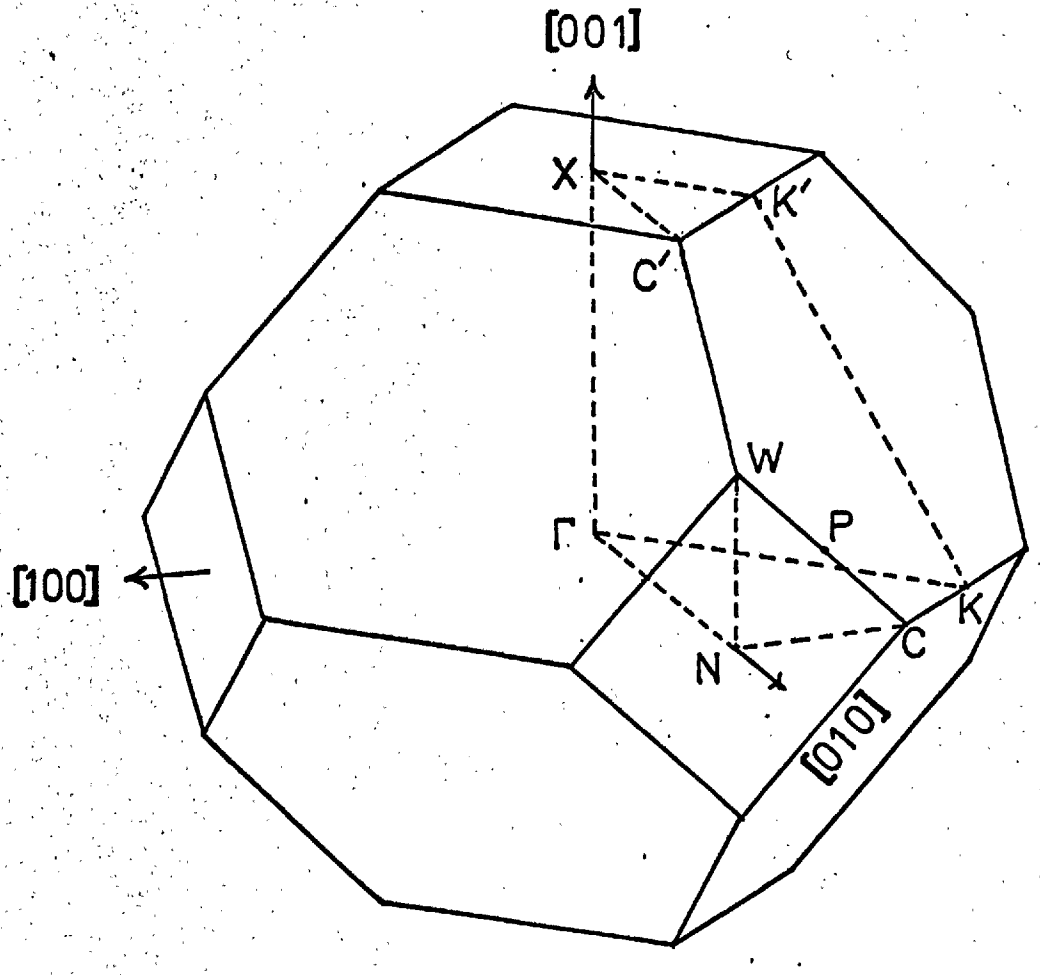

Figure 1.3 The Brillouin-zone for the indium structure (after Hughes and Shepherd, 1969).

explain the various experimental correlations of these properties with composition and axial ratio. The superconductivity measurements in particular indium alloy systems will be reviewed at the end of this section.

Besides being invoked to explain general axial ratio trends, the models have also been used to account for abrupt kinks or changes of slope in the T_c and axial ratio plots with composition. The first instance of a fermi surface model for indium being used for discussion of this kind, appears in a paper by Tomasch and Reitz (1958), who attempted to explain a series of deviations from a smooth curve for their thermoelectric-power plot against composition in In-Pb.

In the absence of direct measurements of the topography of the fermi surface in indium, Tomasch and Reitz suggested that this surface overlaps both the {111} and the {002} faces of the Brillouin zone (illustrated in Figure 1.3). The effect of alloying with lead was considered to complete the filling of the first zone points C' whilst further kinks were related to overlap at N and filling of the corners W successively. Later de Haas-van Alphen measurements by Brandt and Rayne (1964), however, demonstrated that indium was nearly-free-electron like in nature and hence approximates closely to the first four band zone picture (for free electrons) shown in Figure (1.4) which is clearly inconsistent with the proposals of Tomasch and Reitz. Whatever the fine details of the fermi surface, it is unlikely that the second zone hole surface will be very different from the nearly closed surface of the free electron model.

Merriam (1963), in attempting to explain small kinks in T_c and lattice parameter plots in In-Sn, suggested that the fermi surface was not as free-electron like as Rayne's (1963) measurements indicated. In particular he suggested that certain extremal dimensions could be interpreted as first zone holes rather than third zone electrons. His interpretation involved the filling-up of these first zone holes and overlap into the third zone at the corners C' and W (four zones are coincident at these points).

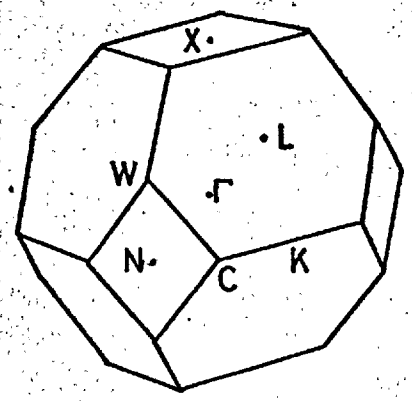

First zone (full)

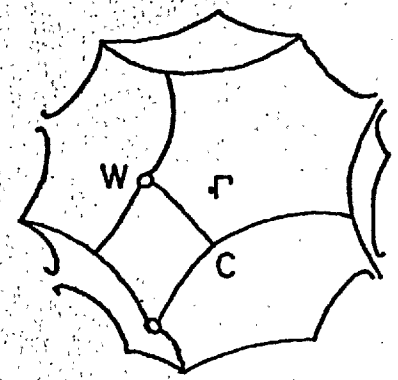

Second zone (hole surface)

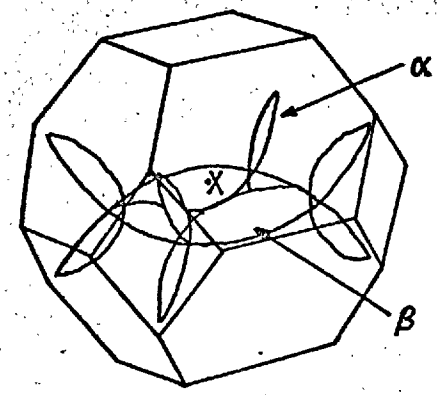

Third zone electron surface
(centred on X)

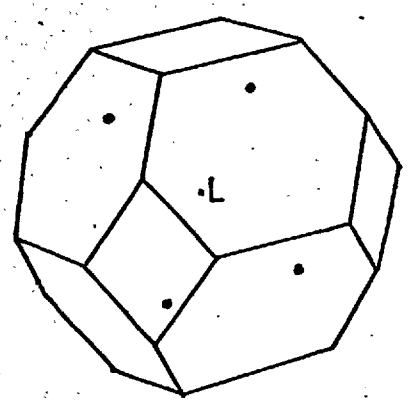

Fourth zone electron pockets
(centred on L)

Figure 1.4 The free electron zones for the first four bands of indium.

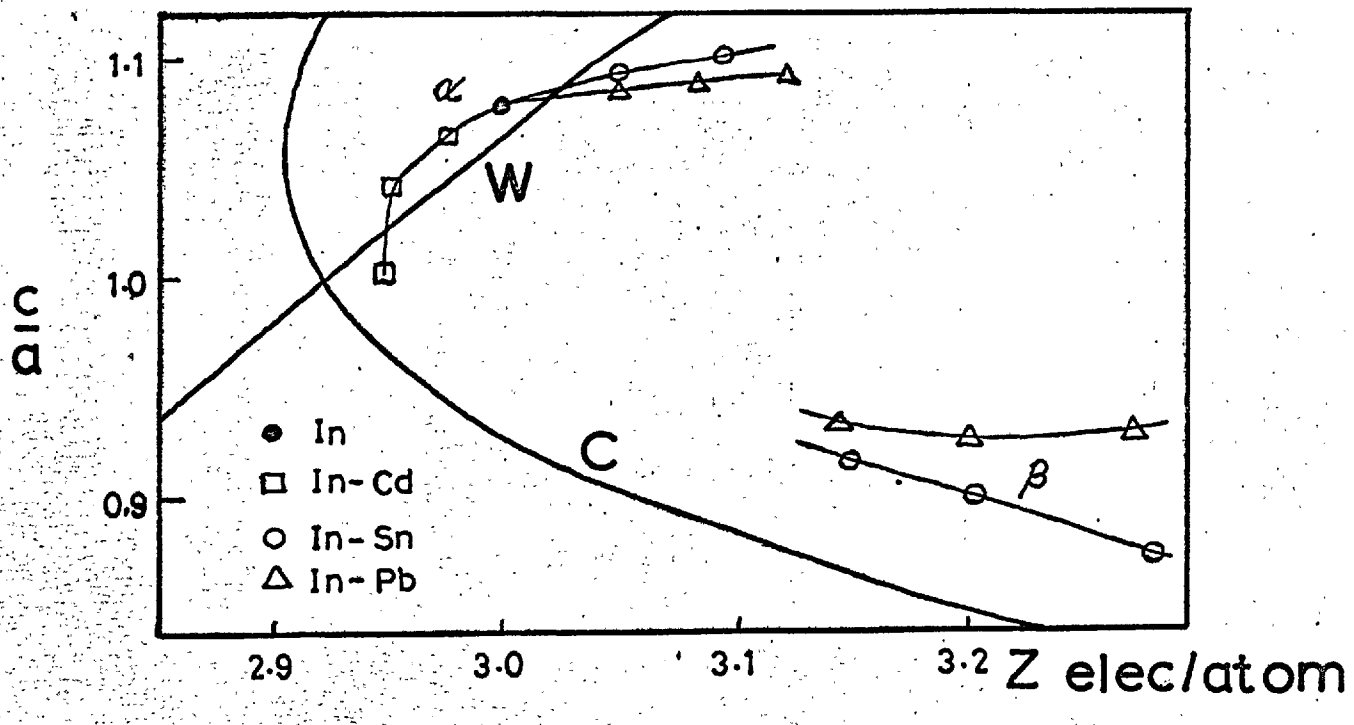

Figure 1.5 Illustrating the Svechkarev model for indium alloys.

The later band structure calculations of Hughes and Shepherd (1969) have invalidated this proposal by showing the first zone to be full.

Svechkarev (1965) proposed a model, based on the fermi surface measurements of Rayne (1963), which approximated the free electron picture very closely (see Figure 1.4). Proposing that the critical regions of the surface were at the zone corners, Svechkarev drew a pair of graphs (Figure 1.5) representing the axial ratios at which a free electron sphere would remain in contact with the corners (C and W) of the zone. Experimental values of axial ratio for various solutes are included in the Figure and the valence shifts required to bring these points on to the graphs were interpreted in terms of the energy gap at the corners. Furthermore, the assumption of free electrons implies that the corners C and, depending on the degree of tetragonality, the corners W, should be just occupied in the fourth zone.

A detailed criticism of the Svechkarev paper will not be attempted but a number of points may be made. The behaviour of the indium alloys in the region Z = 2.95 to 2.98 was interpreted in terms of the fermi surface sticking to the corner W in the first zone with a consequent adjustment of the axial ratio. Because the experimental curve in this region is roughly parallel to the model curve, Svechkarev concludes that the energy gap must remain the same but does not state whether he is considering the gap between the first and second zone or between the first and third. In other words the band structure remains rigid, which presumably could happen by coincidence even though the rigid band is not a general feature of the polyvalent simple metals.

A second point is that Svechkarev virtually ignores the third zone in his discussion whereas the most recently available band structure calculations indicate this zone to be most important.

Ashcroft and Lawrence (1968) fitted a phenomenological pseudopotential form-factor to the de Haas-van Alphen data of Brandt and

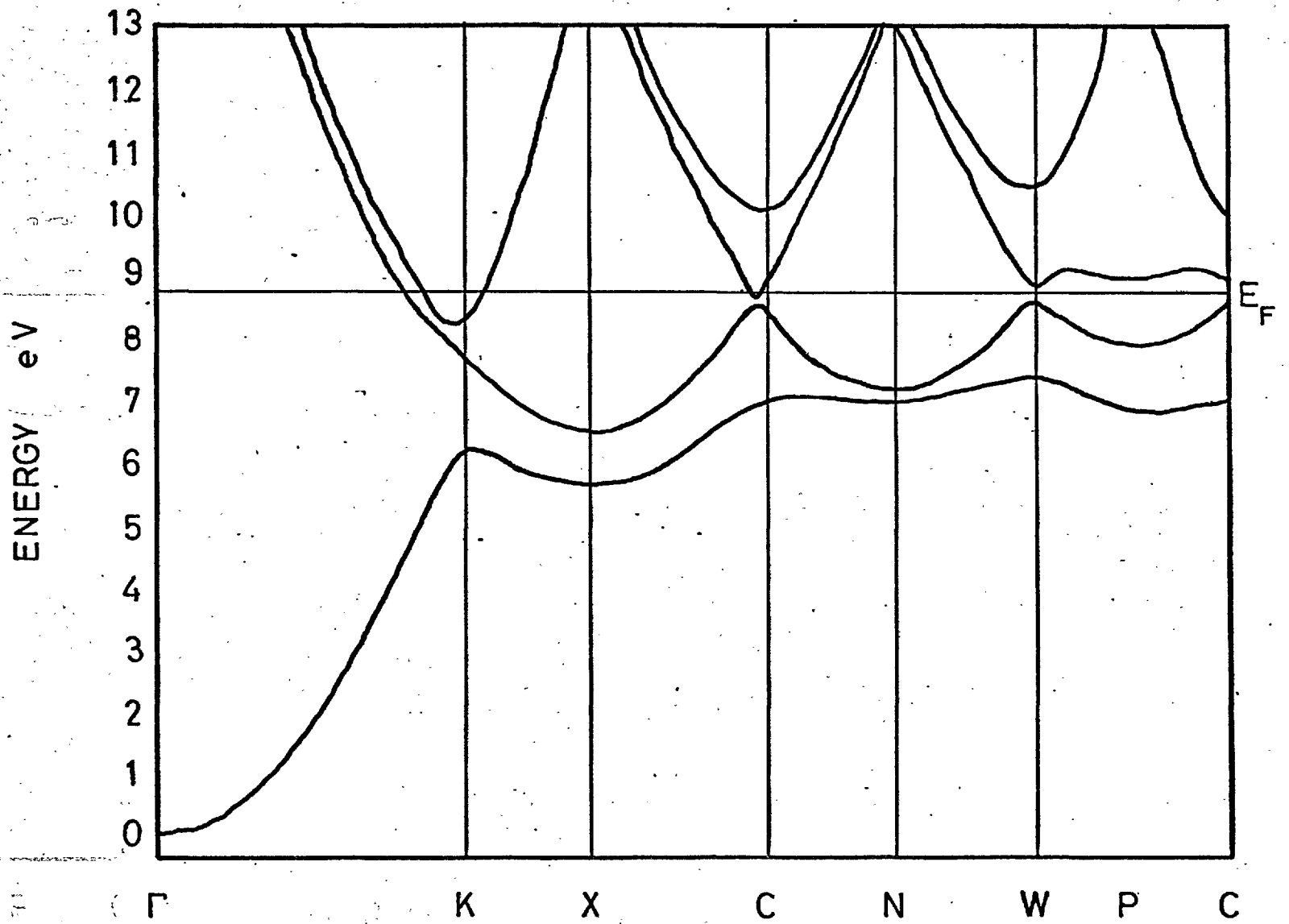

Figure 1.6 The band-structure of indium (from Hughes and Shepherd, 1969)

Rayne (1964). Two functions were found to fit the data, one of which indicated that the so-called α arms (Figure 1.4) do not exist in pure indium, whilst the other indicated the existence of very small α arms. The lowest energy level of the fourth band, in either case, is significantly above the fermi level (~ 1.5 eV). The Svechkarev proposal of fourth band pockets of electrons is, therefore, unrealistic. Some multiple connectivity was apparent at the corners of the zone and consequently the second zone hole surface was not considered to be closed. Hughes and Shepherd (1969), however, clarified the picture by making fresh de Haas-van Alphen measurements. They, too, fitted a pseudopotential to the data, but included a spin-orbit interaction correction in the manner of Anderson and Gold (1965). They concluded that the α arms did not exist and that previous experimental evidence for them was due to polycrystallinity of samples (Shepherd,(1969). Furthermore, the spin-orbit interaction correction closed the second zone hole surface which Gaidukov (1966) had already concluded from his failure to find any open orbits in his magnetoresistance work.

The band structure resulting from the pseudopotential of Hughes and Shepherd is shown in Figure (1.6). It can be seen that the β arms come near to C and in fact they appear to form closed rings.

It can now be seen that all the models used to explain alloying behaviour are invalidated by the experimental facts. The Svechkarev picture is the most interesting but the discussion appears to be too detailed for the amount of information available at the time. Even the band structure calculations of Ashcroft and Lawrence (1968) and Hughes and Shepherd (1969) differ in the sort of fine detail that is required to explain the singularities in axial ratio and T_c plots. This writer considers, however, that the Svechkarev approach still has some value in a qualitative discussion of these singularities.

It may justifiably be asked: "Why, if fermi surfaces can be measured accurately, there is any need for the models attempting

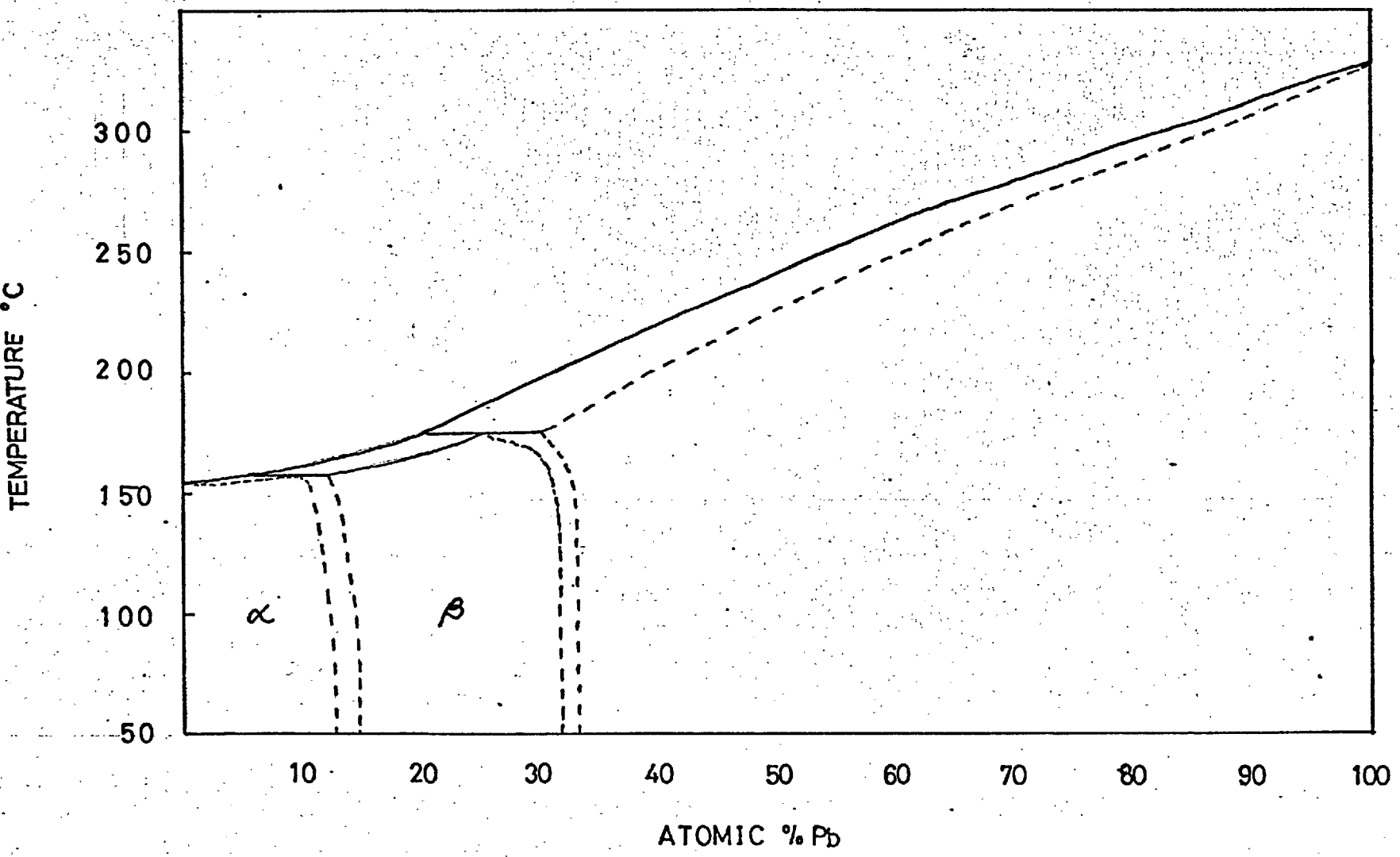

Figure 1.7 The phase diagram of the system indium-lead (from Hansen, 1958).

to describe the effect of alloying on the fermi surface?" The reason is the great difficulty in making de Haas-van Alphen measurements in the presence of impurity scattering. In order to circumvent this difficulty it is necessary to increase the magnitude of the magnetic field used in these measurements. The existence of high field superconducting magnets should enable the fermi surface in alloys to be measured.

The System Indium-Lead

The phase diagram for indium-lead alloys is taken from Hansen (1958) and shown in Figure (1.7). There are three solid phases: the indium solid solution (α), extending to about 12 at.% Pb, has the face centred tetragonal (FCT) structure with axial ratio, c/a, greater than unity (~ 1.08); an intermediate phase (β), extending from 12 at.% to 33 at.% Pb, is also FCT but with c/a less than one (~ 0.92); beyond 33 at.% Pb the structure merges into the FCC lead solid solution.

The structure of the α phase has been examined at 18°K, at seven compositions up to 11 at.% Pb, by Russell (1966) using a precision X-ray diffractometer technique. The α-β phase boundary was examined, in the temperature range 200 - 145°C, by Moore et al (1955) and found to be a two phase region, the α-β transition being thought to be diffusionless second order.

The only lattice parameter data available for the β phase are five Debye-Scherrer results, at different compositions, given by Tyzack and Raynor (1954). No diffractometer or low temperature work has been reported on this phase.

Apart from two values, at about 14 % Pb near the α-β phase boundary, given by Merriam (1963), no T_c data are available for the β phase. These two points were found to lie on a smooth extrapolation of the T_c/composition curve for the α phase.

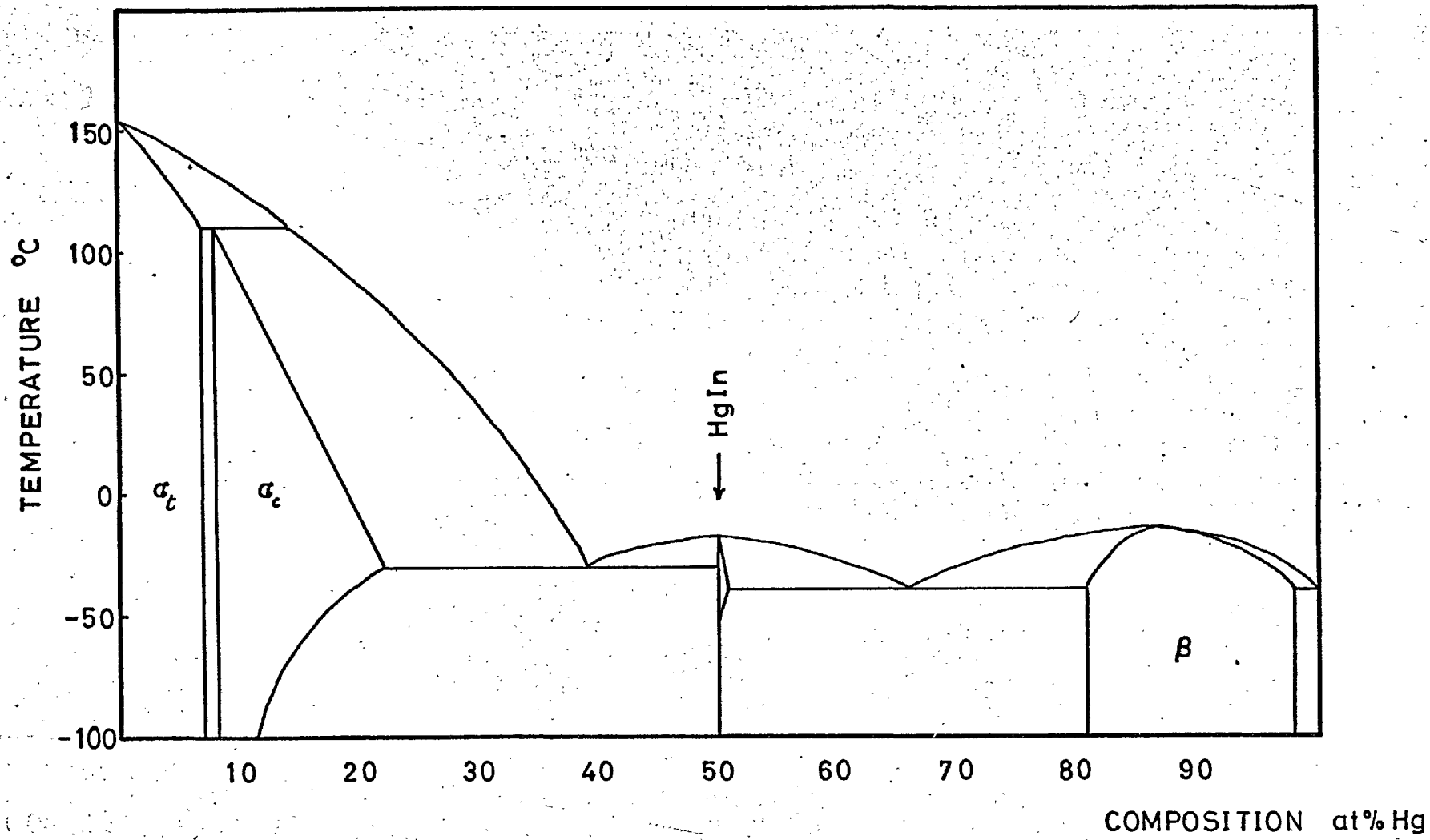

Figure 1.8 The phase diagram of the system indium-mercury (from Shunk, 1969).

The System Indium Mercury

The phase diagram of this system, shown in Figure (1.8) and taken from Shunk (1969), was established using thermal analysis, X-ray measurements and T_c measurements.

The solubility limit of indium in mercury was estimated at about 0.3 at.% while the crystal structure of the β substitutional solid solution and the HgIn compound have not yet been identified. At the indium rich end, the α_c phase is FCC and the indium solid solution α_t is FCT. The α_c and α_t phases are separated by a narrow two-phase region. The only available X-ray data for these two phases are the room temperature Debye-Scherrer results of Tyzack and Raynor (1954). A steady fall of axial ratio, from 1.0757 to 1.0429, was observed with increasing Hg concentration up to 6 at.%, when the structure transformed abruptly to FCC, no two-phase region being observed.

The superconducting transition temperatures for dilute indium mercury alloys were measured by Reeber (1960) and showed the initial decrease with alloying observed by Chanin et al (1959) except that the drop was not sharp from the pure indium value. The initial decreasing trend is reversed at about 2% Hg, an effect which usually occurs only for impurities of higher valence than the solvent (Lynton, 1969). The system was studied by Merriam, Jensen and Coles (1963) who measured T_c across the entire phase diagram and confirmed the results of Reeber (1960) for the indium rich alloys.

Merriam et al also pointed out the reproducible discontinuity in T_c and $\partial T_c/\partial x$ in the mercury rich β phase at a composition x = 11% indium. They interpreted this as a Fermi surface-Brillouin zone effect of some kind, but were unable to check if lattice parameters showed a similar kink because the structure was unknown.

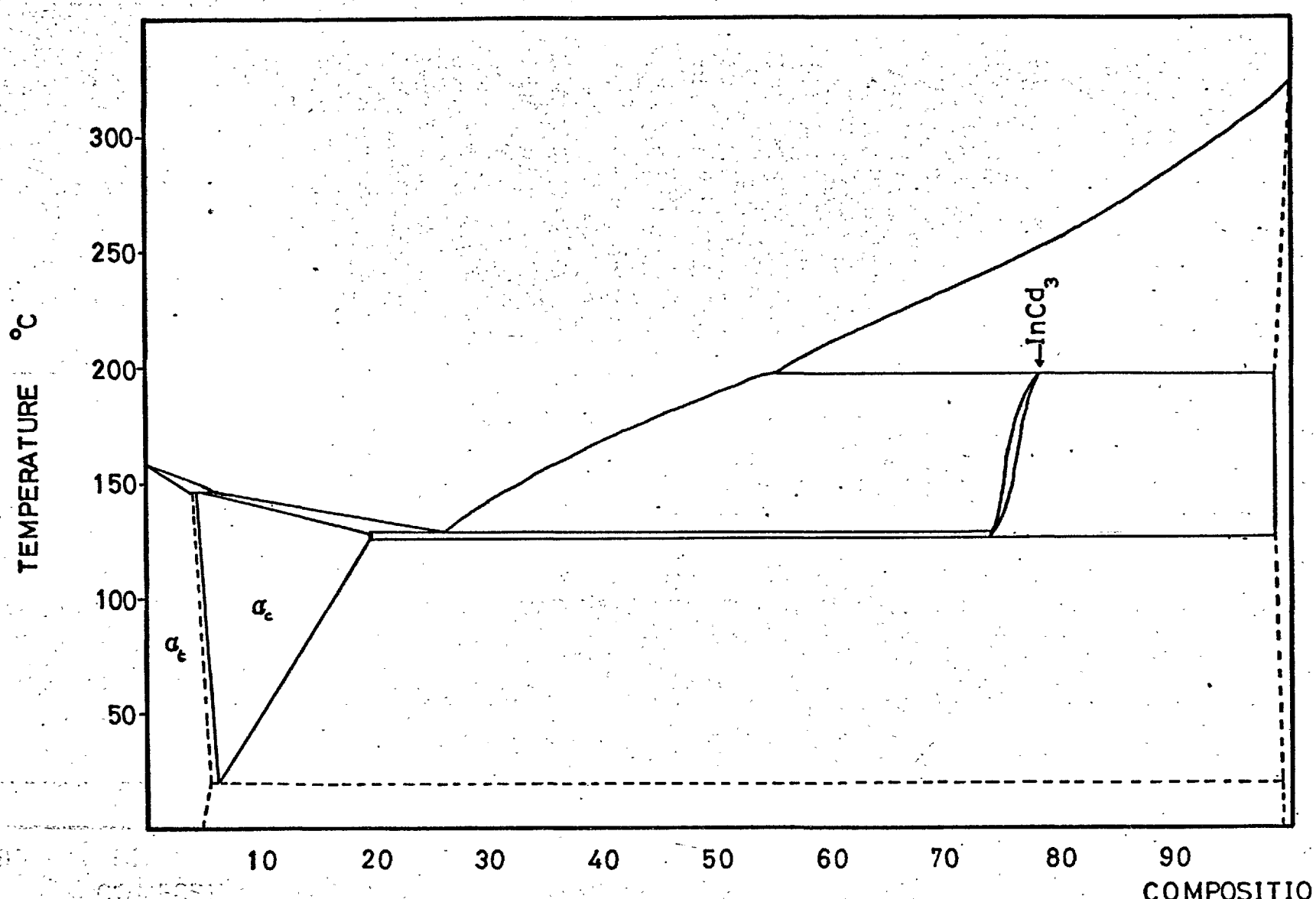

Figure 1.9 The phase diagram of the system indium-cadmium (from Shunk, 1969).

The Indium-Cadmium System

The phase diagram for the system, taken from Shunk (1969), is shown in Figure (1.9). The indium solubility in cadmium is less than 3%. Apart from the compound $InCd_3$, which is unstable below 126°C, there is a two-phase region up to 80% indium when the face-centred cubic α_c phase appears. The phase diagram shows (Figure 1.10) a narrow two-phase region between the indium FCT solid solution α_t and α_c.

Merriam (1966) investigated T_c for these alloys from 0% to 60% Cd and noticed a kink in the region of 2% Cd which he interpreted in terms of the Svechkarev model. Lattice parameters were measured and, although the accuracy was 'rather poor', a corresponding kink was observed at 2% Cd. Verkin and Svechkarev (1965) also detected an anomaly in their diamagnetic susceptibility measurements at this composition. Ridley (1967), using a Debye-Scherrer camera, measured lattice parameters across the region of the T_c kink and was able to show a corresponding kink in c, a and c/a but not in the volume of the unit cell.

The Indium-Tin System

The phase diagram taken from Shunk (1969) is shown in Figure (1.10). The structures of the β and γ phases have not been identified with certainty.

Merriam and von Herzen (1963) investigated the system for transition temperatures T_c and noticed a change in slope of the T_c/composition plot at about 8% Sn. In a later paper Merriam (1963) published a lattice parameter plot showing a pronounced 'wiggle' in the same region. A similar plot was given later, Merriam (1964) for an anomaly in indium lead at about 7% Pb but this was criticised by Russell (1966) because the lattice parameter plots implied an abrupt change in a plot of unit cell volume against composition which was thought to be inconsistent with the

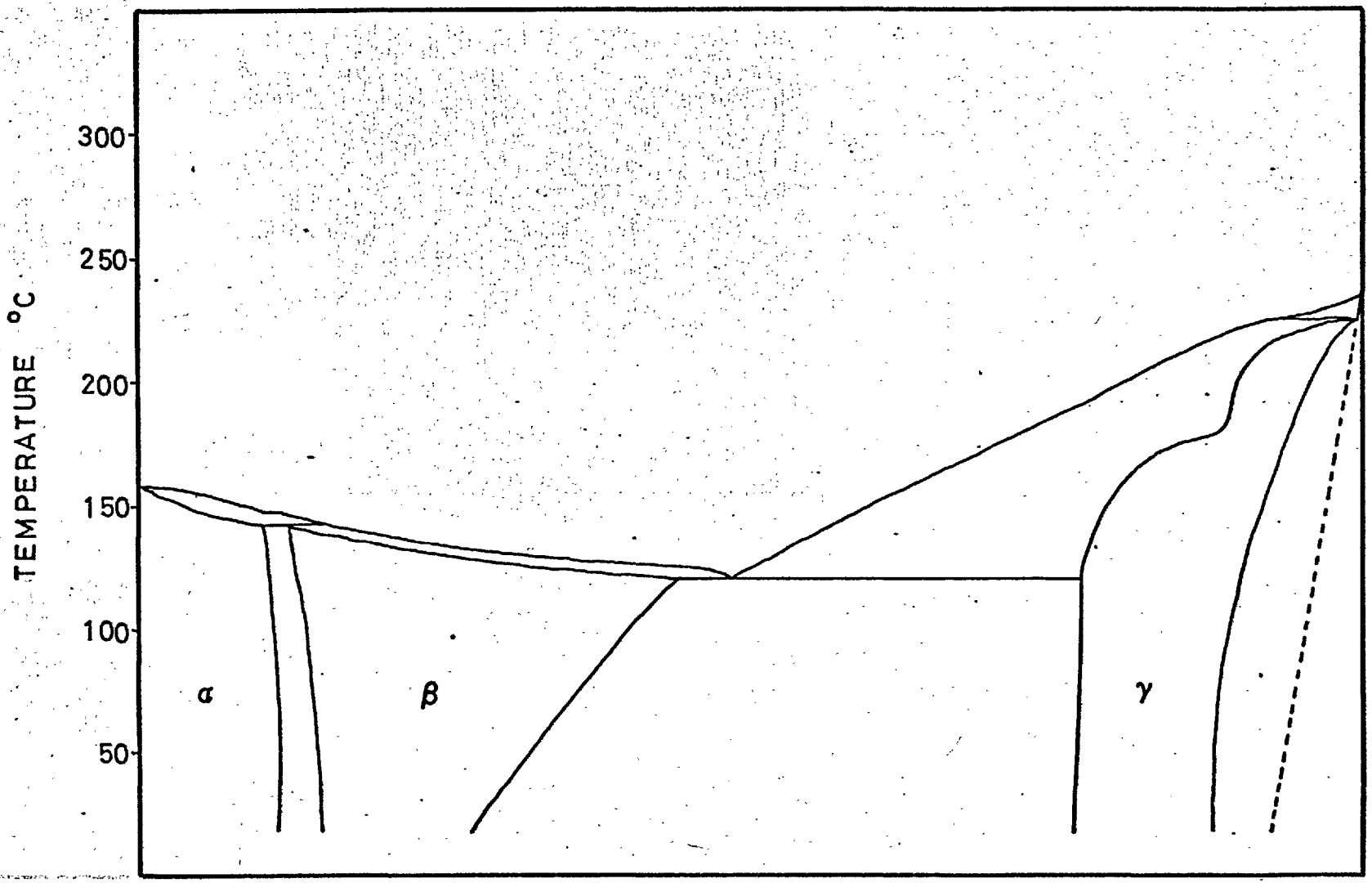

Figure 1.10 The phase diagram of the system indium-tin (from Shunk, 1969).

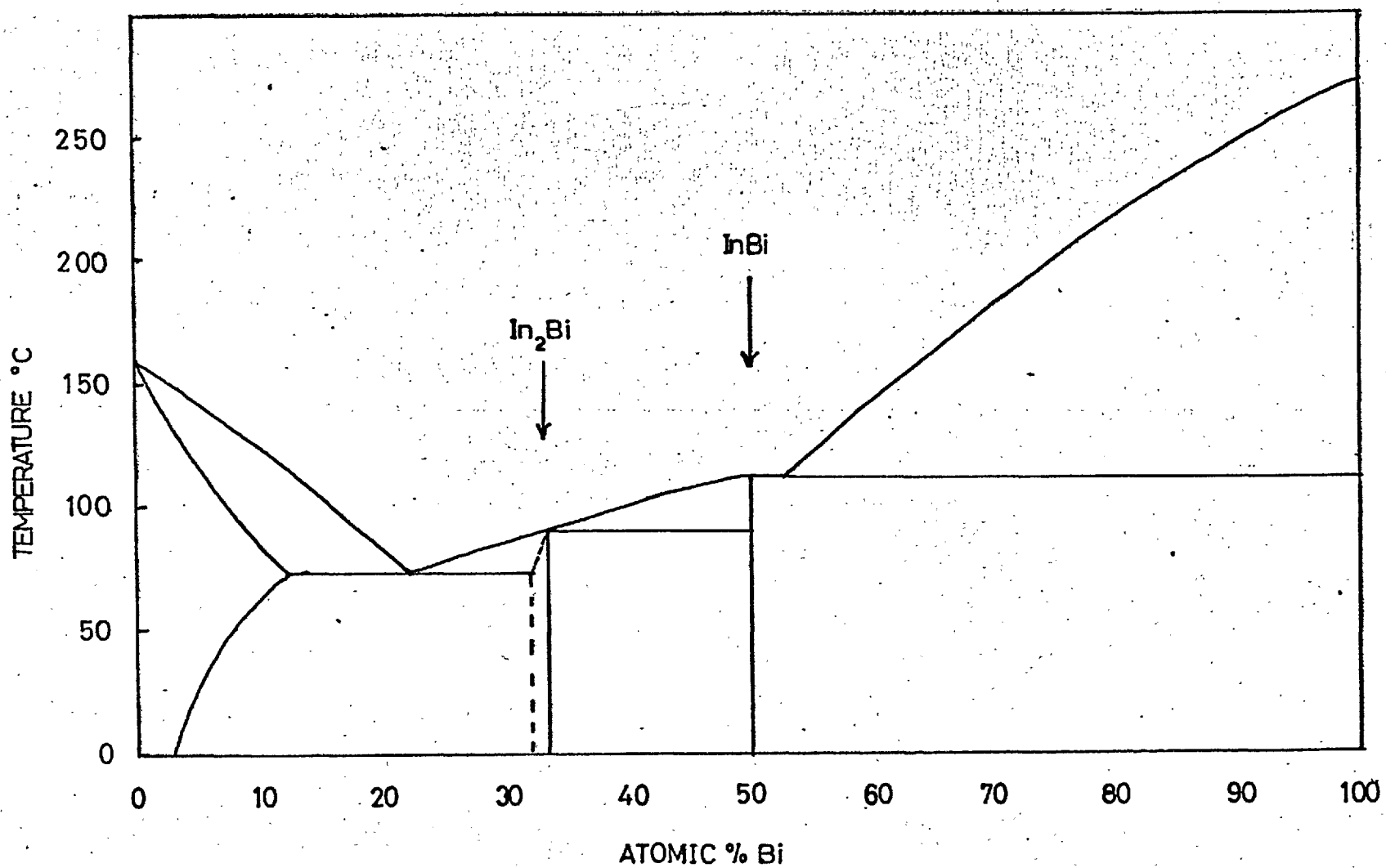

Figure 1.11 The phase diagram of the system indium-bismuth (from Hansen, 1958).

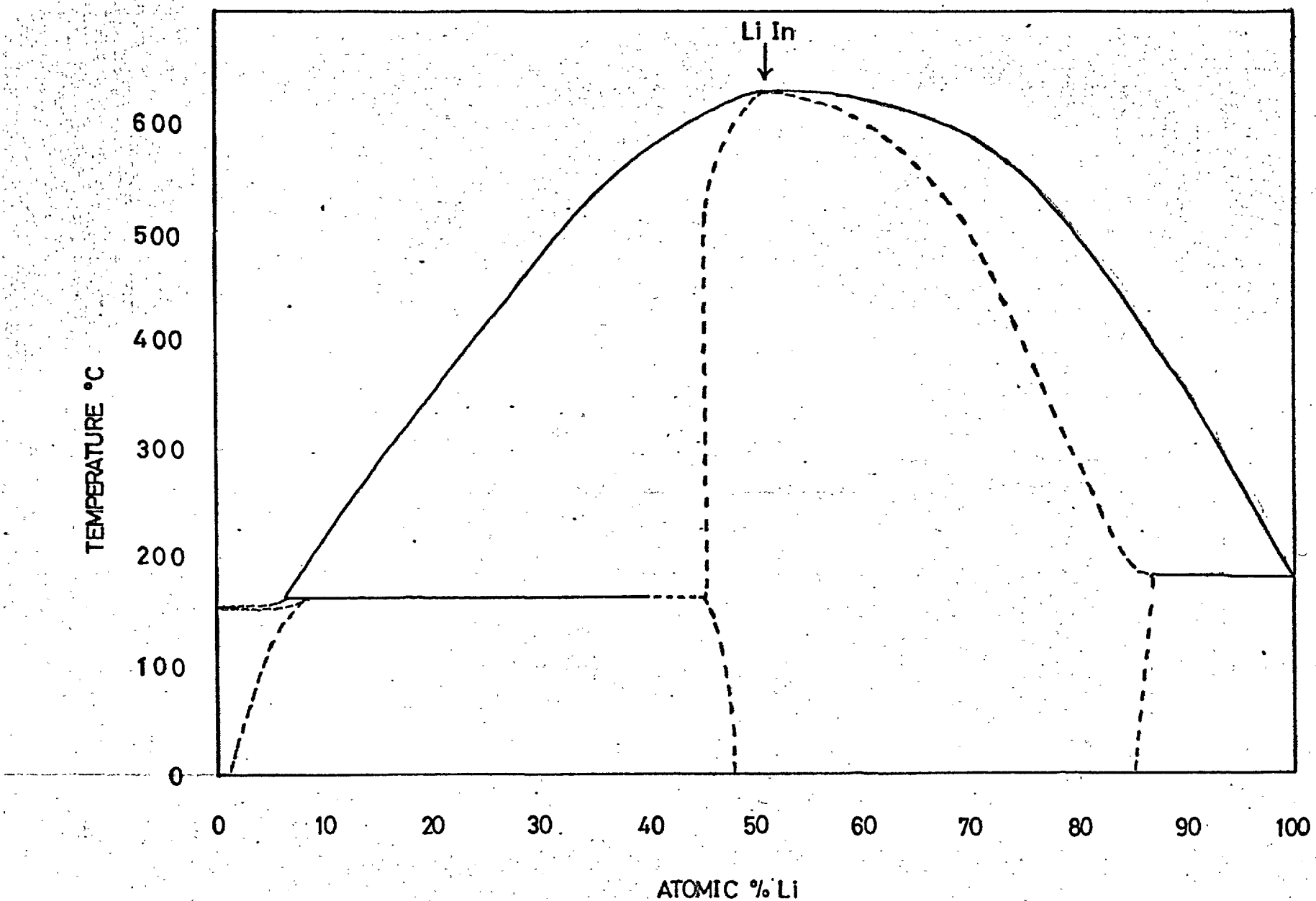

Figure 1.12 The phase diagram of the system indium-lithium (from Hansen, 1958).

kind of energy change likely to occur due to small changes in the density of states. The same criticism would seem to apply to his In-Sn plots and perhaps with even more validity as in these the c and a parameters rise and fall together.

The Indium-Bismuth System

The phase diagram for indium-bismuth is taken from Hansen (1958) and shown in Figure (1.11). There are two intermediate compounds InBi with a tetragonal PbO (B10) structure and In_2Bi which is complex hexagonal.

The only lattice parameter determinations in the indium phase are due to Peretti and Carapella (1949) who used a Debye-Scherrer method for four compositions. The only T_c measurements that appear to have been made are those of Chanin, Lynton and Serin (1959), up to 0.3 at.% Bi. These appear to conform to the general pattern for 'dirty' superconductors (Lynton, 1967).

The Indium-Lithium System

The phase diagram, from Hansen (1958), is shown in Figure (1.12). Very little is known about the system, the only work on it, reported since Hansen, is that of Graham and Raynor (1957). They measured axial ratios for lithium concentrations up to 15% and found very little change from pure indium. The extent of the lithium solubility appears to be in conflict with the phase diagram as Graham and Raynor detected no phase change in the alloys they examined. Very little change in axial ratio was observed.

There appear to have been no T_c measurements on this system whatsoever.

REFERENCES

Allen, P.B. and Cohen, M.L., (1969), Phys. Rev. 187, 525.

Anderson, J.A. and Gold, A.V., (1965), Phys. Rev. 139, 1459.

Anderson P.W., (1959), J. Phys. Chem. Sol. 11, 26.

Animalu, A.O.E., (1966), Proc. Roy. Soc. A, 294, 376.

Animalu, A.O.E. and Heine, V., (1965), Phil. Mag. 12, 1249.

Ashcroft, N.W. and Lawrence, W.E., (1968), Phys. Rev. 175, 938.

Austin, B.J., Heine, V. and Sham, L.J., (1962), Phys. Rev. 127, 276.

Bardeen, J., Cooper, L.N. and Schrieffer, J.R., (1957), Phys. Rev. 108, 1175.

Barrett, C.S. and Trautz, (1948), Am. Inst. Min. Met. Eng., 175, 579.

Blatt, J.M., (1964), Theory of Superconductivity, Academic Press, London.

Bloch, F., (1928), Zeits. Phys. 52, 555.

Bogoliubov, N.N., Tolmachov, V.V. and Shirkov, D.V., (1958), "A New Method in the Theory of Superconductivity", Dubna.

Brandt, G.B. and Rayne, J.A., (1964), Phys. Lett. 12, 87.

Brillouin, L., (1930), J. Phys. Radium, 1, 377.

Callaway, J., (1964), Energy Band Theory, Academic Press, London.

Carbotte, J.P. and Dynes, R.C., (1968), Phys. Rev. 172, 476.

Chanin, G., Lynton, E.A., Serin, B., (1959), Phys. Rev. 114, 719.

Cohen, M.H. and Heine, V., (1958), Adv. Phys. 7, 395.

Cohen, M.H. and Heine, V., (1961), Phys. Rev. 122, 1821.

Cooper, L.N., (1956), Phys. Rev. 104, 1189.

Dirac, P.A.M., (1928), Proc. Roy. nSoc. A, 117, 610.

Drude, P., (1900), Ann. Physik., 1, 566.

Feynman, R.P., (1953), Proc. Tnt. Conf. Theor. Phys., Kyoto, Tokyo, Japan.

Fock, V., (1930), Zeits. Phys. 61, 126.

Frohlich, H., (1950), Phys. Rev. 79, 845.

Gaidukov, Yu. P., (1966), J.E.T.P., 22, 734.

Ginzburg, V.L., (1945), J. Phys. (U.S.S.R.), 9, 305.

Ginzburg, V.L., (1952), Usp. Fiz. Nauk. 48, 25.

Ginzburg, V.L., (1953), Fortschr. Physik, 1, 99.

Ginzburg, V.L. and Landau, L., (1950), J.E.T.P., 20, 1064.

Goodenough, J.B., (1953), Phys. Rev. 89, 282.

Graham, J. and Raynor, G.V., (1957), Phil. Mag. 2, 1354.

Ham, F.S., (1960), in The Fermi Surface, (Ed. Harrison and Webb), Wiley, N.Y.

Hansen, M., (1958), Constitution of Binary Alloys, McGraw Hill, N.Y.

Harrison, W.A., (1966), Pseudopotentials in the Theory of Metals, Benjamin, N.Y.

Hartree, D.R., (1928), Camb. Phil. Soc. 24, 89.

Heine, V., (1969), Electronic Structure of Metals, Physics of Metals, I. Electrons, (Ed. Ziman), Camb. Univ. Press.

Heine, V. and Abarenkov, I., (1964), Phil. Mag. 9, 451.

Heine, V. and Weaire, D., (1966), Phys. Rev. 152, 603.

Heitler, W. and London, F., (1927), Zeits. Physik, 44, 455.

Herring, C., (1940), Phys. Rev., 57, 1169.

Howarth, D.J., (1955), Phys. Rev. 99, 469.

Hubbard, J., (1957), Proc. Roy. Soc. A 240, 539.

Hubbard, J., (1958), Proc. Roy. Soc. A 243, 336.

Hughes, A.J. and Shepherd, J.P.G., (1969), J. Phys. C. (Proc. Phys. Soc.) 2, 661.

Hume-Rothery, W., Mabbott, G.W. and Channel-Evans, (1934), Phil. Trans. A 233, 1.

Hume-Rothery, W., Reynolds, P.W. and Raynor, G.V., (1940), J. Inst. Met. 66, 191.

Hund, F., (1928), Zeits. Phys. 51, 759.

Hund, F., (1931), Zeits. Phys. 73, 1.

Inglesfield, J.E., (1969), J. Phys. C. 2, 1285.

Inglesfield, J.E., (1970), Univ. Cam. Thesis.

Iyengar et al, (1965), Inelastic Scattering of Neutrons in Solids and Liquids, (Int. At. Energy Agency, Vienna), 1, 153.

Jones, H., (1934), Proc. Roy. Soc. A 144, 225.

Jones, H., (1934), Proc. Roy. Soc. A 147, 396.

Jones, H., (1937), Proc. Phys. Soc. A 49, 250.

Kohn, W. and Rostoker, N., (1954), Phys. Rev. Lett. 5, 8.

Kuhn, T.S. and Van Vleck, J.H., (1950), Phys. Rev. 79, 382.

Leigh, R.S., (1956), Proc. Phys. Soc. A 69, 388.

London, F., (1937), Actualites Sci. Ind. No. 458.

London, F. and London H., (1935), Physica, 2, 341.

Lorentz, H.A., (1904), Amsterdam. Proc.

Lynton, E.A., (1969), Superconductivity, Methuen, London.

Lynton, E.A., Serin, B. and Zucker, M., (1957), J. Phys. Chem. Sol., 3, 165.

McClure, J.W., (1955), Phys. Rev. 98, 449.

McMillan, W.L., (1968), Phys. Rev. 167, 331.

Markowitz, D. and Kadanoff, L.P., (1963), Phys. Rev. 131, 563.

Matthias, B., (1957), Progress in Low Tem. Physics. 2, 138.

Matthias, B., (1960), J. Appl. Phys. 31, 235.

Maxwell, E., (1950), Phys. Rev. 78, 477.

Meissner, W. and Ochsenfeld, R., (1933), Naturwiss. 21, 787.

Merriam, M.F., (1963), Phys. Rev. Lett. 11, 321.

Merriam, M.F., (1964), Rev. Mod. Phys. 36, 152.

Merriam, M.F., (1966), Phys. Rev. 144, 300.

Merriam, M.F.,and von Herzen, (1963), Phys. Rev. 131, 637.

Merriam, Jensen, M.A. and Coles, B.R., (1963), Phys. Rev. 130, 1719.

Moore, A., Graham, J., Williamson, G.K. and Raynor, G.V., (1955), Acta Met., 3, 579.

Morel, P. and Anderson, P.W., (1962), Phys. Rev. 125, 1263.

Mulliken, R.S., (1928), Phys. Rev. 32, 186, 761.

Onnes, H.K., (1911), Commun. Phys. Lab. Univ. Leiden, 12, 119.

Pearson, W.B., Handbook of Lattice Spacing, structures and metals and alloys, Pergamon, London, (1967), 1, and 2.

Peierls, R., (1930), Ann. Physik. 4, 121.

Perretti, E.A. and Carapella, S.C., (1949), Trans. A.S.M. 41, 947.

Phillips, J.C. and Kleinman, L., (1959), Phys. Rev. 116, 287, 880.

Pippard, A.B. (1953), Proc. Roy. Soc. A 216, 547.

Pippard, A.B.,(1953), Nature, 172, 896.

Pippard, A.B.,(1957), Phil. Mag. 2, 1147.

Pippard, A.B.,(1957), Proc. Roy. Soc. A 250, 325.

Raimes, S., (1962), J. Phys. Rad. 23, 639.

Rayne, J.A., (1963), Phys. Rev. 129, 652.

Reeber, M.D., (1960), Phys. Rev. 117, 1476.

Reynolds, C.A., Serin, B.,,Wright, W.H. and Neskitt, L.B., (1950), Phys. Rev. 78, 487.

Ridley, N., (1967), Phys. Lett. 25A, 134.

Russell, C., (1966), Thesis, Imperial College, London.

Schafroth, M.R., (1954), Phys. Rev. 96, 1442.

Schrödinger, E., (1926), Ann. Physik, 79, 361.

Shaw, R.W., (Jr.), (1968), Phys. Rev. 174, 769.

Shaw, R.W., (Jr.) and Harrison, W.A., (1967), Phys. Rev. 163, 604.

Shepherd, J.P.G., (1969), Private communication.

Slater, J.C., (1937), Phys. Rev. 51, 846.

Sommerfeld, (1928), Zeits. Physik. 47, 1.

Svechkarev, I.V., (1965), J.E.T.P., 20, 643.

Tomasch, W.J. and Reitz, J.R., (1958), Phys. Rev. 111, 757.

Tyzack, C. and Raynor, G.V., (1954), Trans. Farad. Soc., 50, 675.

Verkin, B.I. and Svechkarev, I.V., (1965), J.E.T.P. 20, 267.

Wigner, E. and Seitz, F., (1933), Phys. Rev. 43, 804.

Wigner, E. and Seitz, F., (1934), Phys. Rev. 46, 509.

Zubarev, D.N., (1960), Soviet Phys. Doklady, 5, 570.

CHAPTER 2

CHAPTER 2

PRECISION LATTICE PARAMETER MEASUREMENTS IN HIGH ABSORPTION MATERIALS

2.1 INTRODUCTION

Indium alloys are not the most suitable materials for X-ray analysis due principally to the thermal broadening of the peaks at room temperature and some additional broadening due to Compton scattering. As a result both Debye-Scherrer (D-S) films and diffractometer traces show reflections, whose positions, for $2\theta < 90^{o}$, are very difficult to measure, and are, in most cases, undetectable at higher angles.

The problem of thermal broadening may be circumvented by using a low temperature technique (Russell, 1966). A diffractometer was used by Russell, instead of a camera, because of the better resolution and because the transparency error decreases with increasing absorption coefficient for the diffractometer, in contrast to the camera, which makes the former more suitable for the highly absorbing indium alloys.

There may still be some debate as to whether the diffractometer is the superior instrument or not. There is no doubt whatsoever that, if a great deal of time and care is put into a lattice parameter determination, the diffractometer is limited only by uncertainties in the X-ray emission profile. Provided sufficient care is taken the camera is reported to have accuracies of the same order as the diffractometer (Straumanis, 1959). This is surprising because, in order to obtain these accuracies, the mid-point of a (curved) line on a photograph has to be fixed, with a cursor and vernier scale, to within a twentieth part, or better, of the maximum resolution of the human eye. Least-square error minimisations certainly indicate a small variance of these measurements, but that does not preclude a systematic

physiological error. The subjectivity of D-S film measurements was noted by Ekstein and Siegel (1949) who used four different observers to measure the same line and found considerable differences in the interpretation of the line 'centre'.

Initial experiments on the indium alloys were performed on a Siemens' diffractometer using the double-scanning technique (King and Russell, 1965) and a helium cryostat (King and Preece, 1967). While the peak-to-background ratio was markedly increased for the low angle reflections, the higher angle profiles were still poor. The main problem was the level of the intensity which was usually on the lowest scale (1×10^3 c.p.m. full scale deflection) the signal-to-noise ratio being correspondingly small. The intensity may be increased by illuminating a larger specimen area using a wider divergent beam aperture, but this results in asymmetrical broadening of the peaks in conventional, parafocusing, (Bragg-Brentano) geometry (Fig. 2.1). An obvious solution is to change the geometry from Bragg-Brentano (BB) to fully-focusing (Seemann-Bohlin, SB) also shown in Fig. (2.1).

The focusing principle of the SB geometry is the equality of angles subtended by a chord of a circle at the perimeter. Advantages of SB geometry in diffractometry have been discussed by Parrish and Mack (1967) who envisaged a multiple-counter system for reduction of recording time or simultaneous observation of different peaks whilst a specimen undergoes some transformation. No such system has been reported as yet. Another advantage pointed out by Parrish and Mack is that the stationary specimen makes subsidiary instrumentation much simpler, which is desirable, for example, when cooling or heating apparatus is to be attached. A rather esoteric proposal for the method was that of Das Gupta, Schnopper, Metzer and Shields (1964) for the on-the-spot analysis of moon dust!

One of the principal weaknesses of most of the SB instruments reported, has been the limited angular ranges available, due to having only single fixed specimen positions. The instruments of Parrish and Mack (1967) and Das Gupta et al (1964) both have low angle specimen positions but the dimensions of the apparatuses preclude the back-

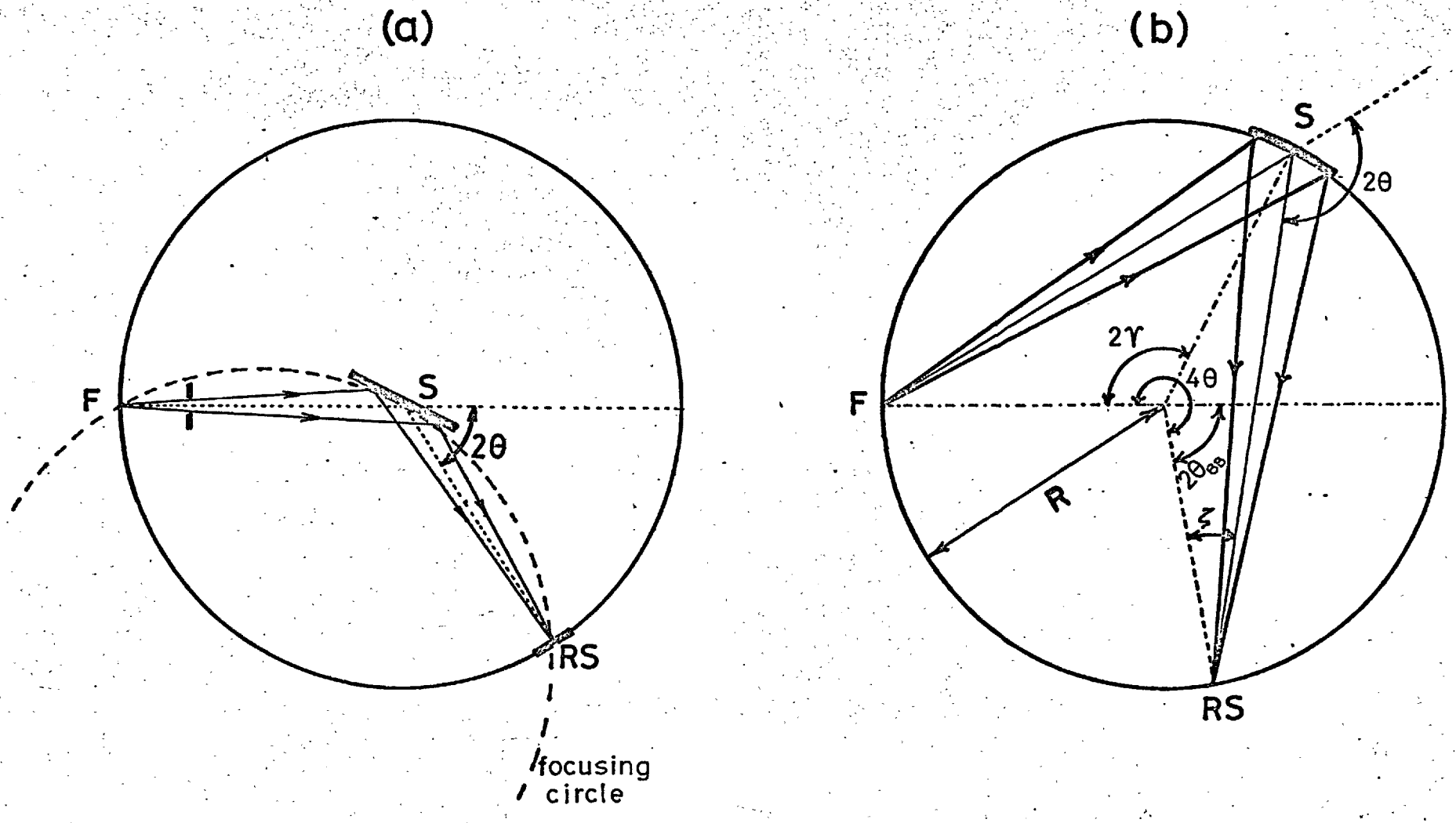

Figure 2.1 Diffractometer geometries - (a) parafocusing (b) fully-focusing

reflection region from about $110^{\circ}2\theta$ upwards. The Baun and Renton (1963) instrument has the specimen positioned opposite the source which limits measurements to the back-reflection region. Furthermore, when a similar device, made by the Hilger and Watts Company, was tested by this writer, the available range of angles was found to be even more limited. Apart from the dimensions of the instrument a restriction on the lowest angle available was imposed by the type of mechanical linkage used to direct the counter tube towards the specimen and, as a result, the available range was only from 130° to $170^{\circ}2\theta$. The linkage was of a rod and yoke type which was found to frictionally seize if the angle between the driving force on the rod and the axis of the rod exceeded about 45°. All the diffractometers mentioned so far make use of this type of linkage.

The only Seeman-Bohlin diffractometer that showed any versatility of range was that of Wassermann and Wiewiorowski (1953) where the focusing condition was satisfied with a complex mechanism which involved bodily rotation of the diffractometer, rod and yoke sliding of the specimen and a lazy-tongs linkage between counter and specimen.

All these diffractometers suffer from the very serious defect that they cannot be aligned except by calibration against standard substances. Parrish and Mack assert that since the zero angle position is located at the source it must be impossible to align a SB diffractometer. A fully focusing diffractometer which overcomes all these difficulties is described below. This instrument is a modification of a conventional BB diffractometer and the two geometries are interchangeable. The zero-point of the BB system can thus be established by standard procedure and since this point is, identically, the $90^{\circ}2\theta$ point of the SB system the angular scale of the SB system can be determined without reference to a standard substance.

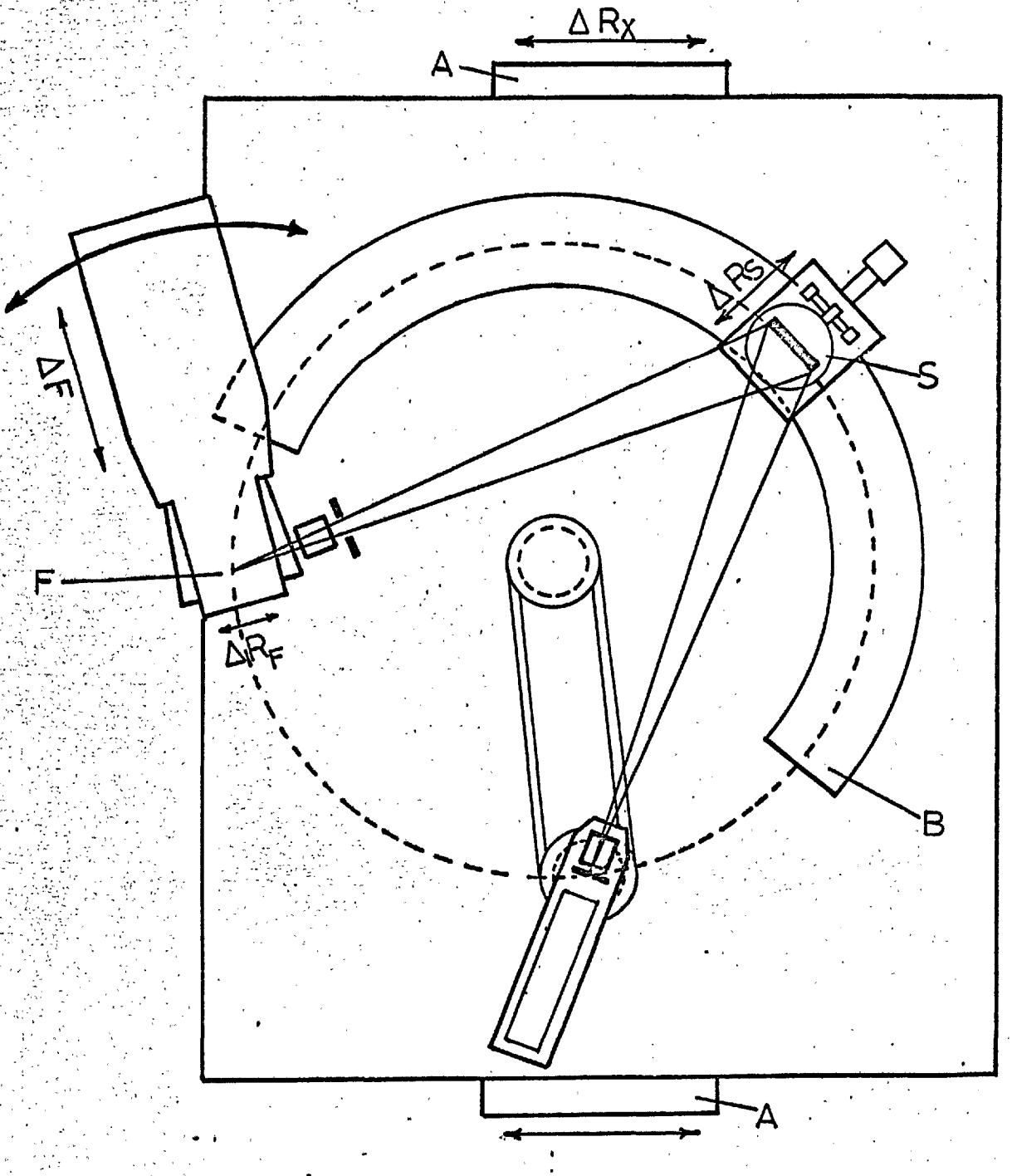

Figure 2.2 Schematic plan of the modified Wooster-Martin diffractometer.

2.2 THE DIFFRACTOMETER

The instrument, which is a modification of a Wooster-Martin diffractometer, is shown schematically in Fig. (2.2) and photographically in Fig. (2.3).

A line was inscribed on the base plate to define a 0^{o}–$180^{o}2\theta$ (BB) diameter to a first approximation. A pair of horizontal slides A (Fig. 2.2), parallel to this line, are used as a base for the adjustable legs of the Wooster-Martin diffractometer. These slides can be clamped and a linear scale indicates (nominally) the separation of the axis of rotation of the X-ray tube and the goniometer axis. The X-ray source which is a sealed-off Philips 2 kW type tube, is mounted horizontally on a bracket which is free to rotate about a pivot point in the base plate. This rotation (from -10^{o} to $+90^{o}$ from the BB position) enables the tube to be directed towards various points on the diffractometer circle. An angular scale engraved on the base plate indicates the direction in which the tube is pointing.

The vertical line focus F may be brought into colinearity with the axis of tube rotation by means of a screw-thread adjustment, ΔF, perpendicular to the target. A horizontal adjustment, ΔR_F, parallel to the target is achieved by simply enlarging the bolt holes securing the tube to the bracket.

An annular dovetailed track, B, is accurately fixed concentric with the goniometer axis. The specimen table, S, slides along this track and may be clamped at any angular position, 2γ, between 34^{o} and 200^{o} from the X-ray source. The specimen holder is seated in a Siemens' cone mount (e.g. see Russell, 1966) and has a micrometer rotational adjustment $\Delta\tau$ with respect to the axis of the cone. A further adjustment to the specimen position ΔR_S, is provided by a micrometer translation of the specimen table along a goniometer radius.

The specimen holder was originally provided (as has been customary with all other SB diffractometers) with a flat reference surface, the

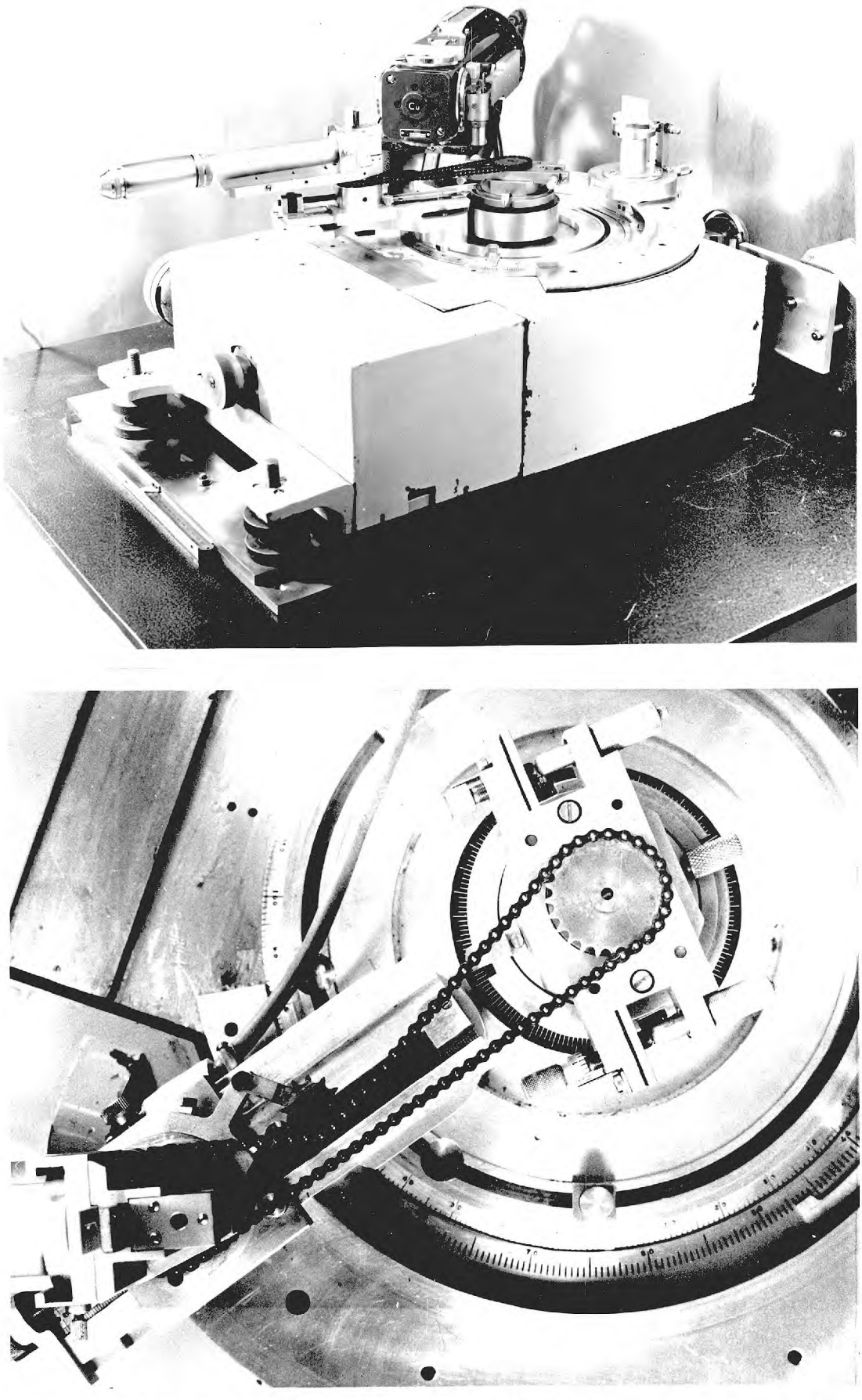

Figure 2.3 Top - the diffractometer in the Seemann-Bohlin mode
Bottom - the Renold chain linkage

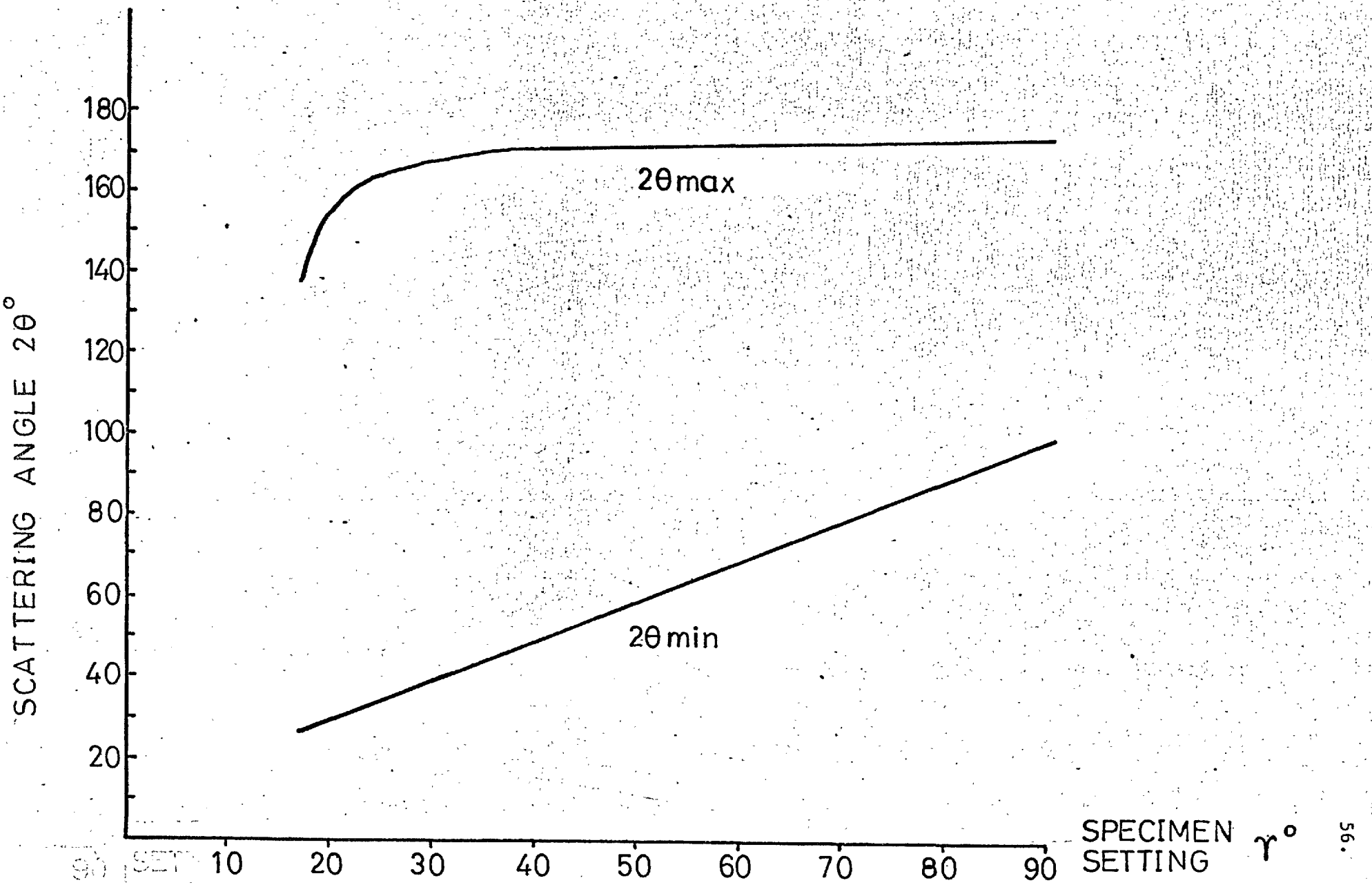

Figure 2.4 The ranges of available Bragg angles on the SB diffractometer.

curved specimen frame being machined with a flat face to match. The orientation of the curved surface (that is the tangent at its mid-point) to the flat surface was found to vary significantly from specimen frame to specimen frame, however. Parrish and Mack (1967) assert that a specimen rotation error only causes symmetrical broadening of the peak. In practice, of course, this is only true if the X-ray beam illuminates symmetrically about the axis of specimen rotation, a condition slightly difficult to satisfy. Another error that may arise from machining a flat surface on a specimen frame is a slight specimen displacement. These two errors would mean that each specimen would need to be separately aligned. The obvious solution was to machine a 17.5 cm radius convex reference surface to match the curvature of the specimen frames. Besides making the construction of the frames much easier, this means that once this reference surface has been aligned, changing the specimen does not alter the alignment.

The focusing circle is here defined as the locus of the receiving slit. A rigid counter arm is bolted to the 2θ-drive of the BB diffractometer and a dovetailed sliding assembly supports a vertical shaft, with a ball race, accurately set such that the counter bracket can rotate freely about an axis through the centre of the receiving slit. Below the bracket is attached a sprocket wheel which allows a Renold chain linkage to a similar sprocket wheel attached to the θ-drive of the BB diffractometer thus providing a 1:1 linkage between the counter rotation (about its receiving slit) and the θ rotation of the goniometer.

The angle between the goniometer radius through the receiving slit and the line joining the receiving slit to the centre of the specimen is (Fig. 2.1) $\zeta = \gamma - 2\theta + \pi/2$. Since $4\theta = \pi + 2\theta_{BB}$, where $2\theta_{BB}$ is the angle indicated, in BB geometry, for the counter position, $\zeta = \gamma - \theta_{BB}$ and in order that the counter should always point at the specimen (once it has been set that way) $\dot{\zeta} = -\dot{\theta}_{BB}$. When the θ-drive, $\dot{\theta}_{BB}$, is transmitted to the counter it is opposed by the $2\dot{\theta}_{BB}$ rotation of the counter arm i.e. $\dot{\theta}_{BB} - 2\dot{\theta}_{BB} = -\dot{\theta}_{BB} = \dot{\zeta}$ the counter will remain directed at the specimen.

A small sprocket wheel, on a hinged arm attached to the counter assembly, is used to tension the chain. The counter bracket may also be fixed in two, well-defined orientations (i.e. at $\zeta = 0^{o}$ or 45^{o}) by suitably positioned dowel pins. The first position is primarily for running in the BB mode whilst either position may be utilized for the initial directing of the counter at the specimen, by racking the counter to a suitable $2\theta_{SB}$ position (i.e. $2\theta = 90 + \gamma - \zeta$). The receiving slit assembly (including soller slits) and the counter bracket are standard Siemens' parts. A Mullard geiger counter is used because the bulky proportional counter restricted the angular range.

In order to make the change-over from BB to SB very simple, the central sprocket was set in a cone of identical taper to that of the specimen mount. When the counter is pointed in the correct direction the sprocket is locked in this cone and is thus linked to the θ-drive. When using the BB arrangement, the standard specimen holder is placed in the central cone. The $2\theta:\theta$ setting of the specimen at $0^{o}2\theta$(BB) for scanning both sides of the beam, is made with two micrometer rotation adjustments provided on the Siemens' cone mount.

In order to set the take-off angle at 5^{o} a Philips divergence slit and soller slit holder is attached directly to the tube and provided with a translational adjustment.

The Wooster-Martin machine has two built-in angular scales, one from the θ-drive and one from the 2θ-drive. Each scale has a cyclometer reading to 0.1^{o} and a calibrated drum, at the end of the drive shaft, reading to 0.01^{o}, interpolation in the third decimal place being achieved on a synchronised chart record. It is readily shown that the scattering angle 2θ in the SB geometry is given by

$$2\theta_{SB} = \pi/2 + \theta_{BB}$$

where θ_{BB} is the apparent θ recorded on the BB scales. Thus, if the zero point of the BB geometry is identified with 90^{o} on the θ_{BB} scale

(merely by disconnecting the θ scale cyclometer and running it on) then this scale can be taken as reading the scattering angle 2θ in the SB geometry. The scale on the drum may also be adjusted relative to the position of the worm-drive shaft so that the $90^{o}2\theta_{SB}$ position may be accurately defined.

Both the main gears of the diffractometer were checked for eccentricity by comparing points 30^{o} apart using an optical polygon and an autocollimator (Evans and Taylerson, 1961). They were found to be accurate to better than 0.01^{o}.

The driving motor and subsidiary gearing of the Wooster-Martin, however, were found to be unreliable and were, therefore, replaced by a Siemens step-scanning motor in its (1^{o}/min) continuous driving mode. The linkage was arranged so that the scanning speed could be changed by using different pairs of matched gears.

The ranges of measurable Bragg angles are determined primarily by the specimen position and secondarily by the dimensions of the X-ray tube, counter and specimen assemblies. The ranges achieved in practice are shown in Fig. (2.4) as a function of specimen position. The lowest possible Bragg angle obtainable is $28^{o}2\theta$ and the highest possible angle is just over $172.5^{o}2\theta$. The largest range available is from $33^{o}2\theta \rightarrow 162^{o}2\theta$ at about $25^{o}\gamma$ and the two ranges used most are for $45^{o}\gamma$ (53^{o} - $171.5^{o}2\theta$) and $60^{o}\gamma$ (68^{o} - $172.5^{o}2\theta$).

2.3 SOURCES OF ERROR IN THE SB METHOD

If the Seemann-Bohlin principle is to be used to advantage in diffractometry, it is necessary to be aware of all the sources of error, their significance and minimisation. The mathematical theory of errors involved in para-focusing powder diffractometry, has been thoroughly elucidated by Wilson (1963) and the same general principles can be applied to SB geometry. The lack of symmetry in the latter arrangement merely makes the calculations lengthier.

The problem is conceptually the same as that of the electrical engineer's 'Black box'. An input signal will in general be changed at the output by two essentially different mechanisms. In one, the total content (integrated intensity) of the signal remains unchanged and the signal profile itself distorted according to the convolution principle. In this each δ-function element of the input signal $g(z)$ is smeared out into a function of the form of $f(y)$ which is a characteristic of the black box. The resulting signal $h(x)$ is given by the convolution

$$h(x) = \int f(y)\, g(x - y)\, dy$$

All the purely geometrical aberrations in diffractometry are of this type.

The second mechanism of distortion is that of the differential response of the black box to the input signal, whereby the gain or attenuation of a signal may vary across the signal profile. Aberrations of this type occur, for example, with filters and counters.

A systematic evaluation of all the errors associated with SB geometry (where these are different from the corresponding expressions in BB geometry) will be given here. Some of the results have been derived previously but others are analysed here for the first time.

It is necessary, first of all, to define the position of a Bragg

profile $g(2\theta)$ and the aberration functions $f(\varepsilon)$ (ε being a variable in the scale of θ). The most convenient definition, from the point of view of error analysis, is the centroid of the profile, $\langle 2\theta \rangle$ or $\langle \varepsilon \rangle$, where

$$\langle w \rangle = \frac{\int w\, q(w)\, dw}{\int q(w)\, dw}$$

$q(w)$ being the profile function. The advantage of this definition is that the centroid shift of a profile due to a number of aberrations is merely the sum of the centroid shifts of each aberration (Wilson, 1963). In order to calculate the shift in the peak of the profile due, for example, to a number of geometrical aberrations, it is necessary to compute the aberration functions and then fold these sequentially with the spectral function. The two common functional forms attributed to this spectral function (a Gaussian or a Cauchy 'witch') are both awkward for solving convolution integrals analytically. As a result of this the following analyses will be in terms of the centroid. The centroid of the profile under exact Bragg reflection with no errors will be termed $\langle 2\theta_B \rangle$ while the centroid of the profile subjected to response errors is given by $\langle 2\theta \rangle$. The centroid shift for these errors is $\langle 2\theta \rangle - \langle 2\theta_B \rangle$ whilst the shift for geometrical errors (convolution) will be given directly by the centroid of the aberration profile $\langle 2\varepsilon \rangle$.

Only if there is no broadening of the profile will the peak shift be the same as the centroid shift. The most convenient measure of the breadth of a profile, $q(w)$, is that of the variance W (see for example Wilson, 1963) defined as

$$W = \langle w^2 \rangle - \langle w \rangle^2 \qquad \ldots (2.1)$$

The aberrations and errors associated with SB geometry and the particular instrument described in section 2.2, are listed in a convenient order, as follows. (Note: Errors for which previous analyses were unavailable or incomplete are indicated by an asterisk, *, while those common to the BB geometry are indicated thus, †)

I. Errors due to Physical Effects

† (1) Errors in the definition of wavelength
† (2) Refraction
† (3) Dispersion
* (4) Lorentz-factor and polarisation
* (5) Chord length of diffraction cone
* (6) Absorption as a differential response
† (7) Differential response of filters, counters and monochromators

II. Errors Arising from the SB Geometry

* (1) Errors due to wrong specimen curvature
(2) Transparency errors
(3) Specimen displacement
* (4) Specimen rotation error
(5) Specimen tilt error
* (6) Axial divergence with and without Soller slits
* (7) Finite breadth of focal line and receiving slit
* (8) Mis-setting of focus and receiving slit
* (9) X-ray beam not in diffractometer plane
* (10) Rotational following of counter tube
(11) Specimen condition

III. Errors Inherent in the Instrument

† (1) Eccentricity in the main gear
† (2) Backlash in the gears
* (3) Eccentricity of specimen track
* (4) Diffractometer slides not parallel to 0 - 180° (BB) line

I. Errors due to Physical Effects

Refraction (apart from a small geometrical term) and dispersion are not aberrations at all but become sources of error if they are ignored. The refraction term merely implies that the Bragg condition should be written with the wavelength the crystal sees inside it. The refractive

index is dependent on wavelength, but since the total correction itself is very small (~ 1 part in 10^5 in the lattice parameter) any differential response to the spectral profile is completely negligible.

Dispersion only arises if there is a non-equivalence of scale for input and output so that if the output were in the scale of sin θ there would be no error. It is usually simpler, however, to make the requisite correction than to plot the profile on a sin θ scale.

To account for the effects of dispersion, Lorentz factor, polarisation and chord length, it is necessary to compute the total angle factor arising from diffraction. Perhaps the most easily understood approach is that of Ladell (1961) but a slightly different term arises with the change to SB geometry. Following Ladell

$$f(\varepsilon) = h * (j * k(\varepsilon))$$

is to be construed as a convolution of the intrinsic diffraction profile of the powder with the instrumental aberration $j(\varepsilon)$ (itself a series of convolutions) followed by the convolution with the spectral profile on the same angular scale. The instrumental functions can be unfolded away (the order of folding is immaterial) so that

$$f(\varepsilon) = h * k(\varepsilon)$$

For a monochromatic incident beam (λ) the intrinsic profile, k, is given by

$$k(\varepsilon) = E(2\theta)\, U(\mu)\, I_o\, SR_1(\varepsilon) \qquad \ldots (2.2)$$

Where $U(\mu) = \frac{1}{2\mu}$ and μ is the linear absorption coefficient corresponding to λ. I_o is the incident intensity of the beam, S is its cross section and $R_1(\varepsilon)$ is the single crystal interference function for unpolarised radiation given by James (1950). $E(2\theta)$ is the powder method factor and the chord length factor combined. The first of these is given by the probability of a crystallite being at the correct glancing

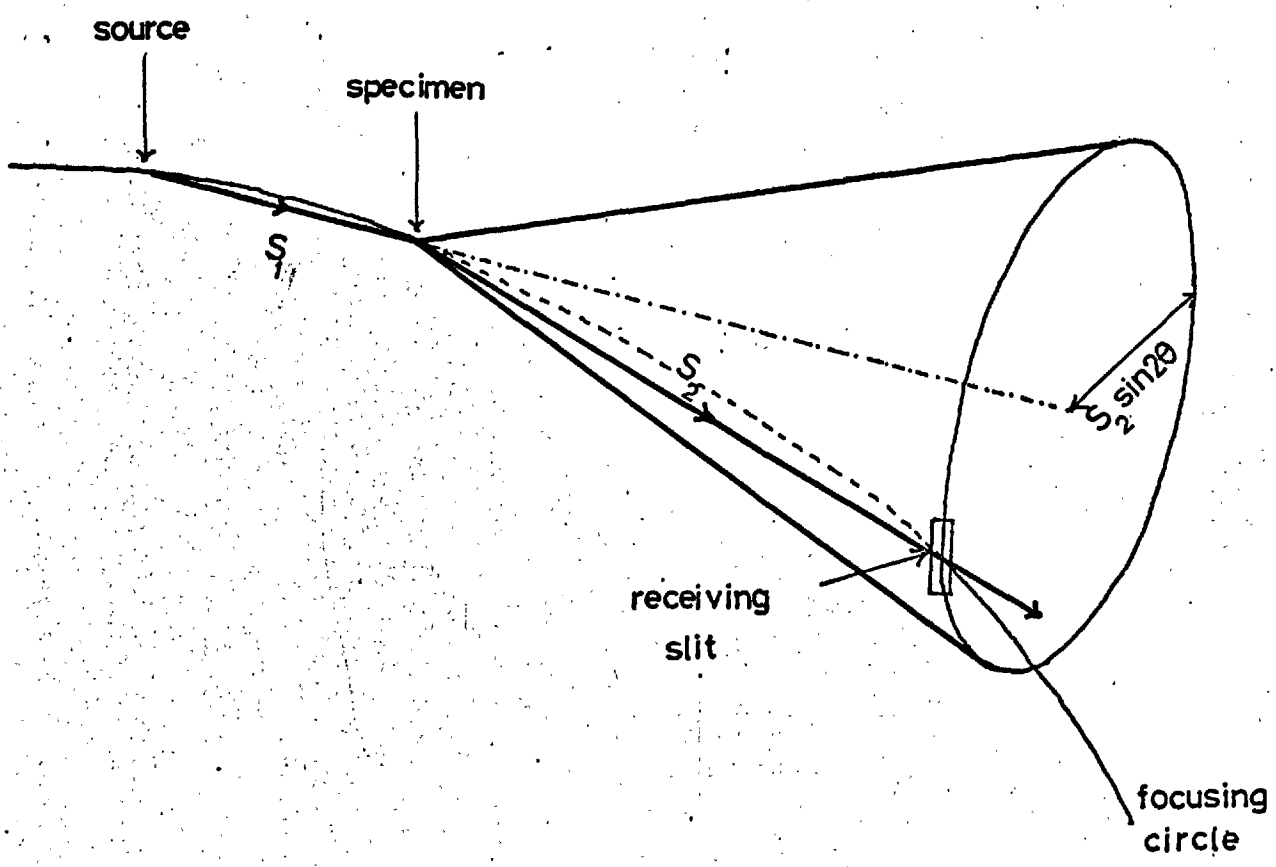

Figure 2.5 Illustrating the chord-length factor.

angle of incidence to the beam within $d2\theta$ i.e. -

$$\rho\ (2\theta)\ d2\theta \quad = \quad \cos\theta\ d2\theta$$

The chord length factor is illustrated in Fig. (2.5) which shows the scattering cone from the specimen, in the Seemann-Bohlin geometry, intercepted by the receiving slit. The circumference of the cone at this point is $2\pi S_2 \sin 2\theta$ where S_2 is the specimen-counter distance which is equal to $2R \sin (2\theta - \gamma)$. The intensity received by a receiving slit of fixed height is clearly in inverse proportion to this circumference. The total factor E is thus given by

$$E(2\theta) = \frac{\cos\theta}{\sin 2\theta \sin (2\theta - \gamma)} \qquad \ldots (2.3)$$

This appears to be the only term in equation 2.2 which is dependent on the geometry. Following Ladell it is possible, assuming $R_1(\varepsilon)$ to be very sharp, to show that

$$f(\varepsilon) \quad = \quad E\ U\ \tau\ h(\varepsilon)$$

$$\text{where } \tau(2\theta) \propto \frac{(1 + \cos^2 2\theta)\lambda^3}{\sin 2\theta} \qquad \ldots (2.4)$$

or that

$$f(2\theta) \quad = \quad h(2\theta) \ / \ j(2\theta) \qquad \ldots (2.5)$$

$$\text{where} \quad E(2\theta)\ U(2\theta)\ \tau(2\theta) \quad = \quad 1/j(2\theta) \qquad \ldots (2.6)$$

Ladell's consideration of absorption by K and L electrons leads to a term*

$$U(2\theta) \quad \propto \quad \text{cosec}^3\theta \qquad \ldots (2.7)$$

Using (2.3), (2.4) and (2.7) in (2.6) it follows that

$$j(2\theta) \quad = \quad K \quad \frac{\sin^2\theta \cos\theta \sin (2\theta - \gamma)}{(1 + \cos^2 2\theta)} \qquad \ldots (2.8)$$

---

* This is misprinted as $\cos^3\theta$ in Ladell's paper.

In order to find the shift of the centroid of the profile due to this factor, the procedure of Pike (1959) is followed, replacing his factor $B(\theta)$ with $1/j\ (2\theta)$

$$B(\theta) = \frac{(1 + \cos^2 2\theta)}{\sin^2\theta \cos\theta \sin(2\theta - \gamma)} \quad \ldots (2.9)$$

In the absence of all other aberrations the observed profile $Q(2\theta)$ is given by

$$Q(2\theta)\, d2\theta = 2B(\theta)\, F(\lambda)\, d\lambda \quad \ldots (2.10)$$

where $F(\lambda)$ is the spectral profile and

$$\theta = \sin^{-1}\left(\frac{\lambda}{2d}\right)$$

in the usual notation.

Now let $B(\theta) = B_1(\lambda)$

then the centroid $\langle 2\theta \rangle$ of the observed profile is given by

$$\langle 2\theta \rangle = \frac{\int 2\theta(\lambda)\, B_1(\lambda)\, F(\lambda)\, d\lambda}{\int B_1(\lambda)\, F(\lambda)\, d\lambda} \quad \ldots (2.11)$$

The true centroid of the spectral profile is given by

$$\lambda_B = \langle \lambda \rangle = \frac{\int \lambda F(\lambda) d\lambda}{\int F(\lambda) d\lambda} \quad \ldots (2.12)$$

By expanding $B_1(\lambda)$ and $2\theta(\lambda)\, B_1(\lambda)$ about $\lambda = \lambda_B$ using Taylor's theorem, to second order, it follows that

$$\langle 2\theta \rangle - \langle 2\theta_B \rangle = 2V \left\{ \tfrac{1}{2}\theta''(\lambda_B) + \theta'(\lambda_B) \frac{B_1'(\lambda_B)}{B_1(\lambda_B)} \right\} \quad \ldots (2.13)$$

where $\theta_B = \sin^{-1}\left(\frac{\lambda_B}{2d}\right)$, V is the variance of the spectral profile

for given limits, and the primes refer to differentiation with respect to λ. The calculation of (2.13) using (2.9) is not very difficult and gives

$$\langle 2\theta \rangle - \langle 2\theta_B \rangle = \frac{V}{\lambda_B^2} \tan^3\theta_B \{3-4\cot^2\theta_B - \frac{16\cos 2\theta_B \cos^2\theta_B}{(1+\cos^2 2\theta_B)} - 4\cot\theta_B \cot(2\theta_B - \gamma)\} \quad \ldots (2.14)$$

The first three terms in the brackets are identical with those of Pike and Ladell (1961) while the fourth arises from the SB geometry. The asymptotic function (as $2\theta \to \pi$) still varies as $\tan^3\theta_B$ and the new SB term reduces to zero when the counter is diametrically opposite the specimen.

Since the error (2.14) increases rapidly as θ tends to 90° it is to be expected that an extrapolation plot would reveal a depression in the apparent lattice parameter at higher angles. The error would barely be detectable even for a well aligned BB diffractometer, because Bragg angles cannot be measured above $162^\circ 2\theta$. The SB geometry adds about $10^\circ 2\theta$ to the measurable range and hence lends itself to the detection of the Lorentz factor and dispersion error.

An experiment was devised to demonstrate the existence of the $\tan^3\theta$ error. Silver has a number of sharp, intense profiles up to the moderately high angle ($157^\circ 2\theta$) 511,333 reflection for CuK_α radiation. Considerable solid solubility of zinc in silver and an associated lattice parameter change made it possible to 'move' the 511,333 reflection, on alloying, through higher Bragg angles up to the angle limit of the diffractometer.

The diffractometer was set with a specimen at $\gamma = 60^\circ$ to enable the five reflections, 222, 331, 420, 422 and 511,333 to be scanned continuously. Point readings were taken from the chart record and fed into a machine programme for the calculation of the centroid and the corresponding lattice parameter. An explanation and a listing of this programme are given in Appendix 1.

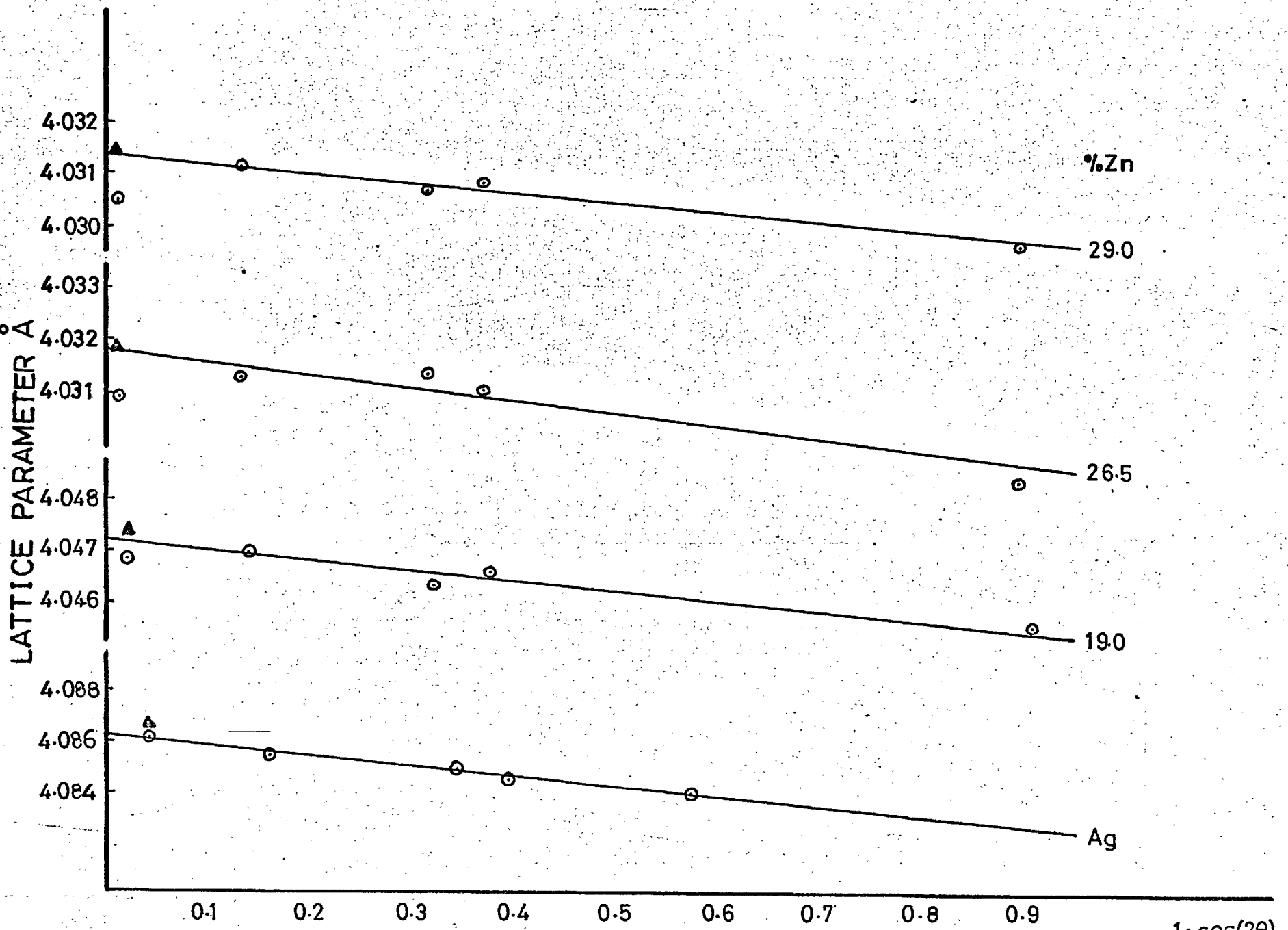

Figure 2.6 Illustrating the $\tan^3\theta$ error.

The lattice parameter values were plotted against the error function for low transparency specimens (see section 2.5) and the results are shown in Fig. (2.6). The deviation from linearity is clearly seen in the higher zinc composition specimens where $2\theta_{511,333}$ is greater than about 160^{o}. Also shown on the plots are the positions of the 511,333 points corrected for Lorentz factor and dispersion using the $\tan^{3}\theta$ term in (2.14). For this correction the variance of the spectral profile V was taken as one third the square of the doublet separation (Wilson, 1963). Inspection of Fig. (2.6) reveals that this correction is sufficient to return the points to the linear extrapolation plot.

According to Wilson (1963) the peak displacements due to the Lorentz factor and dispersion should cancel exactly and so there should be no major divergent term in the high angle region. (Axial divergence in the presence of Soller slits is about an order of magnitude smaller than these errors in the region $160^{o} - 170^{o} 2\theta$.) When the lattice parameters calculated from the peak positions are plotted against the extrapolation function, as in Fig. (2.7), no systematic displacement of the high angle points is apparent.

The remaining errors listed in categoryI are differential response errors comprising distortions to the profile due to counter, filter and monochromator response. These are independent of geometry and have been dealt with before (see for example Wilson, 1963). Should the effect of air-path absorption ever be considered important as an aberration, it is calculated here. The response is given by (2.10) with $B(\theta)$ replaced by

$$B(\theta) = e^{-2\mu R \sin(2\theta - \gamma)}$$

where μ is the absorption coefficient of the air and R is the radius of the diffractometer. The centroid shift will be given by (2.13) without the dispersion term. Recalling that $\mu \propto \sin^{3}\theta$ the calculation gives

$$\langle 2\theta \rangle - \langle 2\theta_B \rangle = - \frac{8\mu_B R V}{\lambda_B^2} \tan^2\theta_B \{ 3 \cot\theta_B \sin(2\theta_B - \gamma) + 2\cos(2\theta_B - \gamma) \} \quad \ldots (2.15)$$

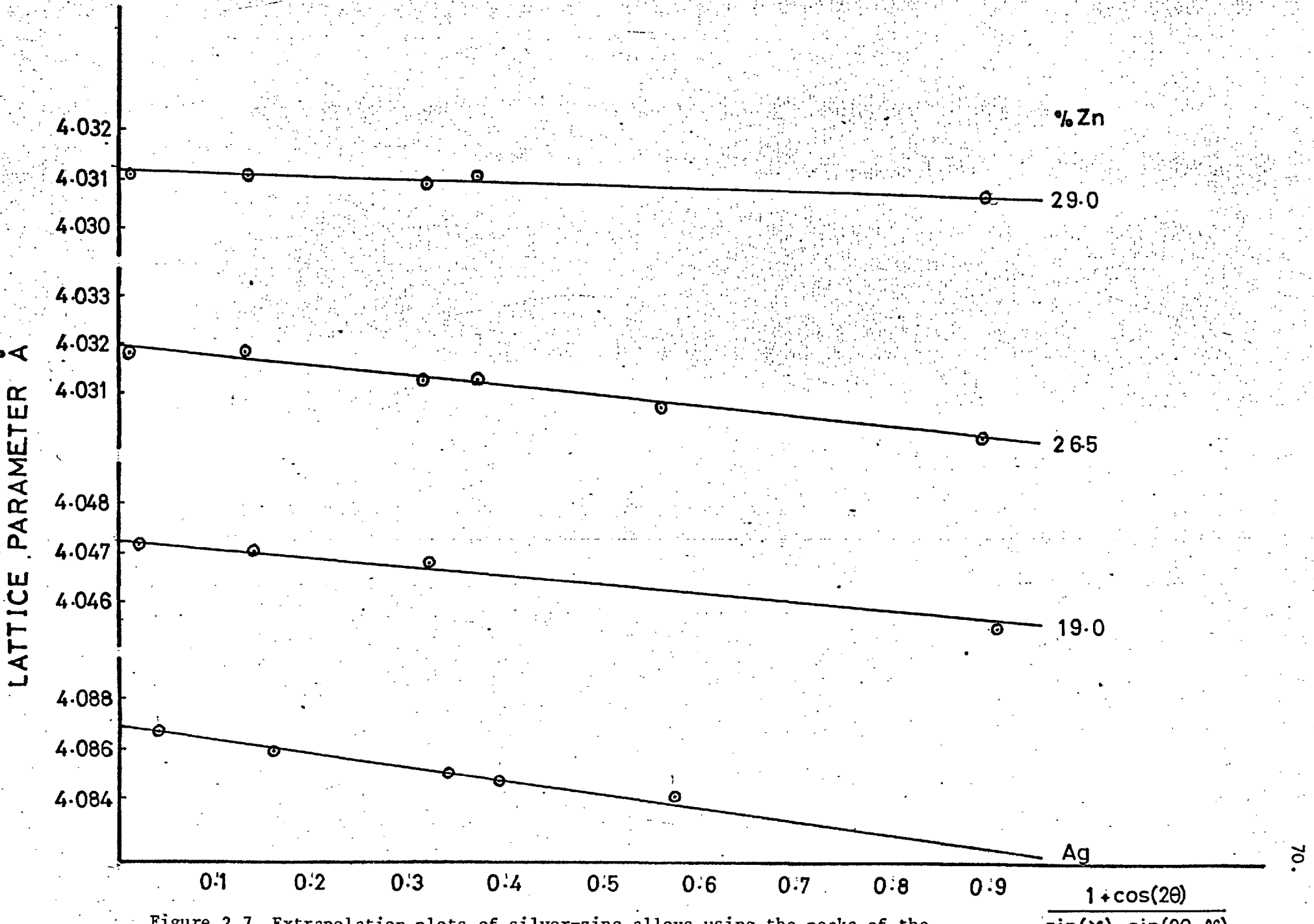

Figure 2.7 Extrapolation plots of silver-zinc alloys using the peaks of the Bragg profiles.

II. Errors Arising from the SB Geometry

The principal geometrical errors, associated with the specimen, in the SB method, have been analysed by Segmuller (1957). These are the flat-specimen error, the specimen displacement error and the specimen transparency errors. Kunze (1964) has, rather unnecessarily, taken these calculations to several higher orders of approximation in both SB and BB geometries. Since the broadening effects and the centroid shifts of several other aberrations remain to be analysed, it is thought desirable to treat all the geometrical errors in one scheme. The method used is analogous to that used by Pike (1957) for the conventional diffractometer. The SB geometry is illustrated in Fig. (2.8), the curve AQB being a section of the focusing circle and (x, y, z) are normal coordinates of a point P, such that the y-z plane is tangent to AQB at Q. The focus at A and the receiving slit at B are (for the moment) both assumed to be sharp lines and f and r are any points along them. The diffractometer is set to receive an X-ray reflection at $4\theta_m$ where $\theta_m = \theta - \varepsilon$, θ being the Bragg angle and ε is a small deviation in the scale of θ. Let the crystal grain at P have an orientation mis-set, from that corresponding to exact Bragg reflection, by δ

$$\text{i.e.} \quad \hat{APB} = \pi - (2\theta - 2\delta)$$

to first order then

$$\delta = \frac{-\cos 2\theta - \cos \hat{APB}}{2 \sin 2\theta} \qquad \ldots (2.16)$$

$$\text{Now} \quad \cos \hat{APB} = \frac{\underline{PA}.\underline{PB}}{|\underline{PA}||\underline{PB}|} \qquad \ldots (2.17)$$

where

$$\underline{PA} = (-s_1 \sin\gamma - x)\,\underline{i} + (s_1 \cos\gamma - y)\,\underline{j} + (f - z)\underline{k} \qquad \ldots (2.18)$$

$$\underline{PB} = (-s_2 \sin(2\theta_m - \gamma) - x)\underline{i} + (-s_2 \sin(2\theta_m - \gamma) - y)\underline{j} + (r - z)\underline{k}$$

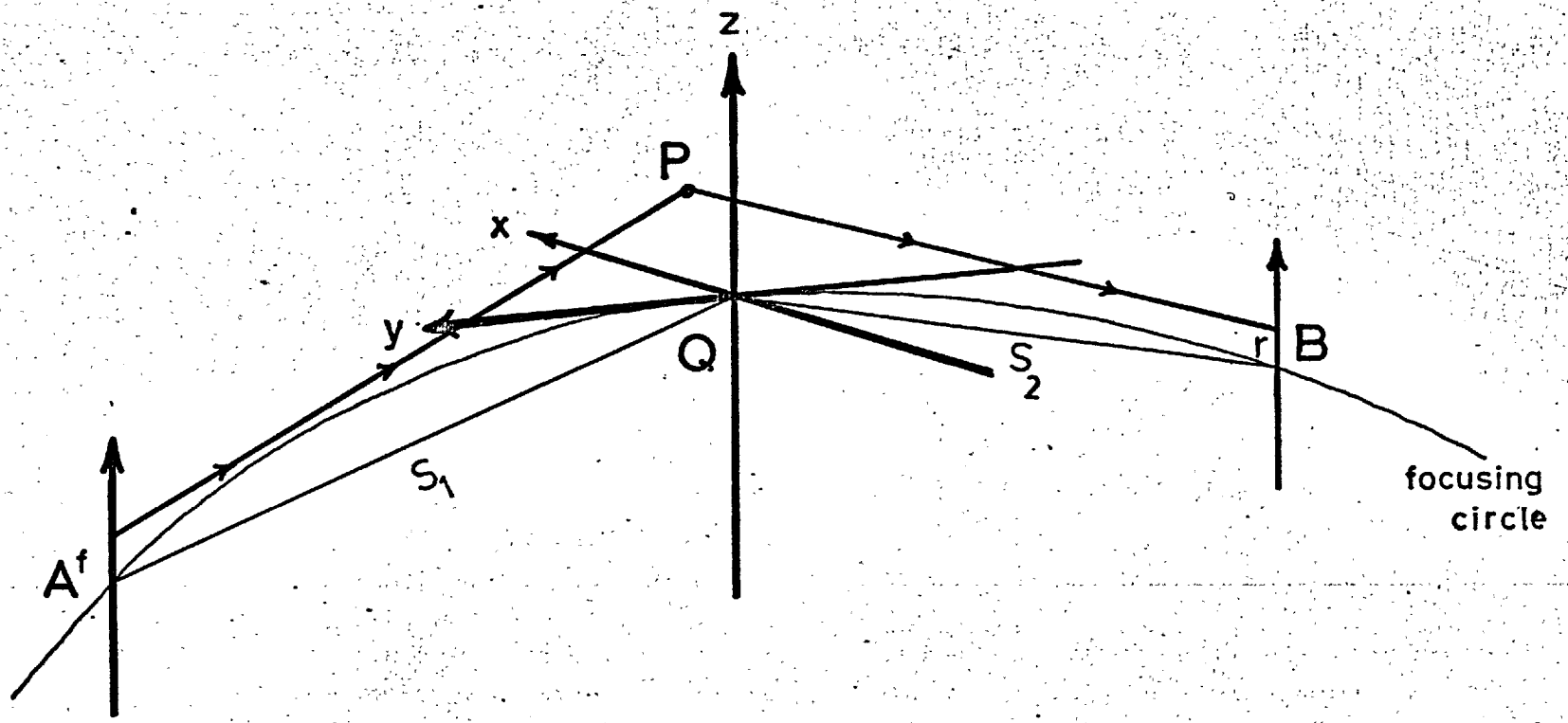

Figure 2.8 Seeman-Bohlin geometry.

and $s_1 = \sin\gamma$, $s_2 = \sin(2\theta_m - \gamma)$ in units where $2R = 1$ (R being the radius of the focusing circle).

Using 2.18 and 2.17, $\cos \hat{APB}$ can be evaluated to first order in ϵ where $\cos 2\theta_m = \cos 2\theta + 2\epsilon \sin 2\theta$. Apart from the term in x, the first significant terms in other parameters are second order. Using 2.16 it is found, after tedious calculation, that

$$\delta = \epsilon - (Ax + Bx^2 + Cy^2 + Dz^2 + Erz + Ffz + Gr^2 + Hf^2 + Jxy + Kfr) \quad \ldots (2.19)$$

where $A = \dfrac{\sin 2\theta}{2s}$

$$B = \frac{2s + (c - 5s)(s_1^2 + s_2^2) + 8s^2(s - c)}{4s^2 \sin 2\theta}$$

$$C = A$$

$$D = \frac{2s - (s - c)(s_1^2 + s_2^2)}{4s^2 \sin 2\theta}$$

$$E = \frac{s_1^2(s - c) - s}{2s^2 \sin 2\theta}$$

$$F = \frac{s_2^2(s - c) - s}{2s^2 \sin 2\theta}$$

$$G = \frac{-s_1^2(s - c)}{4s^2 \sin 2\theta}$$

$$H = \frac{-s_2^2(s - c)}{4s^2 \sin 2\theta}$$

$$J = \frac{\left[4s(s-c) - (s_1^2 + s_2^2)\right](s_1c_2 - s_2c_1) - 2s(s_2c_2 - s_1c_1)}{2s^2 \sin 2\theta}$$

$$K = \frac{1}{2s \sin 2\theta}$$

and $c_1 = \cos\gamma$, $c_2 = \cos(2\theta - \gamma)$, $c = c_1 c_2$, $s = s_1 s_2$

The expressions A, C, D and K correspond exactly to those of Pike (1957) for BB geometry, which is the limiting case where $s_1 = s_2 = \sin\theta$. The expressions B and J correspond to second order terms neglected by Pike and E, F, G, H are in direct correspondence with his expressions except for the sign. This change in sign makes no difference in any of the following calculations.

The efficiency of reflection of a grain with mis-setting δ is some even function $f(\delta)$ i.e.

$$\int_{-\infty}^{\infty} \delta\, f(\delta)\, d\delta = 0 \quad \text{and} \quad \int_{-\infty}^{\infty} f(\delta)\, d\delta = 1$$

The intensity diffracted by an element of volume $\delta x \delta y \delta z$, from an element of source δf, through an element of receiving slit δr, whilst the counter moves through $\delta\varepsilon$ at constant velocity, (the angular velocity of the receiving slit about the specimen is constant in the SB system too) is:

$$I(\varepsilon)\,\delta\varepsilon = f(\delta) \exp(-\mu p)\ \delta x \delta y \delta z\ \delta f \delta r \delta\varepsilon \qquad \ldots (2.20)$$

where p is the path length in the specimen and μ is the absorption coefficient of the powdered specimen. The shift of the centroid from θ_B (i.e. from the centroid of the spectral profile under exact Bragg reflection from Q with r = f = 0) is then given by

$$\langle\varepsilon\rangle = \frac{\int\int\int\int\int\int \varepsilon\ f(\delta) \exp(-\mu p)\, dx dy dz\, df dr d\varepsilon}{\int\int\int\int\int\int f(\delta) \exp(-\mu p)\, dx dy dz\, df dr d\varepsilon} \qquad \ldots (2.21)$$

The principal specimen errors are associated with the equatorial terms, that is terms in x and y only, and these terms are separable because all the integrations in 2.21 are independent.

Flat Specimen Error

If a flat specimen is used the error, which arises out of the y term in (2.19) is given by

$$\langle\varepsilon\rangle_{\text{flat}} = C \frac{\int_{-\ell}^{\ell} y^2 \, dy}{\int_{-\ell}^{\ell} dy} \qquad \ldots (2.22)$$

where the specimen is of length 2ℓ. Hence

$$\langle\varepsilon\rangle_{\text{flat}} = \frac{C\ell^2}{3} = \frac{\alpha^2}{6} \frac{\sin 2\theta}{\sin\gamma \sin(2\theta - \gamma)} \qquad \ldots (2.23)$$

where 2α is the divergence angle.

The variance of the aberration, i.e. the mean square broadening, defined in equation 2.1, is given by

$$W = \langle\varepsilon^2\rangle - \langle\varepsilon\rangle^2 \quad \text{and hence}$$

$$W_{\text{flat}} = C^2\ell^4 \left(\frac{1}{5} - \frac{1}{9}\right)$$

or

$$W_{\text{flat}} = \frac{\alpha^4 \sin^2 2\theta}{45 \sin^2\gamma \sin^2(2\theta - \gamma)} \qquad \ldots (2.24)$$

The flat specimen error arises as a special case of a wrong curvature for the specimen surface. A more general error in curvature can arise from inaccurate machining of the specimen frame or if a specimen is taken from one SB diffractometer to another of slightly different radius (commercial diffractometers on which SB attachments have been fitted

tend to have similar but not identical radii - Vassamillet and King 1963). Without repeating the calculation, the error arising from the wrong radius of curvature, R_c, is

$$\langle\varepsilon\rangle_{R_c} = \frac{\alpha^2 \sin 2\theta}{6 \sin\gamma \sin(2\theta - \gamma)} \cdot R\left[\frac{1}{R} - \frac{1}{R_c}\right] \quad \ldots (2.25)$$

and the broadening is given by

$$W_{R_c} = \frac{\alpha^4 \sin^2 2\theta}{\sin^2\gamma \sin^2(2\theta - \gamma)} \cdot \frac{R^2}{180}\left(\frac{4}{R_c^2} + \frac{4}{R^2} + \frac{13}{RR_c}\right) \quad \ldots (2.26)$$

An estimate of the size of the flat-specimen error calculated for $2\theta = 90^\circ$, $\gamma = 45^\circ$, $\alpha = 2^\circ$ when (2.22) gives

$$\langle\varepsilon\rangle_{flat} \simeq 0.02^\circ\,\theta$$

If a small error occurs of say 5 mm in the radius of curvature then the centroid shift is

$$\langle\varepsilon\rangle_{R_c} \simeq 0.0005^\circ\theta$$

Since machine shop errors, in the manufacture of specimen mounts, and specimen preparation errors are not likely to exceed 5mm in the radius of curvature, their effects can thus be safely ignored.

Transparency Errors

a. High absorption

The transparency error arises from the x term in equation 2.19 i.e.

$$\langle\varepsilon\rangle_{\mu\to\infty} = A\int_0^\infty xe^{-Mx}\,dx \Big/ \int_0^\infty e^{-Mx}\,dx \quad \ldots (2.27)$$

where $M = \mu\left(\frac{s_1}{s_1} + \frac{s_2}{s_2}\right)$

whence

$$\langle\varepsilon\rangle_{\mu \to \infty} = \frac{A}{M} = \frac{\sin 2\theta}{4\mu R (\sin\gamma + \sin(2\theta - \gamma))} \quad \ldots (2.28)$$

The broadening is given by 2.1 with

$$\langle\varepsilon^2\rangle_{\mu \to \infty} = \frac{A^2 \int_0^\infty x^2 e^{-Mx} dx}{\int_0^\infty e^{-Mx} dx} \quad \ldots (2.29)$$

whence $W_{\mu \to \infty} = \langle\varepsilon\rangle^2_{\mu \to \infty}$ ... (2.30)

The magnitude of the centroid shift, due to this transparency error, may be estimated by taking $\gamma = 45^\circ$, $2\theta = 90^\circ$, R = 175 mm and μ (for permaquartz) = 212 cm^{-1} (for CuK_α radiation). The centroid shift is

$$\langle 2\varepsilon\rangle_{\mu \to \infty} \simeq 0.003^\circ 2\theta$$

b. Low absorption

When the specimen is highly transparent it can no longer be assumed that all X-rays are scattered inside it. The geometrically effective region is governed by slit dimensions and specimen size. For the highest precision the errors should be evaluated for the particular experimental situation. The usual limiting case, of an infinitesimally thick specimen, can be evaluated, however. Again it is only the first order term in x that is important

$$\langle\varepsilon\rangle_{t \to 0} = \frac{A \int_0^t x e^{-Mx} dx}{\int_0^t e^{-Mx} dx}$$

where t is the thickness of the specimen.

To second order in t this becomes

$$\langle\varepsilon\rangle_{t\to o} = \frac{A\frac{t^2}{2}}{t} = \frac{At}{2} = \frac{t \sin 2\theta}{8R \sin\gamma \sin(2\theta - \gamma)} \qquad \ldots (2.31)$$

and the associated broadening is given by

$$W_{t\to o} = A^2 t^2 \left[\frac{1}{3} - \frac{1}{4}\right]$$

whence $$W_{t\to o} = \frac{t^2 \sin^2 2\theta}{192 R^2 \sin^2\gamma \sin^2(2\theta - \gamma)} \qquad \ldots (2.32)$$

For $\gamma = 45^o$, $2\theta = 90^o$, $R = 175$ mm and $t = 0.1$ mm the centroid shift

$$\langle 2\varepsilon\rangle_{t\to o} \simeq 0.015^o 2\theta$$

Specimen Displacement

If the specimen is displaced a distance ΔR_s from the focusing circle and there is no transparency error, then

$$\langle\varepsilon\rangle_{\Delta R_s} = \frac{\int Ax\, e^{-Mx}\, \delta(x - \Delta R_s)\, dx}{\int e^{-Mx}\, \delta(x - \Delta R_s)\, dx}$$

therefore

$$\langle\varepsilon\rangle_{\Delta R_s} = A\,\Delta R_s = \frac{\Delta R_s \sin 2\theta}{4R \sin\gamma \sin(2\theta - \gamma)} \qquad \ldots (2.33)$$

The variance of this aberration appears to be zero when calculated to the same order of approximation as the centroid shifts. Since there is no broadening of the profile the expression, 2.33, for the centroid shift will also apply to the peak shift as was found in the case of BB geometry (Wilson, 1963). To demonstrate the validity of the expression for peak shifts and to provide an estimate of the effects of specimen displacement a shift ΔR_s of 1.25 mm ($1/20''$), from the as-aligned position,

TABLE 2.1

THEORETICAL AND OBSERVED PEAK SHIFTS FOR ΔR_S = 1.25 mm, FOR VARIOUS SPECIMEN SETTINGS, γ.

γ^o	$\Delta 2\theta^o$ Obs.	$\Delta 2\theta^o$ Theor.
20	0.653	0.647
25	0.528	0.538
35	0.434	0.437
45	0.390	0.409
55	0.446	0.432
65	0.535	0.523
70	0.628	0.617
75	0.790	0.781
80	1.103	1.106

was given to the specimen. Table (2.1) shows the peak shift, as a function of γ, for the 132 profile of permaquartz (~$90^{o}2\theta$ for CuK_{α}), compared with the theoretical shift (2.33).

Specimen Rotation Error

A rotation of the specimen through an angle τ about the z axis poses a similar problem to that of $2\theta{:}\theta$ mis-set in the BB geometry. To simplify the calculation a flat specimen, of length 2ℓ, is considered and the flat specimen error is removed later in the derivation. The absorption factor is

$$e^{-M'(x\cot\tau - y)}$$

where

$$M' = \mu\left[\frac{\operatorname{cosec}\gamma}{\cot\gamma + \cot\tau} + \frac{\operatorname{cosec}(2\theta-\gamma)}{\cot\tau - \cot(2\theta-\gamma)}\right] \qquad \ldots (2.34)$$

The centroid shift is

$$\langle\varepsilon\rangle_{\tau} = \frac{A \iint (x + y^2)\, e^{-M'(x\cot\tau - y)}\, dx\, dy}{\iint e^{-M'(x\cot\tau - y)}\, dx\, dy}$$

The ranges of integration are

for x , $y \tan\tau$ to ∞

and for y , $-\ell$ to $+\ell$

Then

$$\langle\varepsilon\rangle_{\tau} = \frac{A}{2\ell}\int_{-\ell}^{\ell}\left(y\tan\tau + y^2 + \frac{1}{M'\cot\tau}\right) dy$$

The first term in the integrand integrates to zero while the second is

the flat specimen error which is removed. Hence using just the third term the centroid shift due to specimen rotation is

$$\langle\varepsilon\rangle_\tau = \frac{A}{M'\cot\tau} \qquad \ldots (2.35)$$

To first order in small τ this is identical with the (high absorption) transparency error (2.28) and consequently no additional shift results. In order for a centroid shift due solely to specimen rotation to appear, τ has to be of the same order as γ or $(2\theta - \gamma)$ and, since in practice, the specimen rotation can easily be set to $\pm 2^o$ the error (2.35) is negligible.

Broadening of the profile due to specimen rotation is of far more importance. In order to derive the variance, equation 2.1 requires

$$\langle\varepsilon^2\rangle_\tau = \frac{A^2 \iint (x^2 + 2xy^2 + y^4)\, e^{-M'(x\cot\tau - y)}\, dx\, dy}{\iint e^{-M'(x\cot\tau - y)}\, dx\, dy}$$

which becomes

$$\langle\varepsilon^2\rangle_\tau = A^2\left[\frac{\ell^2}{3}\tan^2\tau + \frac{2}{M'^2}\tan^2\tau + \frac{2\ell^2}{3M'}\tan\tau + \frac{\ell^4}{5}\right]$$

The variance is then

$$W_\tau = \langle\varepsilon^2\rangle_\tau - \langle\varepsilon\rangle_\tau^2 = A^2\left[\frac{\tan^2\tau}{M'^2} + \frac{\ell^2\tan^2\tau}{3} + \frac{4}{45}\ell^4\right] \qquad \ldots (2.36)$$

Again, except where τ is large, M' is negligibly different from M. The first term in (2.36) is, therefore, just the broadening resulting from the low transparency error and the third term is that due to the flat specimen error. Hence, the variance arising out of the rotation is given by

$$W = \frac{1}{3}\left[\frac{\alpha \sin 2\theta \tan \tau}{2 \sin\gamma \sin(2\theta-\gamma)}\right]^2 \qquad \ldots \quad (2.37)$$

Specimen Tilt Error

If the specimen surface is tilted through an angle σ, about the y axis then the equation of the front surface of the specimen may be given by $x_\sigma = z \tan\sigma$. For a particular z, and no vertical divergence of the rays, the coordinates f and r are each equal to z. The centroid shift is given by

$$\langle\varepsilon\rangle_\sigma = \frac{\int_{-h}^{h}\int_{z\tan\sigma}^{\infty}\left[Ax + (D + E + F + G + H + K)z^2\right] e^{-M(x-x_\sigma)}\,dxdz}{\int_{-h}^{h}\int_{z\tan\sigma}^{\infty} e^{-M(x-x_\sigma)}\,dxdz}$$

where the focus, specimen and receiving slit are of height 2h. The coefficient of z^2 is identically zero and the expression simplifies to

$$\langle\varepsilon\rangle_\sigma = \frac{1}{2h}\int_{-h}^{h}\left(\frac{A}{M} + Az\tan\sigma\right) dz$$

The first term is the small transparency error (2.28) and the second term integrates to zero. There is no centroid shift arising out of tilt. The second moment of the aberration is

$$\langle\varepsilon^2\rangle = \frac{M}{2h}\int_{-h}^{h}\int_{x_\sigma}^{\infty} A^2x^2 e^{-M(x-x_\sigma)}\,dxdz$$

Neglecting the broadening due to transparency gives

$$W = \langle\varepsilon^2\rangle_\tau = \frac{A^2h^2\tan^2\sigma}{3}$$

or

$$W = \frac{1}{3}\left[\frac{h \sin 2\theta.\ \tan\sigma}{4R\sin\gamma \sin(2\theta-\gamma)}\right]^2 \qquad \ldots \quad (2.38)$$

Machine shop accuracy is probably such that the tilt error is less than 1^{o} which means an additional breadth ($\sqrt{W_{\sigma}}$) of less than $0.015^{o}2\theta$ which is quite tolerable. It is probably not necessary, therefore, to provide a tilting adjustment to the specimen.

Axial terms

In order to deal with the axial divergence of rays, (i.e. divergence from the plane of diffraction x-y) the axial terms (f, r, z) must be considered. If any two of the vertical extensions of the specimen, focus and receiving slit are symmetrical about the same equatorial plane, all the cross terms in (2.19) cancel under integration. Assuming all three are symmetrical about the same plane with extensions of 2F(f), 2T(r) and 2Z(z) the centroid shift is

$$\langle\varepsilon\rangle_{AD} = \frac{DZ^2}{3} + \frac{GT^2}{3} + \frac{HF^2}{3}$$

$$\text{or } \langle\varepsilon\rangle_{AD} = \langle\varepsilon\rangle_{Z} + \langle\varepsilon\rangle_{T} + \langle\varepsilon\rangle_{F} \qquad \ldots (2.39)$$

where

$$\langle\varepsilon\rangle_{Z} = \frac{Z^2}{R^2} \cdot \frac{\sin 2\theta \cos 2(\theta - \gamma)}{48 \sin^2\gamma \sin^2(2\theta - \gamma)} \qquad \ldots (2.40)$$

$$\langle\varepsilon\rangle_{T} = \frac{T^2}{R^2} \cdot \frac{\cot 2\theta}{48 \sin^2(2\theta - \gamma)} \qquad \ldots (2.41)$$

$$\langle\varepsilon\rangle_{F} = \frac{F^2}{R^2} \cdot \frac{\cot 2\theta}{48 \sin^2\gamma} \qquad \ldots (2.42)$$

The last two terms, far from going to zero in an extrapolation to $2\theta = 180^{o}$, go to infinity. In the usual case of equal heights (2h) for specimen, receiving slit and focus the broadening simplifies to

$$W_{AD} = \frac{4h^4}{45}(D^2 + G^2 + H^2) + \frac{h^4}{9}(E^2 + F^2 + K^2) \qquad \ldots (2.43)$$

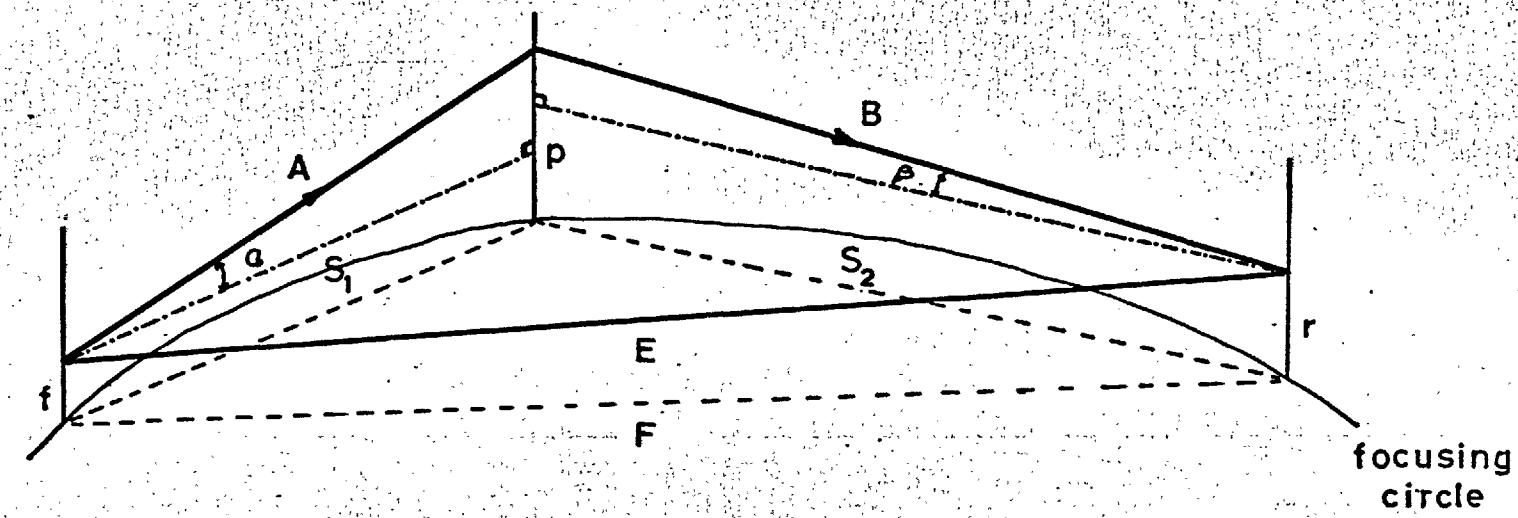

Figure 2.9 Axial divergence in SB geometry.

where D, E, F, G, H, K are given in (2.19)

Axial Divergence with Soller Slits

The formidable task of calculating axial divergence, with one or two sets of Soller slits in the beam, has been completed here. The method is essentially that of Pike (1957), but the asymmetry considerably complicates the arithmetic.

Following Pike and from Fig. (2.9):

$$A^2 = (p - f)^2 + s_1^2$$

$$B^2 = (p - r)^2 + s_2^2 \qquad \ldots (2.44)$$

$$E^2 = (r - f)^2 + F^2$$

where the path of the ray is traced from a point f through p to r. Using the same convention as before and, using the cosine rule:

$$F^2 = s_1^2 + s_2^2 + 2s_1 s_2 \cos 2\theta \qquad \ldots (2.45)$$

and $E^2 = A^2 + B^2 + 2AB \cos 2\theta_m$

If α and β are the angles that the incident and reflected rays respectively make with the plane of diffraction, then

$$\alpha = \frac{p - f}{s_1}, \qquad \beta = \frac{p - r}{s_2}$$

and

$$\varepsilon = \frac{\alpha^2 + \beta^2}{4} \cot 2\theta - \frac{\alpha\beta}{2} \operatorname{cosec} 2\theta \qquad \ldots (2.46)$$

If a set of Soller slits is placed in the incident beam, it can be

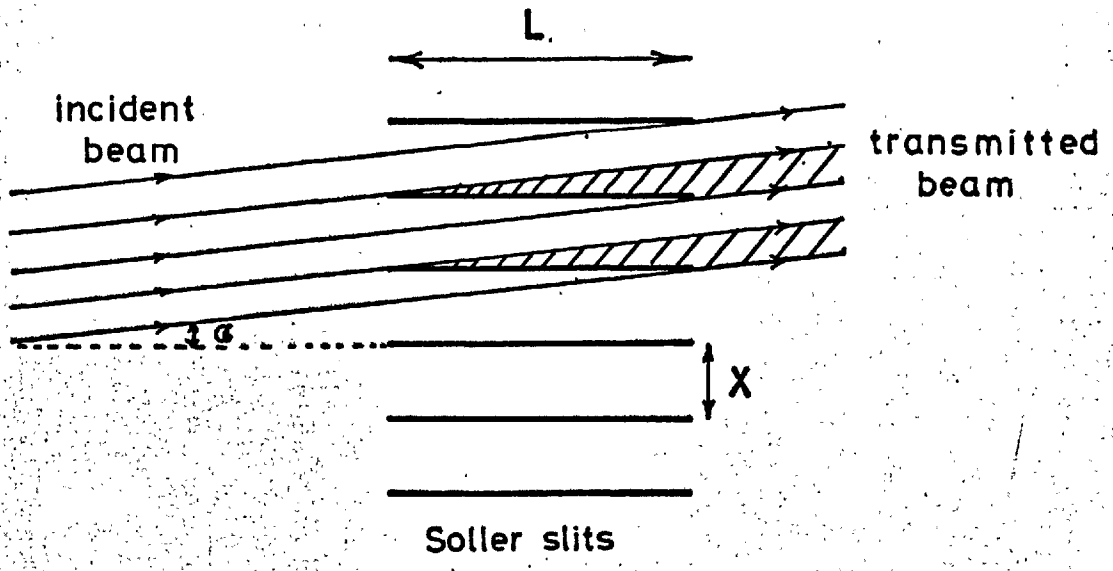

Figure 2.10 Transmission through Soller slits.

seen from Fig. (2.10) that the amount of X-rays allowed through for one foil is proportional to X - Lα and the amount stopped is proportional to Lα. The fractional transmission is then $(1 - \frac{\alpha}{\Delta})$ where Δ is the foil spacing per unit length of slit. The transmission through the second set of slits depends on the relative positions of the foils in the two slits and is an intractably complicated function of α and β. Pike adequately justified replacing this transmission function by an average transmission $(1 - \frac{\beta}{\Delta})$. Integrals can be taken over positive α only, but must be taken over both signs of β.

The displacement of the centroid is then given by

$$\langle\varepsilon\rangle = \frac{\iiint\left[\frac{\alpha^2+\beta^2}{4}\cot 2\theta - \frac{\alpha\beta}{2}\operatorname{cosec} 2\theta\right](1-\frac{\alpha}{\Delta_1})(1-\frac{\beta}{\Delta_2})\,d\alpha d\beta dp}{\iiint (1-\frac{\alpha}{\Delta_1})(1-\frac{\beta}{\Delta_2})\,d\alpha d\beta dp} \qquad \ldots (2.47)$$

For convenience two q values similar to that of Pike are introduced:

$$q_1 = \frac{s_1 \Delta_1}{h}, \qquad q_2 = \frac{s_2 \Delta_2}{h} \qquad \ldots (2.48)$$

All the combinations of ranges of integration, as a function of the q variables, are given in Tables (2.2, 2.3, 2.4). The integrations were performed over all possible combinations. The centroid shift can be represented as in Pike's paper by expressions of the kind

$$\langle\varepsilon\rangle = h^2 (\langle\varepsilon\rangle_x (1) \cot 2\theta + \langle\varepsilon\rangle_x (2) \operatorname{cosec} 2\theta) \qquad \ldots (2.49)$$

The two $\langle\varepsilon\rangle_x$ each have seven distinct functional forms depending on the particular combination of q_1 and q_2. There are thirteen distinguishable types of combination of the q's and these are given in Table (2.5) along with a letter designating the particular function that applies. Of the seven pairs of functions four are basic and three may be derived via the operator T which interchanges the suffices on the q and the s i.e.

TABLE 2.2

RANGES OF INTEGRATION - $q_1 \geq 2$

$-h \leq p \leq h$ $\alpha_{max} = \frac{p+h}{s_1}$	$q_2 \geq 2$	$-h \leq p \leq h$, $\frac{p-h}{s_2} \leq \beta \leq \frac{p+h}{s_2}$
	$1 \leq q_2 \leq 2$	$h(1-q_2) \leq p \leq h(q_2-1)$, $\frac{p-h}{s_2} \leq \beta \leq \frac{p+h}{s_2}$
		$h(q_2-1) \leq p \leq h$, $\frac{p-h}{s_2} \leq \beta \leq \Delta_2$
		$-h \leq p \leq h(1-q_2)$, $-\Delta_2 \leq \beta \leq \frac{p+h}{s_2}$
	$q_2 \leq 1$	$-h \leq p \leq h(q_2-1)$, $-\Delta_2 \leq \beta \leq \frac{p+h}{s_2}$
		$h(q_2-1) \leq p \leq h(1-q_2)$, $-\Delta_2 \leq \beta \leq \Delta_2$
		$h(1-q_2) \leq p \leq h$, $\frac{p-h}{s_2} \leq \beta \leq \Delta_2$

TABLE 2.3 RANGES OF INTEGRATION $1 \leq q_1 \leq 2$

$-h \leq p \leq h(q_1-1)$ $\alpha_{max} = \frac{p+h}{s_1}$	$q_2 \geq 2$		$-h \leq p \leq h(q_1-1)$	$\frac{p-h}{s_2} \leq \beta \leq \frac{p+h}{s_2}$
	$1 \leq q_2 \leq 2$	$q_2 \geq q_1$	$-h \leq p \leq h(1-q_2)$	$-\Delta_2 \leq \beta \leq \frac{p+h}{s_2}$
			$h(1-q_2) \leq p \leq h(q_1-1)$	$\frac{p-h}{s_2} \leq \beta \leq \frac{p+h}{s_2}$
		$q_2 \leq q_1$	$-h \leq p \leq h(1-q_2)$	$-\Delta_2 \leq \beta \leq \frac{p+h}{s_2}$
			$h(1-q_2) \leq p \leq h(q_2-1)$	$\frac{p-h}{s_2} \leq \beta \leq \frac{p+h}{s_2}$
			$h(q_2-1) \leq p \leq h(q_1-1)$	$\frac{p-h}{s_2} \leq \beta \leq \Delta_2$
	$q_2 \leq 1$	$q_2 \geq 2-q_1$	$-h \leq p \leq h(q_2-1)$	$-\Delta_2 \leq \beta \leq \frac{p+h}{s_2}$
			$h(q_2-1) \leq p \leq h(1-q_2)$	$-\Delta_2 \leq \beta \leq \Delta_2$
			$h(1-q_2) \leq p \leq h(q_1-1)$	$\frac{p-h}{s_2} \leq \beta \leq \Delta_2$
		$q_2 \leq 2-q_1$	$-h \leq p \leq h(q_2-1)$	$-\Delta_2 \leq \beta \leq \frac{p+h}{s_2}$
			$h(q_2-1) \leq p \leq h(q_1-1)$	$-\Delta_2 \leq \beta \leq \Delta_2$
$h(q_1-1) \leq p \leq h$ $\alpha_{max} = -\Delta_1$	$q_2 \geq 2$		$h(q_1-1) \leq p \leq h$	$\frac{p-h}{s_2} \leq \beta \leq \frac{p+h}{s_2}$
	$1 \leq q_2 \leq 2$	$q_2 \geq q_1$	$h(q_1-1) \leq p \leq h(q_2-1)$	$\frac{p-h}{s_2} \leq \beta \leq \frac{p+h}{s_2}$
			$h(q_2-1) \leq p \leq h$	$\frac{p-h}{s_2} \leq \beta \leq \Delta_2$
		$q_2 \leq q_1$	$h(q_1-1) \leq p \leq h$	$\frac{p-h}{s_2} \leq \beta \leq \Delta_2$
	$q_2 \leq 1$	$q_2 \leq 2-q_1$	$h(q_1-1) \leq p \leq h(1-q_2)$	$-\Delta_2 \leq \beta \leq \Delta_2$
			$h(1-q_2) \leq p \leq h$	$\frac{p-h}{s_2} \leq \beta \leq \Delta_2$
		$q_2 \geq 2-q_1$	$h(q_1-1) \leq p \leq h$	$\frac{p-h}{s_2} \leq \beta \leq \Delta_2$

TABLE 2.4 RANGES OF INTEGRATION $q_1 \leq 1$

$-h \leq p \leq h(q_1-1)$ $\alpha_{max} = \frac{p+h}{s_1}$	$q_2 \leq 2$		$-h \leq p \leq h(q_1-1)$	, $\frac{p-h}{s_2} \leq \beta \leq \frac{p+h}{s_2}$
	$1 \leq q_2 \leq 2$	$q_2 \geq 2-q_1$	$h(1-q_2) \leq p \leq h(q_1-1)$	, $\frac{p-h}{s_2} \leq \beta \leq \frac{p+h}{s_2}$
			$-h \leq p \leq h(1-q_2)$	, $-\Delta_2 \leq \beta \leq \frac{p+h}{s_2}$
		$q_2 \leq 2-q_1$	$-h \leq p \leq h(q_1-1)$	, $-\Delta_2 \leq \beta \leq \frac{p+h}{s_2}$
	$q_2 \leq 1$	$q_2 \leq q_1$	$h(q_2-1) \leq p \leq h(q_1-1)$	, $-\Delta_2 \leq \beta \leq \Delta_2$
			$-h \leq p \leq h$	, $-\Delta_2 \leq \beta \leq \frac{p+h}{s_2}$
		$q_2 \geq q_1$	$-h \leq p \leq h(q_1-1)$	, $-\Delta_2 \leq \beta \leq \frac{p+h}{s_2}$
$h(q_1-1) \leq p \leq h$ $\alpha_{max} = \Delta_1$	$q_2 \geq 2$		$h(q_1-1) \leq p \leq h$	, $\frac{p-h}{s_2} \leq \beta \leq \frac{p+h}{s_2}$
	$1 \leq q_2 \leq 2$	$q_2 \leq 2-q_1$	$h(q_2-1) \leq p \leq h$	, $\frac{p-h}{s_2} \leq \beta \leq \Delta_2$
			$h(1-q_2) \leq p \leq h(q_2-1)$	, $\frac{p-h}{s_2} \leq \beta \leq \frac{p+h}{s_2}$
			$h(q_1-1) \leq p \leq h(1-q_2)$	, $-\Delta_2 \leq \beta \leq \Delta_2$
		$q_2 \geq 2-q_1$	$h(q_2-1) \leq p \leq h$	, $\frac{p-h}{s_2} \leq \beta \leq \Delta_2$
			$h(q_1-1) \leq p \leq h(q_2-1)$	, $\frac{p-h}{s_2} \leq \beta \leq \frac{p+h}{s_2}$
	$q_2 \leq 1$	$q_2 \leq q_1$	$h(1-q_2) \leq p \leq h$	, $\frac{p-h}{s_2} \leq \beta \leq \Delta_2$
			$h(q_1-1) \leq p \leq h(1-q_2)$	, $-\Delta_2 \leq \beta \leq \Delta_2$
		$q_2 \geq q_1$	$h(1-q_2) \leq p \leq h$	, $\frac{p-h}{s_2} \leq \beta \leq \Delta_2$
			$h(q_2-1) \leq p \leq h(1-q_2)$	, $-\Delta_2 \leq \beta \leq \Delta_2$
			$h(q_1-1) \leq p \leq h(q_2-1)$	, $-\Delta_2 \leq \beta \leq \frac{p+h}{s_2}$

TABLE 2.5

KEY TO THE FUNCTION $\langle \varepsilon \rangle_x$ TO BE USED IN EQUATION (2.49)

Range of q_1	Range of q_2		X
$q_1 \geq 2$	$q_2 \geq 2$		A
	$1 \leq q_2 \leq 2$		B
	$q_2 \leq 1$		C = B
$1 \leq q_1 \leq 2$	$q_2 \geq 2$		D = TB
	$1 \leq q_2 \leq 2$	$q_2 \geq q_1$	E
		$q_2 \leq q_1$	F = TE
	$q_2 \leq 1$	$q_1+q_2 \geq 2$	G = F = TE
		$q_1+q_2 \leq 2$	H
$q_1 \leq 1$	$q_2 \geq 2$		I = TB
	$1 \leq q_2 \leq 2$	$q_1+q_2 \geq 2$	J = E
		$q_1+q_2 \leq 2$	K = TH
	$q_2 \leq 1$	$q_2 \leq q_1$	L = H
		$q_2 \geq q_1$	M = K = TH

$$T\,\langle\varepsilon\rangle(q_1 s_1,\ q_2 s_2) \;=\; \langle\varepsilon\rangle\ (q_2 s_2,\ q_1 s_1)$$

The four basic pairs of functions are

$$\langle\varepsilon\rangle_A(1) = \frac{105q_1q_2(s_1^2+s_2^2)+96(s_1^2+s_2^2)-s_1^2(126q_1+77q_2)-s_2^2(126q_2+77q_1)}{21s_1^2s_2^2\left[30q_1q_2-20q_1-20q_2+14\right]}$$

and

$$\langle\varepsilon\rangle_A(2) = \frac{105q_1q_2 - 126q_1 - 126q_2 + 152}{21s_1s_2\left[30q_1q_2-20q_1-20q_2 + 14\right]}$$

$$\langle\varepsilon\rangle_B(1) = \frac{2s_1^2q_2^2\left[(-140 + 63q_2 - 21q_2^2 + 5q_2^3) + q_1(210 - 63q_2)\right] + s_2^2\left[3(-672 + 280q_2 - 140q_2^2 + 42q_2^3 - 7q_2^4 + q_2^5) + 2q_1(840 - 280q_2 + 105q_2^2 - 21q_2^3)\right]}{84s_1^2s_2^2\left[20q_1(6-q_2) + (-80 + 20q_2 - 5q_2^2 + q_2^3)\right]}$$

and

$$\langle\varepsilon\rangle_B(2) = \frac{q_2^2\left[21q_1(10 - 3q_2) + (-280 + 126q_2 - 28q_2^2 + 5q_2^3)\right]}{42s_1s_2\left[20q_1(6 - q_2) + (-80 + 20q_2 - 5q_2^2 + q_2^3)\right]}$$

$$\langle\varepsilon\rangle_E(1) = \frac{s_1^2V_1 + s_2^2V_2}{84\,s_1^2s_2^2\,D} \qquad \ldots (2.50)$$

$$\langle\varepsilon\rangle_E(2) = \frac{W}{42s_1s_2\,D}$$

where

$$V_1 = 2(-192 + 224q_2 - 140q_2^4 + 126q_2^5 - 42q_2^6 + 5q_2^7)$$
$$+ 6q_1(224 - 224q_2 + 70q_2^4 - 42q_2^5 + 7q_2^6)$$
$$+ q_1^2(-2016 + 1680q_2 + 210q_2^4 - 63q_2^5)$$
$$+ q_1^3(1680 - 1120q_2) + 3q_1^4(-280 + 140q_2)$$
$$+ 2q_1^5(126 - 42q_2) + 7q_1^6(-6) + 6q_1^7$$

$$V_2 = 2(-192 + 224q_1 - 140q_1^4 + 126q_1^5 - 42q_1^6 + 10q_1^7)$$
$$+ 6q_2(224 - 224q_1 + 70q_1^4 - 42q_1^5)$$
$$+ q_2^2(-2016 + 1680q_1 + 210q_1^4)$$
$$+ q_2^3(1680 - 1120q_1 - 35q_1^4) + 3q_2^4(-280 + 140q_1)$$
$$+ 2q_2^5(126 - 42q_1) + 7q_2^6(-6 + q_1) + 3q_2^7$$

$$W = (256 - 448q_1 + 560q_1^3 - 560q_1^4 + 252q_1^5 - 56q_1^6 + 10q_1^7)$$
$$+ (-448q_2 + 560q_2^3 - 560q_2^4 + 252q_2^5 - 56q_2^6 + 5q_2^7)$$
$$+ 672q_1q_2 + 140q_1^3q_2^3 - 35q_1^3q_2^4$$
$$+ q_1(-560q_2^3 + 420q_2^4 - 126q_2^5 + 14q_2^6)$$
$$+ q_2(-560q_1^3 + 420q_1^4 - 126q_1^5)$$

$$D = (-32 + 80q_1 - 80q_1^2 + 40q_1^3 - 10q_1^4 + 2q_1^5)$$
$$+ (80q_2 - 80q_2^2 + 40q_2^3 - 10q_2^4 + q_2^5)$$
$$+ q_1(120q_2^2 - 40q_2^3 + 5q_2^4) + q_2(120q_1^2 - 40q_1^3)$$
$$- 160q_1q_2 + 60q_1^2q_2^2 - 10q_1^2q_2^3$$

and finally

$$\langle\varepsilon\rangle_H(1) = \frac{s_1^2(-63q_1^2q_2^5 - 42q_1q_2^6 + 10q_2^7 + 420q_1^2q_2^4 - 70q_1^3q_2^4) + s_2^2(420q_1^4q_2^2 - 126q_1^5q_2^2 - 35q_1^4q_2^3 + 3q_2^7 - 7q_1q_2^6)}{84s_1^2s_2^2\left[q_2^5 - 5q_1q_2^4 - 10q_1^2q_2^3 + 120q_1^2q_2^2 - 20q_1^3q_2^2\right]}$$

and

$$\langle\varepsilon\rangle_H(2) = \frac{-28q_1q_2^6 + 10q_2^7 + 70q_1^3q_2^4}{84s_1^2s_2^2\left[q_2^5 - 5q_1q_2^4 - 10q_1^2q_2^3 + 120q_1^2q_2^2 - 20q_1^3q_2^2\right]}$$

The coefficients of cot 2θ and cosec 2θ besides being functions of Δ_1 and Δ_2 are clearly rather complicated functions of γ and θ itself. To check for arithmetic errors the functions were worked out at all the boundaries of the q ranges and shown to match in every case. The numerical evaluation of the coefficients in general was completed by computer. The centroid shifts in $^o2\theta$ are shown for various γ, for the three cases of no Soller slits, one pair of Soller slits and two pairs in Figs. (2.11) to (2.14). Two values of Δ (0.05 and 0.1) have been used in the calculations. For completeness the tabulated values are shown direct from the computer output in Appendix 2.

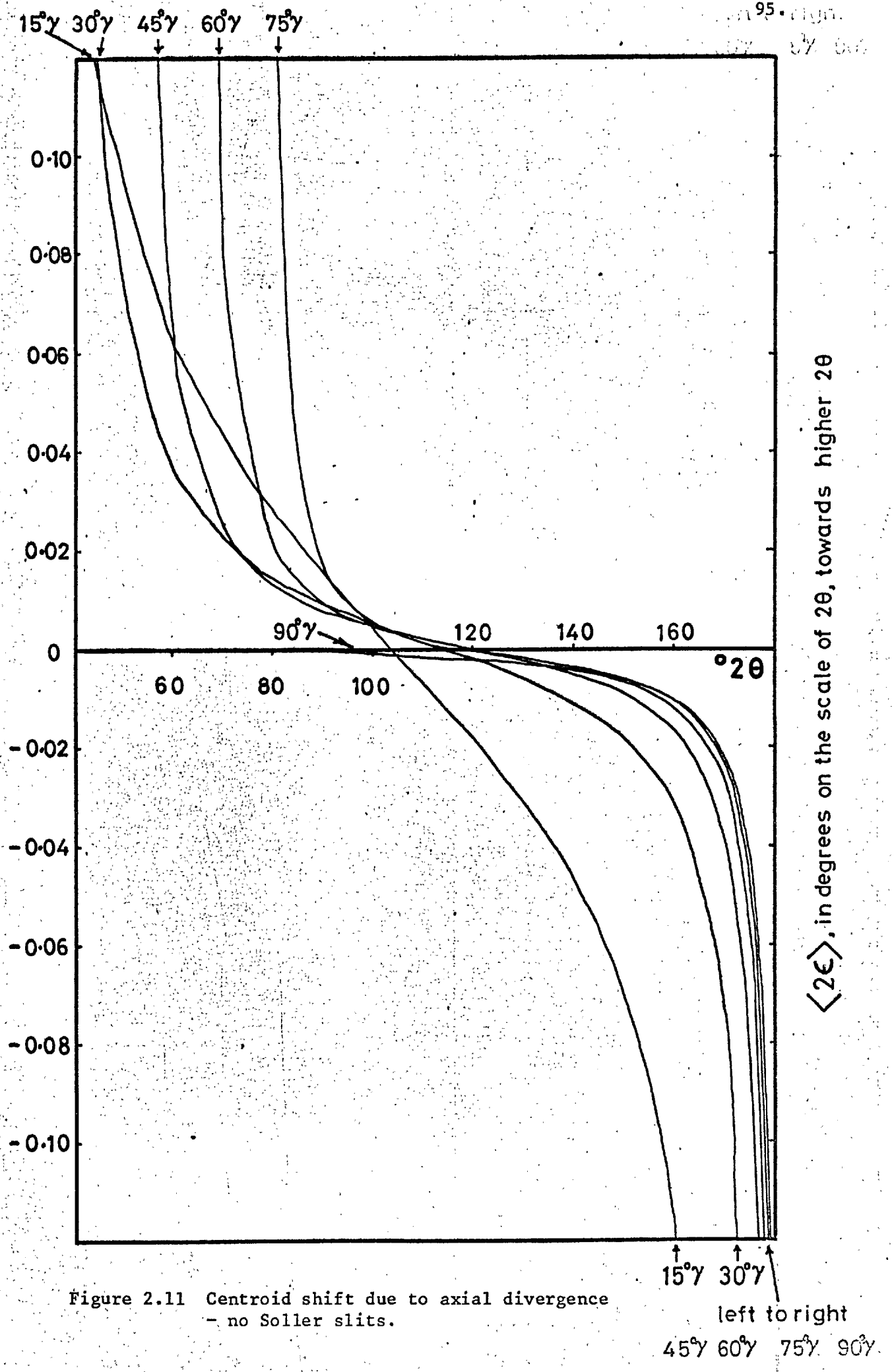

Figure 2.11 Centroid shift due to axial divergence - no Soller slits.

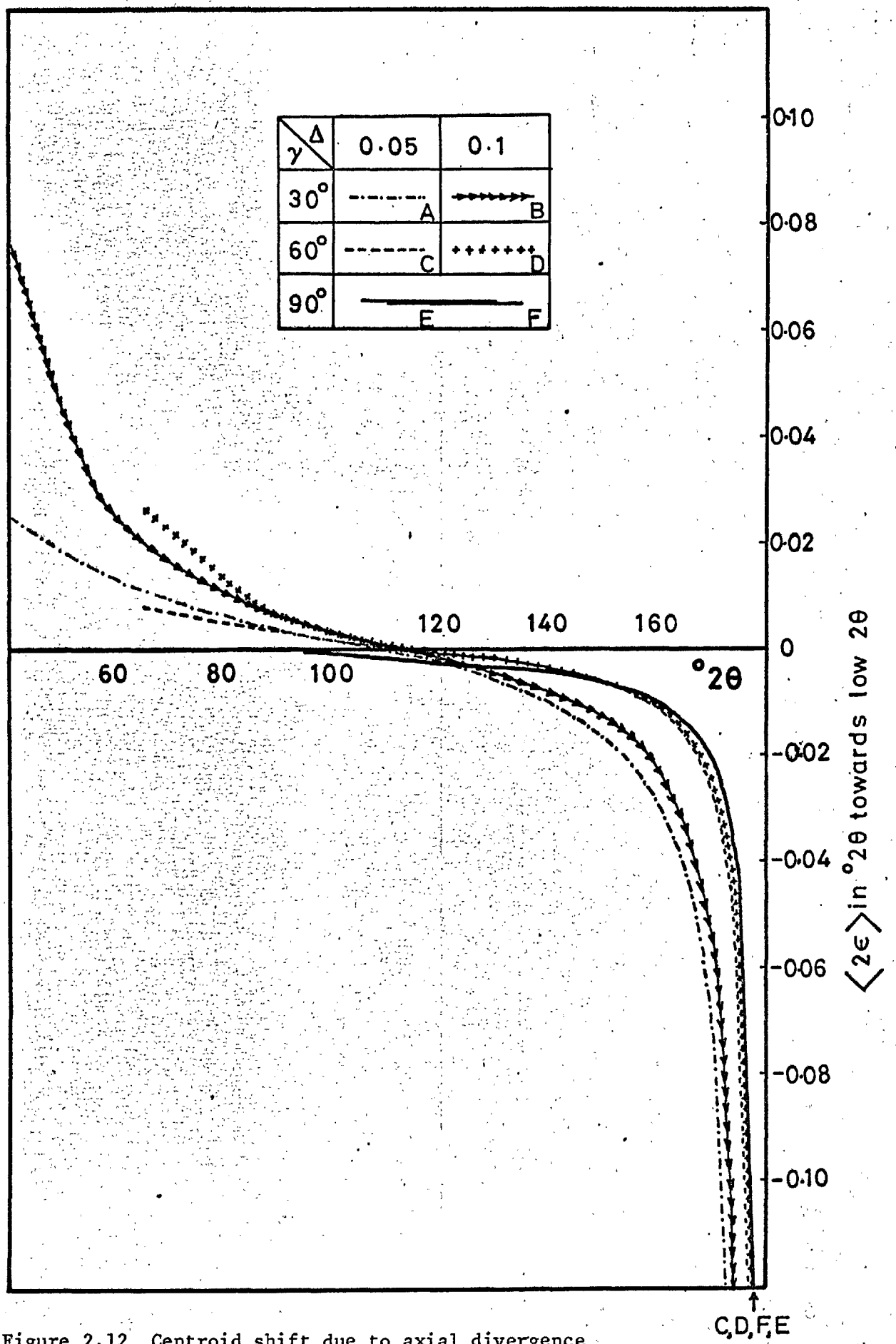

Figure 2.12 Centroid shift due to axial divergence - 2 sets of Soller slits,

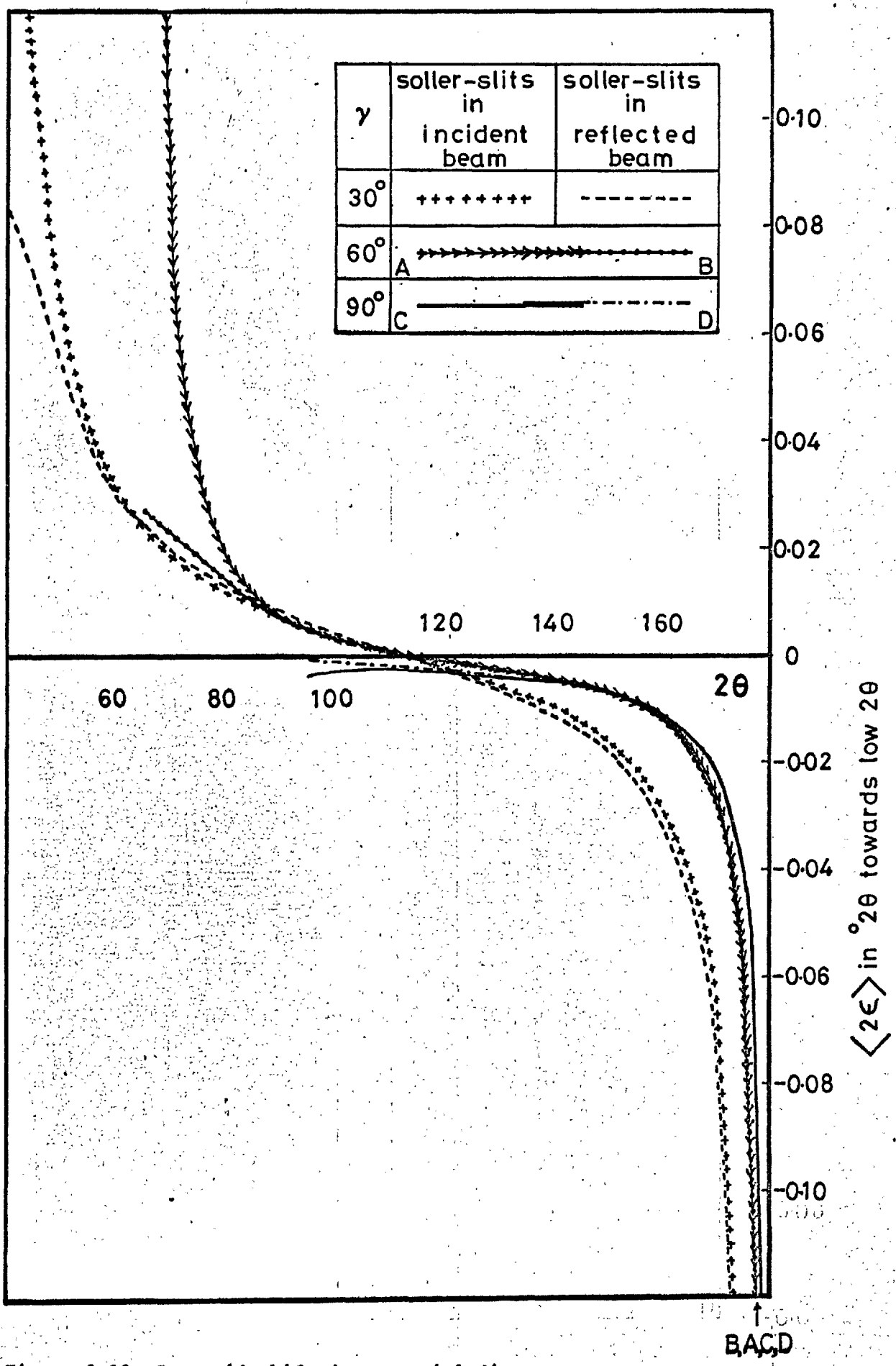

Figure 2.13 Centroid shift due to axial divergence - 1 set of Soller slits. $\Delta = 0.1$

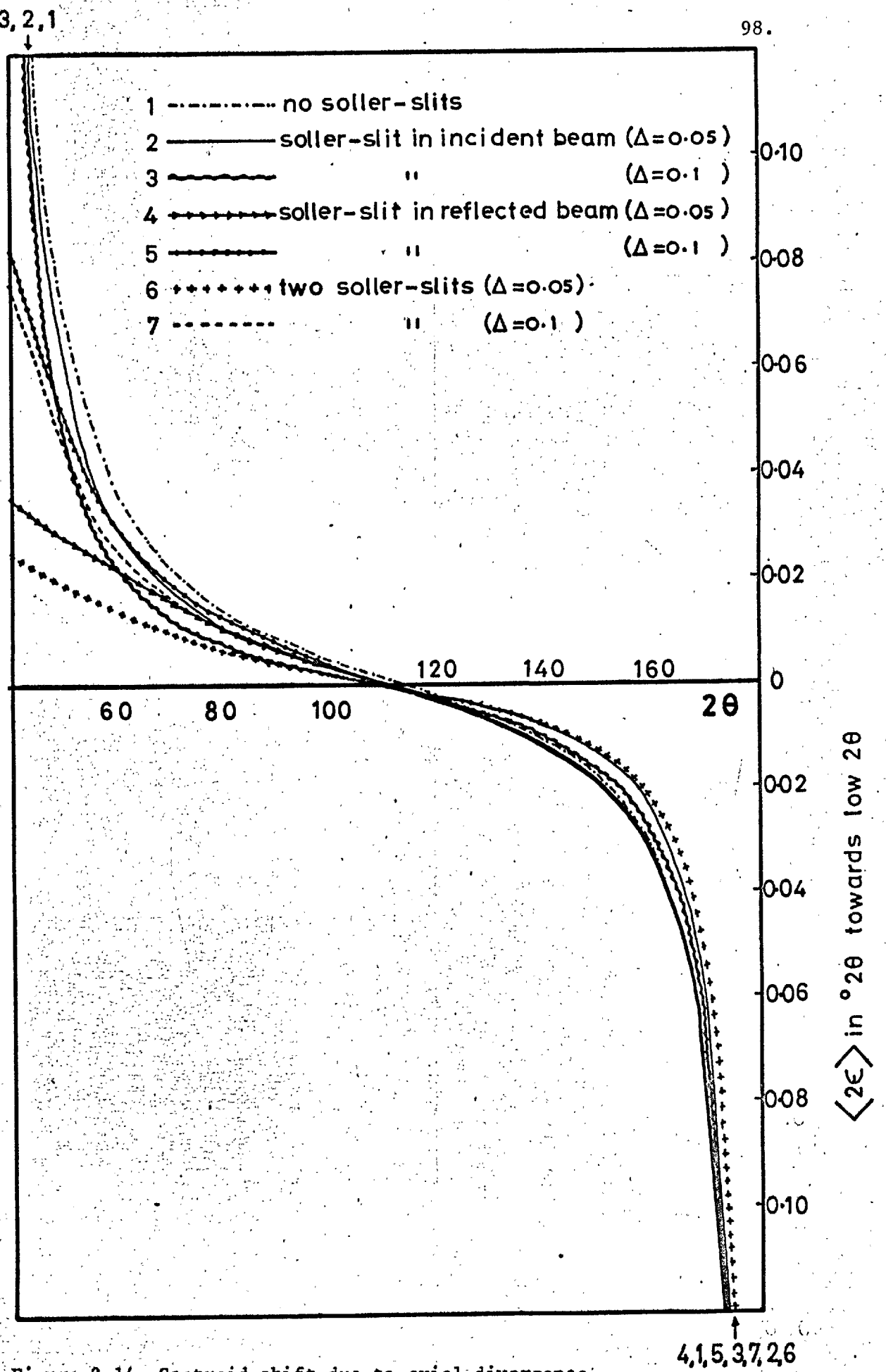

Figure 2.14 Centroid shift due to axial divergence at $\gamma = 30^{\circ}$.

Geometrical Errors Associated with Focus and Receiving Slit

In order to evaluate these errors three coordinate systems, in the equatorial plane, are defined with origins F, Q and R, as shown in Fig. (2.15). The transparency error is ignored so that a point P in the specimen has coordinates (o,y) and a ray is traced from the point $A(x_1,y_1)$ through P to $B(x_2,y_2)$. It is readily shown that

$$\underline{PA} = -(x_1s_1 + y_1c_1 + s_1^2)\underline{i} + (x_1c_1 - y_1s_1 + s_1c_1 - y)\underline{j}$$

$$\underline{PB} = (-x_2s_2 + y_2c_2 - s_2^2)\underline{i} - (x_2c_2 + y_2s_2 + s_2c_2 + y)\underline{j}$$

where $\underline{i}$, $\underline{j}$ are unit vectors of the system (x,y). It follows directly that

$$\frac{\underline{PA} \cdot \underline{PB}}{|\underline{PA}|\ |\underline{PB}|} = \frac{1}{S}\left[A + Dy_1 + Ey_2 + Fx_1y + Gx_2y\right] \qquad \ldots (2.51)$$

where $A = s(s - c) = -s \cos 2\theta$

$D = s_2(s_2c_1+s_1c_2) = s_2 \sin 2\theta$

$E = -s_1(s_2c_1+s_1c_2) = -s_1 \sin 2\theta$

$F = -(c_2 \cos 2\theta + c_1)$

$G = c_1 \cos 2\theta + c_2$

The terms in x alone cancel as would be expected and the term in y^2 has been neglected as it is just the flat specimen error. The last two terms vanish under integration, when computing the centroid of any of the following aberrations. They are important, however, for determining broadening. By argument similar to before

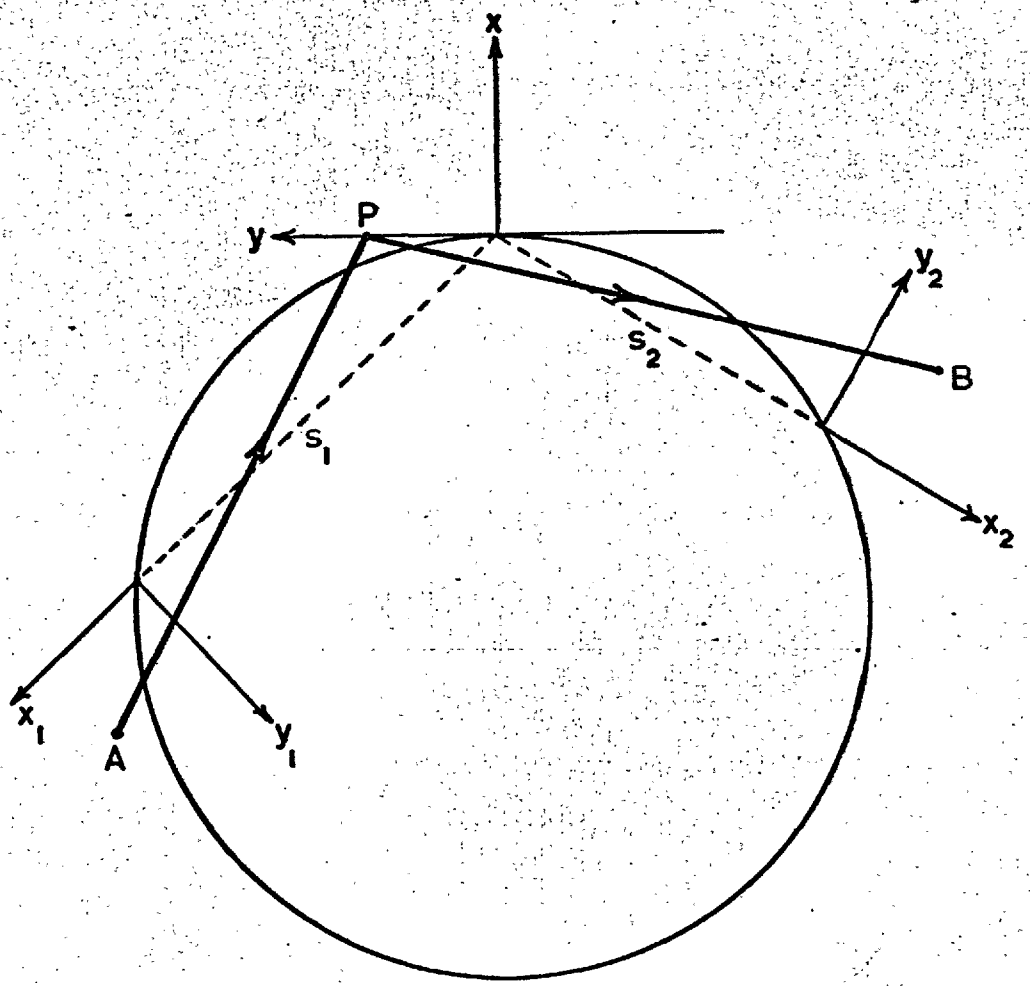

Figure 2.15 SB geometry with coordinate systems at the focus and at the receiving slit.

$$\delta = (\varepsilon - \frac{1}{2s_1} y_1 + \frac{1}{2s_2} y_2 + F'x_1y + G'x_2y) \qquad \ldots (2.52)$$

where $F' = \frac{- F}{2s \sin 2\theta}$

and $G' = \frac{- G}{2s \sin 2\theta}$

Finite breadth of focal line and receiving slit

Assuming the coordinates (x_1,y_1) have their origin in the centre of the spot, and that the intensity distribution across the spot is uniform (which is an assumption which has been made throughout these error calculations), then the centroid shift due to the finite width of the focus is clearly zero.

If w_f is the projected width of the focus the resultant broadening is

$$W_f = \frac{w_f^2}{48R^2 \sin^2\gamma} \qquad \ldots (2.53)$$

By similar argument it may readily be demonstrated that the broadening due to the finite width of the receiving slit, w_{rs}, is

$$W_{rs} = \frac{w_{rs}^2}{48R^2 \sin^2(2\theta - \gamma)} \qquad \ldots (2.54)$$

Broadening due to a finite extension of the focus d in the x_1 direction is given by

$$W_d = \frac{F'^2 \alpha^2 d^2}{9} \qquad \ldots (2.55)$$

A similar term will arise due to a finite depth of focusing at the receiving slit when the resultant broadening is

$$W_{df} = \frac{G'^2 w_{rs}^2}{9} \qquad \ldots (2.56)$$

Mis-setting of focus and receiving slit

There are four cases of focus mis-setting as illustrated in Fig. (2.16). For each case there is a corresponding case for the mis-setting of the receiving slit and analogous expressions may be derived. For each of the following expressions the analogy is drawn by changing the sign (of any centroid shift) and interchanging γ and $(2\theta - \gamma)$.

a. ΔX

The focus is colinear with the axis of rotation of the tube but shifted, tangential to the focusing circle, away from the zero of the 2θ scale. If this shift is ΔX then the focus has coordinates ($x_1 = \Delta X \cos\gamma$, $y_1 = \Delta X \sin\gamma$). As there is no term, in x alone, in 2.52 this variable only appears at a higher order than the term in y_1. It seems justifiable, therefore, to neglect it and then

$$\langle\varepsilon\rangle_{\Delta X} = \frac{\Delta X}{4R} \qquad \ldots (2.57)$$

There is no broadening and so 2.57 is, identically, the peak shift. The error is rather trivial being merely an incorrect definition of the zero point of the 2θ scale.

b. ΔR_X

The focus is colinear with the axis of rotation but shifted ΔR_X away from the focusing circle. For low γ this is little different from the ΔX case in that the 2nd order x_1 terms are negligible in

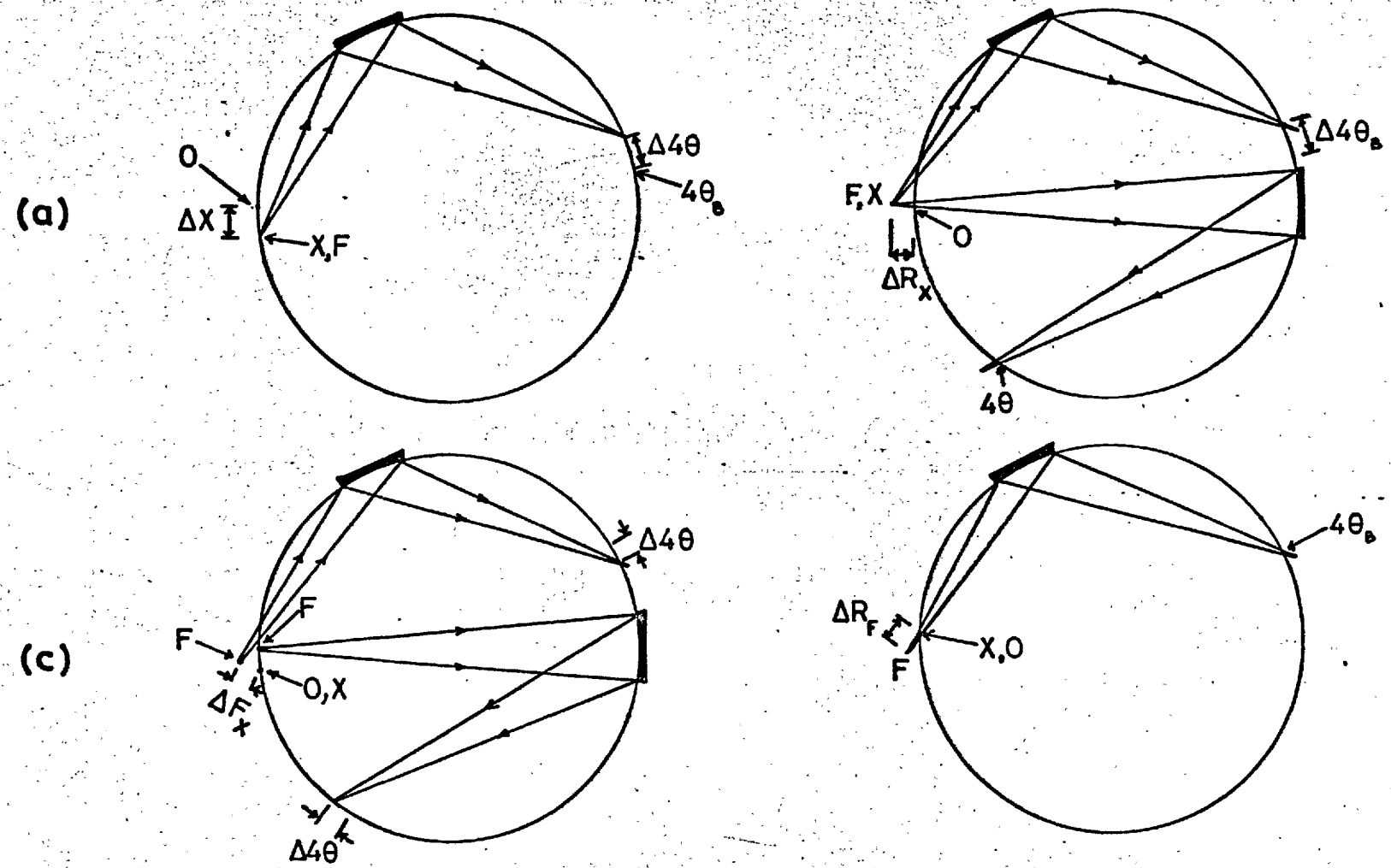

Figure 2.16 Four cases of mis-setting of focus.

comparison with the y_1 term. For higher γ the term predominating would be the $x_1 y$ term. As it is a term in y there can be no centroid shift but there will be a broadening

$$W_{\Delta R_X} \doteq \frac{F'^2 \alpha^2 \Delta R_X^2}{3} \qquad \ldots (2.58)$$

c. $\underline{\Delta F_X}$

The axis of the tube runs through the $0^\circ 2\theta$ position but the focus is shifted ΔF_X longitudinally with respect to the tube. There is clearly just a bodily shift of the profile

$$\langle \varepsilon \rangle_{\Delta F_X} = \frac{\Delta F_X}{4R \sin\gamma} \qquad \ldots (2.59)$$

with no broadening except at low γ.

d. $\underline{\Delta R_F}$

The axis of rotation of the tube is correct but the focus is shifted transversely with respect to the length of the tube. There will be no centroid shift but a broadening

$$W_{\Delta R_F} = \frac{F'^2 \alpha^2 \Delta R_F^2}{3} \qquad \ldots (2.60)$$

Errors inherent in the Instrument

If the main gear is inaccurately machined, this can be observed using a calibrated optical polygon with an autocollimator (Evans and Taylerson, 1961). This compares points say 30° apart (with a 12 sided polygon) with perhaps several cycles starting with an orientation a few degrees advanced each time. Alternatively the autocollimator may be

used with sets of calibrated wedges. It is even possible to do this with a wedge of unknown angle. If necessary, the complete gear can be calibrated by processes of this sort and a correction curve drawn up for all angle readings.

Any error from backlash in the gears is minimised by running the gears up to the starting point in the direction in which the motor is to run for scanning the profile.

If the counter fails to stay pointed at the specimen the effective width of the receiving slit is diminished which reduces the intensity and the breadth of the profile with no shift of the centroid. This was confirmed experimentally for rotational mis-settings, of the counter tube, up to 10° (the slit cannot 'see' the specimen with a greater rotation). The fact that no centroid shift was observed in this experiment also confirmed that no detectable eccentricity of the receiving slit occurs during rotation of the counter tube. No instrumental adjustment is provided for such a mis-setting since accurate setting should be well within the machining capabilities of a good workshop.

A serious source of error (and where the operator is completely dependent on machine-shop accuracy) is in the setting and curvature of the dovetail track. In practice any eccentricity will become apparent with a failure to align the instrument after several attempts. No error was detected on the present instrument for specimen positions between $20^{\circ}\gamma$ and $75^{\circ}\gamma$ and all experiments carried out in the present project employed specimen positions in this range. It has since been demonstrated, however, (Gunnell, 1970) that the specimen track, above $75^{\circ}\gamma$, is somewhat distorted. A distortion of this kind can only be eliminated by re-machining the track, although a correction chart, for the distorted region, may be drawn. If the curvature of the track is correct but not set concentric with the goniometer axis, the only cure is to have the track re-set in a machine shop.

If the diffractometer support slides are not parallel to the

0 - 180° (BB) line there is no error because the 0° point of the angular scale is adjustable and in the alignment sequence for the instrument this adjustment is made after any bodily shift of the diffractometer.

IV Remaining Errors

If the diffractometer plane is tilted with respect to the X-ray tube then for a small tilt (of say 1 or 2°) any additional axial terms are negligibly small and the only effect would be equivalent to a combination of extensions of the focus in the x_1 and y_1 direction resulting only in a slight broadening.

Parrish and Mack (1967) have pointed out the possibility of errors due to poor specimen condition at the surface. This would become apparent as either γ or $(2\theta - \gamma)$ became small when the surface roughness could be 'seen' by the focus or the receiving slit.

Discussion of errors

Inspection of equations (2.22, 2.25, 2.28, 2.31, 2.33) reveals that all the principal specimen errors have a functional form given by one or other of the expressions

$$\frac{\sin 2\theta}{\sin\gamma \sin(2\theta - \gamma)} \qquad \frac{\sin 2\theta}{\sin\gamma + \sin(2\theta - \gamma)} \qquad \ldots (2.61)$$

Both these expressions go to zero as $2\theta \to \pi$ and, furthermore, the variance of the aberrations are proportional to the squares of these functions and thus will also go to zero. In addition the error in the lattice parameter will go more rapidly to zero as $2\theta \to \pi$ because of the relationship

$$\frac{\Delta a}{a} = - \cot\theta \, \Delta\theta \qquad \ldots (2.62)$$

Using 2.62 and 2.61 the systematic error in the lattice parameter is given by functions of the form

$$\text{A.} \quad \frac{1 + \cos 2\theta}{\sin\gamma \sin(2\theta - \gamma)} \qquad \ldots (2.63)$$

$$\text{B.} \quad \frac{1 + \cos 2\theta}{\sin\gamma + \sin(2\theta - \gamma)}$$

which suggest themselves as suitable extrapolation functions. For a well-aligned instrument the systematic error function will be a mixture of the two functions. If one is chosen as the extrapolation function the presence of the other is not likely to impress a large deviation from a straight line. The choice of function must depend on the particular experiment. Both functions have been tabulated by computer for a number of specimen positions and are given in Appendix 3.

As a test of the extrapolation method samples of I.U.Cr. silicon and tungsten were measured and plotted against each of the two functions as shown in Fig. (2.17). For both cases the low transparency error is seen to be dominant by the better fit of the data to 2.63B than 2.63A.

2.4 THE ALIGNMENT PROCEDURE

Parrish and Mack (1967) record, as a major criticism of the SB method, the impossibility of locating the zero-point. The present diffractometer is essentially of convertible geometry, so that the $0^{\circ}2\theta_{BB}$ point can be found by standard procedure and this can be identified with the $90^{\circ}2\theta$ point on the SB scale. The full alignment procedure which follows is basically an iterative procedure which will converge

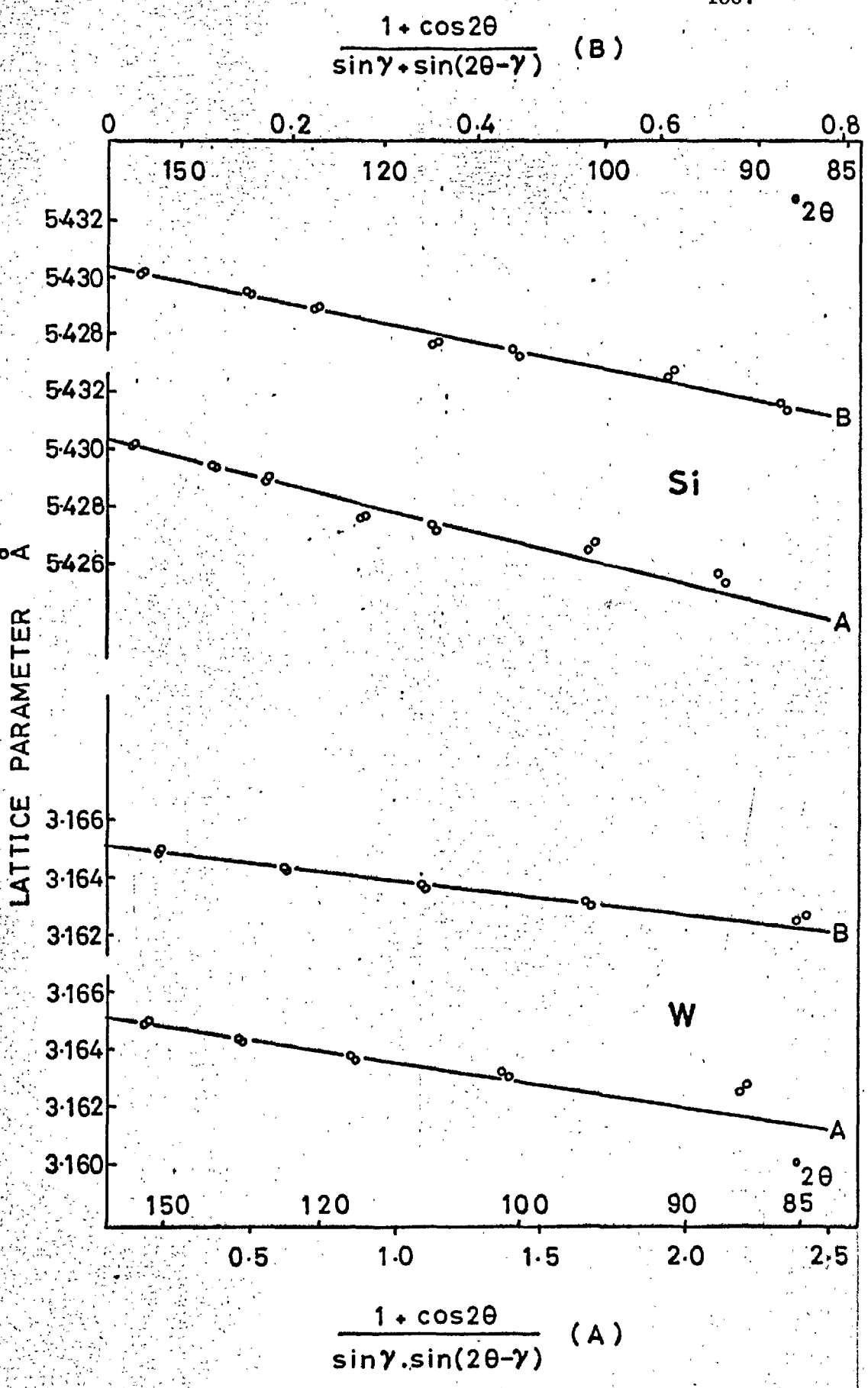

Figure 2.17 Extrapolation plots against the error functions for A. thin high transparency B. low transparency specimens.

provided that there are no significant errors arising from the manufacture of the instrument, (see section 2.3 III).

There are two references which are not altered throughout the alignment. One is the axis of the X-ray tube rotation and the other is the radius of the focusing circle. The latter is fixed by sliding the counter along its bracket until the receiving slit is 175 mm (or any other preferred value) from the axis of the diffractometer, and locking it in place with a dowel pin. The various adjustments on the instrument must now be made such that the focusing circle so defined shall pass through the focus of the X-ray tube (which itself must be colinear with the axis of X-ray tube rotation) and through the concave surface of the specimen.

For convenience the alignment may be divided up into a set of distinct operations:

1. The diffractometer axis is brought to ~175 mm from the axis of rotation of the X-ray tube using the scale provided on the slide (Fig. 2.2).

2. In order to establish the $0^{o}2\theta_{BB}$ position, to a first approximation, two needles are established in colinearity with the axes of rotation of the X-ray tube and the goniometer by a simple optical alingment process. Removing the counter tube and viewing through the receiving slit, the two needles are brought into line with the slit by rotation of the counter bracket.

3. In order to set the take-off angle, the divergence slit holder must be centralised in the window of the X-ray tube which is set for a take-off angle $\psi = 5^{o}$. With the tube pointing towards the centre of the goniometer the main beam is scanned (with a suitably protected counter) first with no slits at all and then with a 4^{o} (2α) slit. The slit-holder is translated across the window until the second image is central within the first. All the divergence slits should be checked in case they are not all properly centred.

4. To bring the focus into colinearity with the axis of X-ray tube rotation, to a first approximation, the direct beam is scanned while a needle (as supplied by Siemens) is set in the central cone of the diffractometer. The X-ray tube is translated, by means of the longitudinal adjustment screw (ΔF), until the shadow of the needle is symmetrical about the $0^{o}2\theta_{BB}$ position.

5. The surface of a sample of G.E. permaquartz was ground to a concave cylindrical section of 175 mm radius. Using this specimen, in the SB configuration, the 132 quartz profile ($\sim 90^{o}2\theta$) is scanned for the specimen in positions $\gamma = 20^{o}$ and 70^{o}. These two positions are selected because all the systematic specimen errors have a kind of exchange symmetry i.e.

$$\langle\varepsilon\rangle \quad (\gamma,\ 2\theta - \gamma) \quad = \quad \langle\varepsilon\rangle \quad (2\theta - \gamma, \gamma) \qquad \ldots (2.64)$$

For a given 2θ there is an infinite choice of pairs of γ that give rise to the same specimen errors. All other errors are assumed to be non-existent or second order, except for the positioning of the focus. The error due to a longitudinal displacement of the focus, ΔF_X, (eqn. 2.59) decreases with increasing γ and the sensitivity to this error is thus increased by choosing γ values far apart. From the form of the error function (2.59) the angular displacement of the profile for $\gamma = 70^{o}$ is known to be less than that for $\gamma = 20^{o}$ and hence the direction of the corrective adjustment to the X-ray tube may be deduced. This adjustment is applied until the profiles for both γ settings are superimposed when recorded on the same piece of chart paper.

On the second iteration through this alignment stage the peak intensity is maximised by making the transverse adjustment of the X-ray tube, ΔR_F. This translation was found to be rather coarse so that several adjustments were necessary before achieving maximum intensity.

6. The specimen surface is aligned with the focusing circle (except for a rotation error) by making the micrometer adjustment ΔR_s until the quartz 132 profiles for $\gamma = 20^o$ and 45^o superimpose. The direction of adjustment can be deduced from the relative positions of the two profiles, the profile for $\gamma = 45^o$ being the nearest (for $2\theta = 90^o$) to the correct position at any one time.

7. The rotational adjustment of the specimen is checked by irradiating the two extremes of the specimen in turn using a narrow ($0.25^o 2\alpha$) divergence slit and recording the scans on the same chart paper. Failure to superimpose the profiles implies a rotation of the specimen surface with respect to the focusing circle and the necessary adjustment is made accordingly.

8. The focusing of the instrument is achieved by moving the goniometer bodily on its support slides until the intensity of the 132 quartz reflection is maximised, for $\gamma = 20^o$. Since no mechanism is provided, this operation must be performed by loosening two locking bolts and gently tapping the goniometer.

9. As all the adjustments described above refer to profile displacement errors which are not wholly separable, steps (5) to (8) must be repeated once or twice until consistency is achieved. At this stage, provided the specimen track is properly set, the goniometer is aligned to $\pm 0.005^o 2\theta$ which is about the limit of measurement for normal scans using a chart recorder. It was found to be possible to superimpose peaks to this accuracy for all specimen positions, every 5^o from $20^o\gamma$ to $75^o\gamma$. To this order of accuracy the residual error due to permaquartz is virtually negligible and in any case is amenable to elimination by extrapolation procedures. If a higher precision SB instrument were ever built or if a shorter wavelength radiation were used the residual absorption error could be reduced by aligning with a fine grained high absorption material such as tantalum.

If the alignment is successfully completed to this stage the specimen track is a true annulus over the range of γ used.*

10. The final test of the alignment is to select any sharp high angle of reflection and to scan the profile for all the γ used in (9). If the profiles fail to match up then the specimen track is mis-set.

11. If the diffractometer is aligned it may be calibrated by changing it into its BB mode without disturbance of the SB specimen. The centre sprocket is replaced by a specimen holder with a flat reference surface and a Siemens' glass slit (which is etched symmetrically about the reference surface) is mounted. A narrow divergence slit is used and the glass slit rotated using one of the micrometer adjustments until the beam passes through the slit and is received with maximum intensity. The θ:2θ relationship is also established for scanning on the other side of the $0^{o}2\theta_{BB}$ position by a similar process. The glass slit is then replaced by a Siemens gold standard sample, the 111 peak of which is scanned, towards higher values of 2θ, on both sides of the beam. The angular scales on the drum and the cyclometer are adjusted so that the peaks match up. The zero of the BB scale is thus calibrated and hence the $90^{o}2\theta$ point on the SB scale is calibrated also.

12. The diffractometer is returned to the SB mode and the state of alignment checked to make sure the focus has not moved during the change-over of geometries.

13. The direct beam is scanned as in (3) and the angle of X-ray tube rotation, for which the beam is symmetrical about the $90^{o}2\theta_{SB}$ position, is noted. This angle, which should be the take-off

---

* I am grateful to Mr. B.J. Gunnell for pointing out that this does not mean that the specimen track is concentric with the goniometer rotation. See also section 2.3 III.

angle $\psi = 5^{o}$, was found to be nearer $4\frac{1}{2}^{o}$. The angular scale of the tube rotation is thus effectively calibrated. In theory the new take-off angle should be used in stage (10) again, in case of a slight $\theta 2\theta$ mis-setting but this did not appear to be necessary.

2.5 SELECTION OF INSTRUMENTAL SETTINGS

The resolution of a line is governed ultimately by the effective width of the source. It is general practice to match the angular aperture of the source, seen by the specimen, with that of the receiving slit. For the SB method the selection of a receiving slit width is dependent both on 2θ and γ. Table (2.6) gives the angular aperture of the source, $E_{SB}(^{o}2\theta)$, for standard 2KW, 1KW and fine-focus tubes, for different specimen positions. Also Table (2.7) gives the angular apertures, $\varepsilon_{SB}(^{o}2\theta)$, of a standard 0.1 mm receiving slit as a function of γ and 2θ. For comparison the equivalent values of $E_{BB}(^{o}2\theta)$ are also given in Table (2.6) for the BB system, and lines are drawn in Table (2.7) to indicate the equivalent value of $E_{BB}(^{o}2\theta)$. The angular apertures of other standard slits can be found by multiplying by a suitable value (e.g. for 0.2 mm multiply by 2).

The proper receiving slit width is picked by examination of Table (2.7) to match the source aperture in Table (2.6). This is also necessary for the picking of the electronic time constant. This is usually set (see, for example, Vassamillet and King, 1967) at one-half the time width of traverse of the receiving slit. The time constant is then

$$TC = \frac{\varepsilon_{SB}(^{o}2\theta).30}{\omega} \quad \text{secs}$$

where ω is the scanning speed in $^{o}2\theta$/min.

TABLE 2·6

Angular Aperture of X-ray source $E_{S-B}(^{o}2\theta)$, as a function of Source Width W_o, Take-off angle ψ, and specimen Setting γ, for R = 175 mm

W_o (mm)	ψ	$E_{S-B}(^{o}2\theta)$ at various values of γ						E_{B-B} ($^{o}2\theta$)
		15°	30°	45°	60°	75°	90°	
2.0	3°	0.066	0.034	0.024	0.020	0.018	0.017	0.034
	6°	0.132	0.068	0.048	0.040	0.036	0.034	0.068
1.0	3°	0.033	0.017	0.012	0.010	0.009	0.009	0.017
	6°	0.066	0.034	0.024	0.020	0.018	0.017	0.034
0.4	3°	0.013	0.007	0.005	0.004	0.004	0.003	0.007
	6°	0.026	0.014	0.010	0.008	0.007	0.007	0.014

TABLE 2·7

Angular Aperture of 0.1 mm Receiving Slit $\varepsilon_{S-B}(0.1\text{ mm}, ^{o}2\theta)$ as a Function of Bragg Angle $2\theta_B$ and specimen setting γ, for R = 175 mm.

$2\theta_B$	S-B (0.1 mm $^{o}2\theta$) for various values of γ					
	15°	30°	45°	60°	75°	90°
20°	0.188					
30°	0.063					
40°	0.039	0.094				
50°	0.029	0.048	0.188			
60°	0.023	0.033	0.063			
70°	0.020	0.025	0.039	0.094		
80°	0.018	0.021	0.029	0.048	0.188	
90°	0.017	0.019	0.023	0.033	0.063	
100°	0.016	0.017	0.020	0.025	0.039	0.094
110°	0.016	0.017	0.018	0.021	0.029	0.048
120°	0.017	0.016	0.017	0.019	0.023	0.033
130°	0.018	0.017	0.016	0.017	0.020	0.025
140°	0.020	0.017	0.016	0.017	0.018	0.021
150°	0.023	0.019	0.017	0.016	0.017	0.019
160°	0.029	0.021	0.018	0.017	0.016	0.017
170°	0.039	0.025	0.020	0.017	0.016	0.017

Notes: 1. The horizontal lines indicate the position of the equivalent value of $\varepsilon_{B-B}(0.1\text{mm}, ^{o}2\theta) = 0.033^{o}$.

2. To obtain $\varepsilon_{S-B}(^{o}2\theta)$ for other slit sizes multiply by 10 x W_{RS}(mm).

the proper time constant is given by

$$\text{Time constant (S-B)} = \varepsilon_{S-B}(^{o}2\theta).\ 30/\omega(^{o}2\theta/\text{min}) \qquad (14)$$

Thus for $\omega = \frac{1^{o}}{8}2\theta$/min, the proper time constant for all the receiving slits in the example quoted above is 4.8 sec.

2.6 SELECTION OF OPTIMUM GEOMETRY AND SPECIMEN SETTING

The availability of an interchangeable Bragg-Brentano/Seeman-Bohlin diffractometer poses the practical problem of selecting the appropriate geometry and specimen setting to obtain maximum resolution and intensity, with minimum angular displacement, when recording a specified diffraction profile.

It is evident from the data listed in Table (2.6) that the basic angular resolution of the SB diffractometer falls below that of the BB instrument at specimen settings below $\gamma = 30^{o}$. Since the minimum measurable Bragg angle ($^{o}2\theta$) at any specimen position is equal to $(\gamma + 10^{o})$ (Figure 2.4), it follows that all measurements of $2\theta_B$ less than 40^{o} are subject to a loss of resolution, due to the increased angular aperture of the X-ray source. Thus at low Bragg angles the "doubled" $2\theta_B$ scale associated with the SB geometry is really empty magnification, since the profiles are broader than those recorded with the BB diffractometer. Further, as demonstrated by Parrish and Mack (1967) at low Bragg angles the SB geometry is more susceptible than the BB method to systematic errors due to wrong curvature, absorption and specimen displacement. At $\gamma = 15^{o}$ the systematic errors are greater than the equivalent BB errors over the entire range of $2\theta_B$. The cross-over point between the two methods occurs at $\gamma = 30^{o}; 2\theta_B = 60^{o}$.

The relatively short source-specimen and specimen-receiving slit distances, required by the SB method at low $2\theta_B$ values, also cause intensity losses due to micro-absorption arising from surface irregularities and particle size roughness (Parrish and Mack, 1967). Thus on all three accounts, of resolution, angular error and diffracted intensity, the Bragg-Brentano diffractometer is definitely to be preferred for precision work at $2\theta_B$ values below 60^{o}. This conclusion is much the same as that reached by Parrish and Mack, on the basis of their experience with a SB diffractometer with γ fixed at 15^{o}. It does not, of course, rule out the use of the SB diffractometer for

qualitative studies at low angles, e.g. when indexing a known pattern prior to making precision measurements in the back-reflection region.

To compare the relative advantages of the two geometries at intermediate γ values, i.e. between 30° and 45°, the overlapping 122, 203 and 301 profiles of permaquartz, which occur near $68^{\circ}, 2\theta$, were studied using a flat specimen in the BB position and a specimen ground to a radius of 175 mm set at $\gamma = \frac{1}{2}(2\theta_B) = 34^{\circ}$. This particular setting approximates to the special condition, $\gamma = 30^{\circ}, 2\theta_B = 60^{\circ}$, at which both the source-specimen and specimen-receiving slit distances are equal to the diffractometer radius R, so that the angular aperture of the source and the receiving slit are the same for both geometries (Tables 2.6 and 2.7). The length of specimen irradiated, and hence the diffracted intensities, should also be approximately the same for the two methods. When using a divergent aperture of $2\alpha = 2^{\circ}$, the fine structure of the three overlapping profiles is clearly revealed by both geometries as shown in Figure (2.18a). On increase 2α to 4° the diffracted intensity is doubled in both cases, but while the profiles recorded with SB geometry remain equally well resolved, the BB profiles show considerable broadening and loss of resolution. The SB geometry is thus undoubtedly superior to the BB even in the intermediate region just beyond the theoretical cross-over point. The advantage of being able to increase the area of specimen irradiated without loss of resolution, is of particular importance when it is required to make precision back reflection measurements on coarse grained powders.

Although the present SB method has the advantages of high resolution and intensity, it is not convenient for quantitative measurements of relative intensities of widely spaced diffraction profiles because of the corrections required as a result of the variable angular aperture of the receiving slit. This limitation is best overcome by using the variant of the geometry suggested by Pike (1962) in which the counter-tube is directed towards the axis of the diffractometer instead of at the specimen. This geometry results in a constant angular aperture for the receiving slit (Parrish and Mack, 1967) but is not easy to achieve because it involves the efficient detection of oblique irradiation.

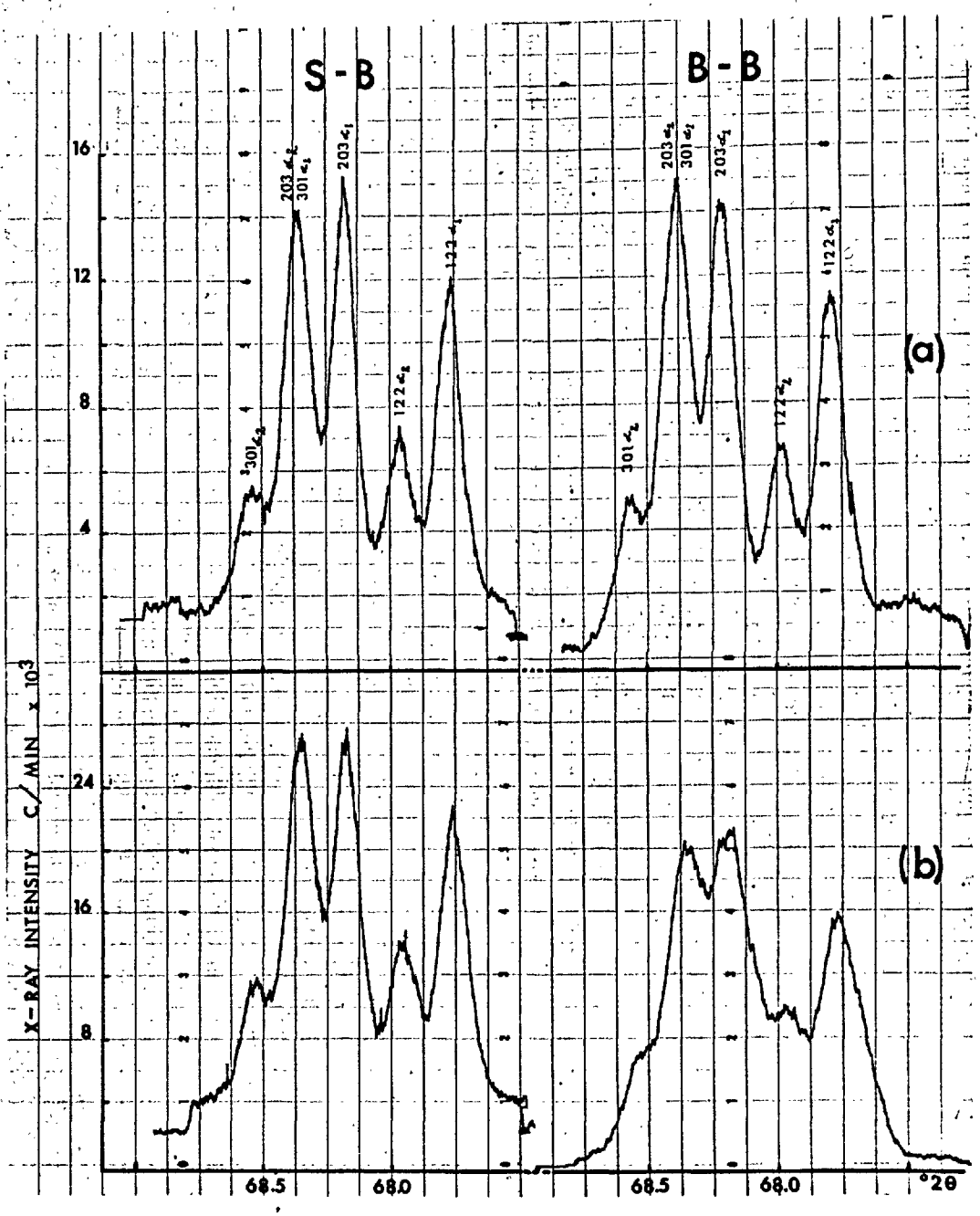

Figure 2.18 Overlapping 122, 203 and 301 profiles from Permaquartz, recorded with SB and BB geometries.

a. $2\alpha = 2^{o}$, b. $2\alpha = 4^{o}$.

The selection of the optimum γ setting for precision measurements using SB geometry depends on a number of slightly contradictory factors. From the aspect of the angular resolution of the X-ray source, and of the systematic errors contributing to a shift in angular position, γ should be set at 90^{o}. This position is also convenient because it demands no rotation of the X-ray source from the BB position, as pointed out by Pike (1962) and Baun and Renton (1964), and it is certainly to be recommended for precision measurements of individual profiles in the far back reflection region. When determining precision lattice parameters, however, it is usually necessary to use Bragg angles down to $90^{o}2\theta$, in order to obtain sufficient points to make an accurate extrapolation plot. At $\gamma = 90^{o}$ this is prevented by the lower limit of $(\gamma + 30^{o})$ set for $2\theta_{B}$, below which the angular aperture of the receiving slit falls below the equivalent BB resolution (Table 2.7). The use of $\gamma = 90^{o}$ also means that the finest resolution of the receiving slit lies in the inaccessible region of $2\theta_{B}$ above 172^{o} (Table 2.7).

A careful examination of the data listed in Tables (2.6) and (2.7) indicates that the optimum specimen setting for precision lattice parameter determination lies between $\gamma = 45^{o}$ and 60^{o}. At $\gamma = 60^{o}$, the angular aperture of the X-ray source is less than two thirds that of the BB method, and this degree of resolution can be maintained over the important range of Bragg angles from $115^{o} - 172^{o}$ 2θ, without requiring a change in receiving slit. Maximum resolution is achieved from $100^{o} - 170^{o}$ 2θ, at $\gamma = 45^{o}$, but this is partly off-set by the cut-off of 2θ max at 170^{o}, (Figure 2.4) and by the slightly larger source aperture ($0.7\ E_{BB}$) at this setting.

REFERENCES

Baun, W.L. and Renton, J.J., (1963), J.Sci.Inst. 40, 498.

Das Gupta, K., Schnopper, H.W., Metzer, A.E. and Shields, A.R., (1964), Adv. X-ray Anal. 7, 302.

Ekstein, H. and Siegel, (1949), Acta Cryst. 2, 99.

Evans, J.C. and Taylerson, C.O., (1961), "Measurement of Angle in Engineering", N.P.L. Notes on Appl. Sci. 26, H.M. Stationery Office.

Gunnell, B.J., (1970), Private communication.

James, R.W., (1948), "The Crystalline State", Vol. 2, Bell, London.

King, H.W. and Preece, C.M., (1967), Adv. X-ray Anal. 10, 354.

King, H.W. and Russell, C.M., (1965), Adv. X-ray Anal. 8, 1.

Kunze von G., (1964), Z. ang. Phys. 17, 412; 522;
18, 28.

Ladell, J., (1961), Acta Cryst. 14, 47.

Parrish, W. and Mack, M., (1967), Acta Cryst. 23, 687, 693.

Pike, E.R., (1957), J. Sci. Inst. 34, 355.

Pike, E.R., (1959), Acta Cryst. 12, 87.

Pike, E.R., (1962), J. Sci. Instr. 39, 222.

Pike, E.R. and Ladell, J., (1961), Acta Cryst. 14, 53.

Russell, C.M., (1966), Thesis, Imperial College.

Segmuller, A., (1957), Z. Metall. 48, 448.

Straumanis, M.E. and Ievens, A., (1959), 'The Precision Determination of Lattice Constants by the Assymmetric Method'. Springer Berlin (1940), Tr K.E. Beu, USAEC Rept. GAT-T-643, Goodyear Atomic Corp.

Vassamillet, L.F. and King, H.W., (1963), Adv. X-ray Anal. 6, 142.

Wassermann, G. and Wiewiorowsky, (1953), Z. Metall. 44, 567.

Wilson, A.J.C., (1963), The Mathematical Theory of X-ray Powder Diffractometry. Philips Technical Library, Eindhoven.

CHAPTER 3

CHAPTER 3

APPARATUS AND EXPERIMENTAL PROCEDURES

3.1 THE PREPARATION OF SPECIMENS

Preparation of Alloys

The metals used for preparing the alloys were supplied by the Johnson-Matthey Company to spectrographic standards as follows (in the usual notation): indium (5N5), cadmium (5N), lead (6N), bismuth (5N), tin (5N), mercury (6N), lithium (3N), silver (5N) and zinc (5N5).

In the production of the indium alloys the desired quantities of metals to give a 20 g ingot were weighed out to $\pm$ 0.0001 g in cleaned, dried Pyrex test-tubes which were then necked down. For convenience a multiple seal-off unit was made to enable four specimen tubes to be evacuated simultaneously. After the initial evacuation the tubes were flushed four times with argon, finally evacuated and sealed off. The metals were melted by heating the capsules in a bunsen flame, the resulting molten alloy shaken vigorously for five minutes to ensure complete mixing, before quenching into iced water. The cast alloys were homogenised, in their original capsules, in an oil bath operational between room temperature and 165^{o}C (Russell, 1966), or in a platinum-wound vertical tube furnace.

Since the alloys were not chemically analysed, their compositions were calculated from the initial weighings. As the ingots were bright and clean and as there was no evidence of gettering of the glass, it was assumed that no material was lost. This was checked, in a few cases only, by weighing the ingot, when the losses were found to be less than 0.001 g which is equivalent to a maximum

error of about 0.01 at.%. Indium-lithium alloys were slightly discoloured since it was difficult to remove all the protective oil, beneath which it has to be stored, but this was not thought to significantly affect the composition. The compositions and homogenising temperatures of the alloys studied in the project are given in Tables (3.1) to (3.6).

The silver-zinc alloys, being of higher melting points, were sealed under reduced pressure of argon in silica capsules, made by interdiffusion, and later homogenised in a Pt-wound tube furnace. The compositions and homogenising temperatures for these alloys are given in Table (3.7).

Specimens for T_c Measurements

Rod-shaped specimens, 4 mm in diameter, to fit inside the coils of the T_c probe, were obtained by extruding the cast ingots in a simple press constructed for use on a hand-operated hydraulic jack. During this operation the piston was prevented from becoming barrel-shaped (and hence seizing up) by the simple expedient of placing the press on a block of wood, the compression of which compensated for any lack of parallelism in the plates of the jack. Lubrication of the piston with glycol also helped to extend the life of a piston and die.

Specimens for X-ray Measurements

To obtain powder specimens of the mechanically soft indium alloys, which tend to clog any file used, it was found necessary to frequently dip the alloys in liquid nitrogen in order to harden them. With this process it was possible to produce a sufficient quantity of powder, fine enough to go through 250 mesh, in a reasonably short time.

A perspex former was made with reverse curvature to that of the specimen holders (see section 2.2), on to which was placed a thin sheet

TABLE 3.1

THE ALLOYS IN THE SYSTEM In-Pb

Composition at.% Pb	Homogenising Temperature °C
11.003	145
11.504	"
12.002	"
12.501	"
13.000	"
13.061	"
13.501	"
13.994	"
14.500	"
15.000	"
15.322	"
17.251	"
18.905	"
21.209	"
23.009	"
24.821	"
27.043	"
28.924	"
30.870	"
32.997	"

TABLE 3.2

THE ALLOYS IN THE SYSTEM In-Hg

Composition at.% Hg	Homogenising Temperature ^{o}C
0.467	120
0.753	"
1.008	"
1.052	"
1.187	"
1.756	"
1.763	"
1.921	"
2.000	"
3.000	"
3.393	"
3.477	"
4.000	"
5.000	"
6.000	100
6.156	"
6.500	"
7.000	"
7.500	"
8.000	70
9.000	"
11.162	60
12.008	"

TABLE 3.3

THE ALLOYS IN THE SYSTEM In-Cd

Composition at.% Cd	Homogenising Temperature °C
0.943	135
0.976	"
1.517	"
1.527	"
1.682	"
1.814	"
1.907	"
1.934	"
1.991	"
1.998	"
2.115	"
2.196	"
2.281	"
2.399	"
2.482	"
2.983	"
3.927	"
5.007	"
6.073	"
6.480	"
7.009	"

TABLE 3.4

THE ALLOYS IN THE SYSTEM In-Sn

Composition at.% Sn	Homogenising Temperature ^{o}C
0.997	130
2.002	"
2.524	"
3.002	"
4.001	"
6.000	"
8.000	"
10.000	"
11.002	"
12.010	"
12.997	"
13.983	"
15.996	"
17.988	"

TABLE 3.5

THE ALLOYS IN THE SYSTEM In-Bi

Composition at.% Bi	Homogenising Temperature °C
1.000	125
2.001	"
2.996	"
3.996	100
5.006	"
6.002	"
7.002	70
8.002	"
9.001	"
10.004	"

TABLE 3.6

THE ALLOYS IN THE SYSTEM In-Li .

Composition at.% Li	Homogenising Temperature ^{o}C
1.011	135
2.170	"
2.997	"
3.519	"
4.810	"
6.161	"
6.904	"

TABLE 3.7

THE Ag-Zn ALLOYS

Nominal Composition at.% Zn	Homogenising Temperature °C
0	-
19.0	550
26.5	550
29.0	550

Homogenising time = 5 hrs.

Filings strain-relieved under reduced pressure of argon at 450°C for ½ hour.

of Mylar. A drop of acetone helped the specimen holder to stick to this sheet. The sieved powder was packed into the cavity of the specimen frame and two or three drops of dilute acetone-collodion added which was set by warming with an air blower. A thermometer bulb was held on the specimen while it was dried, and the air blower was kept at such a distance that the temperature was close to the homogenising temperature. The Mylar sheet could be peeled off after drying without damaging the specimen.

As room temperature is greater than half the melting point of the alloys (on the absolute scale) it was not considered necessary to strain-relieve the powders after filing. One powder specimen was furnace annealed under the appropriate conditions (Table 3.5), while in its frame and no change in X-ray profile shapes was observed on re-examination.

The silver-zinc alloys were filed at room temperature and the powders annealed, at the homogenising temperature, in silica capsules. The specimens were mounted in a similar way to the indium alloys. In the large (2ℓ = 25 mm) specimen holders, used for room temperature measurements, the powders were still found to hold together perfectly well.

3.2 LOW TEMPERATURE DIFFRACTOMETRY

Preliminary measurements were made on a Siemens' diffractometer using a cryostat designed by King and Preece (1967). Liquid helium was used as a coolant and a temperature of 13°K was obtained using a modified copper block. Even at this temperature, however, poor diffraction profiles were obtained when indium-lead and indium-cadmium alloys were examined in the back-reflection region, as was experienced previously by Russell (1966). These poor profiles were attributed to coarse grain size and as a result the SB diffractometer project was

KEY TO FIGURE 3.1

1. Main can
2. Liquid nitrogen reservoir
3. Liquid helium reservoir
4. Valve for pumping inner specimen space
5. Rack and pinion for raising specimen
6. Valve for pumping outer specimen space
7. Connects helium boil-off to outer specimen space for pre-cooling
8. Helium boil-off line
9. Valve for evacuation of main can
10. Nitrogen radiation shield
11. Helium radiation shield
12. Cone joint for changing specimen base when using the magnet
13. Reference pin
14. Spring plunger for keeping reference surface on reference pin
15. Indium O-ring seals
16. Heater
17. Rotational adjustment
18. Lead-through for helium transfer siphon
19. Lead-through for electrical connections
20. Double O-ring seal
21. Lead-through for helium transfer siphon
22. Needle valve
23. Magnet
24. Specimen
25. Alignment slit for use on BB diffractometer
26. Translational adjustment-superfluous on Wooster-Martin

NOTE: The cryostat base shown on the left of the diagram is the one used in all experiments here. Liquid nitrogen is used instead of liquid helium.

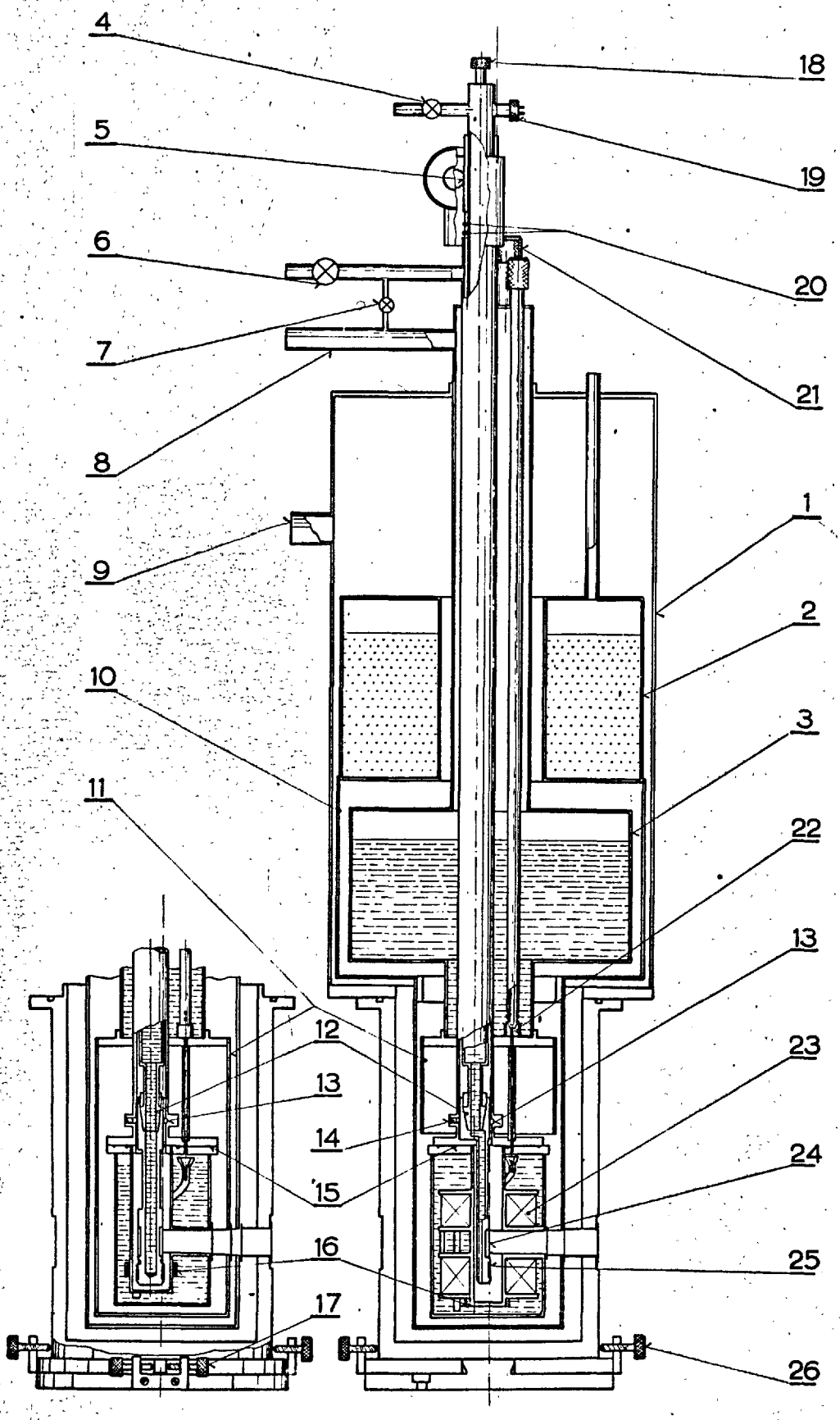

Figure 3.1 The X-ray cryostat after Čabelka (1970). The base on the left of the diagram was used in the present work.

started. At this time other work in the laboratory demanded low temperature measurements within a magnetic field involving considerable modification to the cryostat (Cabelka, 1970), as a result of which helium consumption would have been prohibitive, if the specimens were run at liquid helium temperatures. Since, in any case, Russell (1966) has demonstrated that virtually no improvement of the profiles of indium alloys occurs by going below 78°K, it was decided that all specimens would be measured at this temperature using liquid nitrogen as a coolant and relying on the SB geometry to give a well-resolved profile for a wide divergent beam.

Copper specimen frames were machined, with the correct SB curvature (175 mm) to fit in place of the flat frames in the Cabelka arrangement and giving a specimen length 2ℓ = 10 mm. The specimen frame is attached to the base of a probe which feeds through an O-ring seal at the top of the cryostat, thus allowing the operator to change specimens while the cryostat remains cold (see Figure 3.1).

In order to set the cryostat on the SB diffractometer, the cone mount is removed from the sliding specimen stage. As a matter of policy in this laboratory there is a certain amount of interchangeability of machine parts, so that the cryostat mounts readily on the specimen stage, with the specimen at the right height for the X-ray beam. The adjustments to the specimen comprise the micrometer translation ΔR_S of the specimen stage and a rotation mechanism built into the base of the cryostat (Cabelka, 1970). A general view of the cryostat, mounted on the Wooster-Martin diffractometer, is shown in Fig. (3.2).

Specimens were aligned at 78°K using an I.U.Cr. tungsten powder specimen (Parrish, 1960). A given surface on the probe (rather than on the specimen surface itself) is brought up against a reference point (Fig. 3.1). Hence once the cryostat is aligned the specimen can be interchanged without disturbing the alignment, except for a small ΔR_S error (~ 0.025 mm) representing the limit of reproducibility in the machining of specimen frames and which, in any case, is effectively eliminated by extrapolation.

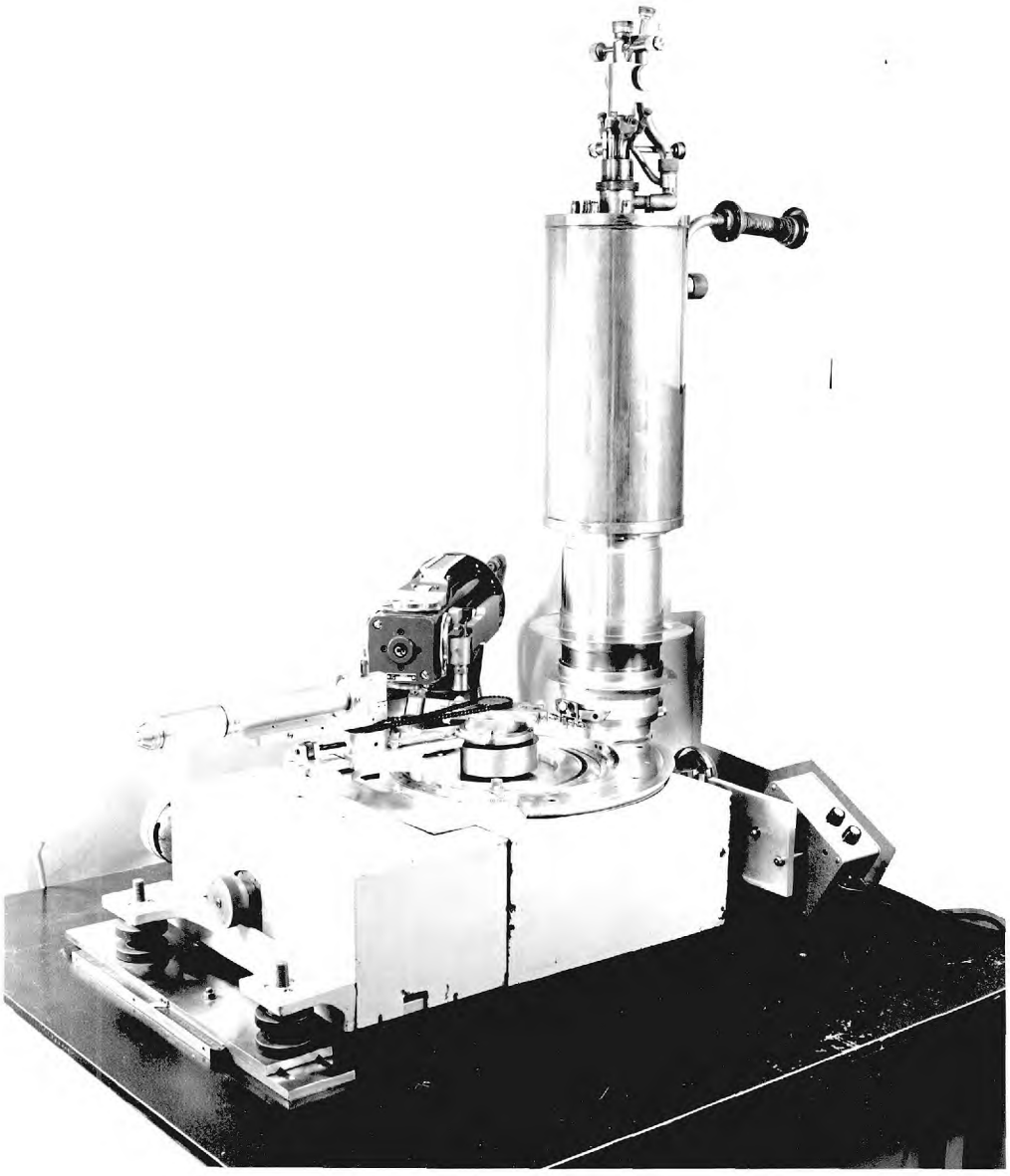

Figure 3.2 The cryostat mounted on the Wooster-Martin diffractometer.

The measurement of temperature in the liquid nitrogen range was achieved with a copper resistance thermometer. To facilitate the rapid reading of resistance a Wheatstone bridge arrangement was made, using a Beckman (calibrated) 'helipot' potentiometer and 'scalamp' galvanometer.

Experimental procedure

The main cryostat spaces were evacuated to 2×10^{-5} torr and closed off with a safety valve in the seal. The exchange gas space was evacuated (to ~1×10^{-4} torr) and flushed with helium gas and sealed off (under a small over-pressure of helium). Liquid nitrogen was poured into a funnel on one of the three inlets of the nitrogen reservoir. One of the other inlets was capped and the third was connected by tube to (what is normally) the helium reservoir, so that the evaporating nitrogen from the nitrogen reservoir was used to pre-cool the inner reservoir which was then filled with nitrogen to a level below the O-ring seals (Fig. 3.1). The total time of filling with nitrogen was about 4 hours and the specimen stayed cold (i.e. 78°K) for up to 15 hours.

In the SB mode a specimen setting of $\gamma = 45^{\circ}$ was chosen since there is little truncation of the high angle end of the 2θ range ($2\theta_{max} = 170.5^{\circ}$) whilst some lower angle peaks could be reached. By 'lower angle' here is meant from about $62^{\circ}2\theta$, the bulk of the cryostat base prohibiting closer approach to the specimen. This range just brings in the strong 222 line (~ $64^{\circ}2\theta$) of all the alloys, which is useful particularly for those alloys where poorer high angle profiles reduce the number of reliable readings (and in some cases even make indexing difficult). For most alloys, however, reflections were only measured at angles above $90^{\circ}2\theta$. After preliminary runs, some ten or eleven of the best profiles were selected (amounting to about twenty points when both α_1 and α_2 peaks were used) as the pattern for a run. Profiles were scanned at $\frac{1}{8}^{\circ}2\theta$/min, in every case towards higher angles. Scanning conditions and instrumental settings used are shown in Table (3.8).

TABLE 3.8

SCANNING CONDITIONS

Divergence slit aperture	2^{o} or 4^{o}
Receiving slit	0.1 mm
Scanning speed	$\frac{1}{8}^{o}2\theta$ per minute.
Time constant	≈4.8 secs
Ratemeter full scale deflection	2.10^{3} and 4.10^{3}
Statistical error	5 % 4 %

Despite the use of flexible couplings it was found necessary to disconnect the vacuum line during the actual scans since a slight peak displacement could be observed on connection. This is only a serious limitation if the cryostat develops a minor leak (e.g. through the electrical feed-throughs).

Specimens were exchanged by drawing the probe up through a cloth wad while passing helium through the exchange gas space. This space was then sealed with a rubber bung, while a new specimen was fitted to the probe. After the probe had been reinserted, the exchange gas space was re-evacuated and filled with helium. With these precautions few icing-up problems occurred.

3.3 THE ELIMINATION OF ERRORS IN THE DIFFRACTION MEASUREMENTS

Profile positions

All the routine lattice parameter determinations were derived from the positions of the peaks rather than the centroids of the diffraction profiles. To the order of accuracy required (~ 1:40,000) this is a quite adequate definition of profile position. Furthermore, although the diffraction profiles were, relatively, well-defined for the soft, coarse-grained specimens used here, they were, nevertheless, poor enough (i.e. of low intensity with considerable random fluctuation) to make the determination of the centroid quite difficult. A more practical reason for using peaks, however, was one of time. As it was, the process of computing the lattice parameters of over 80 indium alloys required the punching of some 30,000 digits of data.

In order to justify using the extrapolation procedure (section 2.3) it is necessary to know whether the error function is valid for peak shifts. Wilson (1963) has demonstrated that for the geometrical

errors, the peak shift, to a first order of approximation, is the same as the centroid shift and to second order is lessened by a quantity proportional to the variance of the aberration. For peak measurements the Lorentz factor and dispersion errors tend to cancel out (Wilson, 1963). The errors arising out of axial divergence are small, especially with two sets of Soller slits, and in this case can safely be ignored.

Random Errors

All the non-systematic human errors are assumed to obey the normal law of errors, the random error being in the variable θ. The minimisation of errors is thus the least-squares procedure. Analyses of this kind are clearly tasks for the computer and as such might just as well be expanded to contain the extrapolation procedure in analytic form. Analyses of this type are commonplace now and hence the procedure will only be briefly reviewed. The standard paper on the subject is that of Vogel and Kempter (1961) in which credit is given to Deming (1943) for an iterative procedure. In fact a far more understandable and thorough analysis of processes of this kind is given in an excellent book by Whittaker and Robson (1924).

The quadratic Bragg equation for tetragonal crystals for the observation is

$$A_o(h_i^2 + k_i^2) + C_o l_i^2 + D_o f(\theta_i) = \sin^2 \theta_i \quad \ldots (3.1)$$

where $A_o = \frac{\lambda^2}{4a_o^2}$

$C_o = \frac{\lambda^2}{4c_o^2}$

and c_o, a_o are the lattice parameters and $f(\theta)$ is the error function of known functional form. The aim of the calculation is an expression for the 'best' values of A,C and D which gives a 'best' function to

describe the left-hand side of 3.1, say y_i (best). A function is also described by the values of A,C and D taking the particular approximation of the moment, say y_i (approx).

$$\text{If } A_{approx} = A_{best} - a$$

$$C_{approx} = C_{best} - c$$

$$D_{approx} = D_{best} - d$$

then

$$y_i(\text{approx}) = y_i(\text{best}) - a\frac{\partial y_i}{\partial A_o} - c\frac{\partial y_i}{\partial C_o} - d\frac{\partial y_i}{\partial D_o}$$

The failure of the best function to fit the ith observation is then

$$F_i = y_i(\text{obs}) - y_i(\text{approx}) - a\frac{\partial y_i}{\partial A_o} - c\frac{\partial y_i}{\partial C_o} - d\frac{\partial y_i}{\partial D_o} \quad \ldots (3.2)$$

where $y_i(\text{obs})$ is $\sin^2\theta_i$. The observation is θ_i which is assumed to have an error probability derived from the normal law. Let the distribution of probable measurements of θ at $\theta = \theta_i$ be $\sigma^2_{\theta_i}$. There is no fixed empirical or theoretical functional form to this quantity and it is usually assigned the value 1. In the poorer quality specimens, such as the indium alloys under discussion, there are clearly peaks of quite different quality and hence the reliability of measurement of peaks (in degrees) differs from peak to peak. It was, therefore, decided to assign a value of $\sigma^2_{\theta_i}$ to each peak as it was measured. Thus if the observer judges that one peak can only be read to, say, 2mm of chart paper, whereas the best peaks in that run can be read to 1mm, then relative values of 4 and 1 are assigned to the variance of the measurement. This is clearly somewhat subjective, but it is argued that such a procedure cannot be worse than taking all the variances as unity.

The standard deviation of the distribution of the failures F_i is

$$\sigma^2_{F_i} = \left(\frac{\partial F_i}{\partial \theta_i}\right)^2 \sigma^2_{\theta_i} \qquad \ldots (3.3)$$

Standard error theory demonstrates that the greatest probability of the set of measurements F_i occurring is when

$$\sum_i \frac{F_i^2}{\sigma^2_{F_i}} \quad \text{is least}$$

It is easily demonstrated that minimisation of this sum with respect to a, c and d, is given by

$$\sum_i \{y_i(\text{obs}) - y_i(\text{approx}) - [a\frac{\partial y_i}{\partial A_o} + c\frac{\partial y_i}{\partial C_o} + d\frac{\partial y_i}{\partial D_o}]\}W_i\frac{\partial y_i}{\partial A_o} = 0 \qquad \ldots (3.4)$$

and similar expressions in C_o and D_o where W_i is the weight of the observation given by the inverse of the variance of F_i. These are the 'normal' equations for the solution of a, c and d, all the other quantities being known.

Now if $n_i = y_i(\text{obs}) - y_i(\text{approx})$ it can be elegantly shown (see Whittaker and Robson) that the variance of this quantity is

$$\sigma^2_{n_i} = \frac{\Sigma W_i n_i^2}{(N-3)W_i} \qquad \ldots (3.5)$$

and furthermore that the errors in the quantities a, c and d are given by equations of the kind

$$\sigma_a^2 = \frac{\begin{vmatrix} q_2 & r_2 \\ q_3 & r_3 \end{vmatrix}}{D_T} \sigma^2_{n_i} W_i \qquad \ldots (3.6)$$

where D_T is the determinant

$$\begin{vmatrix} p_1 & q_1 & r_1 \\ p_2 & q_2 & r_2 \\ p_3 & q_3 & r_3 \end{vmatrix}$$

where $D_T(ij)$ are the coefficients of a, c and d in the simultaneous equations 3.4. Quantities required for these coefficients are

$$\frac{\partial y_i}{\partial A_o} = (h_i^2 + k_i^2)$$

$$\frac{\partial y_i}{\partial C_o} = \ell_i^2$$

$$\frac{\partial y_i}{\partial D_o} = f(\theta_i)$$

$f(\theta_i)$ is the systematic error in $\sin^2 \theta$

i.e. $\Delta \sin^2 \theta = \sin 2\theta \Delta_{syst}\theta$

where $\Delta_{syst}\theta$ is given by (2.61) whence

$$f(\theta_i) = \frac{\sin^2 2\theta_i}{\sin(2\theta_i - \gamma)\sin\gamma} \qquad \ldots (3.7)$$

or $$f(\theta_i) = \frac{\sin^2 2\theta_i}{\sin(2\theta_i - \gamma) + \sin\gamma}$$

depending on which error predominates. The weight W_i is obtained by differentiation of 3.2 using 3.7.

Once the values a, c and d are determined, a new approximation to A, C and D is found. A computer programme has been written to do this and to iterate to consistency. A listing of the programme is given in Appendix 4. Three alternative sets of indices are fed in for each peak and the best selection is made each iteration. α_2 peaks are converted to equivalent α_1 peaks within the programme. Error limits are closed in until one peak is rejected in each run.

Values of a_o and c_o were read in and the programme was found to converge whatever values were used (these were always reasonable). Occasional specimens resulted in the (crude) convergence of the process to quite a different set of parameters from the real ones. Strangely enough, the alteration of one of the alternative sets of indices for just one peak would often correct this.

3.4 THE MEASUREMENT OF T_c

The onset of zero resistance in a superconductor occurs at a temperature dependent on the current being used to detect it. This uncertainty, and the fact that electrical connection must be made to the specimen in the resistive technique, suggests that a better approach to measurement would be the inductive method based on the Meissner effect (see section 1.3). For reasonably small fields ($<< H_c(0)$) there is no implicit uncertainty in this method. Furthermore the inductive method may be used for scraps of material or even powders.

The T_c Probe

A multi-specimen probe has been designed to be used in an Oxford Instruments helium dewar and is shown, schematically, in situ, in Fig. (3.3). The limiting factor in the design is the width of the tail of the helium dewar (~ 55 mm) into which the specimen chamber must fit.

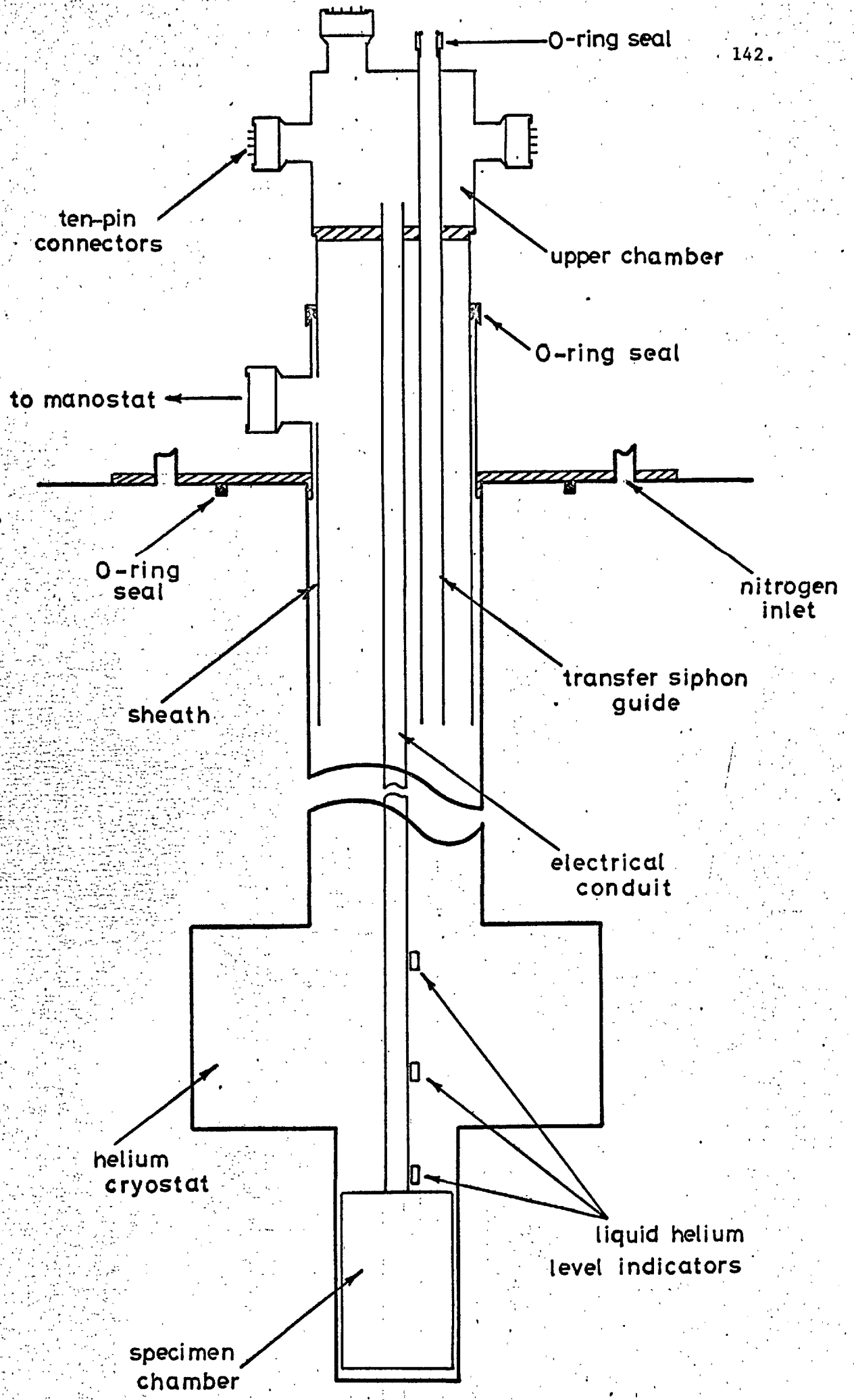

Figure 3.3 Schematic picture of the T_c probe in situ.

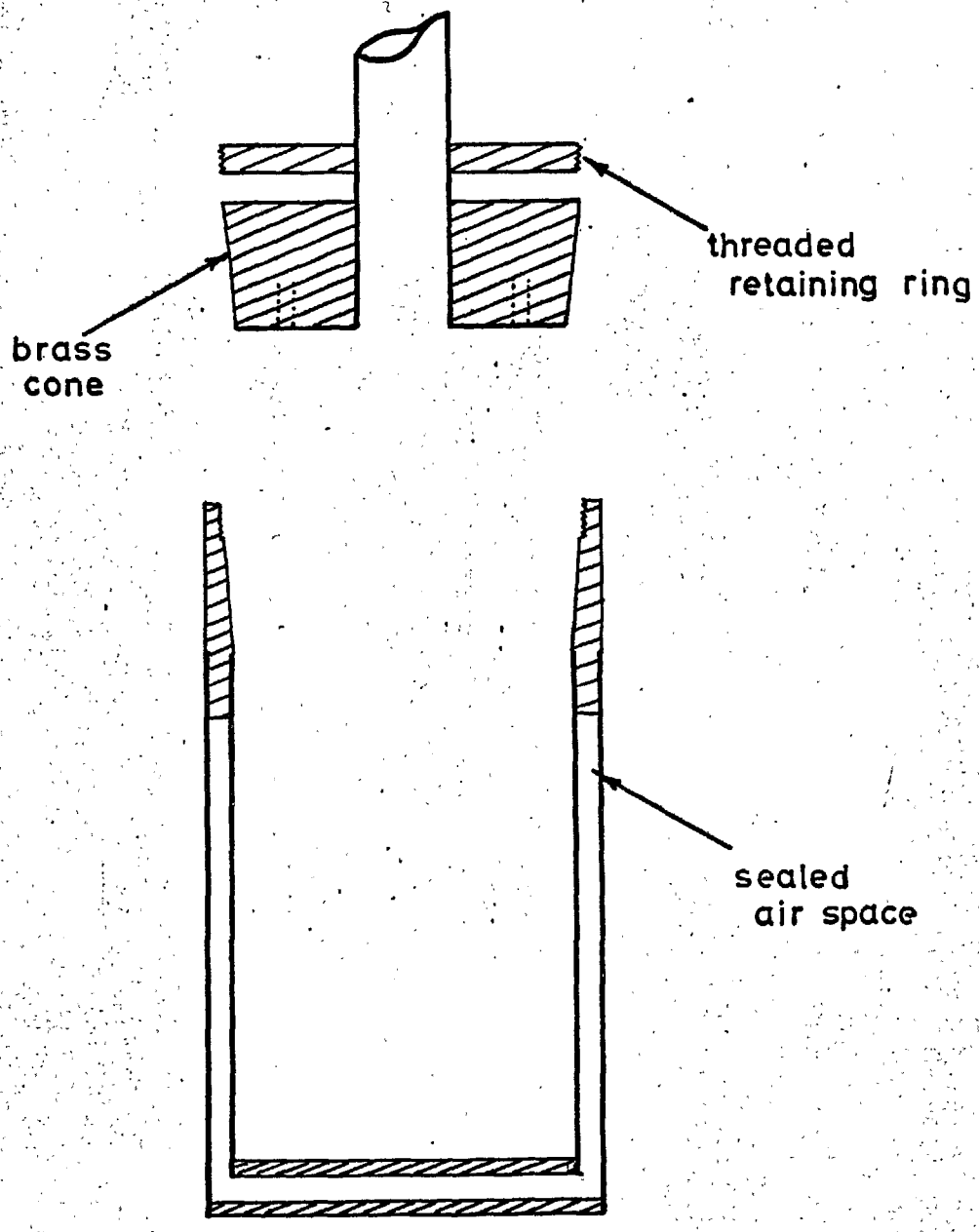

Figure 3.4. The specimen chamber.

The cavity between the double walls of the brass specimen chamber, shown in Fig. (3.4), evacuates by condensation (of the air at low temperature) to provide insulation from the liquid helium when working at temperatures above 4.2°K. Access to the specimens is made via a brass cone joint, greased with silicone vacuum grease, which effectively seals the chamber even when immersed in liquid helium.

As shown diagrammatically in Fig. (3.5), the specimen arrangement consists of a framework of perspex discs and brass studding. The two discs A are drilled with 6.4mm ($\frac{1}{4}$") holes to hold the secondary coil and heater formers. The twelve coils are wound on rigid plastic tubes, about 50 mm long, with about 5,000 turns of 49 S.W.G. enamelled copper wire. The heater coil consisted of about 100 turns of 44S.W.G. eureka insulated wire wound on a solid perspex former.

A piece of copper foil wrapped, nearly but not quite around (a good conductor will shield by eddy currents if there is a closed path) the specimen framework, acts as a former for the primary coil and also as a radiation shield. The primary coil consists of about 300 turns of 42 S.W.G.enamelled copper wire.

A Texas Instruments doped germanium thermometer, previously calibrated (to $\pm$ 0.02°K at 4.2°K) against a standard thermometer in another probe, was screwed into a small copper block which was itself screwed into one of the perspex discs. A thick electrically insulated copper wire was wound round the terminals of the thermometer and connected as a thermal sink to the brass cone joint.

The specimen chamber is suspended by 12.8 mm ($\frac{1}{2}$") stainless steel tube (which also acts as a conduit for the electrical connections) from an upper chamber (Fig. 3.3) which shares the same vacuum or exchange gas space. Evacuation and flushing of this space is achieved by means of a $\frac{1}{4}$" Edwards vacuum fitment whilst electrical connections to the exterior are made with three Ether ten-pin vacuum connectors sealed into $\frac{3}{4}$" Edwards vacuum unions.

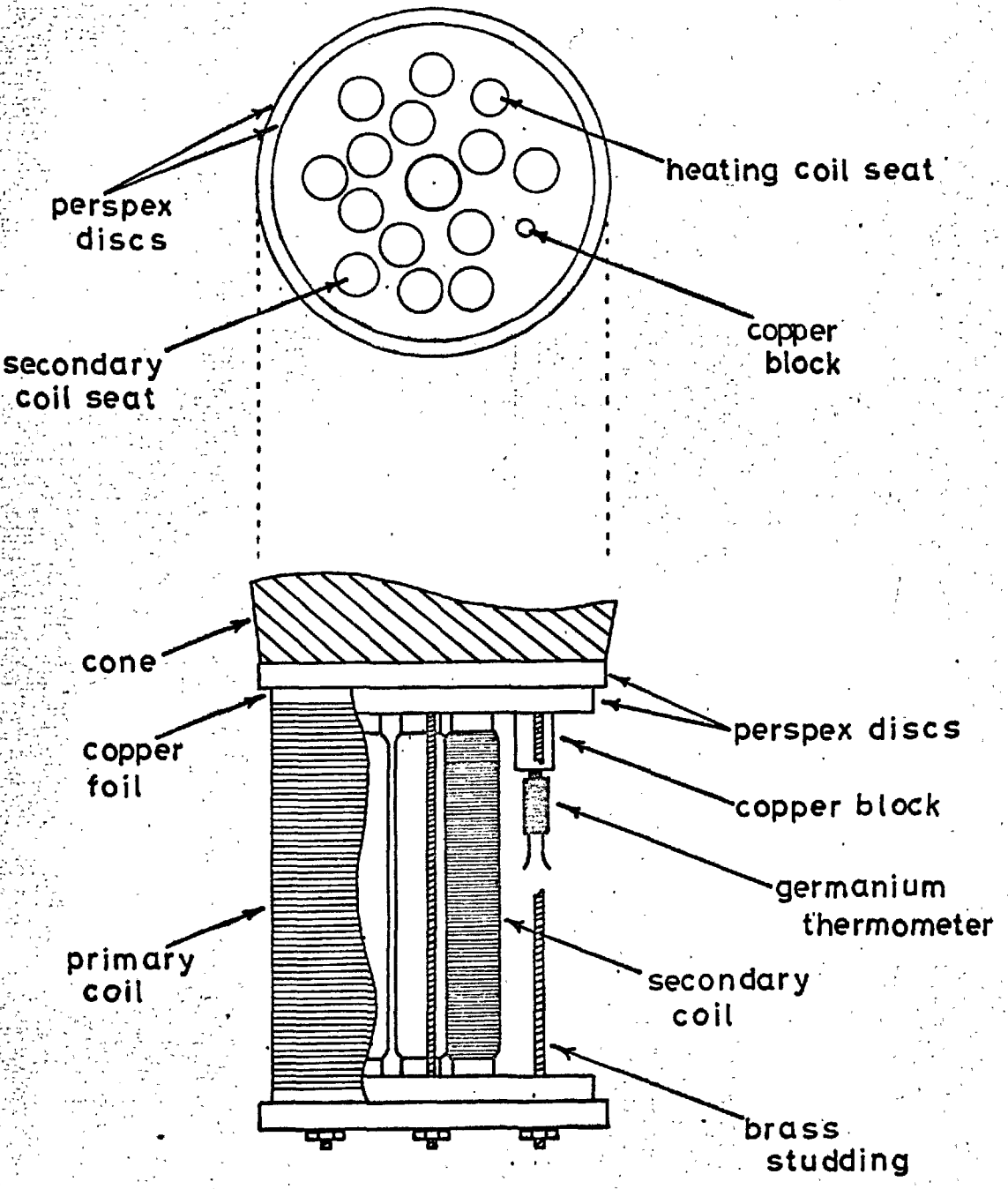

Figure 3.5 The specimen arrangement.

The probe slides vertically, through an O-ring seal (Fig. 3.3), so that the specimen chamber may be raised above the liquid helium level when necessary. The helium dewar is filled via a transfer siphon which slides through a $\frac{3}{8}$" O-ring seal and 12.8 mm ($\frac{1}{2}$") stainless tube passing through the upper can. The outlet for the helium gas is via a 1" Edwards vacuum union connected to a manostat (Larbalestier, 1970) and from thence to a heavy duty (450 ℓ/min) Edwards pump, via a 1" pipe line. Vacuum tap connections on this pipe line provide possible outlets to a helium gas collection bag or to the atmosphere.

The level of the liquid helium in the dewar is determined by three 'Silec' diodes attached to the central tube of the probe, the electrical connections to these diodes being via a five-pin Ether connector sealed into a $\frac{1}{2}$" Edwards union.

Measuring Circuits

The resistances of the Silec diodes, which were previously calibrated in a helium transfer dewar, are measured by an Avometer. All other electrical connections are made from the three ten-pin seals, via earthed-sheath twelve-bore cable, to a control panel with snap connectors.

A simple heater circuit consists of an input to the panel from a power pack, a current regulator (coarse and fine control potentiometers) and a milliammeter.

An A.C. signal, between 500 and 1,000 Hz, from an oscillator is fed to the primary coil via the control panel. It was found necessary to earth one side of the primary coil. The secondary coils have one side in common and a single pole, 12-way switch is used to select the appropriate coil. The return signal is full wave rectified by a simple bridge circuit and fed directly to one channel of a two-pen strip chart recorder. No amplification or smoothing of the signal was found to be necessary.

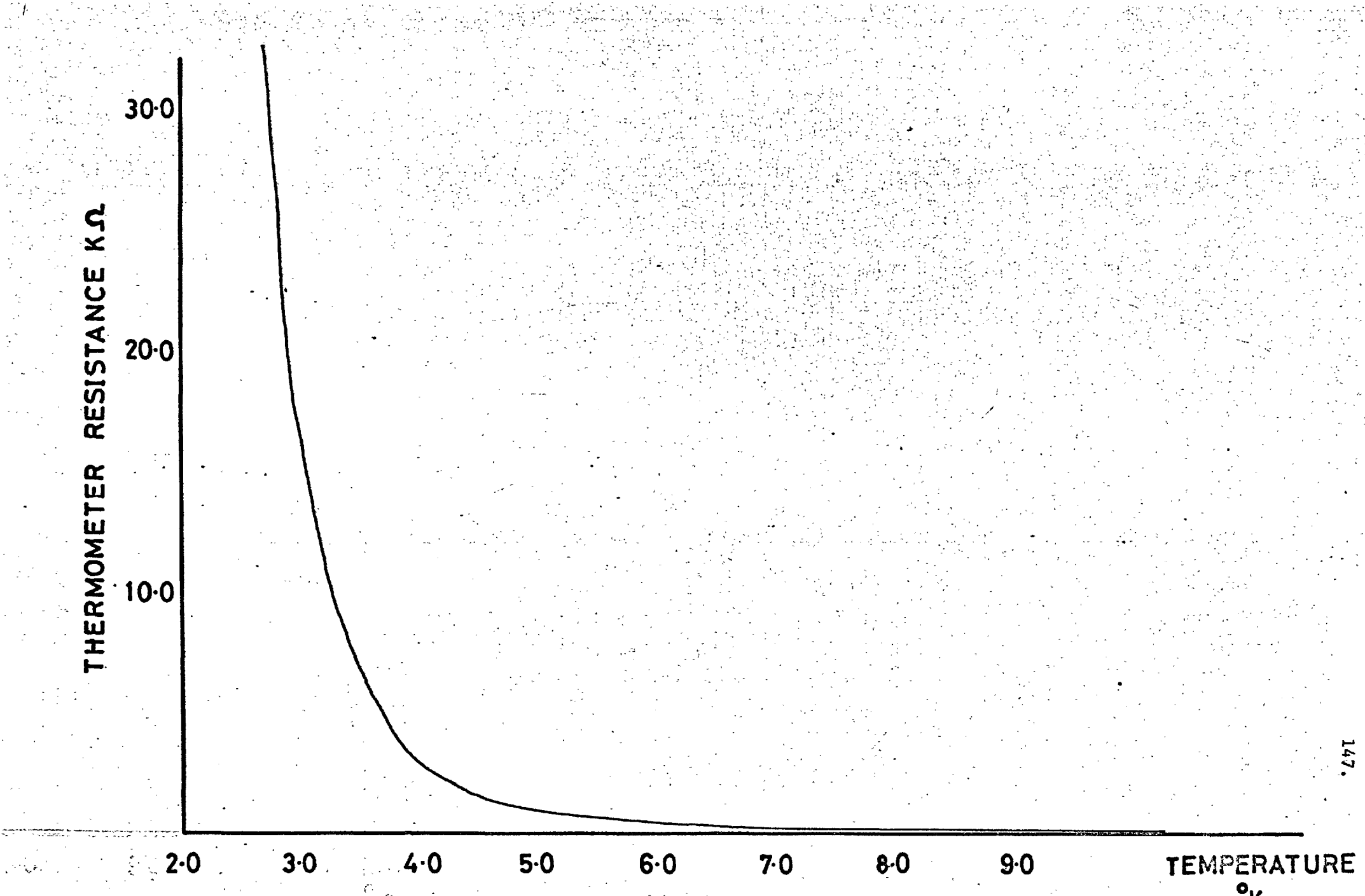

Figure 3.6 The temperature-resistance characteristic of the germanium thermometer.

It was thought desirable to record the transition to superconductivity on a strip chart showing simultaneously the temperature and the coil signal. The temperature measurement presented a problem because the calibration of the thermometer ceases to apply if the power dissipation within it exceeds a microwatt. In consideration of this and of the logarithmic form of the temperature-resistance curve (Fig. 3.6) a special bridge circuit was developed. The out-of-balance current on a Wheatstone bridge is a function of the resistances and, as a consequence, by selecting two of the resistances a given range of current corresponds to a particular range of the measured resistance. Thus, by a simultaneous switching of pairs of standard resistances, any range of resistance may be chosen at will. The circuit used is shown in Fig. (3.7) and can be seen to include the common modification designed to cancel the contribution, to the measured resistance, of the leads to it. This is achieved by having two leads to one of the thermometer terminals. If all three leads have equal resistance R_ℓ, it is easily shown that they effectively cancel when the bridge is balanced. The solution of Kirchoff's equations for the system shows that some sort of rough cancellation occurs at off-balance and so the method was employed. It is somewhat pedantic, however, as the lead resistances are insignificant for all temperatures measured here.

In the Figure (3.7) R_G is the germanium resistance and each R is a 1KΩ (which is the order of magnitude of most of the likely R_G values) metal oxide high-stability resistor. R_X and R_L are the variables that determine the ranges, whilst R_S is a resistance to reduce the power dissipation in R_G. The Kirchoff's equations are solved exactly and the power dissipation in R_G maximised with respect to R_X, R_L and R_G. The resultant expression is made less than a microwatt if R_S is greater than 2×10^4 ohms. A resistance of $10^5\,\Omega$ was used to make sure. Consideration of the temperature-resistance chart for the germanium thermometer, and the Kirchoff calculations led to the choice of twelve suitable ranges of resistances and the corresponding pairs of resistances, R_X and R_L. The simultaneous switching of these resistors is achieved with a two-wafer, single pole, twelve-way switch and the

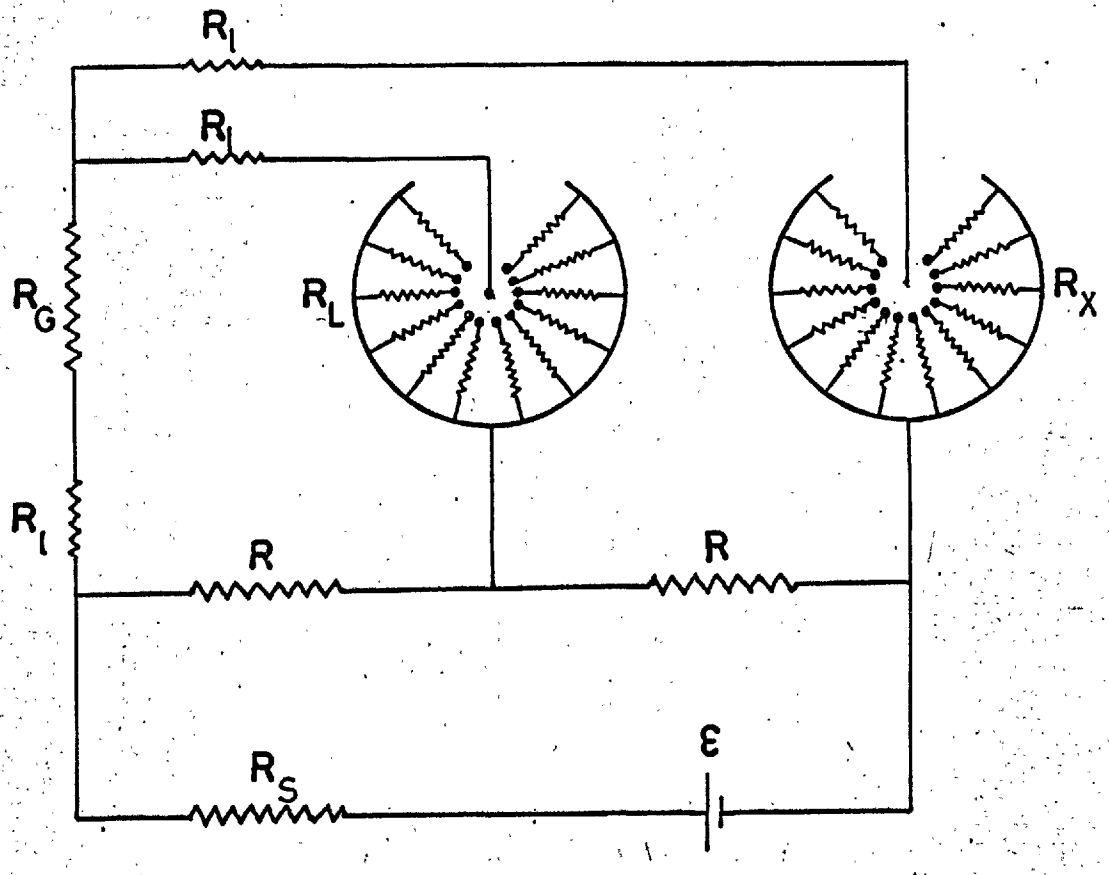

Figure 3.7 The measuring bridge for the germanium thermometer.

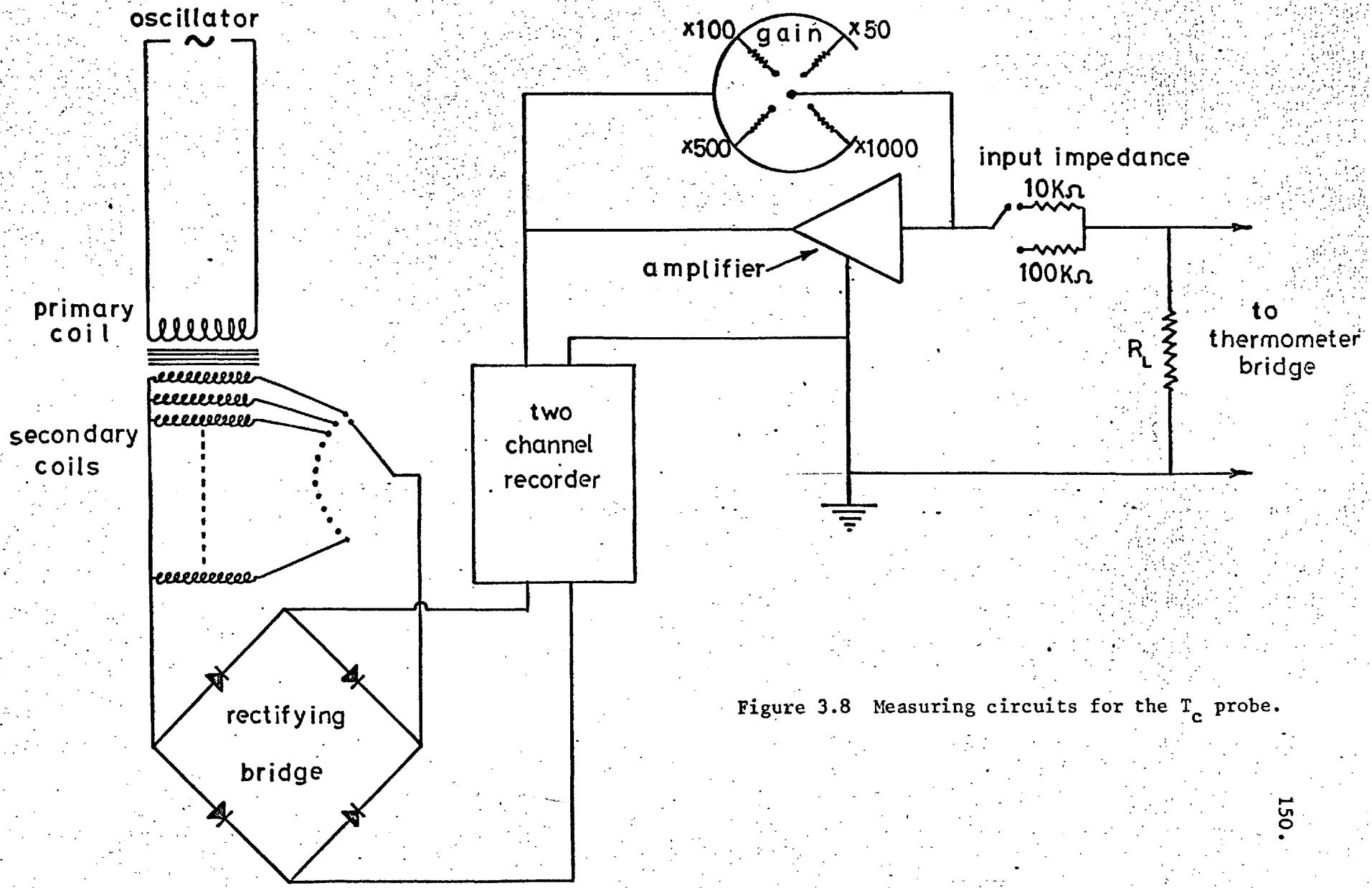

Figure 3.8 Measuring circuits for the T_c probe.

values of R_L and R_X are shown in Table (3.9). Unfortunately the voltage across R_L cannot be made large enough to display on the chart recorder directly and amplification is required.

An Analog Devices amplifier was built into the circuit, as shown in Fig. (3.8) and was usually used with a gain of 100 and an input impedance of 10KΩ , which was the value taken into account in the calculations of R_L. One side of the amplifier is earthed and the output is zeroed by means of a fine control potentiometer (Bourn's 'trimpot') with the input short circuited.

The E.M.F. across the bridge was provided by a 2-volt accumulator which remained stable within the accuracy required, but in order to be sure, ranges were calibrated against a resistance box before and after every experiment.

The off-balance current as a function of temperature is shown, for a typical range, in Fig. (3.9) and can be seen to be nearly linear over most of the range.

Modes of Operation

There are two distinct problems in transition temperature measurement according to whether that temperature is above or below 4.2°K, the boiling point of helium.

The first specimens measured were those of the indium-lead system, all of which have T_c above 4.2°K. The probe was evacuated and flushed with helium gas a couple of times and then sealed with an overpressure of helium. The helium dewar was pumped out to a hard vacuum and the outer reservoir filled with liquid nitrogen. The specimen chamber of the probe and the helium reservoir were both pre-cooled with liquid nitrogen. After the probe was placed in the dewar an evacuated double-walled siphon was used to transfer liquid helium from the transport dewar.

TABLE 3.9

BRIDGE CIRCUIT - RESISTANCE VALUES

R_X ohms	R_L ohms	Range of R_G ohms
200 K	560	200 K → 40K
50 K	36	50 K → 15K
22 K	120	22 K → 7K
9.1 K	56	9.1 K → 2.5K
3.3 K	37	3.3 K → 1K
1.2 K	43	1.2 K → 450
560	75	560 → 270
330	96	330 → 150
180	200	180 → 95
110	220	110 → 38
47	2.2 K	47 → 22
27	1.5 K	27 → 0

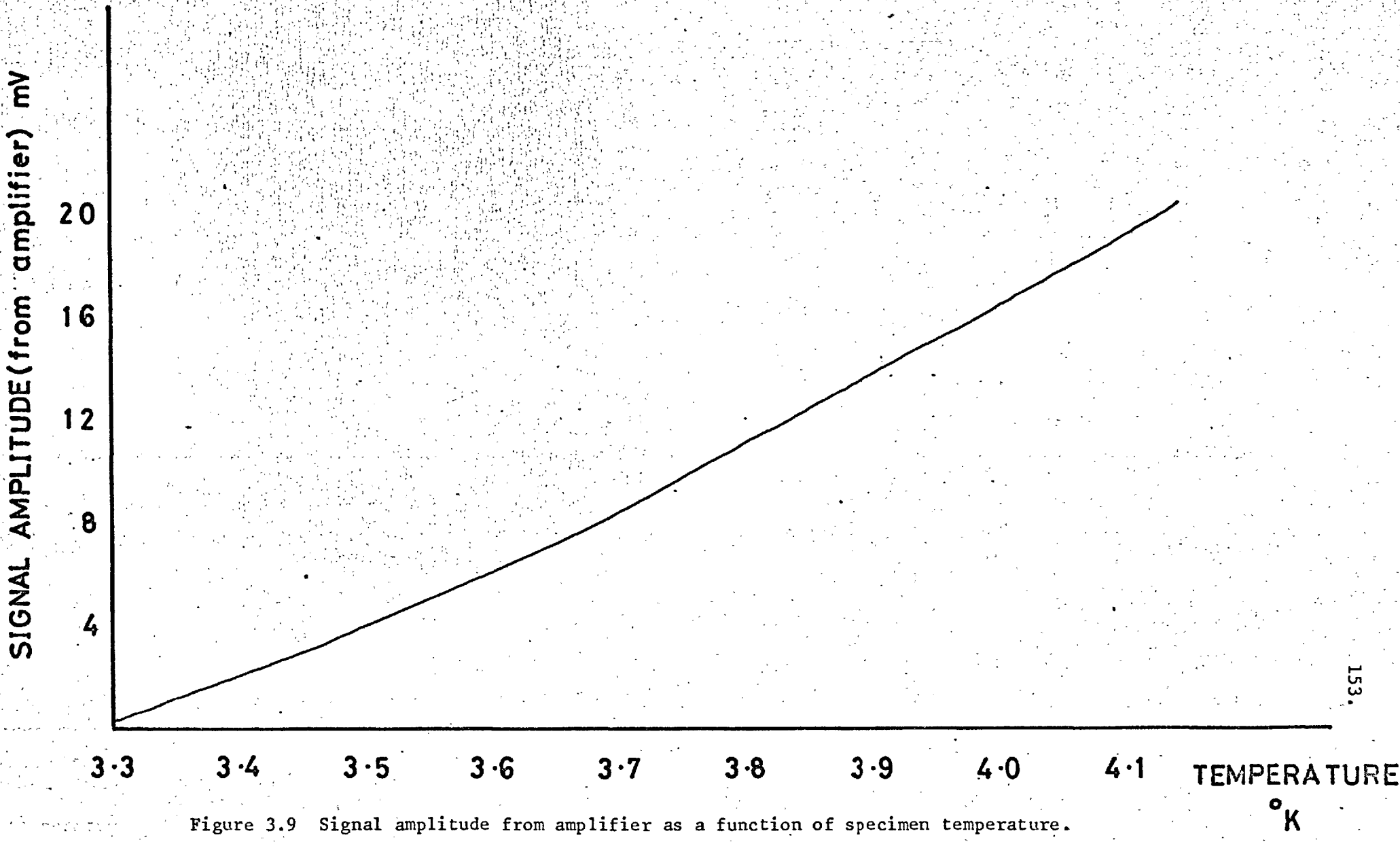

Figure 3.9 Signal amplitude from amplifier as a function of specimen temperature.

When the transfer was complete, the exchange gas in the specimen chamber was heated gradually, until the superconducting transition of a pure lead specimen was observed on the chart recorder. Unfortunately, it was not always possible to obtain a uniform temperature distribution, and hence two lead specimens did not always transform at the same thermometer reading. A difference of temperature greater than 0.5°K was often observed but it was never discovered why this was so. The discrepancy appeared to change with exchange gas pressure which makes the method itself seem somewhat dubious.

Most of the high T_c results were obtained, however, when the transition temperatures of both lead specimens were within 0.03°K of the usually accepted value of 7.18°K. In an attempt to circumvent the problem of the lack of temperature uniformity some indium-tin and indium-bismuth alloys were measured by removing the double walled jacket and suspending the probe in the gas above the liquid helium. These specimens were cut to short lengths, to limit the effect of the temperature gradient, and placed at the same level as the germanium thermometer. Since the lead transition gives a very small change in signal (an eddy current effect in pure metals) the reduction of specimen length reduced this change to below the noise level of the signal. An indium-lead specimen which had a signal change much greater than the noise level and had been calibrated previously against the lead specimen (when the latter gave an accurate T_c result using the double-walled jacket) was, therefore, used as an internal standard for these experiments. Since the observed T_c of this specimen was exactly the same as that obtained during the previous runs the confidence of the remaining indium-tin and indium-bismuth results is set at $\pm$ 0.03°K.

The measurement of T_c below 4.2°K is straightforward and entirely satisfactory. The double-walled can is removed, the specimen arrangement immersed in the liquid helium and the temperature controlled by pumping on the liquid and using the manostat referred to above. By changing the reference pressure in the manostat and adjusting the main line tap it was possible to produce a very slow even drift of temperature right through the transition. For these experiments, pure indium was used as the internal standard and its T_c was found to be, on all occasions, within 0.004°K of the usually accepted value of 3.400°K.

REFERENCES

Čabelka, D., (1970), Private communication.

Deming, W.E., (1943), 'Statistical Adjustment of Data', Wiley, N.Y.

King, H.W. and Preece, C.M., (1967), Adv. X-ray Anal. 10, 354.

Larbalestier, D.C. (1970), Thesis, Imperial College.

Parrish, W., (1960), Acta Cryst. 13, 838.

Russell, C.M., (1966), Thesis, Imperial College.

Vogel, R.E. and Kempter, C.P., (1961), Acta Cryst. 14, 1130.

Whittaker, Sir E., and Robinson, G., (1924), 'The Calculus of Observations, Blackie, London.

CHAPTER 4

CHAPTER 4

RESULTS

THE SEEMANN-BOHLIN DIFFRACTOMETER

The report of most of the preliminary X-ray diffraction measurements, associated with the SB geometry, fell more naturally into the description of apparatus in Chapter 2 and will not be repeated here.

The difference in practice, between the SB and BB methods at low temperature, is illustrated in Fig. (4.1) by the chart record of scans through the 402 and 511 profiles of an In-1.682 at.% Cd alloy. Chart A refers to liquid helium temperatures (13^{o}K) using the original cryostat (Russell, 1966) mounted on the Siemens' diffractometer. Chart B was obtained with the present SB arrangement at 78^{o}K and can be seen to compare very favourably in resolution with chart A. The chart speed was the same for each trace but the scanning speed ($\frac{1}{8}^{o}2\theta$ per min.) for B was half that for A.

X-RAY EXAMINATION OF THE INDIUM ALLOYS

The quality of peaks scanned varied markedly across each alloy system and from one system to another. In some cases the solute (Hg for example) sharpened the peaks whilst in other cases (in In-Pb in particular) the indium peaks were broadened considerably with alloying. In most cases, however, the highest angle peaks (which cannot be detected at room temperature) were easily measurable.

The lattice parameters, axial ratios and volumes of the FCT cell are given, for all the indium alloys measured, in Tables 4.1 to 4.6.

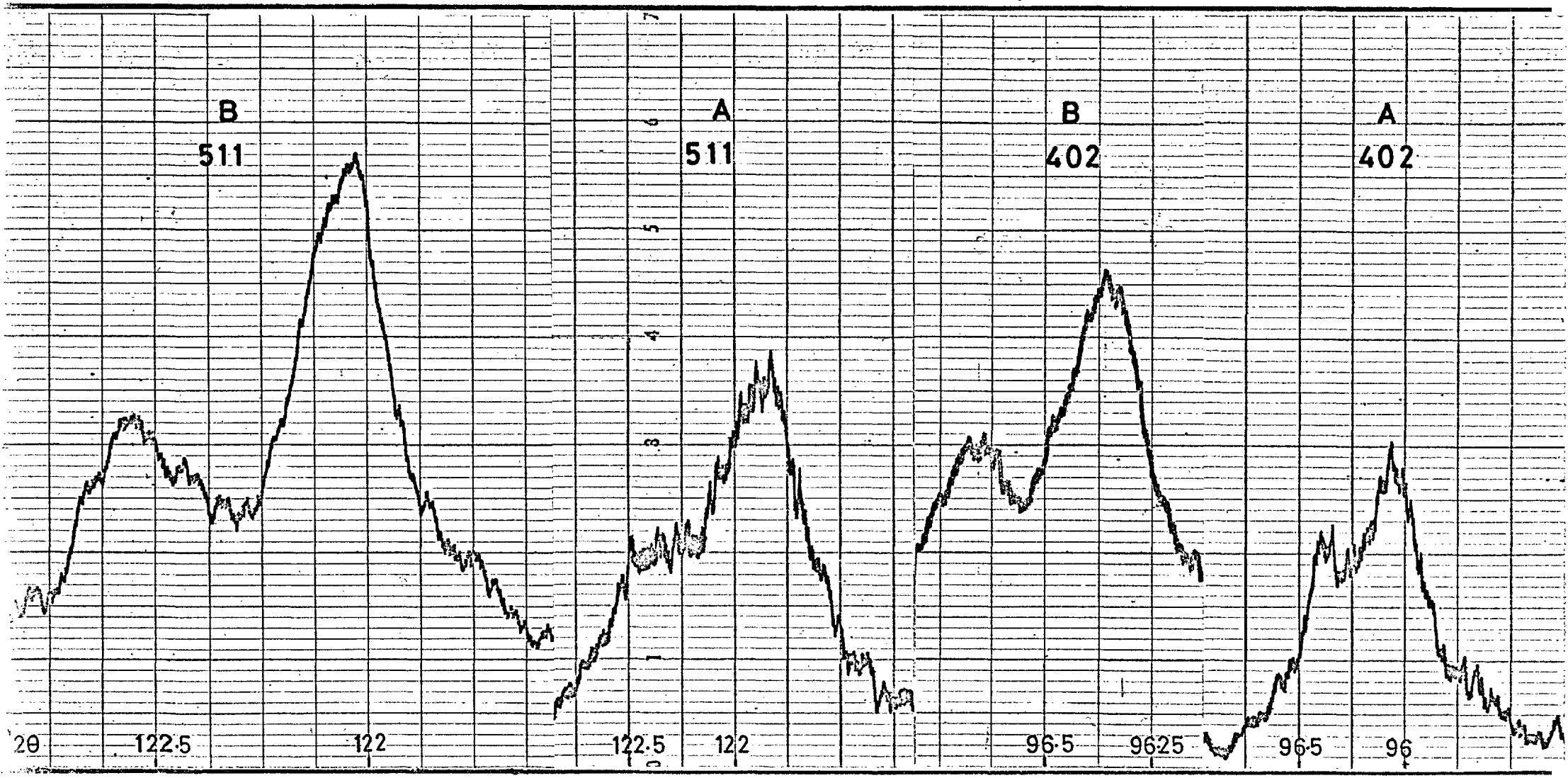

Figure 4.1 Low temperature diffraction profiles of the indium-1.682 at.% Cd alloy.

TABLE 4.1

LATTICE PARAMETERS FOR THE SYSTEM In-Pb

Composition at.% Pb	c Å	a Å	$c/_a$	ca^2 Å^3
11.003	5.01336	4.56702	1.09773	104.567
	± 0.00171	± 0.00129	± 0.00049	± 0.069
11.504	5.01867	4.56880	1.09846	104.759
	± 0.00176	± 0.00112	± 0.00047	± 0.063
12.002	5.01963	4.56499	1.09959	104.604
	± 0.00635	± 0.00424	± 0.00173	± 0.263
12.501	5.02289	4.56766	1.09966	104.795
	± 0.00640	± 0.00133	± 0.00144	± 0.147
13.061	5.03296	4.56601	1.10227	104.929
	± 0.00286	± 0.00354	± 0.00106	± 0.173
13.994	4.54017	4.81667	0.94260	105.334
	± 0.01224	± 0.01259	± 0.00354	± 0.619
15.322	4.50413	4.85311	0.92809	106.084
	± 0.00680	± 0.00418	± 0.00161	± 0.243
17.251	4.43993	4.88889	0.90817	106.120
	± 0.02018	± 0.00857	± 0.00442	± 0.609
18.905	4.49722	4.86067	0.92523	106.252
	± 0.00388	± 0.00182	± 0.00087	± 0.121
21.209	4.49806	4.87290	0.92308	106.807
	± 0.00309	± 0.00229	± 0.00077	± 0.124
23.009	4.49058	4.87913	0.92036	106.902
	± 0.00372	± 0.00271	± 0.00092	± 0.148
24.821	4.49210	4.87879	0.92074	106.924
	± 0.00394	± 0.00311	± 0.00099	± 0.166
27.043	4.48845	4.88505	0.91881	107.111
	± 0.00205	± 0.00267	± 0.00066	± 0.127
28.924	4.48567	4.88578	0.91811	107.077
	± 0.00188	± 0.00280	± 0.00065	± 0.130
30.869	4.50489	4.87894	0.92333	107.234
	± 0.00772	± 0.00367	± 0.00173	± 0.245
32.997	4.88543	4.69082	1.04149	107.498
	± 0.01651	± 0.02503	± 0.00658	± 1.204

TABLE 4.2

LATTICE PARAMETERS FOR THE SYSTEM In-Sn

Composition at.%Sn	c $\mathring{A}$	a $\mathring{A}$	c/a	ca^2 $\mathring{A}^3$
0.997	4.94729	4.55521	1.08607	102.656
	± 0.00111	± 0.00096	± 0.00033	± 0.049
2.002	4.95999	4.55056	1.08997	102.710
	± 0.00118	± 0.00081	± 0.00032	± 0.044
2.524	4.96651	4.54732	1.09218	102.698
	± 0.00080	± 0.00050	± 0.00021	± 0.028
3.002	4.97187	4.54571	1.09375	102.736
	± 0.00058	± 0.00037	± 0.00016	± 0.020
4.001	4.98265	4.54294	1.09679	102.834
	± 0.00074	± 0.00042	± 0.00019	± 0.024
6.000	5.00120	4.53650	1.10244	102.924
	± 0.00088	± 0.00046	± 0.00022	± 0.028
8.000	5.01805	4.53105	1.10748	103.023
	± 0.00065	± 0.00039	± 0.00017	± 0.022
10.000	5.03017	4.52698	1.11115	103.086
	± 0.00097	± 0.00051	± 0.00025	± 0.033
12.010	5.04197	4.52460	1.11435	103.219
	± 0.00093	± 0.00061	± 0.00026	± 0.034
12.997	5.04397	4.51911	1.11614	103.010
	± 0.00172	± 0.00119	± 0.00048	± 0.064

TABLE 4.3

LATTICE PARAMETERS FOR THE SYSTEM In-Hg

Composition at.% Hg	c $\mathring{A}$	a $\mathring{A}$	$c/_a$	ca^2 $\mathring{A}^3$
0.467	4.92845	4.56104	1.08055	102.527
	± 0.00038	± 0.00034	± 0.00012	± 0.017
0.753	4.92465	4.56194	1.07951	102.488
	± 0.00052	± 0.00034	± 0.00014	± 0.019
1.008	4.92111	4.56158	1.07882	102.398
	± 0.00052	± 0.00031	± 0.00013	± 0.017
1.756	4.91046	4.56525	1.07562	102.341
	± 0.00065	± 0.00055	± 0.00019	± 0.028
1.921	4.90892	4.56502	1.07533	102.299
	± 0.00079	± 0.00063	± 0.00023	± 0.033
3.000	4.89194	4.56996	1.07046	102.166
	± 0.00109	± 0.00062	± 0.00028	± 0.036
3.393	4.88534	4.57174	1.06859	102.108
	± 0.00064	± 0.00041	± 0.00017	± 0.023
4.000	4.87622	4.57408	1.06606	102.021
	± 0.00108	± 0.00050	± 0.00026	± 0.032
5.000	4.85313	4.58150	1.05929	101.868
	± 0.00094	± 0.00053	± 0.00024	± 0.031
6.000	4.82669	4.59092	1.05136	101.730
	± 0.00080	± 0.00046	± 0.00020	± 0.027
7.000	4.76863	4.61173	1.03402	101.420
	± 0.00339	± 0.00093	± 0.00076	± 0.083
7.500	4.66571	4.65578	1.00213	101.135
	± 0.00103	± 0.00443	± 0.00098	± 0.194
8.000	4.66722	4.66176	1.00117	101.428
	± 0.00061	± 0.00039	± 0.00016	± 0.022
9.000	4.66236	4.66047	1.00041	101.266
	± 0.00010	± 0.00011	± 0.00003	± 0.005
11.162	4.67051	4.65246	1.00388	101.095
	± 0.00410	± 0.00108	± 0.00091	± 0.100
12.008	4.68085	4.64566	1.00758	101.023
	± 0.00571	± 0.00185	± 0.00129	± 0.147

TABLE 4.4

LATTICE PARAMETERS FOR THE SYSTEM In-Cd

Composition at.% Cd	c $\overset{o}{A}$	a $\overset{o}{A}$	$c/_a$	ca^2 $\overset{o}{A}^3$
0.976	4.91840	4.56543	1.07731	102.515
	± 0.00082	± 0.00038	± 0.00020	± 0.024
1.517	4.90452	4.56850	1.07355	102.363
	± 0.00131	± 0.00039	± 0.00030	± 0.032
1.682	4.90348	4.56815	1.07341	102.326
	± 0.00067	± 0.00030	± 0.00016	± 0.019
1.814	4.90182	4.57245	1.07203	102.484
	± 0.00251	± 0.00116	± 0.00061	± 0.074
1.907	4.90115	4.56926	1.07264	102.264
	± 0.00276	± 0.00077	± 0.00063	± 0.021
1.934	4.89601	4.56920	1.07152	102.217
	± 0.00190	± 0.00044	± 0.00043	± 0.044
1.991	4.89246	4.57191	1.07011	102.263
	± 0.00068	± 0.00035	± 0.00017	± 0.022
2.115	4.89282	4.57064	1.07049	102.215
	± 0.00103	± 0.00052	± 0.00026	± 0.032
2.196	4.89750	4.57126	1.07137	102.340
	± 0.00112	± 0.00058	± 0.00028	± 0.035
2.281	4.89268	4.57139	1.07028	102.245
	± 0.00126	± 0.00024	± 0.00028	± 0.028
2.399	4.89020	4.57269	1.06944	102.251
	± 0.00077	± 0.00040	± 0.00019	± 0.024
2.482	4.88788	4.57317	1.06882	102.224
	± 0.00103	± 0.00033	± 0.00024	± 0.026
2.983	4.87703	4.57645	1.06568	102.144
	± 0.00047	± 0.00034	± 0.00013	± 0.018
3.927	4.85552	4.58397	1.05924	102.028
	± 0.00121	± 0.00043	± 0.00028	± 0.032
5.007	4.83204	4.59129	1.05244	101.859
	± 0.00061	± 0.00030	± 0.00015	± 0.018
7.009	4.71377	4.61252	1.02195	100.287
	± 0.00238	± 0.00459	± 0.00114	± 0.206

TABLE 4.5

LATTICE PARAMETERS FOR THE SYSTEM In-Bi

Composition at.% Bi	c $\mathring{A}$	a $\mathring{A}$	$c/_a$	ca^2 $\mathring{A}^3$
1.000	4.95629	4.55547	1.08799	102.855
	± 0.00062	± 0.00044	± 0.00017	± 0.024
2.001	4.97563	4.55299	1.09283	103.143
	± 0.00119	± 0.00070	± 0.00031	± 0.040
2.996	4.99220	4.55325	1.09641	103.499
	± 0.00143	± 0.00116	± 0.00042	± 0.060
3.996	4.99692	4.54096	1.10041	103.038
	± 0.00891	± 0.00594	± 0.00243	± 0.326
5.006	5.03665	4.55123	1.10666	104.328
	± 0.00551	± 0.00246	± 0.00135	± 0.160
6.002	5.03585	4.54976	1.10684	104.244
	± 0.00366	± 0.00286	± 0.00107	± 0.152
7.002	5.02687	4.54455	1.10613	103.820
	± 0.00821	± 0.00528	± 0.00222	± 0.295
8.002	5.02529	4.54398	1.10592	103.761
	± 0.00205	± 0.00219	± 0.00070	± 0.108
9.001	5.02947	4.53848	1.10818	103.596
	± 0.00451	± 0.01269	± 0.00325	± 0.586
10.004	5.00550	4.55122	1.09982	103.682
	± 0.00572	± 0.00220	± 0.00137	± 0.155

TABLE 4.6

LATTICE PARAMETERS FOR THE SYSTEM In-Li

Composition at.% Li	c $\mathring{A}$	a $\mathring{A}$	$c/_a$	ca^2 $\mathring{A}^3$
1.011	4.93029	4.55933	1.08136	102.488
	± 0.00098	± 0.00079	± 0.00029	± 0.041
2.170	4.93060	4.56037	1.08118	102.541
	± 0.00072	± 0.00050	± 0.00020	± 0.027
2.997	4.93134	4.56116	1.08116	102.592
	± 0.00150	± 0.00079	± 0.00038	± 0.047
3.519	4.93259	4.56018	1.08167	102.574
	± 0.00090	± 0.00061	± 0.00025	± 0.033
4.810	4.93072	4.56139	1.08097	102.590
	± 0.00068	± 0.00034	± 0.00017	± 0.021
6.161	4.93136	4.55998	1.08144	102.540
	± 0.00094	± 0.00083	± 0.00028	± 0.042
6.904	4.93027	4.56101	1.08096	102.563
	± 0.00088	± 0.00047	± 0.00022	± 0.028

MEASUREMENT OF SUPERCONDUCTING TRANSITION TEMPERATURES

The automatic, simultaneous registering of the secondary coil signal and the temperature in the T_c probe, using a twin-pen chart recorder, proved very satisfactory, as illustrated by the typical chart record shown in Figure (4.2). The beginning and end of the transition are not clearly defined in all cases, as there is often an asymptotic approach to the normal or superconducting states. The bulk of the transition in almost all cases, however, is very sharp, providing a well-defined mid-point, which was, therefore, taken as the transition temperature.

The values of T_c obtained for the indium alloys are listed in Tables 4.7 to 4.12 with the breadth of transition. These results are compared graphically, with those published by various authors and also with the X-ray results, in the following sections.

Since the alloys were not chemically analysed there may on occasions be some doubt as to the composition. It is necessary, therefore, to check carefully that unusual or anomalous behaviour in the experimental plots, is not due to the wrong composition assigned to one or two specimens. The procedure adopted is one of checking on internal consistency. The suspect point is taken and shifted parallel to the composition axis until it fits smoothly with the other data. This could for example be done with a plot of T_c. An identical composition shift is then given to the same specimen in the plots of the other variables (a, c, c/a, ca^2). If any one of these shifted points does not then fit smoothly with the remaining data then the measurements are not consistent with the same composition shift. Internal consistency does not necessarily mean the stated composition is in error. If, however, the measurements are accurate, lack of consistency must imply that the anomalous behaviour is real.

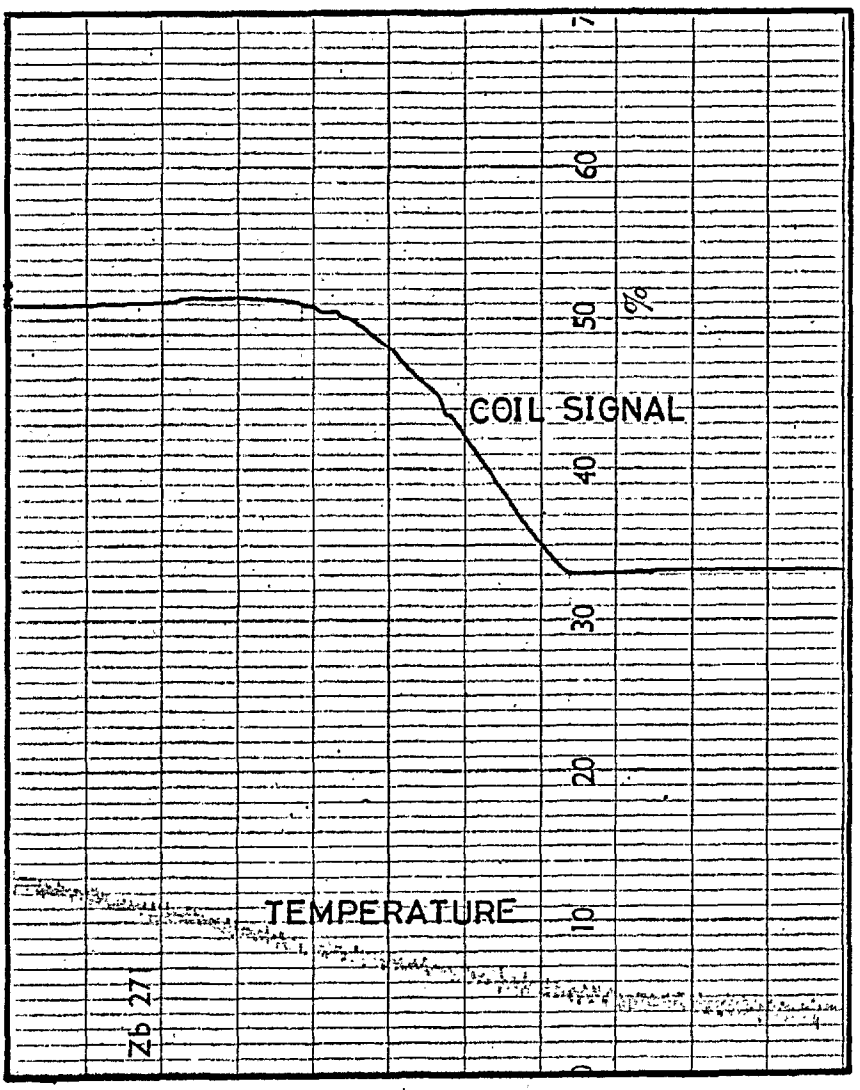

Figure 4.2 A typical superconducting transition, as registered on the twin pen recorder.

TABLE 4.7

TRANSITION TEMPERATURE T_c FOR In-Pb ALLOYS

Composition at.% Pb	T_c ^oK	Breadth of transition ^oK
11.504	4.670	0.04
12.002	4.825	0.06
12.501	4.915	0.07
13.000	5.105	0.05
13.061	5.010	0.10
13.501	4.955	0.07
13.994	5.045	0.10
14.500	5.080	0.02
15.000	5.170	0.03
15.322	5.035	0.02
17.251	5.154	0.04
18.905	5.210	0.03
21.209	5.355	0.10
24.821	5.550	0.04
27.043	5.640	0.03
28.924	5.160	0.05
30.870	5.225	0.03
32.997	5.182	0.01

TABLE 4.8

TRANSITION TEMPERATURE T_c FOR In-Sn ALLOYS

Composition at.% Sn	T_c ^oK	Breadth of transition ^oK
0.997	3.440	.006
2.002	3.518	.025
2.524	3.590	.015
3.002	3.647	.012
4.000	3.738	.013
6.000	3.955	.015
8.000	4.265	.005
10.000	4.744	.021
11.002	4.883	.024
12.010	5.365	.025
12.997	5.835	.060
13.983	5.420	.077
15.996	5.685	.030
17.988	5.855	.020

TABLE 4.9

TRANSITION TEMPERATURE T_c FOR In-Hg ALLOYS

Composition at.% Hg	T_c °K	Breadth of transition °K
0.467	3.370	.011
0.753	3.345	.012
1.008	3.334	.011
1.052	3.337	.012
1.187	3.327	.010
1.756	3.319	.015
1.763	3.336	.009
1.921	3.330	.007
2.000	3.342	.016
2.489	3.364	.012
3.000	3.360	.011
3.477	3.376	.011
4.000	3.382	.004
5.000	3.376	.035
6.000	3.430	.020
	3.415	.022
6.156	3.445	.030
7.000	3.427	.032
7.500	3.611	.021
8.000	3.530	.029
9.000	3.284	.087
11.162	3.294	.017
12.008	3.436	.027

TABLE 4.10

TRANSITION TEMPERATURE T_c FOR In-Cd ALLOYS

Composition at.% Cd	T_c ^oK	breadth of transition ^oK
0.943	3.344	.019
0.976	3.338	.026
1.517	3.296	.016
1.682	3.280	.013
1.814	3.280	.012
1.907	3.280	.018
1.934	3.274	.006
1.991	3.271	.022
2.115	3.267	.019
2.196	3.259	.021
2.281	3.273	.013
2.399	3.275	.018
2.482	3.268	.009
2.983	3.252	.008
3.927	3.236	.009
5.007	3.225	.014
6.073	3.216	.036
6.480	3.214	.018
7.009	3.206	.014

TABLE 4.11

TRANSITION TEMPERATURE T_c FOR In-Bi ALLOYS

Composition at.% Bi	T_c ^oK	Breadth of transition ^oK
1.000	3.430	.015
2.001	3.879	.058
2.996	4.157	.038
5.006	4.557	.043
6.002	4.595	.120
7.002	4.755	.100
8.002	4.785	.080
9.001	4.890	.120
10.004	5.895	.125

TABLE 4.12

TRANSITION TEMPERATURE T_c FOR In-Li ALLOYS

Composition at.% Li	T_c ^oK	Breadth of transition ^oK
1.011	3.358	.028
2.170	3.352	.023
2.997	3.362	.016
3.519	3.355	.012
4.810	3.362	.016
6.161	3.357	.017
6.904	3.367	.012

THE INDIUM-LEAD ALLOYS

The parameters and volume of the FCT cell, as a function of Pb composition are shown in Fig. (4.4). Since there are no published lattice parameters at 78°K, direct comparison is not possible, but the room temperature Debye-Scherrer results of Moore et al (1955) and Tyzack and Raynor (1954) are included in the figure. The present results can be seen to follow much the same pattern as the room temperature results.

The axial ratio values for the In-Pb alloys are plotted in Fig. (4.4) along with the transition temperatures T_c. On the latter plot some points due to Merriam (1963) and Russell (1966), in the region below 14.5 at.% Pb are superimposed. The reasonably close agreement between these results indicates that the present measurements of T_c above 4.2°K are reliable despite the experimental difficulties discussed in section 3.4. The 14 and 14.25 at.% Pb results of Merriam lie on a linear extrapolation of his results for more dilute alloys, whereas the present results show a distinct fall in T_c at 13 at.% Pb which is indicative of a phase boundary at this composition. This is also just the composition at which the axial ratio discontinuously drops. The diffraction profiles in this region, however, become very distorted and the behaviour of T_c is also somewhat erratic. This suggests that between 13 and 15 at.% Pb there is a region of uncertainty, possibly due to the strain field resulting from a mis-match of phases. No diffraction peaks from a second phase were observed, however.

The T_c values show a marked discontinuity between 27 and 29 at.% Pb suggesting that the boundary, between the tetragonal β phase and the lead-based primary solid solution, lies at about 28 at.% Pb. The lattice parameter results, however, indicate a phase change between 31 and 32 at.% Pb. The difference between the two may be due to cold working the X-ray specimens at 78°K to make the powders. The deterioration in the quality of the peaks suggests a strain field possibly associated with a martensite.

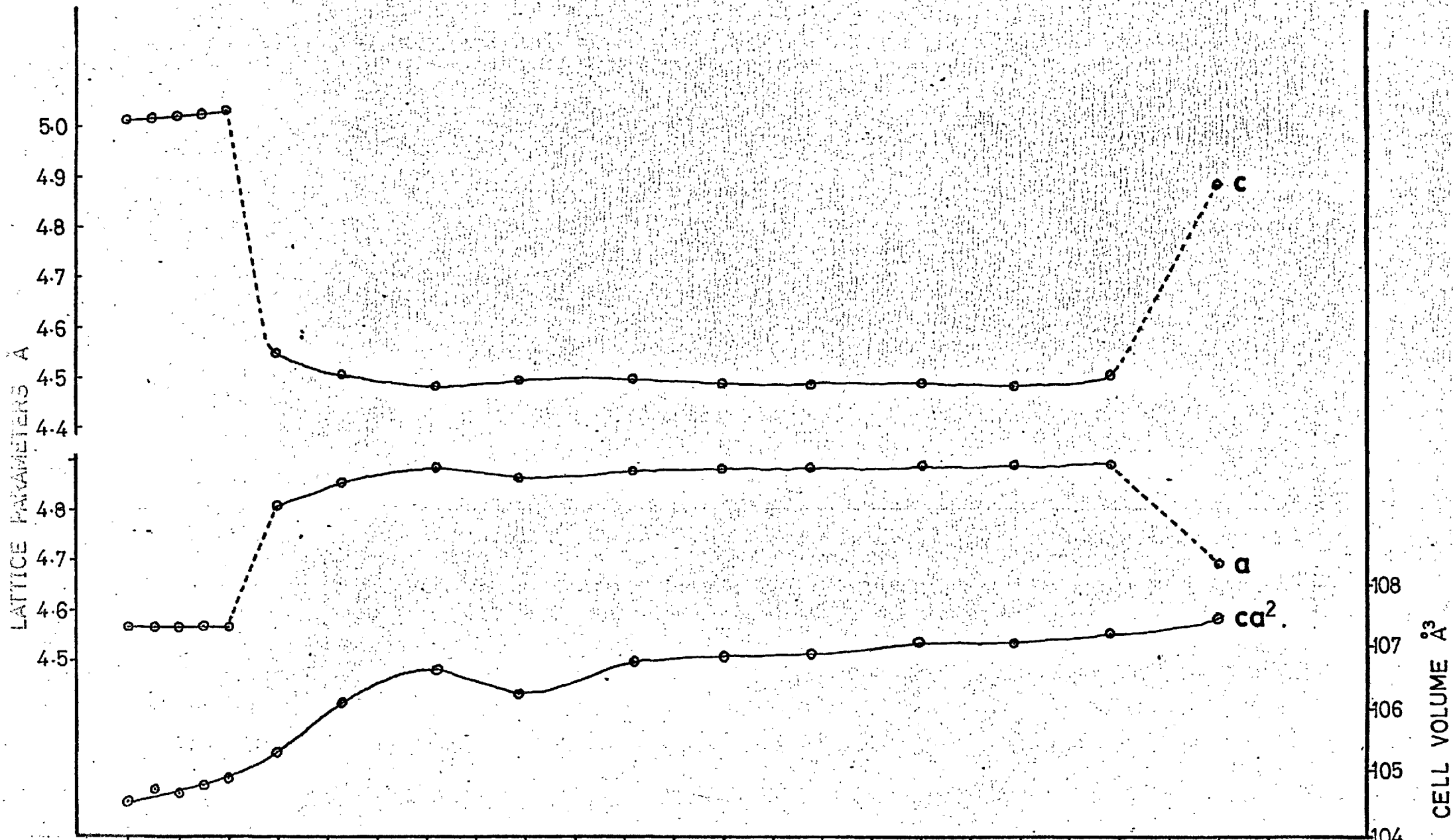

Figure 4.3 The lattice parameters of the indium-lead alloys as a function of Pb composition.

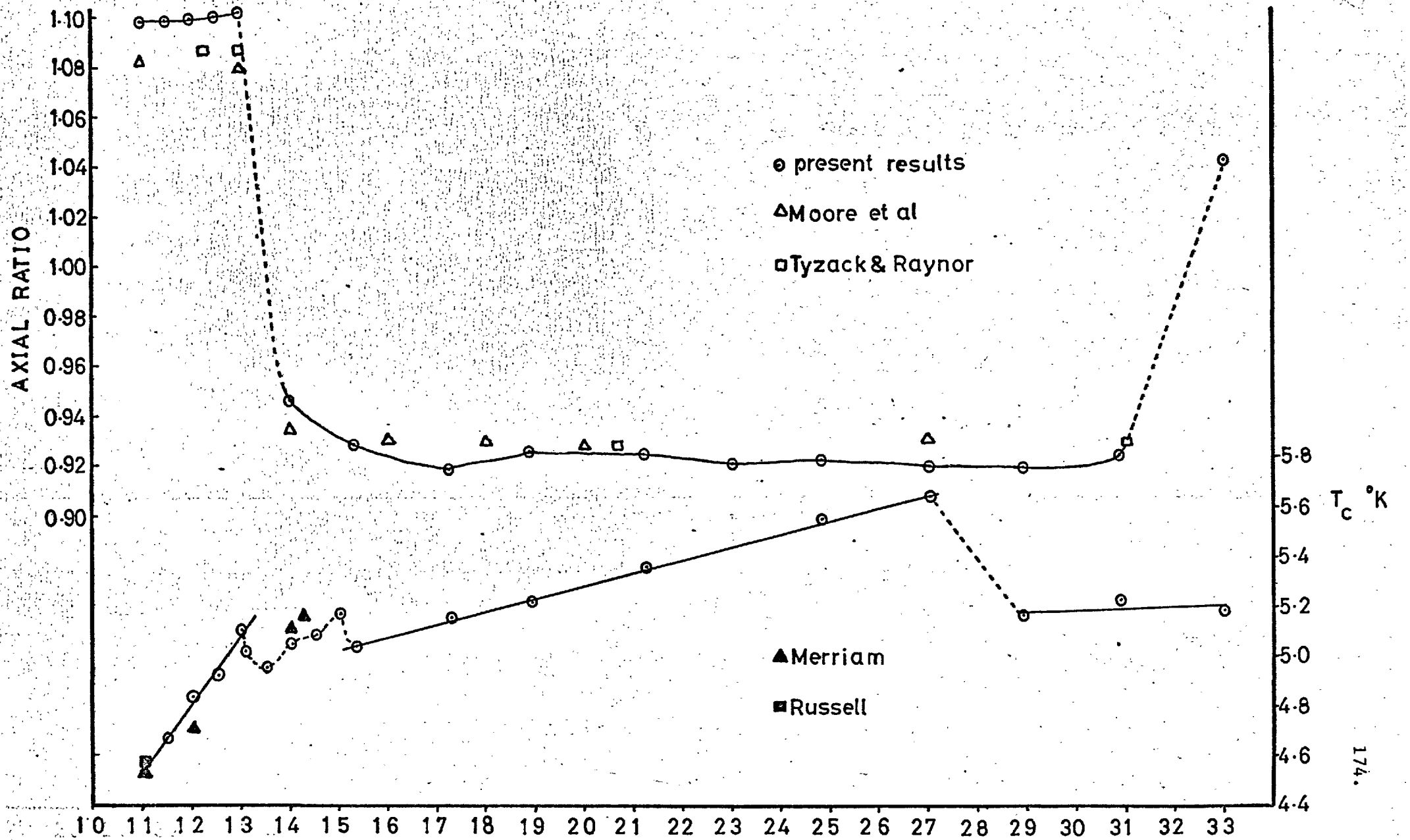

Figure 4.4 The axial ratio of the indium-lead alloys, as a function of Pb composition, compared with T_c.

It is surprising to note that the rather diffuse diffraction pattern of the only specimen in, what should be the Pb solid solution, can be indexed as tetragonal, with an axial ratio of 1.04, rather than cubic.

The axial ratios in the indium solid solution at 78°K are greater than the published room temperature values, as was found for pure indium by Barrett (1962) and Graham, Moore and Raynor (1955). Furthermore the axial ratios in the β phase alloys are lower than the room temperature values, that is they also deviate more from cubic symmetry at lower temperatures. It appears that the tendency to distortion (for axial ratios both greater and less than unity) increases with decreasing temperature.

THE INDIUM-TIN ALLOYS

The lattice parameters and FCT cell volume are plotted, for In-Sn alloys, in Fig. (4.5) along with the room temperature Debye-Scherrer results of Fink et al (1945). Only specimens in the indium solid solution were measured, the profiles in the 16 and 18 at.% Sn specimens being too distorted for measurement.

The axial ratios are plotted along with the T_c values in Fig. (4.6) and superimposed on the latter plot are the published results of Wernick and Matthias (1961) and Merriam and Von Herzen (1963). The values of Wernick and Matthias differ significantly from both the present values and those of Merriam and Von Herzen. This is probably due to Wernick and Matthias failing to anneal their alloys (see Merriam and Von Herzen).

In the low Sn composition region most of the data points of Merriam and Von Herzen are in exact coincidence with the present results and, hence, have been left off the plot. There is very good agreement in general, but the two sets of results diverge above 11 at.% Sn. Whilst the boundary between the In solid

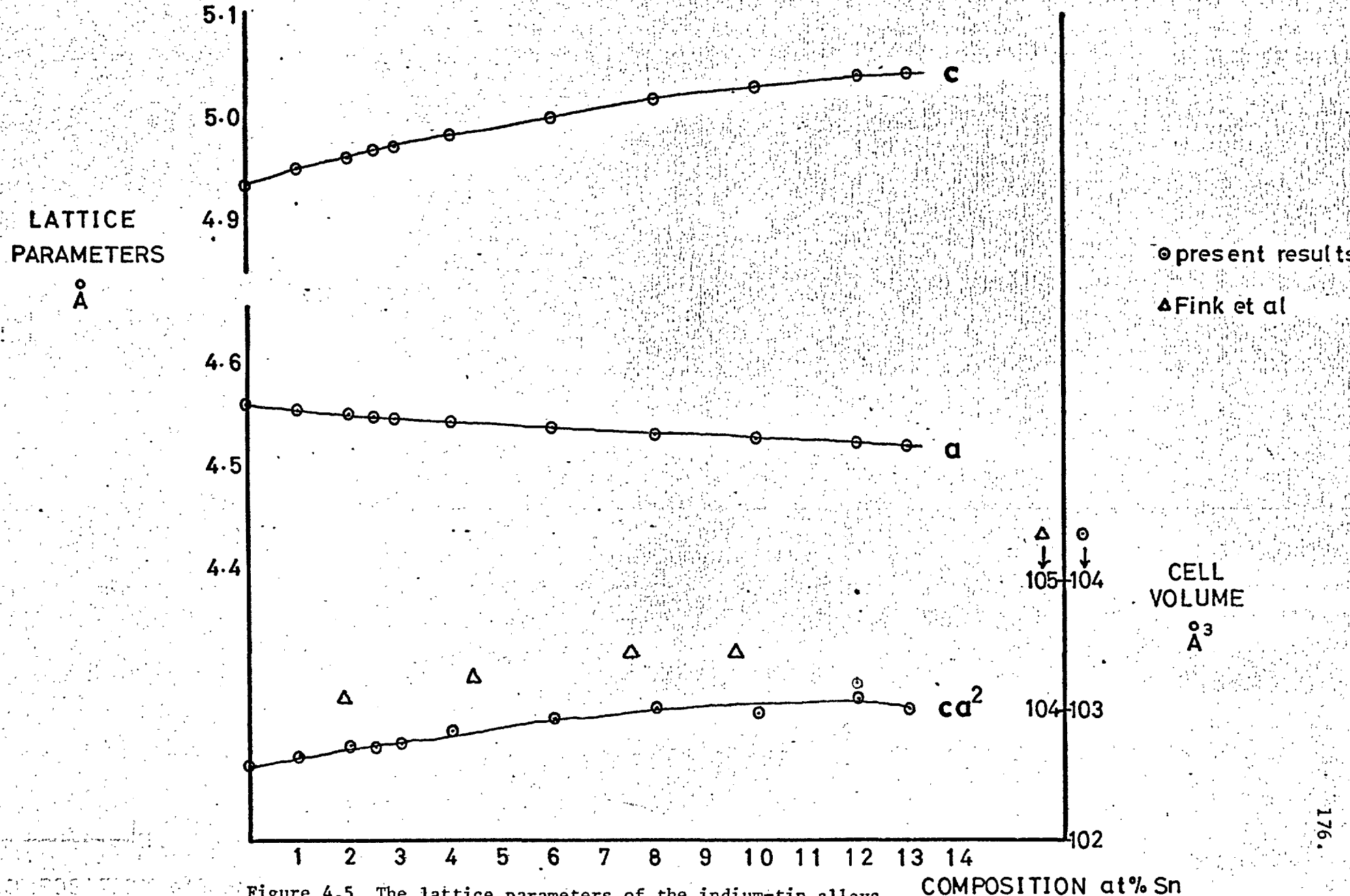

Figure 4.5 The lattice parameters of the indium-tin alloys as a function of Sn composition.

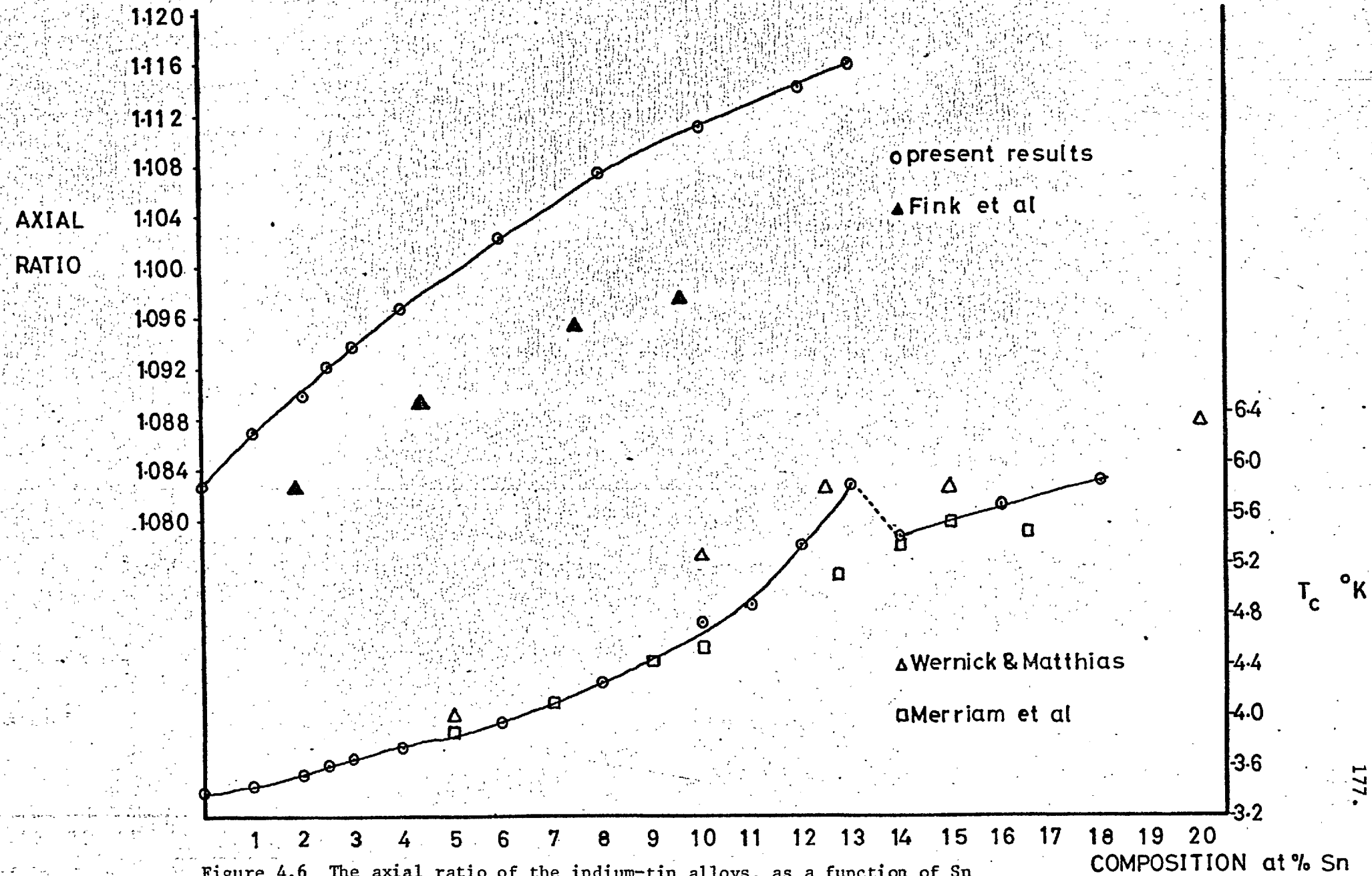

Figure 4.6 The axial ratio of the indium-tin alloys, as a function of Sn composition, compared with T_c.

solution and the β phase appears to lie at 15.5 at.% Sn in the Merriam and Von Herzen paper, the present results indicate a boundary between 13 and 14 at.% Sn.

The axial ratio steadily increases to a maximum of 1.116 at 13 at.% Sn which is the greatest tetragonal distortion of all the indium alloys measured. The 13 at.% Sn appears, thus, to be still in the indium solid solution according to lattice parameter measurements. The very marked deterioration in the peak quality in the 13 at.% Sn and higher Sn composition alloys again suggests the possibility of a martensitic transformation. The axial ratios at 78°K are, again, consistently greater than the published room temperature values.

THE INDIUM-MERCURY ALLOYS

The lattice parameters and cell volume for the In-Hg alloys are plotted in Fig. (4.7) whilst the axial ratios are compared with T_c in Fig. (4.8). Room temperature lattice parameters due to Tyzack and Raynor (1954) and the T_c measurements of Reeber (1960) and Merriam, Jensen and Coles (1963) are included on the plots.

The downward trend in axial ratio with increasing Hg composition is confirmed by the present results. The tetragonal phase extends about 1 at.% Hg further than in the case of Tyzack and Raynor and the tetragonal-cubic discontinuity is somewhat less pronounced. Apart from slight differences in the region of 8 at.% Hg the present T_c results are in good agreement with those of Merriam et al (1963) and act as a more detailed complement to them. The only marked deviation from the low Hg composition values of Reeber (1960) occurs at 5 at.% Hg, the difference being of the order of 50 millidegrees.

Coles et al (1962) showed that at 7 at.% Hg a specimen which was two-phase at room temperature, was wholly tetragonal at 195°K and proposed that a martensitic transformation must have occurred. The

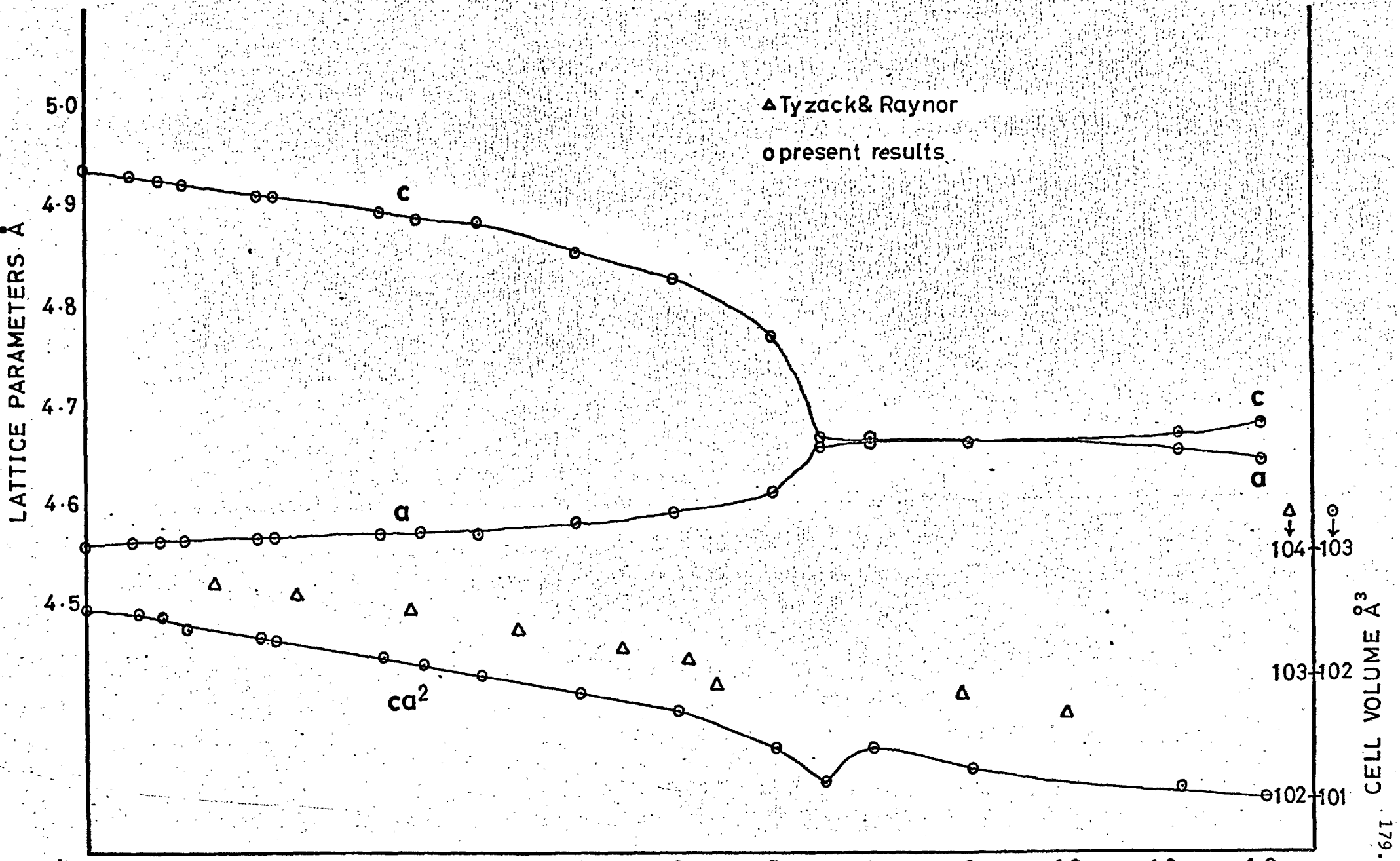

Figure 4.7 The lattice parameters of indium-mercury alloys as a function of Hg composition.

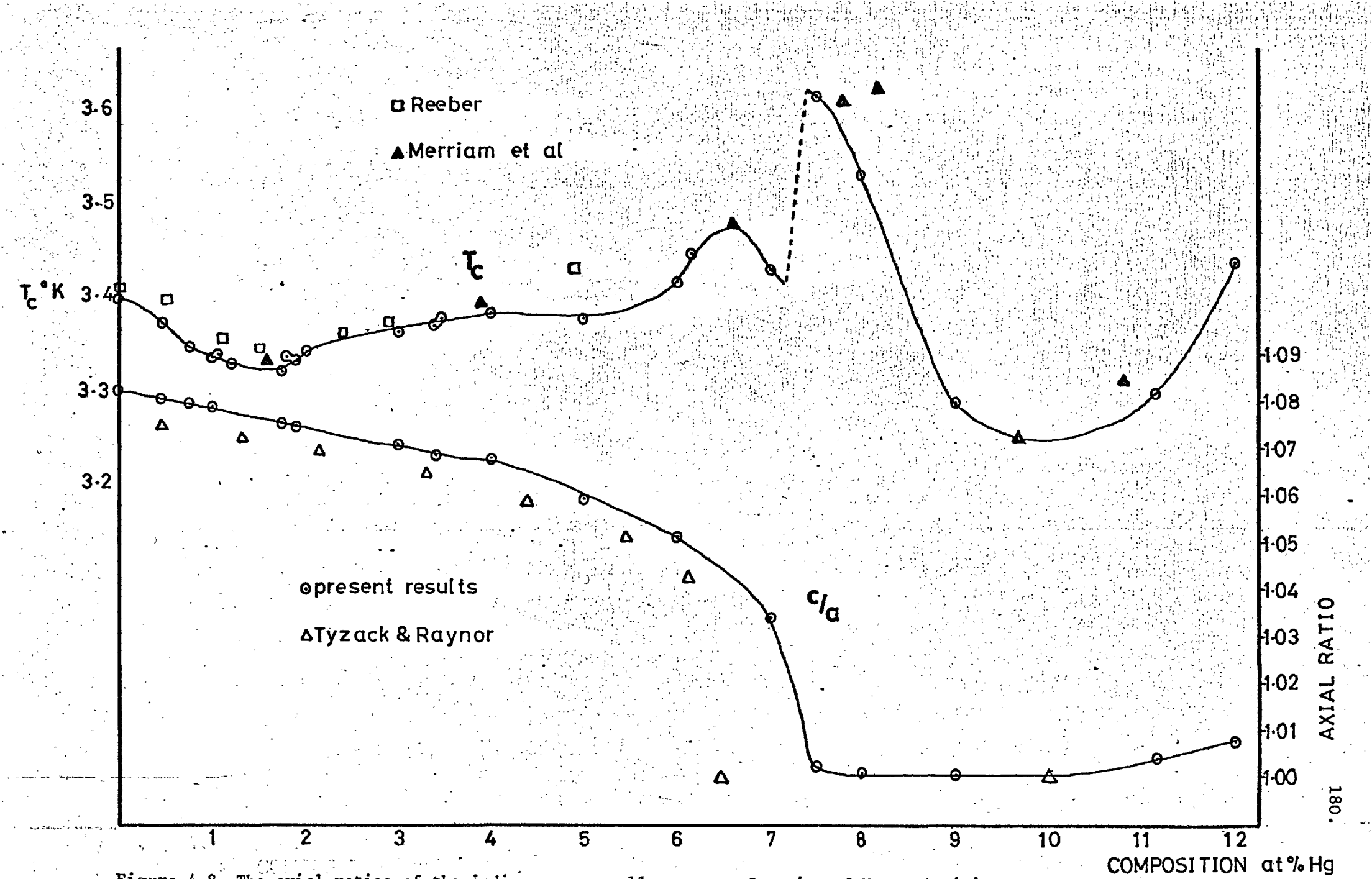

Figure 4.8 The axial ratios of the indium-mercury alloys, as a function of Hg composition, compared with T_c.

T_c data of Coles et al also indicated (or was interpreted as indicating) that at 8 at.% Hg alloys were still tetragonal. If the present lattice parameter results are used in conjunction with the room temperature results of Tyzack and Raynor then the 7 at.% Hg specimen appears to have suffered a martensitic transformation on cooling to 78°K. There were, however, only slight signs of broadening (at 7 at.% Hg) of the diffraction profiles. Furthermore, more specimens are used in the region of the phase boundary than were measured by Coles et al and the fixing of the phase boundary is not quite so clear-cut. Coles et al show a continuous rise in T_c from about 2 to about 8 at.% Hg followed by a drop of about 0.4°K by the next alloy at about 9.5 at.% Hg. This apparent discontinuity was taken as the phase boundary. The present results show the same rise in T_c from about 2 at.% Hg but a small drop occurs at 7 at.% Hg followed by a discontinuous rise at 7.5 at.% Hg. The three points, at 7.5, 8 and 9 at.% Hg, indicate a rapid change of T_c but not necessarily a discontinuous one. If all experimental points are reliable, the more obvious phase boundary lies in the region 7 - 7.5 at.% Hg. The difference in interpretation rests principally on the correctness of the 7% Hg point, but this does not seem to be in error. The lattice parameter results set the composition at the calculated value without ambiguity and the T_c was re-measured on a quite separate run with only a six millidegree difference of reading.

An interesting feature of the lattice parameter plots is the marked dip in the atomic volume between 6 and 8 at.% Hg. On both sides of this dip the data lie on the same (almost) straight line. Atomic volume calculations, from the data of Tyzack and Raynor, also show a sharp dip (only the one point, at 6.5 at.% Hg, is available).

Another feature of interest is that the peaks start to broaden again at 11 at.% Hg and may be indexed as slightly tetragonal.

THE INDIUM-CADMIUM ALLOYS

The lattice parameters and FCT cell volume are plotted in Fig. (4.9) and the axial ratio and T_c shown as functions of composition in Fig. (4.10). The general trends in the lattice constants, axial ratio and cell volume are rather similar to those of the In solid solution in In-Hg. The highest composition alloy measured (7 at.% Cd) appears to be still in the In solid solution.

The T_c values of Merriam are plotted along with the present results, which are consistently lower than the former except for the first 1 at.% Cd. The difference probably lies in the thermometry, since Merriam measured the temperature of the liquid helium using a manometer calibrated at the pure indium point (T_c taken as 3.406) whilst the germanium thermometer used here was calibrated, over all the required temperature range ($2.1^{\circ}K \rightarrow 18^{\circ}K$) against a standard (Texas Instruments) thermometer. Apart from this difference (which is small ~30 millidegrees) the T_c trends are in good agreement with those of Merriam, especially near 2 at.% Cd. Merriam's results indicate a discontinuity somewhere between 6% and 7.5% Cd whilst the present results show continuity up to 7 at.% Cd. Since the agreement between the two sets of values is good, it seems reasonable to combine them in order to set the $\alpha_c - \alpha_t$ phase boundary between 7 and 7.5 at.% Cd.

The most interesting feature of the graphs is the wiggle in the region of 2 at.% Cd. This was first observed by Merriam in his T_c results. The region has been examined in more detail here and, although somewhat sharper in this case, the form of the wiggle in T_c is reproduced more-or-less exactly. The kink is shown in magnification in the insert to Fig. (4.10). The room temperature Debye-Scherrer results of Ridley (1967) show an inflexion in the slope of the lattice parameter and axial ratio plots rather than a wiggle and, furthermore show no detectable change, at all, in the slope of the atomic volume plot. The present results show a distinct wiggle in every single plot. As was pointed out in Chapter 1

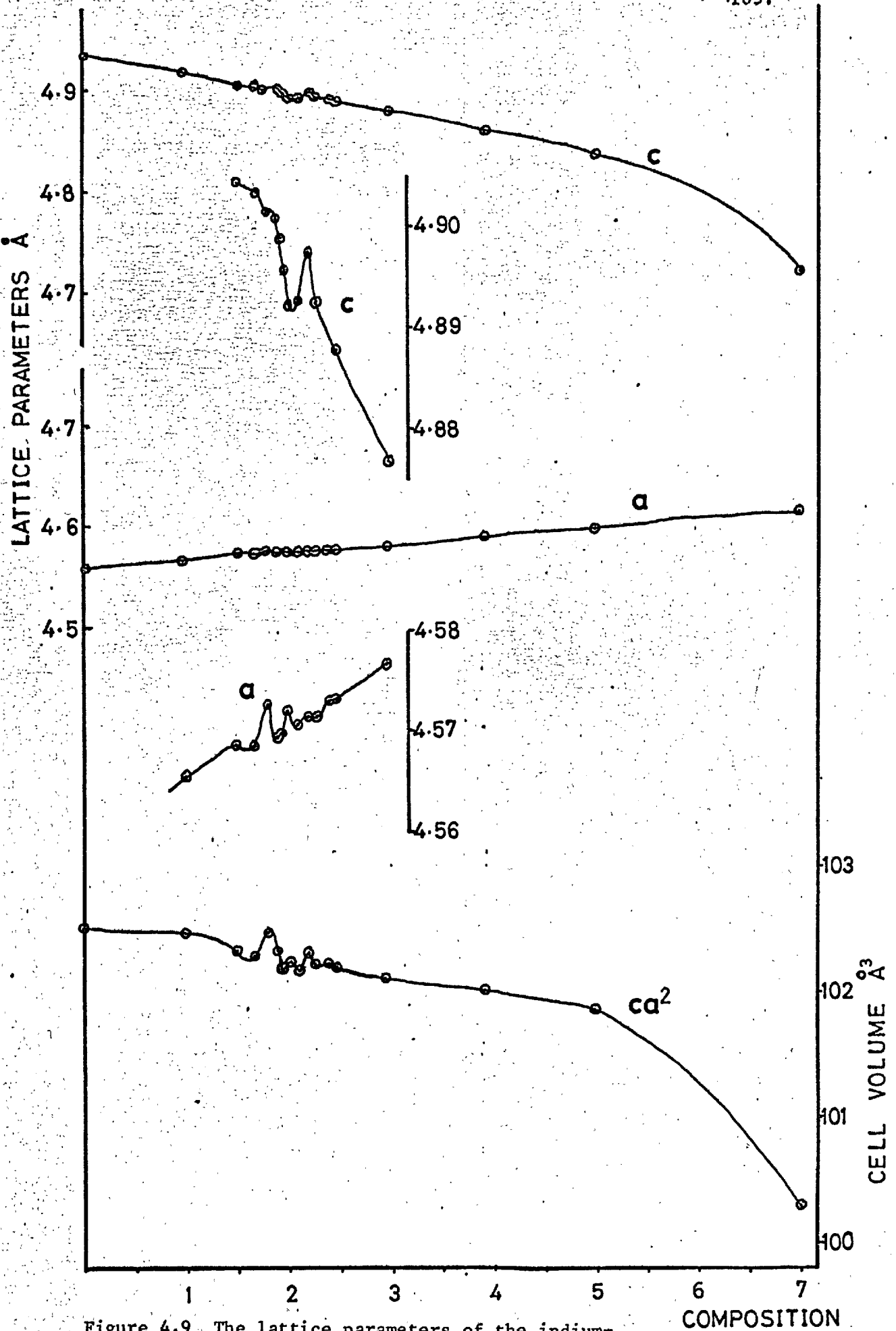

Figure 4.9 The lattice parameters of the indium-cadmium alloys as a function of Cd composition. at% Cd

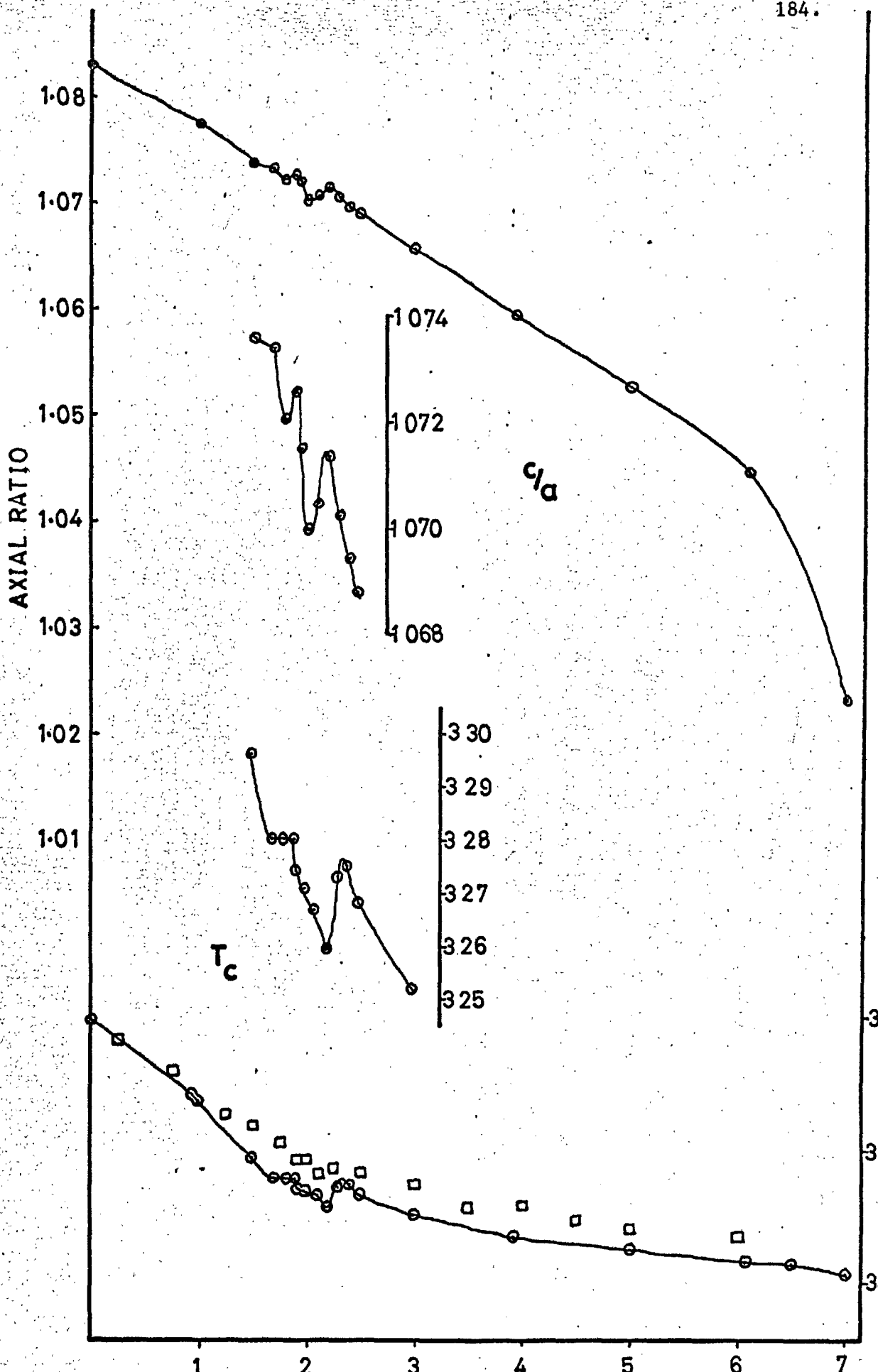

Figure 4.4 The axial ratio of the indium cadmium alloys, as a function of Cd composition, compared with T_c.

the X-ray data of Merriam (1966) was criticised precisely because the wiggles in the lattice parameter plot implied a wiggle in the atomic volume plot. It seems necessary, therefore, to justify the reality of the presently observed wiggle.

First of all the standard deviations of the least square calculations are of the order of 0.02 $\mathring{A}^3$ in the FCT cell volume whereas the amplitude of the wiggle is of the order of 0.3 $\mathring{A}^3$. In the T_c measurement the reproducibility was generally of the order of 4 or 5 millidegrees while the amplitude of the wiggle in T_c is about 18 millidegrees. It is reasonable, therefore, to suppose that the readings are the correct values for the specimens. The only other possible source of error is in the estimate of the composition. In order to check on this it is necessary to employ the internal consistency test discussed at the beginning of this chapter. As an example take the 1.814 at.% Cd point and find a composition where it fits smoothly with the rest of the atomic volume data. The necessary shift is to the left to about 1.1 at.% Cd. If the same procedure is followed using the plot of the a parameter then the necessary shift is to the right, to 2.4 at.% Cd. Similarly on the c plot the shift would be to the left, to 1.6 at.% Cd and on the T_c plot to the right, to about 2.0 at.% Cd. These are all inconsistent and similar inconsistencies arise when using other points in the wiggle so that the wiggle cannot be annihilated by a simple displacement along the composition axis.

THE INDIUM-BISMUTH ALLOYS

The lattice parameters for the In-Bi alloys are plotted as functions of composition in Fig. (4.11) along with the room temperature results of Peretti and Carapella (1949). Beyond 3 at.% Bi, Peretti and Carapella report the presence of a two phase region. The present investigation was unable to show this, but the condition of the profiles, after 3 at.% Bi, rapidly deteriorated as is evinced by the large increase in the standard deviations, shown as error limits in

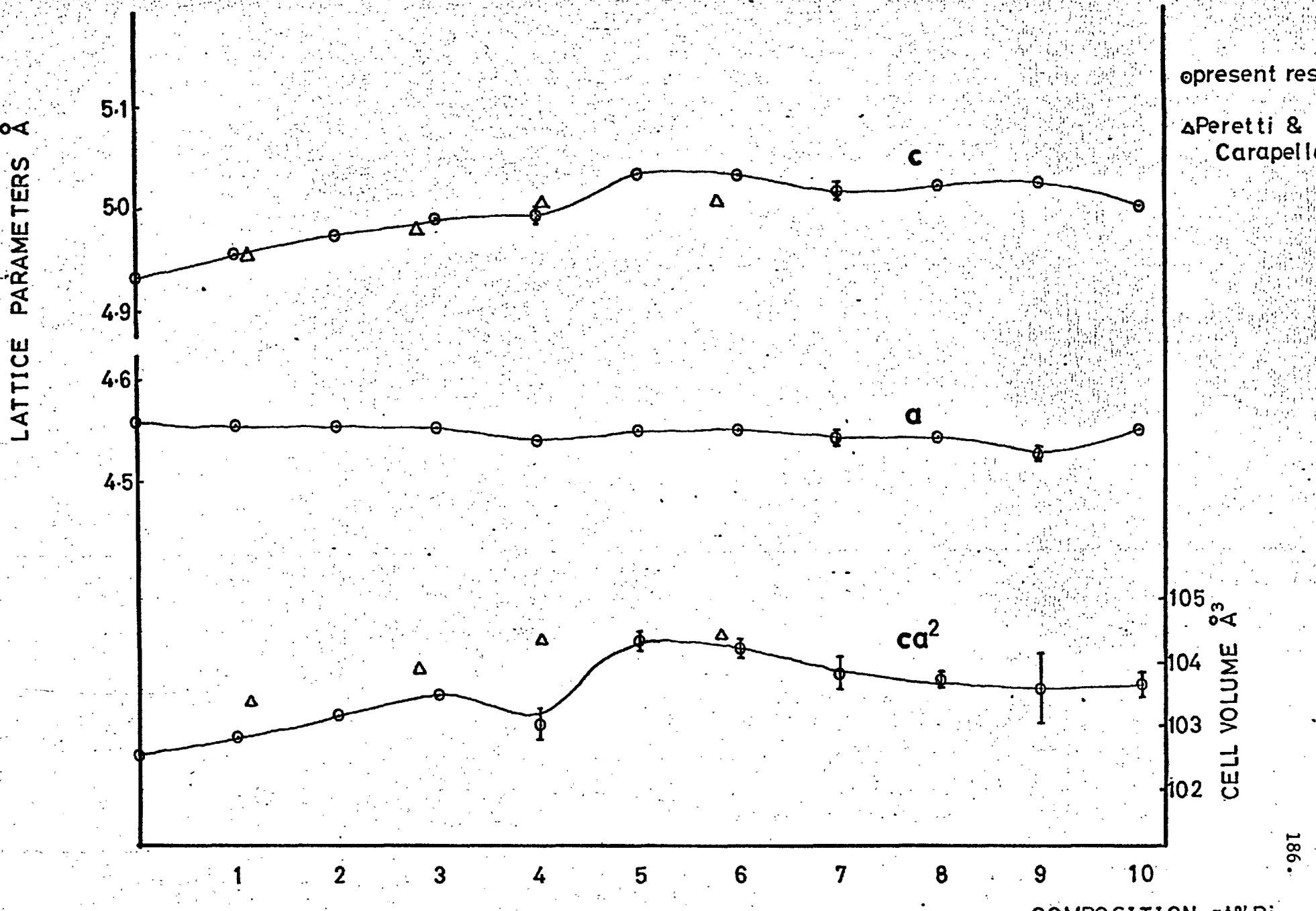

Figure 4.11 The lattice parameters of the indium-bismuth alloys as a function of Bi composition.

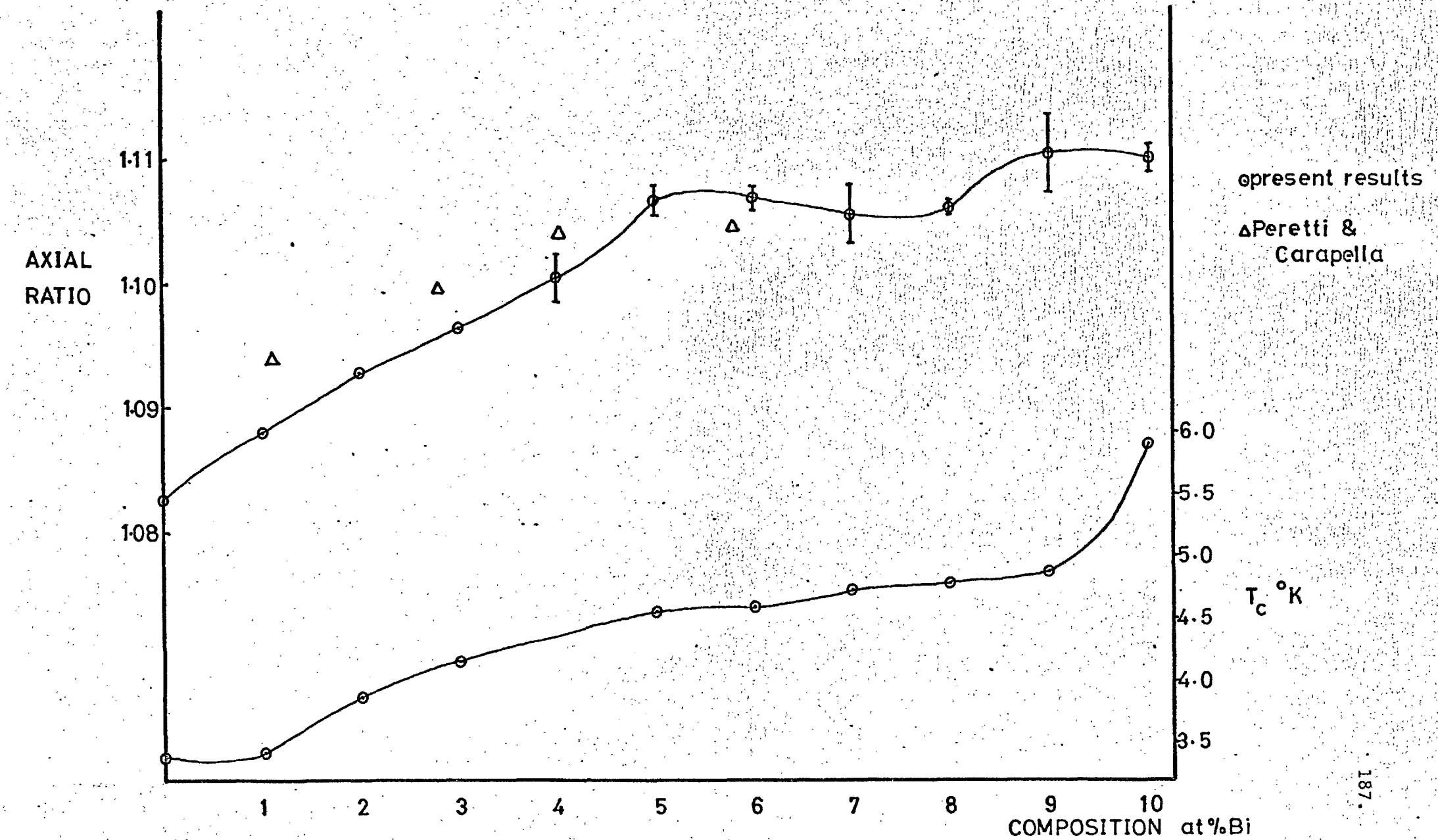

Figure 4.12 The axial ratio of the indium-bismuth alloys, as a function of Bi composition, compared with T_c.

Fig. (4.11) and also in Fig. (4.12) which shows the axial ratios and T_c.

Since no T_c results on this system have been reported hitherto, no comparison can be afforded. The sudden rise in T_c at 10 at.% Bi might indicate a phase boundary but this does not appear to be borne out by the lattice parameter results. The axial ratio increases steadily up to 5 at.% Bi followed by a levelling off and slight decline up to 8 at.% Bi, after which another increase is observed. The atomic volume shows a general rise to about 5 at.% Bi followed by a steady decline to the limit of measurement at 10 at.% Bi. The 4 at.% Bi specimen appears to be somewhat anomalous on the atomic volume plot, although it fits smoothly into the axial ratio plot so that it does not appear likely that the composition is incorrect. One of the points of Peretti and Carapella is at 4% Bi and does not show a dip in atomic volume.

THE INDIUM-LITHIUM ALLOYS

Lattice parameters and cell volume for the In-Li alloys are shown in Fig. (4.13) whilst the axial ratios and T_c values are plotted in Fig. (4.14). The lattice parameter, axial ratio and T_c plots are qualitatively identical - a small initial drop is followed by no further change in any of the properties. This apparent inertness most likely means that only a very small amount of lithium (< 1 at.%) dissolves in indium. The alloys would then have to be two phase in which case lines from the Li-In phase (see Fig. 1.12) should be present whereas in fact no other reflections were observed. Now Li has a very small atomic scattering factor; for example, at

$$\frac{\sin\theta}{\lambda} = 0.5\ \text{Å}^{-1}, \quad f_{Li} = 1.0 \quad \text{whilst} \quad f_{In} = 25.0.$$

When this factor is scaled down by the proportion of lithium in the alloys then the ratio of peak intensities for indium and lithium is at the very least 500:1 so that lithium reflections would almost certainly not be detected. Furthermore, since lithium is not superconducting, no second transition would be detected in the T_c measurements.

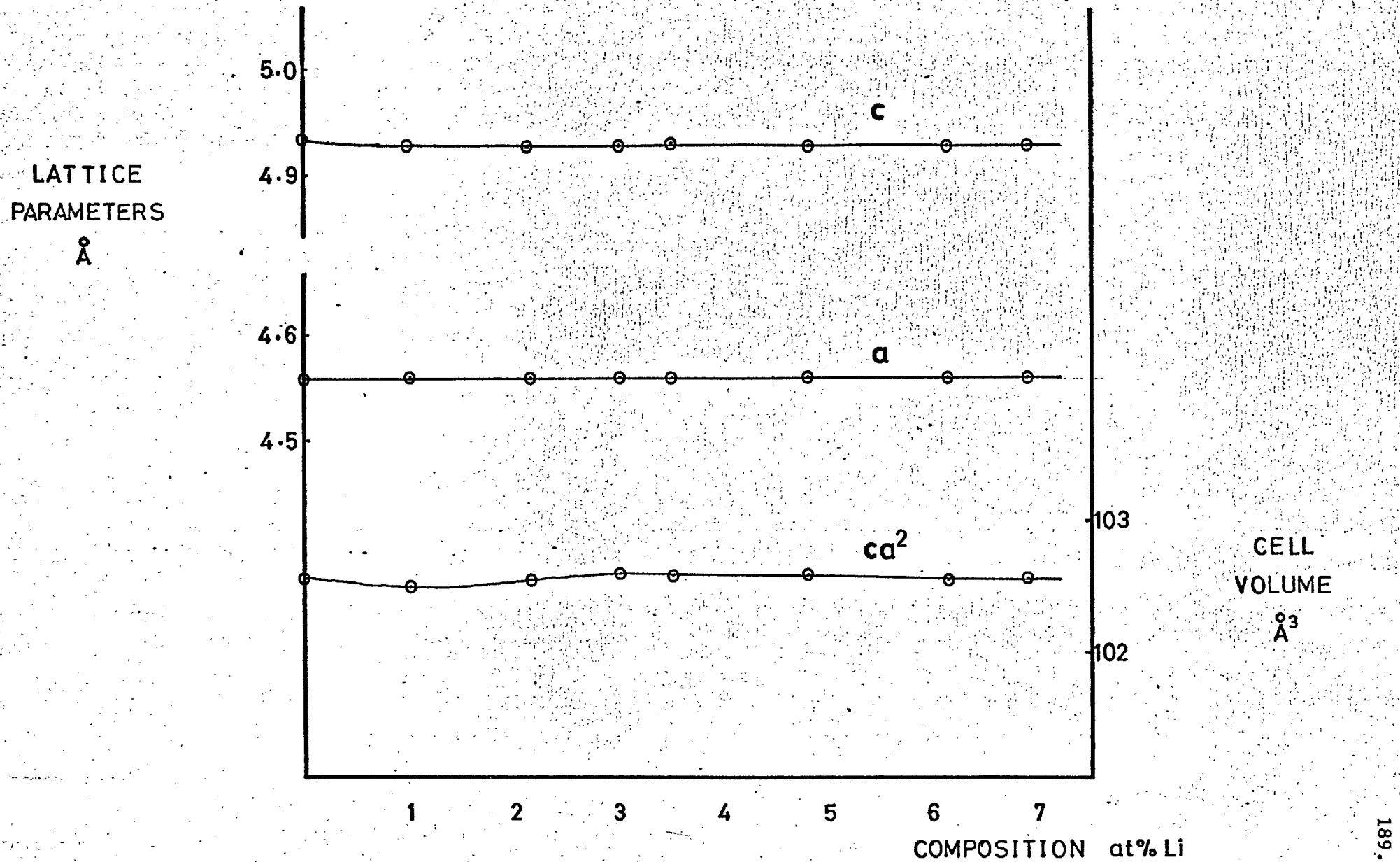

Figure 4.13 The lattice parameters of the indium-lithium alloys as a function of Li composition.

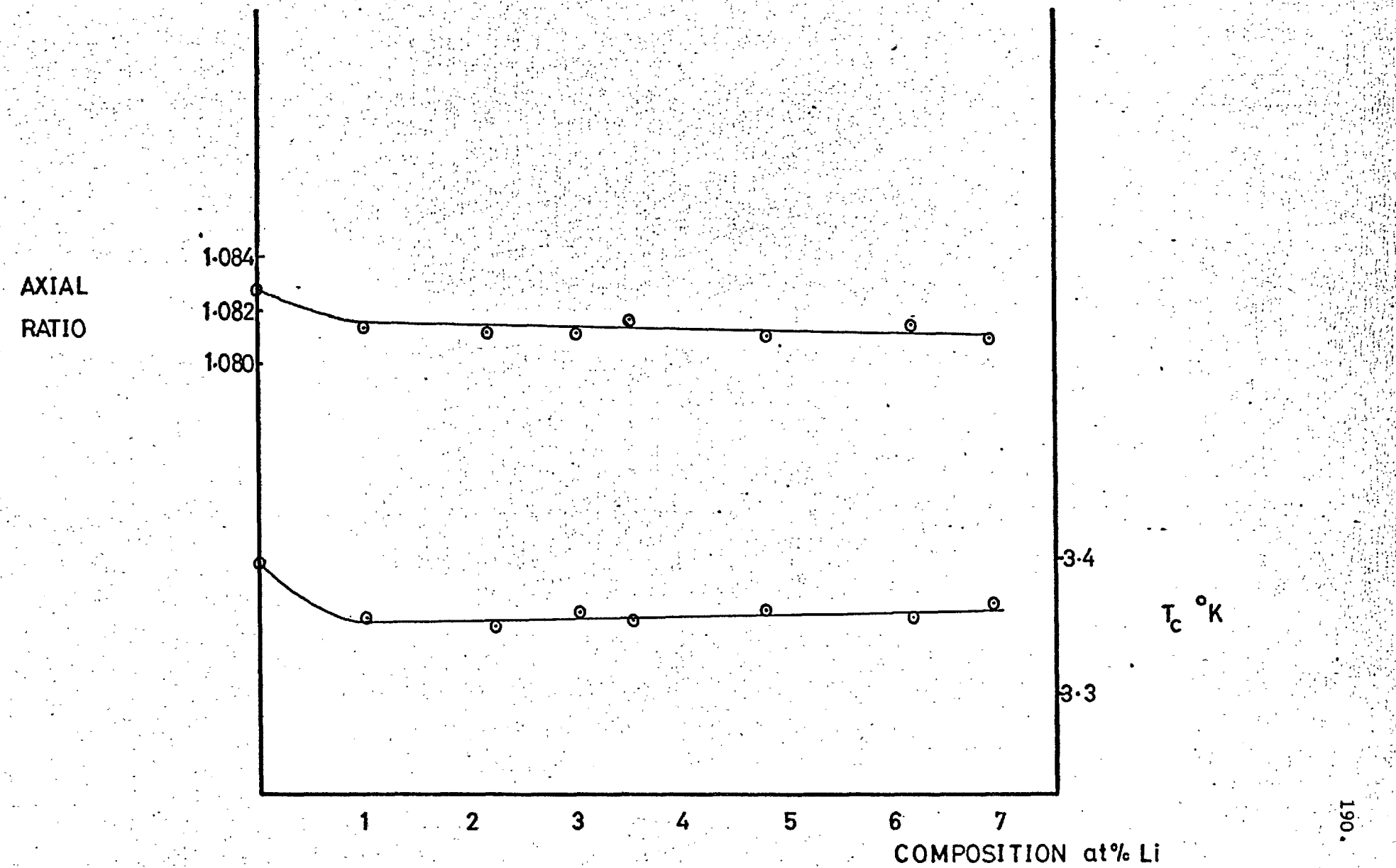

Figure 4.14 The axial ratio of the indium lithium alloys, as a function of Li composition, compared with T_c.

To be set against this conclusion are the results of Farrar and King (1968) for the system Cd-Li. The lattice parameter and axial ratio plots for this system are qualitatively the same as for In-Li (at the solvent-rich end). In the Cd-Li system, however, Farrar and King found that microhardness measurements showed a uniform increase of hardness up to 22 at.% Li (the limit of measurement) which they interpret as meaning that the Li must be going into solution.

REFERENCES

Barrett, C.S., (1962), Adv. X-ray Anal. 5, 33.

Coles, B.R., Merriam, M.F. and Fisk, Z., (1963), J. Less Common Metals, 5, 41.

Farrar, R.A. and King H.W., (1968), Metallography 1, 79.

Fink, C.G., Jette, E.R., Katz, S. and Schnettler, F.J., (1945), Trans. Electrochem. Soc. 88, 229.

Graham, J., Moore, A. and Raynor, G.V., (1955), J. Inst. Met. 84, 86.

Merriam, M.F., (1963), Phys. Rev. Letters., 11, 321.

Merriam, M.F., (1966), Phys. Rev., 44, 300.

Merriam, M.F., Jensen, M.A. and Coles, B.R., (1963), Phys. Rev. 130, 1719.

Merriam, M.F., and von Herzen, M., (1963), Phys. Rev. 131, 637.

Moore, A., Graham, J., Williamson, G.K. and Raynor, G.V., (1955), Acta Met. 3, 579.

Peretti, E.A. and Carapella, S.C., (1949), Tr. Am. Soc. Met., 41, 947.

Reeber, M.D., (1960), Phys. Rev. 117, 1476.

Ridley, N., (1967), Phys. Lett. 25A, 134.

Russell, C.M., (1966), Thesis, Imperial College.

Tyzack, C. and Raynor, G.V., (1954), Trans. Farad. Soc. 50, 675.

Wernick, J.H. and Matthias, B.T., (1961), J. Chem. Phys. 34, 2194.

CHAPTER 5

CHAPTER 5

DISCUSSION

5.1 THE SEEMANN-BOHLIN DIFFRACTOMETER

The present modification of the Wooster-Martin diffractometer has removed the two major criticisms of the earlier SB instruments. Firstly it does not lack versatility: a wide variety of useful angular ranges are available, including the region between 162° and $172^{\circ}2\theta$ (hitherto unobtainable on standard diffractometers) and, of course, the instrument is readily convertible to BB geometry. Secondly, with the dual geometry it is possible to align the instrument without reference to a standard substance. For low temperature studies the apparatus has the advantage that service connections to a cryostat can be maintained during an experiment since the cryostat remains stationary. The SB diffractometer is not seen as a competitor of the BB diffractometer but rather as a complement to it. As such, there seems to be no reason why commercial BB diffractometer manufacturers should not be able to supply SB attachments to their instruments.

The principal improvements that could be made to the present instrument are in the adjustments to the X-ray tube. In particular a micrometer control is desirable for the longitudinal adjustment (ΔF) while a fine screw thread transverse adjustment (ΔR_F) would simplify stage 5 of the alignment procedure.

The upper limit of $172.5^{\circ}2\theta$ may be extended by the use of a smaller proportional counter. For example, side-window proportional counters, less than 1.5 cm in diameter, are now available (20th Century Electronics) which should enable the present instrument to be used up to $\sim 175^{\circ}2\theta$ with a corresponding increase in the precision of lattice parameter determination.

One valuable application of the SB geometry, as pointed out by Segmuller (1959), is in the measurement of lattice parameters in preferred directions in the material. Since the angle of incidence, of the X-rays on the specimen surface, varies with the specimen position, it is clear that a particular, measured Bragg reflection arises from differently oriented sets of planes for different specimen positions (2γ). This principle is now being adopted for use on the present SB diffractometer to determine the distribution of residual stresses in cold-rolled sheets of alloys of copper, aluminium and iron (Gunnell, 1970).

5.2 AXIAL RATIO TRENDS IN THE INDIUM ALLOYS

The general pattern of axial ratios, in the set of indium alloy systems investigated, is shown in Fig. 5.1 and includes the $18^{o}K$ data of Russell (1966) for the indium solid solution in the In-Pb system. The curves of Hg, Cd, Sn, Bi and Pb, in the region $e/a = 2.9$ to 3.1, conform to a single pattern strongly suggesting that the axial ratio is determined principally by the electron/atom ratio. The curve for lithium, however, does not fit into the pattern but, as suggested in section 4.2, the lithium alloys may be in a two-phase region.

The axial ratio of alloys in the In solid solution of the constant valence system In-Tl, shows a marked variation as a function of Tl composition. Thus, although there are clear trends in the axial ratio as a function of the electron/atom ratio, the latter quantity cannot be the sole factor governing the behaviour of c/a. In fact, while there may be a general effect of alloying which could be called the valence effect (dependent only on e/a), there are almost certainly effects depending on particular characteristics of the alloying elements. These effects cannot be taken into account in semi-quantitative explanations (such as Fermi-surface-Brillouin zone interactions) and the only meaningful approach is to attempt an exact calculation of the total energies of different crystal structures for

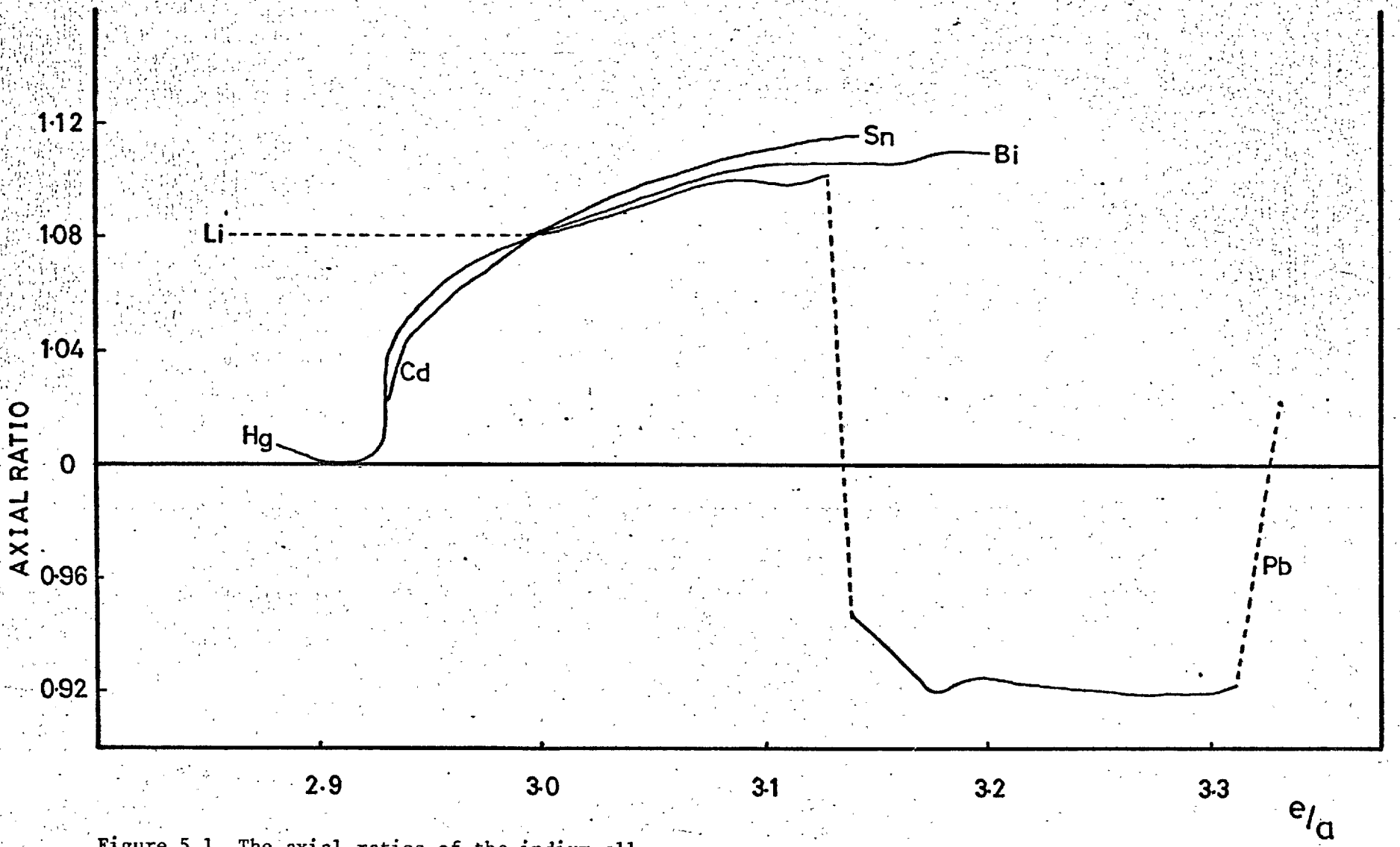

Figure 5.1 The axial ratios of the indium alloys.

each alloy system. As discussed in Chapter 1, the most hopeful approach to such a calculation is that of the pseudopotential method which will, therefore, be applied to the present indium alloys. The ideal goals of this exercise are:

1. To demonstrate that FCT ($c/a > 1$) is a sensible structure for pure indium.

2. Account for the general rise in axial ratio with electron/atom ratio in the range $e/a = 2.9$ to 3.1.

3. To justify the existence of the FCT ($c/a < 1$) and FCC structures and predict the phase changes in the present alloy systems.

Pseudopotential Calculations

In order to reduce the problem to tractable proportions the only structures investigated will be those that are uniaxial distortions of FCC. (These include the FCT and BCC structures.) There are two structurally dependent energies to be calculated, the first of which, the band-structure energy, was discussed in Chapter 1. The other term is the energy arising from the direct interaction of positive ions embedded in a uniform compensating sea of negative charge. This 'electrostatic' energy E_{es} is rather difficult to calculate in general since the long range of the Coulomb force causes convergence problems. Harrison (1966) has demonstrated how the electrostatic energy of HCP structures, which are distorted from the ideal axial ratio, can be calculated and his method has been used here as a basis for the calculation of E_{es} for those structures which can be represented as tetragonal distortions of the FCC structure. The salient point is that the energy can always be represented (Harrison, 1966) by an expression

$$E_{es} = \frac{Z^{*2}\, e^2}{2r_o}\, \alpha \qquad \ldots (5.1)$$

where Z^* is the effective valence (that is the valence corrected for the orthogonalisation or depletion hole - see Chapter 1) and r_o is the radius of the atomic sphere $\left(\frac{3\Omega_o}{4\pi}\right)^{1/3}$. The dimensionless quantity α (the Madelung constant or Ewald constant, to be distinguished from the depletion hole α) is known for some simple structures. In the present case the value for the FCC structure is required and this is given by Fuchs (1935) as $\alpha = -1.79172$. Following Harrison the coulomb interaction between two ions is replaced by

$$v(r) = \frac{Z^{*2}\, e^2}{r} \quad \frac{2}{\sqrt{\pi}} \int_o^{\sqrt{\eta}\, r} e^{-x^2}\, dx \qquad \ldots (5.2)$$

where η is a dummy variable introduced for convergence purposes. This potential is coulombic at large r but Gaussian at small r, approaching the real potential for a point ion, only in the limit of infinite η. The potential energy of an ion at $\underline{r}_i$ due to all other ions at $\underline{r}_j$ is

$$V(\underline{r}_i) = \sum_j{}' v(\underline{r}_i - \underline{r}_j)$$

$$= \sum_j v(\underline{r}_i - \underline{r}_j) - 2Z^{*2}\, e^2 \sqrt{\frac{\eta}{\pi}}$$

because (5.2) tends to the second term as r tends to zero i.e. the ion self energy has been subtracted.

A Fourier expansion of $V(\underline{r}_i)$ gives

$$V(\underline{r}_i) = \sum_q{}' S(\underline{q})\, v_q\, e^{i\underline{q}.\underline{r}_i} - 2Z^{*2}\, e^2 \sqrt{\frac{\eta}{\pi}}$$

where $v_q = \frac{4\pi Z^{*2}\, e^2}{\Omega_o q^2} \quad e^{-q^2/4\eta}$

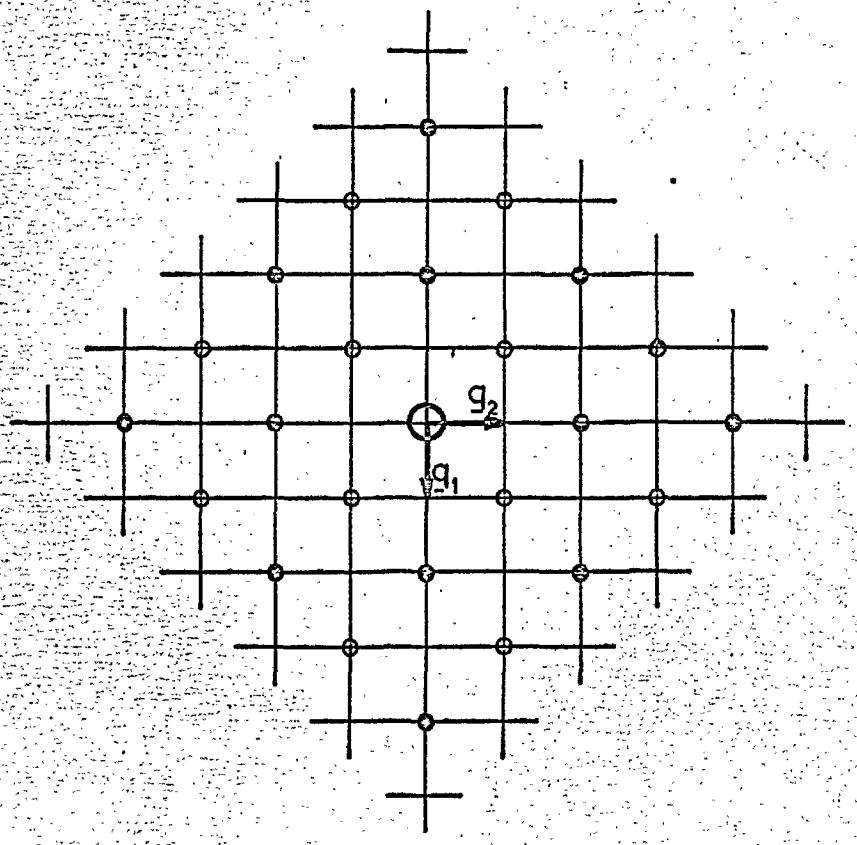

Figure 5.2 The reciprocal lattice of FCT in plan.
• - points in basal plane, o - points
at ½ lattice spacing from basal plane.

The electrostatic energy is half the sum of $V(\underline{r}_i)$ over all ions in the limit as η goes to infinity i.e.

$$E_{es} = \frac{Z^{*2} e^2}{2} \left[\lim_{\eta \to \infty} \Sigma'_q \left(\frac{4\pi}{\Omega_o}\right) |S(q)|^2 \frac{e^{-q^2/4\eta}}{q^2} - 2\sqrt{\frac{\eta}{\pi}} \right] \quad \ldots (5.3)$$

The body centred tetragonal representation of the FCT lattice in reciprocal space is shown in plan in Fig. (5.2). The C axis is perpendicular to the plane of the figure with unit vector $\underline{q}_3$. A vector $\underline{q}_t$ in the basal plane is defined by

$$\underline{q}_t = m_1 \underline{q}_1 + m_2 \underline{q}_2$$

so that

$$\alpha = \lim_{\eta \to \infty} \left[\Sigma_{q_t} \frac{4\pi r_o}{\Omega_o} e^{-q^2/4\eta} \Sigma_{m_3} \frac{e^{-m_3^2 q_3^2/4\eta} |S(q)|^2}{q_t^2 + m_3^2 q_3^2} - 2r_o \sqrt{\frac{\eta}{\pi}} \right]_{q \neq 0} \quad \ldots (5.4)$$

The structure factor can be resolved into separate structure factors, sums over linear chains of atoms perpendicular to the basal plane and two-dimensional sums over the basal plane. The structure factor can then be written as $S(q_t)$ and taken out of the sum over m_3. In this particular case the structure factor for each reciprocal lattice point is unity anyway.

The sum over m_3 is replaced by

$$\Sigma_{m_3} \frac{e^{-m_3^2 q_3^2/4\eta}}{q_t^2 + m_3^2 q_3^2} - K \int_{-\infty}^{\infty}{}' \frac{e^{-m^2 q_3^2/4\eta}}{q_t^2 + m^2 q_3^2} \, dm \quad \ldots (5.5)$$

which is a generalisation of Harrison's calculation since a parameter K has been introduced, to be fixed later. The subtracted term is added back and coupled with the last term of (5.4) to make it

$$\sum_{q_t} \frac{4\pi r_o}{\Omega_o} e^{-q_t^2/4\eta} K \int_{-\infty}^{\infty} \frac{e^{-m^2 q_3^2/4\eta}}{q_t^2 + m^2 q_3^2} dm - 2r_o \sqrt{\frac{\eta}{\pi}} \quad \ldots (5.6)$$

It will be demonstrated that (5.5) will converge for a particular value of K and it is known that (5.4) must be convergent so that (5.6) must also be convergent. By making the substitution $x = mq_3/2\sqrt{\eta}$, the integral in 5.6 becomes

$$\frac{1}{2\sqrt{\eta} q_3} \int_{-\infty}^{\infty} \frac{e^{-x^2}}{q_t^2/4\eta + x^2} dx = \frac{1}{\sqrt{\eta} q_3} f\left(\frac{q_t}{2\sqrt{\eta}}\right)$$

The function f is not known in algebraic form but its explicit argument is known.

Expression 5.6 becomes

$$\frac{4\pi r_o K}{\Omega_o} \cdot \frac{1}{\sqrt{\eta} q_3} \sum_{q_t} e^{-q_t^2/4\eta} f\left(q_t/2\sqrt{\eta}\right) - 2 r_o \sqrt{\frac{\eta}{\pi}}$$

$$\text{or} \quad \frac{1}{\sqrt{\eta} q_3 \Omega_o} g\left(\frac{q_1}{2\sqrt{\eta}}\right) - 2\sqrt{\frac{\eta}{\pi}} \quad \ldots (5.7)$$

since q_t can be represented as $m_t q_1$. If the unknown function g is expanded as a polynomial in $q_1/2\sqrt{\eta}$ there must be a term to cancel the $2\sqrt{\frac{\eta}{\pi}}$ in order to have convergence. This must be a term in $\left(\frac{q_1}{2\sqrt{\eta}}\right)^{-2}$ Furthermore, it is easily seen that terms of lower order in $\left|\frac{q_1}{2\sqrt{\eta}}\right|$ go to infinity in the limit, whereas terms of higher order go to zero. except the term in $(q_1/2\sqrt{\eta})^{-1}$. The surviving term in 5.7 would then be proportional to $1/(q_1 q_3 \Omega_o)$ which in turn is proportional to q_1 and may thus be written Aq_1.

Returning to (5.4), there is now an absolutely convergent quantity within the summations. Mathematically this means that the sum and the

limit may be transposed in which case (5.4) reduces to

$$\alpha = \sum_{q_t} \frac{4\pi r_o}{\Omega_o} \left[\sum_{m_3} \frac{1}{q_t^2 + m_3^2 q_3^2} - K \int_{-\infty}^{\infty} \frac{dm}{q_t^2 + m^2 q_3^2} \right] + r_o A q_1 \quad \ldots (5.8)$$

The integral reduces directly to $-K\pi/q_t q_3$ leaving only the sums over linear chains of atoms to be evaluated. Harrison has solved this problem very neatly and demonstrates that

$$\sum_{n=-\infty}^{\infty} \frac{1}{a^2 + (bn+\delta)^2} = \frac{\pi}{ab} \left[\frac{1}{(e^{2\pi a/b} e^{-2\pi i\delta/b} - 1)} - \frac{1}{(e^{-2\pi a/b} e^{-2\pi i\delta/b} - 1)} \right] \quad \ldots (5.9)$$

where n runs over all the atoms in an infinite chain of atom separation b, and a and δ are the constants shown in Fig. 5.3.

Two types of summation are required for the FCT structure, as shown in Fig. (5.2). The closed circles, •, (except for the origin) denote reciprocal lattice points at $m_3 = 0, \pm 2, \pm 4, \pm 6$, etc. Whilst the open circles, o, represent points at $m_3 = \pm 1, \pm 3, \pm 5$, etc. Summations of the first kind are simply generated from 5.9 with $\delta = 0$, $a = q_t$, $b = 2q_3$, i.e.

$$\sum_{m_3}^{\bullet} = \frac{\pi}{2q_t q_3} \left(1 + \frac{2}{e^{\pi q_t/q_3} - 1}\right) \quad \ldots (5.10)$$

Summations of the second kind can be generated by summing over a chain of atoms at $m_3 = 0, \pm 1, \pm 2, \pm 3, \ldots$ and subtracting the sum over points $m_3 = 0, \pm 2, \pm 4, \ldots$. Whence

$$\sum_{m_3}^{o} = \frac{\pi}{2q_t q_3} \left(1 - \frac{2}{e^{\pi q_t/q_3} + 1}\right) \quad \ldots (5.11)$$

If (5.10) and/or (5.11) are summed over all chains of ions, the result

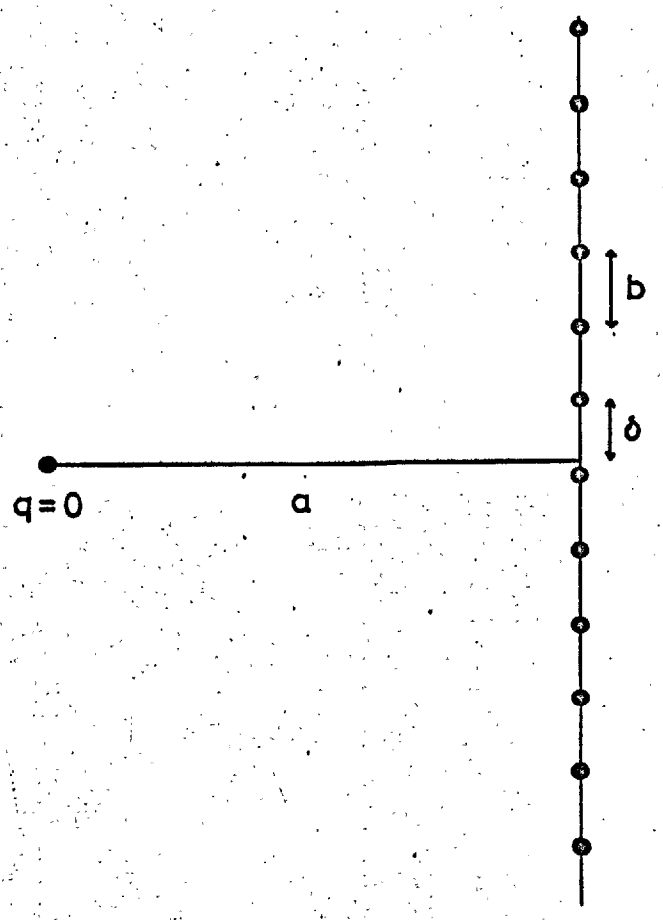

Figure 5.3 A linear chain of atoms - after Harrison (1966).

diverges and hence K is determined by the necessity to cancel the divergent factor. Inspection of (5.10) and (5.11) immediately suggests $K = \frac{1}{2}$.

The remaining term in (5.8) is the summation over the line of ions through the origin excluding the ion at $q = 0$. Harrison provides the answer to this:

$$\sum_{-\infty}^{\infty}{}' \frac{1}{n^2} = \frac{\pi}{3}$$

The ions in this chain are at $\pm 2, \pm 4, \pm 6, \ldots$ and hence this summation goes to $\pi/12$. The final expression for α is then

$$\alpha_{FCT} = \sum_{q_t}{}' \frac{4\pi r_o}{\Omega_o} (\sigma^o;\sigma^\bullet) + \frac{\pi^3 r_o}{3\Omega_o q_3^2} + A r_o q_1 \quad \ldots (5.12)$$

where $\sigma^o(q_t) = \frac{-\pi}{q_t q_3} \cdot \frac{1}{(e^{\pi q_t/q_3} + 1)}$

and $\sigma^\bullet(q_t) = \frac{\pi}{q_t q_3} \cdot \frac{1}{(e^{\pi q_t/q_3} - 1)}$

Equation (5.12) is a function of c/a only and the unknown constant A is obtained by solving it for the FCC structure using the α_{FCC} of Fuchs. The summation is to be made over enough reciprocal lattice points for the accuracy required in α. A machine programme for this has been written and may be found in Appendix 5. Normally ten sets (multiplicity must, of course, be accounted for) of points were found to be sufficient to produce accuracy in the sixth decimal place. The constant A was found to be -0.877857. The value of α at an axial ratio of 0.71, corresponding to the BCC structure, was found to be the same as that given by Fuchs (1935) for that structure thus giving a confirmation of the validity of the present method.

Electrostatic Energy in the Alloy

If the valencies of the two constituents of an alloy are the same, then the electrostatic energy is the same as in the pure metal. Harrison (1966) and Inglesfield (1969) have suggested that the problem can be resolved into an average and a difference energy in much the same way as the band structure energy, (see section 1.2). No attempt to apply this suggestion in practice, has yet been reported. To investigate it further it is necessary to formulate the equivalent of (5.2) in the alloy. This interaction is given by

$$v_{ij}(\underline{r}) = Z_i^* Z_j^* \frac{2}{\sqrt{\pi}} \int_0^{\sqrt{\eta} r} e^{-x^2} dx \qquad \ldots (5.13)$$

The potential energy of an ion at $\underline{r}_i$ is now

$$V(\underline{r}_i) = \sum_j v(\underline{r}_i - \underline{r}_j) - 2Z_i^* e^2 \sqrt{\frac{\eta}{\pi}} \qquad \ldots (5.14)$$

The first term on the right-hand side is expanded in a Fourier series.

$$\sum_j v(\underline{r}_i - \underline{r}_j) = \sum_q' K(q) e^{i\underline{q} \cdot \underline{r}_i} \qquad \ldots (5.15)$$

where

$$K(q) = \frac{1}{N} \int \sum_j v(\underline{r}_i - \underline{r}_j) e^{-i\underline{q} \cdot \underline{r}_i} d\underline{r}_i$$

or

$$K(q) = \frac{1}{N} \sum_j v_{ij}(q) e^{-iq \cdot \underline{r}_j} \qquad \ldots (5.16)$$

where $v_{ij}(q)$ is the Fourier transform of (5.13).

Substituting (5.16) and (5.15) into (5.14), summing over all ions and dividing by the total number of ions the average energy per ion is

$$\frac{1}{N}\sum_i V(\underline{r}_i) = \frac{1}{N^2}\sum_q{}' \sum_i \sum_j (v_{ij}(q)\, e^{-i\underline{q}\cdot\underline{r}_j})\, e^{i\underline{q}\cdot\underline{r}_i} - \frac{2e^2}{N}\sqrt{\frac{\pi}{\alpha}}\sum_i Z_i^{*2} \qquad \ldots (5.17)$$

The term in brackets can be represented by

$$X_i = \sum_j v_{ij}(q)\, e^{-i\underline{q}\cdot\underline{r}_j} = \sum_{A\ \text{ions}} v_{iA}\, e^{-i\underline{q}\cdot\underline{r}_j} + \sum_{B\ \text{ions}} v_{iB}\, e^{-i\underline{q}\cdot\underline{r}_j}$$

or

$$X_i = N v_{iA} S_A + N v_{iB} S_B$$

in the notation of section (1.2). The sum over i then becomes

$$\Sigma X_i = N\sum_i (v_{iA} S_A + v_{iB} S_B) e^{i\underline{q}.\underline{r}_i} = N\sum_A (v_{AA} S_A + v_{AB} S_B)\, e^{i\underline{q}.\underline{r}_i}$$

$$+ N\sum_B (v_{AB} S_A + v_{BB} S_B)\, e^{i\underline{q}.\underline{r}_i}$$

or

$$\Sigma X_i = N^2(v_{AA} S_A + v_{AB} S_B)\, S_A^* + N^2(v_{AB} S_A + v_{BB} S_B)\, S_B^* \qquad \ldots (5.18)$$

Alternatively

$$\Sigma X_i = N^2\left[v_{AA} S + (v_{AB}-v_{AA})\, S_B\right] S_A^* + N^2\left[v_{AB} S + (v_{BB}-v_{AB})\, S_B\right] S_B^*$$

which, by a similar process, itself reduces to

$$\Sigma X_i = N^2\left[v_{AA}|S|^2 + (v_{AB}-v_{AA}) S_B S^* + (v_{AB}-v_{AA}) S_B^* S\right.$$

$$\left. + (v_{BB} + v_{AA} - 2v_{AB})\, |S_B|^2\right] \qquad \ldots (5.19)$$

For $q = q_o$ on the wavenumber lattice, $e^{-i\underline{q}_o \cdot \underline{r}_i}$ is unity (for the structure of interest here). Then $S = 1$, $S_A = (1 - c)$ and $S_B = c$ and hence (5.19) becomes

$$\Sigma X_i = N^2 \sum_{q_o}' \left[v_{AA}(1 - c)^2 + v_{BB}c^2 + 2v_{AB}c(1 - c)\right] \quad \ldots (5.20)$$

whilst for q not on the wavenumber lattice $S = 0$ and then

$$N \sum_{q \neq q_o} (v_{BB} + v_{AA} - 2v_{AB}) |S_B|^2 = Nc(1 - c) \sum_{q \neq q_o} (v_{BB} + v_{AA} - 2v_{AB}) \quad \ldots (5.21)$$

Now the term in square brackets in (5.20) clearly arises from the square of an average valence $\overline{Z^*}$ given by

$$\overline{Z^*} = (1 - c) Z_A^* + cZ_B^* \quad \ldots (5.22)$$

This term may, therefore, be allowed for merely by calculating the energy as in the pure metal according to equation (5.1) only replacing Z^* by $\overline{Z^*}$.

In (5.21) the term $v_{BB} + v_{AA} - 2v_{AB}$ clearly corresponds to a 'difference' valence $\Delta Z^* = Z_A^* - Z_B^*$. Substituting (5.21) into the equation, (5.17), for the energy and ignoring, temporarily, the term in $\overline{Z^*}^2$ results in

$$E = \frac{\Delta Z^{*2}}{N} \frac{c(1 - c)\, 2\pi e^2}{\Omega_o} \sum_{\text{all } q}' \frac{e^{-q^2/4\eta}}{q^2} - 2\sqrt{\frac{\eta}{\pi}}\, \overline{Z^{*2}} \quad \ldots (5.23)$$

in the limit as $\eta \to \infty$. Now, as for the alloying energy in the band structure energy calculation, (see section 1.2) the sum is taken over to an integral over all wavenumber space and this integral is of the type:

$$\int_o^\infty e^{-q^2/4\eta}\, dq \propto \sqrt{\frac{\eta}{\pi}}$$

In other words the difference valence is associated with a divergent term which must cancel with part of the second term in (5.23). Indeed Inglesfield* (1970) points out that the second term, a mean square valence term, can be resolved into terms in $\bar{Z}$ and ΔZ. In fact

$$\overline{Z^{*2}} = \overline{Z^*}^2 + c(1-c)\,(\Delta Z^*)^2$$

and Inglesfield shows the terms in $(\Delta Z^*)^2$ cancel exactly.

In summary there are three terms left in the energy; the average band structure energy (1.20), the 'alloying' energy (1.22) and the average electrostatic energy using (5.22) in (5.1).

Computation of the energy

A computer programme has been generated to evaluate the structural dependent energy at a number of different compositions of different solutes at a number of axial ratios. The programme is shown in Appendix 6 but a short explanation is probably necessary.

The subroutine FFN (an apology is offered for the nomenclature which does not always fit that used in the final formulation of the problem above) generates the energy-wavenumber characteristic $\overline{\Phi(q)}$ (FQ(I) in the programme).

$$\Phi(q) = \overline{v(q)}^2 \; \overline{\chi(q)} \; \overline{\varepsilon_2(q)}$$

To obtain $\overline{v(q)}$, the v(q) for the two elements are read in as a function of q. The HA tables of values in Harrison (1966) are functions of $\eta = q/2k_F$ and have to be converted to functions of q before being read in.

---

* Private communication.

I am very grateful to Dr. Inglesfield for demonstrating this to me.

The Fermi wavenumber (KF) is generated for each composition and $\overline{\varepsilon_2(q)}$ and $\overline{\chi(q)}$ worked out from (1.11) using this k_F. In the calculation of k_F the unit cell volume was taken as a linear interpolation between the volumes for the pure metals. Also for want of anything better, the depletion hole α(ALPHA) was obtained by linear interpolation between the pure metal values from Shaw and Harrison (1967).

The subroutine FFN generates $\Phi(q)$ for q at discrete values (every 0.125 atomic units) the energy being in rydbergs.

The master programme is fed with the first thirty-six sets of reciprocal lattice points with their multiplicities (U(I)) and the volumes of the unit cells of the pure metals. The programme scales between the pure metals for the volume of the unit cell, calculates the lattice parameters corresponding to this volume and the particular axial ratio and then generates the q values appertaining to the (hkl) values. To perform the summation in (1.20) the value of $\Phi(q)$ has to be interpolated between the appropriate values of FQ(I). Newton's method of differences to third order was used originally but the function was such that differences diverged at some points. This was found to occur even when the logarithm of the function was used. A polynomial fit of order 19 was made but the error involved in using this was greater than that arising from linear interpolation, quite apart from the prohibitive use of computer time. The linear interpolation procedure was finally adopted.

The subroutine UES takes the average effective valence, reads in the α(ALPH(J)) and calculates the electrostatic energy from (5.1).

Results of pseudopotential calculations

It has already been indicated that the relative stabilities of crystal structures, in metals and alloys, is determined by a balance of the contributions to the energy, of the electrostatic part and the band-structure part. In the application of the theory to indium and

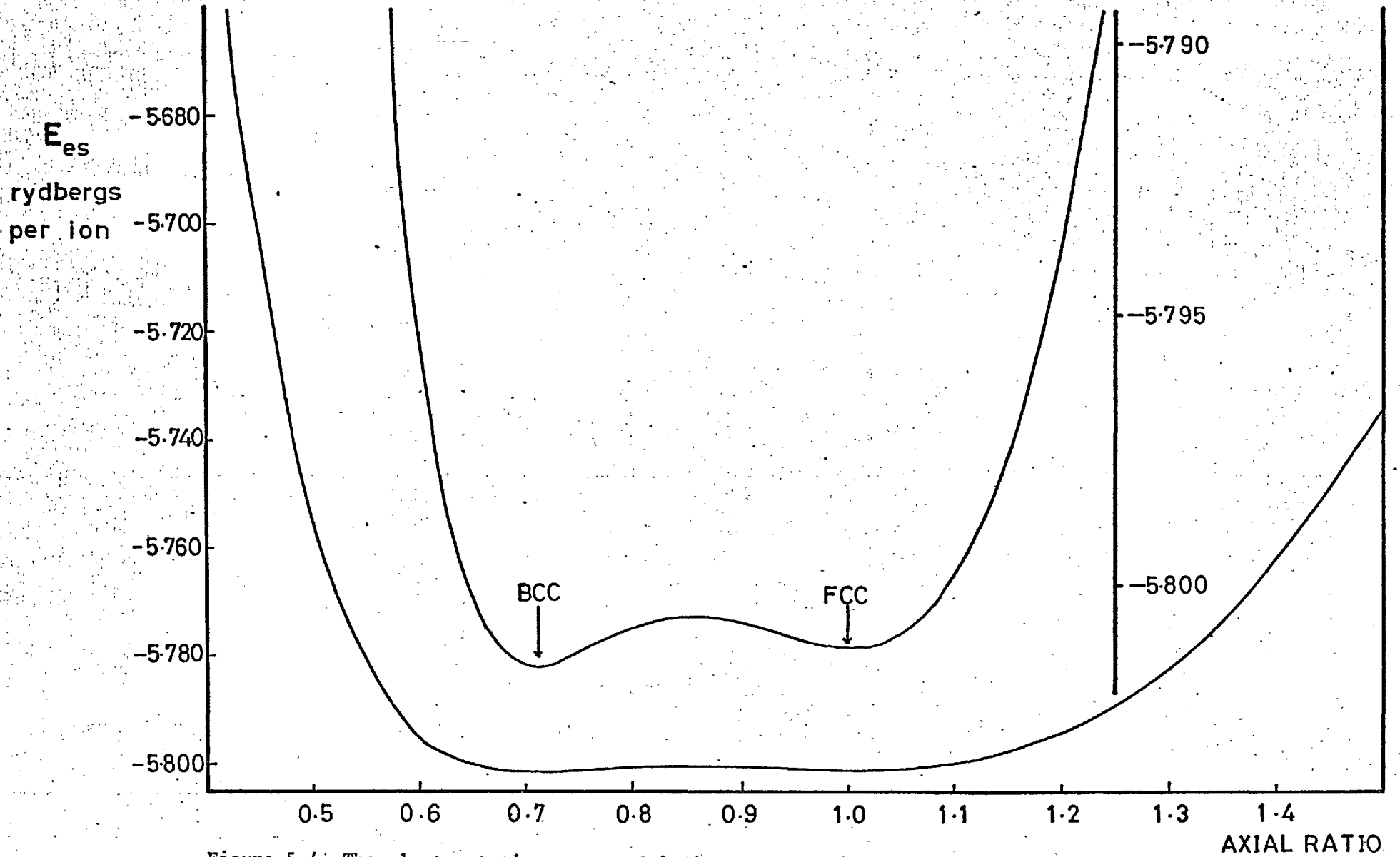

Figure 5.4 The electrostatic energy of indium as a function of axial ratio.

its alloys, it is, therefore, of interest to consider these contributions separately. Accordingly the electrostatic energy for indium, which is effectively a plot of the variable α in equation (5.1), is plotted as a function of the axial ratio of the FCT unit cell in Figure (5.4). This graph reveals two minima, one at an axial ratio corresponding, exactly, to the FCC structure whilst the absolute minimum occurs at an axial ratio which is exactly that of the BCC structure. Although the electrostatic energy might intuitively be expected to minimise in the region of a high symmetry structure, it is difficult to explain just why it does. Harrison (1966) was able to demonstrate that the electrostatic energy for the HCP structure is minimised at the ideal axial ratio and, since the electrostatic energy for this structure is greater (i.e. α is less) than that of the BCC structure, the latter is clearly favoured as the most stable structure for the elements, when the band structure energy is ignored. The simple cubic structure has an even smaller electrostatic energy (Carr, 1961) which probably accounts for its very rare occurrence. The BCC structure is found in all the alkali metals which, perhaps, approximate most closely to the free electron model. In other metals the proximity of the fermi-surface to the Brillouin-zone results in rather rapid changes in the matrix elements of the pseudopotential (Harrison, 1966) which would probably result in more violent variation of the band structure energy with changes of crystal structure.

The second important contributinn to the total energy is the band-structure energy which, for indium, is plotted as a function of axial ratio in Figure (5.5). A small extension in the c direction is seen to result in a very sharp decrease in energy (for c/a greater than 1.05) whilst a similar drop occurs for axial ratios below 0.5. Between $c/a = 0.5$ and $c/a = 1.05$, however, there are three minima and one maximum. In fine detail, the maximum is resolvable into a maximum at $c/a = 0.73$ and a stationary inflexion at $c/a = 0.71$ which corresponds exactly to the BCC structure. There is also a minimum at the axial ratio corresponding to the FCC structure. These are both confirmations of a group theoretical argument that requires the band structure energy to be stationary for the cubic structure (see Heine and Weaire, 1966).

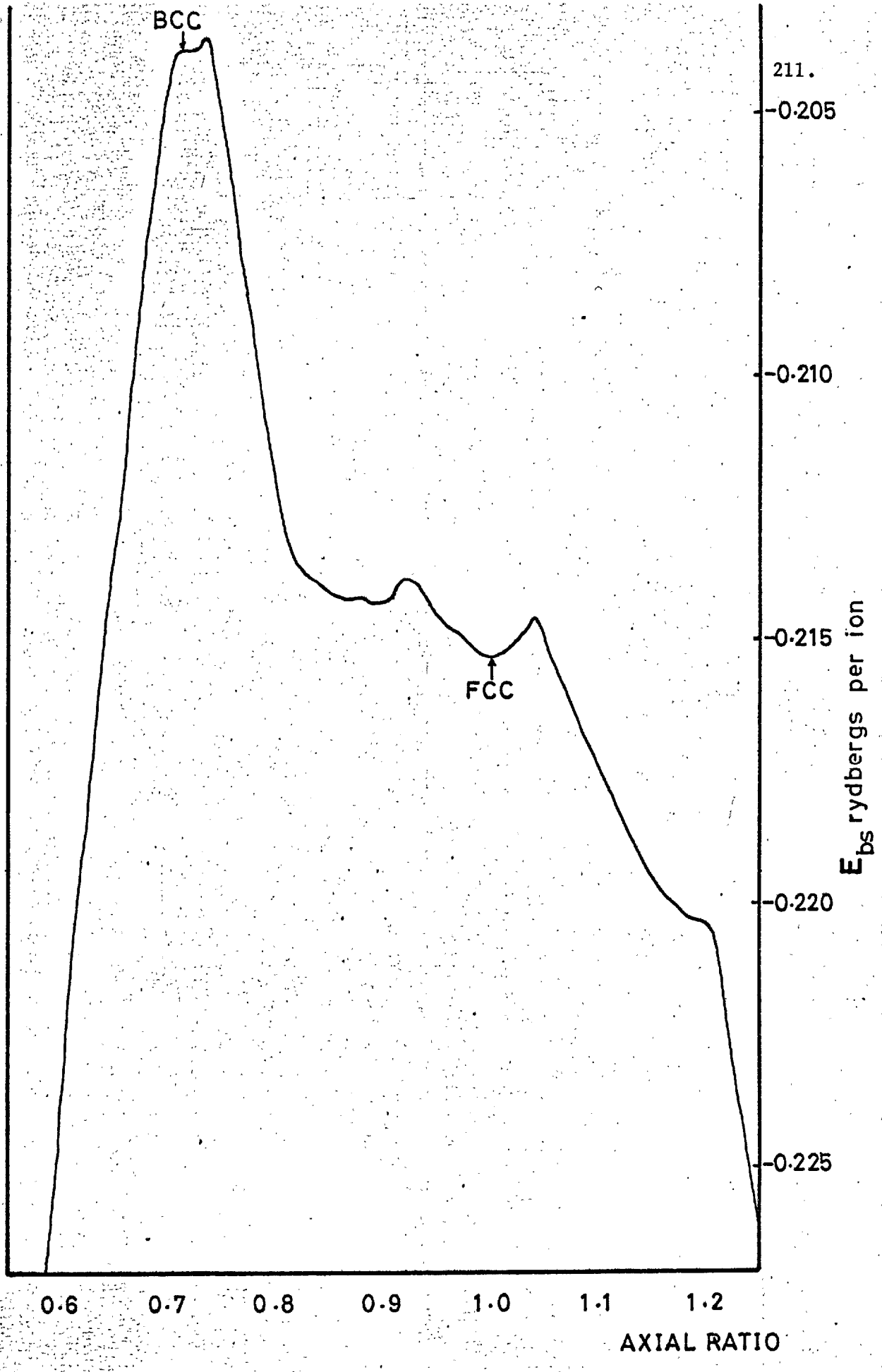

Figure 5.5 The band-structure energy of indium as a function of axial ratio.

When the band structure energy and the electrostatic energy are added, a total of seven minima occur, as shown in Fig. (5.6). The minimum corresponding to the BCC structure, at $^{c}/_{a} = 0.71$ has virtually been annihilated by the maximum in the band structure energy. The lowest energy now occurs at an axial ratio of 0.58 which is close to that of the β-mercury tetragonal structure (Atoji, Schirber and Swenson, 1959). In the region of small distortions from FCC however, the most stable structure corresponds to an energy minimum at $^{c}/_{a} = 1.12$, which thus makes rather good sense of the A6, FCT structure of indium, with $^{c}/_{a} \sim 1.09$ at low temperatures. For convenience this structure will be designated FCTα.

Two other energetically possible structures are indicated in Fig. (5.6). The first, which occurs as a rather flat-bottomed minimum around $^{c}/_{a} = 0.85$, corresponds with the β-phase of the indium-lead system and may thus be conveniently referred to as FCTβ. The other structure should have an axial ratio of 1.25 but no A6 structures with this value of $^{c}/_{a}$ have been reported in the literature (Pearson, 1967). For the present purposes, this hypothetical structure will be referred to as FCTγ.

An important question is whether or not the energy minimum, at $^{c}/_{a} = 0.58$, (and hereafter designated FCTδ) has any physical significance. Since large distortions of the FCC cell, at constant volume, must squash the atoms, the effective radius (along the direction of closest approach) must in the limit reach that of the ionic radius defining the surface of the black box used in the evaluation of the pseudopotential. At an axial ratio of 0.4 the atomic black boxes, used by Animalu and Heine (1965), touch (i.e. the atoms, in the direction of the c-axis, are 4.8 atomic units apart; equal to twice the Animalu-Heine radius R_M). It thus seems rather unlikely that the structure indicated at an axial ratio of 0.46, (which may be called FCTε) has any physical significance. No metallic structure with this axial ratio is recorded in Pearson (1967). At slightly higher axial ratios the proximity of the core electrons of neighbouring atoms may result in a distortion from the ionic sphere, in which case the pseudopotentials would become less valid. A spurious

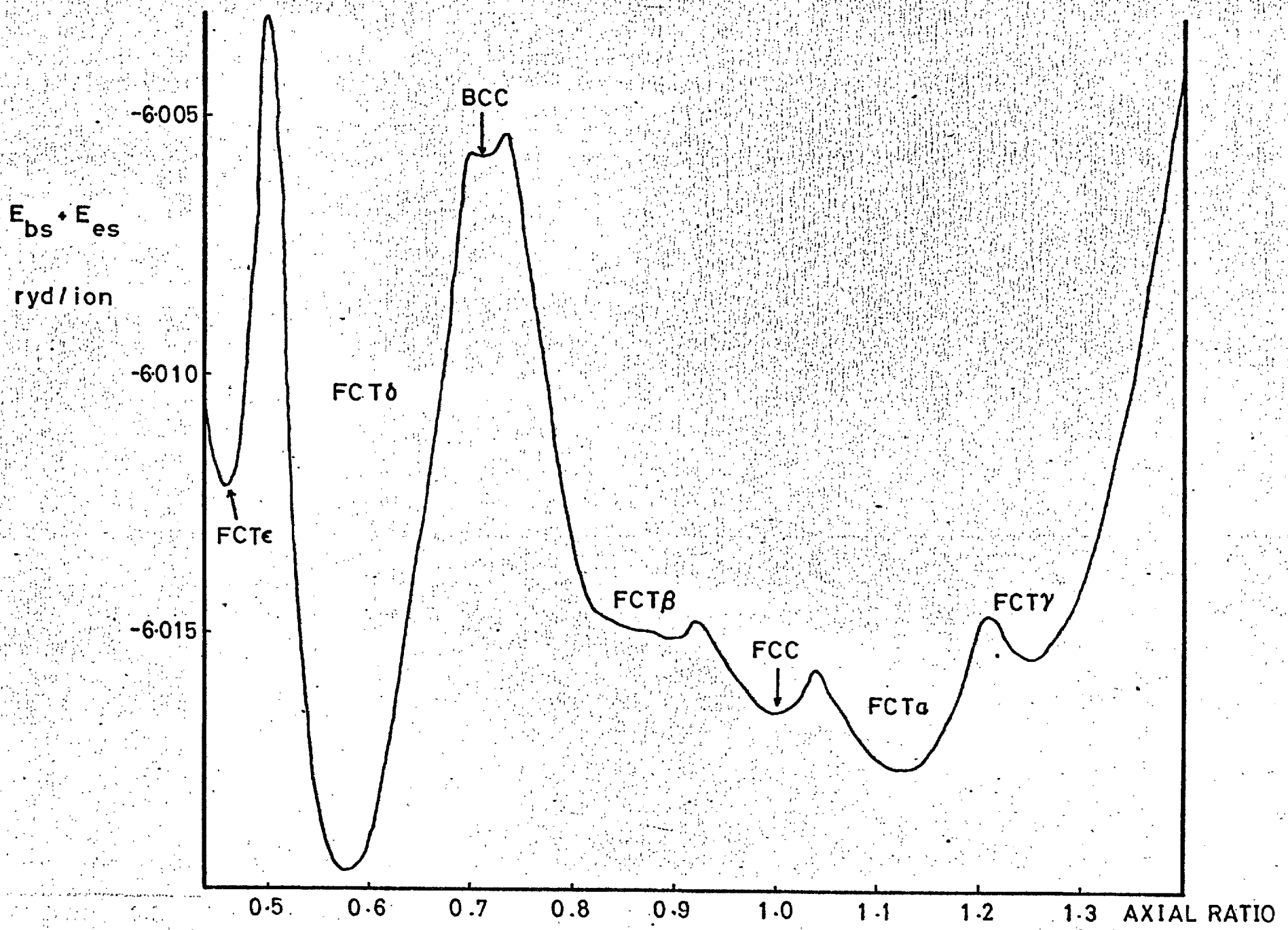

Figure 5.6 The total structural energy of indium as a function of axial ratio.

exaggeration of the FCTδ minimum might result from such a breakdown.

The very marked nature of the FCTδ energy dip suggests, however, that this structure is a real alternative to the FCTα structure observed in indium. If it is, physically, the most stable structure at $0^{o}K$, then the reason for its not being observed must lie in the thermodynamics of the problem. If, first of all, the pattern of Fig. (5.6) is considered to exist, qualitatively, on warming the metal or alloy to a temperature just below its melting point, it is reasonable to consider the problem in relation to the structure in the liquid state. It is well established (see, for example, Ubbelohde, 1965) that some sort of short range order exists in metals and alloys just above their freezing point, the general pattern being that of a random close-packed lattice with about 10 per cent vacancies with respect to the equivalent crystal lattice. The average number of nearest neighbours in the melt is about 10.85. Furukawa (1959) analysed the shape of the radial distribution curve for liquid indium, obtained from X-ray diffraction patterns by Gamertsfelder (1941), and obtained a coordination number, 11.3, i.e. quite close to FCC. Just why this should be so is a question that would require energy calculations using the pseudopotential in liquids and such an analysis will not be considered here. The fact is accepted, however, that atoms in the liquid are arranged in a manner approximating more nearly to FCC than to the FCTδ structure. In the process of nucleation, it seems highly probable that the fine differences in energy in Fig. (5.6) will be unimportant and that the atoms will cluster in the close packed arrangement similar to their arrangement in the liquid. In the initial process of solidification, the solid structure could thus be FCC and once in this region of axial ratio, the atoms would be unable to surmount the large energy barrier at the axial ratio corresponding to the BCC structure. This energy barrier corresponds to a thermal energy of about $4k_B T_M$ (T_M = melting temperature) per ion, above the FCC level. Once in the region between $c/a = 0.8$ and 1.3 then the energy barriers between structures there are much smaller, being all less than $0.25\ k_B T_M$ and present no obstacle to the metal settling into the FCTα structure. If

the nuclei of the solid are formed with the FCTδ structure then the crystal would tend to grow, epitaxially, in the same structure. It is emphasised, however, that the large energy barrier between FCC and FCTδ is only known to exist in the direction of tetragonal distortion. Although distortion along the c-axis is the simplest way to arrive at the FCTδ structure it is not the only conceivable way. A combination of three orthorhombic distortions, for example, may provide a route to FCTδ without crossing a high barrier.

A further possible explanation of why the FCT structure is not observed, lies in the fact that Fig. (5.6) may not be the energy pattern at higher temperatures. According to Zener (1947), the thermal energy, E_{th}, at a temperature T is given by

$$E_{th} = -3k_B T \ln\left(\frac{k_B T}{h\bar{\omega}}\right) \qquad \ldots (5.24)$$

where $\bar{\omega}$ is an average frequency of vibration. While Harrison (1966) has shown how it is possible, in principle to calculate the phonon spectrum from the pseudopotential, in practice the problem is only tractable when particular symmetry directions are considered. The calculation of thermal energy, however, requires integrals over all of wavenumber space to obtain $\bar{\omega}$.

The problem of obtaining $\bar{\omega}$ for hypothetical structures would thus appear to be enormously difficult. It was thought worthwhile to make some attempts at producing a simple model to obtain a mean frequency as a function of the axial ratio. A modification of the Debye approximation was considered, whereby the Debye sphere is replaced by an ellipsoid. This is not likely to be a meaningful approximation, however, since at one point in the tetragonal distortion of FCC cubic symmetry arises again (BCC) for which a Debye sphere would be the proper approximation.

Another approach attempted here was to assume Coulombic forces acting on the atoms, in which case the Hooke's constant is inversely

proportional to the separation of the atoms. The mean frequency was then taken from the mean value of the square-root of the Hooke's constant for nearest neighbours and next nearest neighbours. This approximation produced a maximum energy variation, with axial distortion, of only 0.3 millirydbergs per ion, which is insignificant. A third approach utilised the fact that each point on the wavenumber lattice corresponded to an oscillator frequency. For each distortion a large number of such points were taken and the wavenumbers, $|\underline{q}|$, evaluated and the points arranged in order of increasing $|\underline{q}|$. When a particular number of points (say 300) were taken, the maximum $|\underline{q}|$ value was assumed to be proportional to a Debye cut-off wavenumber. The phonon dispersion curve was assumed to be linear (the Debye approximation) and a characteristic frequency for each distortion was found. Again this resulted in only about 0.3 millirydbergs of energy variation, over the whole range of $^{c}/_{a}$.

If the thermal energy differences between structures were, in reality, as small as these calculations indicated, the number of thermal transformations occurring in nature, would be very small. It would seem that much more sophisticated treatments of thermal energy are needed. The only information on the thermal energy as a function of tetragonal distortion comes from the plot of axial ratio as a function of temperature (Russell, 1966; Barrett, 1962). As pointed out in Chapter 4 the axial ratio of indium increases as the temperature decreases, and a comparison of the present results with published room temperature results, indicates that the axial ratio of alloys with the FCTβ structure (in the In-Pb system), decreases with the temperature. The tendency is, therefore, for the structure to become closer to FCC as the temperature is raised. In order to move the FCTα and FCTβ minima in Fig. (5.6), closer to the FCC, it is necessary to propose an energy-well centred on FCC and increasing in depth with increasing temperature. For lack of any other information, this well is assumed to be parabolic in shape. In order to move the energy minimum at FCT from $^{c}/_{a} = 1.12$ to $^{c}/_{a}=1.11$ (roughly corresponding to the observed axial ratio change 1.084 to 1.075) an energy rise from FCC of about 0.4 millirydbergs at $^{c}/_{a} = 1.12$ is required. An extension of the parabola, that fits this information,

would raise the FCTδ structure 5 or 6 rydbergs but such an extrapolation would be excessively rash. The model may, however, have some sort of meaning when applied to the region closer to FCC and will at times be used in the discussion of the indium alloys.

When everything is taken into account, the FCTδ structure appears to be a possible structure for indium and the question arises as to whether it can be obtained experimentally. It is instructive to examine the case of pure mercury whose β phase has an A6 structure of axial ratio close to that of FCTδ. This phase does not occur on simple cooling, but only after energy is introduced into the metal by high pressure. By analogy, one may speculate that the FCTδ structure may be induced in pure indium by the application of high pressure or, perhaps, as a result of cold-working at low temperatures. Facilities are not available, in this laboratory, to perform such experiments but it is hoped that these may be attempted elsewhere.

Results of Pseudopotential Calculations on Alloys

A glance at Fig. (5.6) reveals that the three disordered structures (FCTα, FCC and FCTβ) observed in the solid solution alloys based on indium all have similar energies, and, furthermore, are not separated from each other by very formidable energy barriers. While this makes qualitative sense of the phase changes to FCC (when alloying with Hg, Cd, Tl) or to FCTβ (in In-Pb) the energy balance is so delicate that the correct structure is unlikely to be predicted with 100% certainty in every instance. One conclusion that may be drawn instantly, however, is that the BCC structure is clearly not favoured, a conclusion which is confirmed by the phase diagrams of the indium alloy systems (see, for example, Hansen 1958).

The indium-lead system

Figures (5.7) to (5.10) show the results of energy calculations

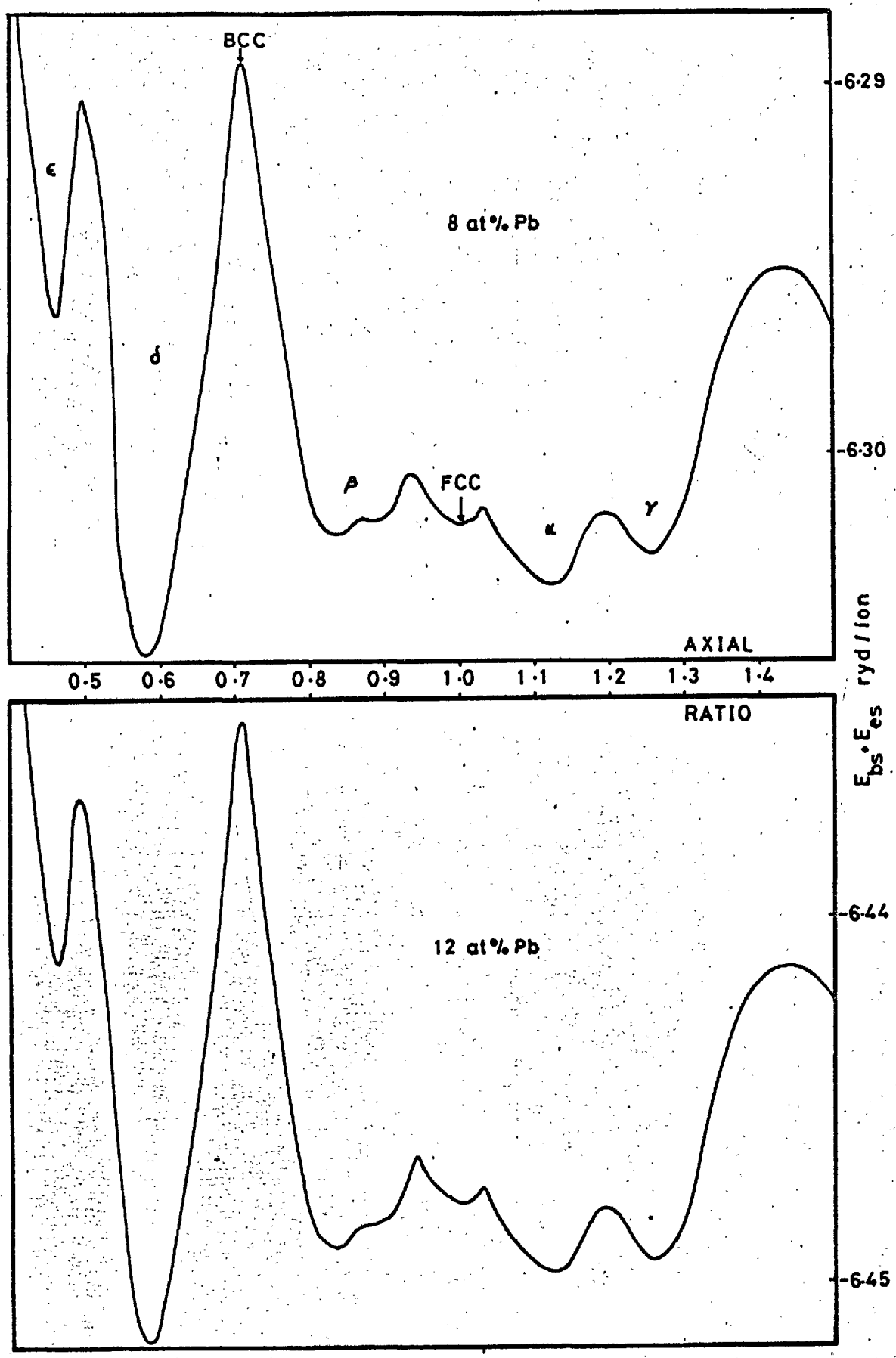

Figure 5.7 Total structural energy in the system In-Pb.

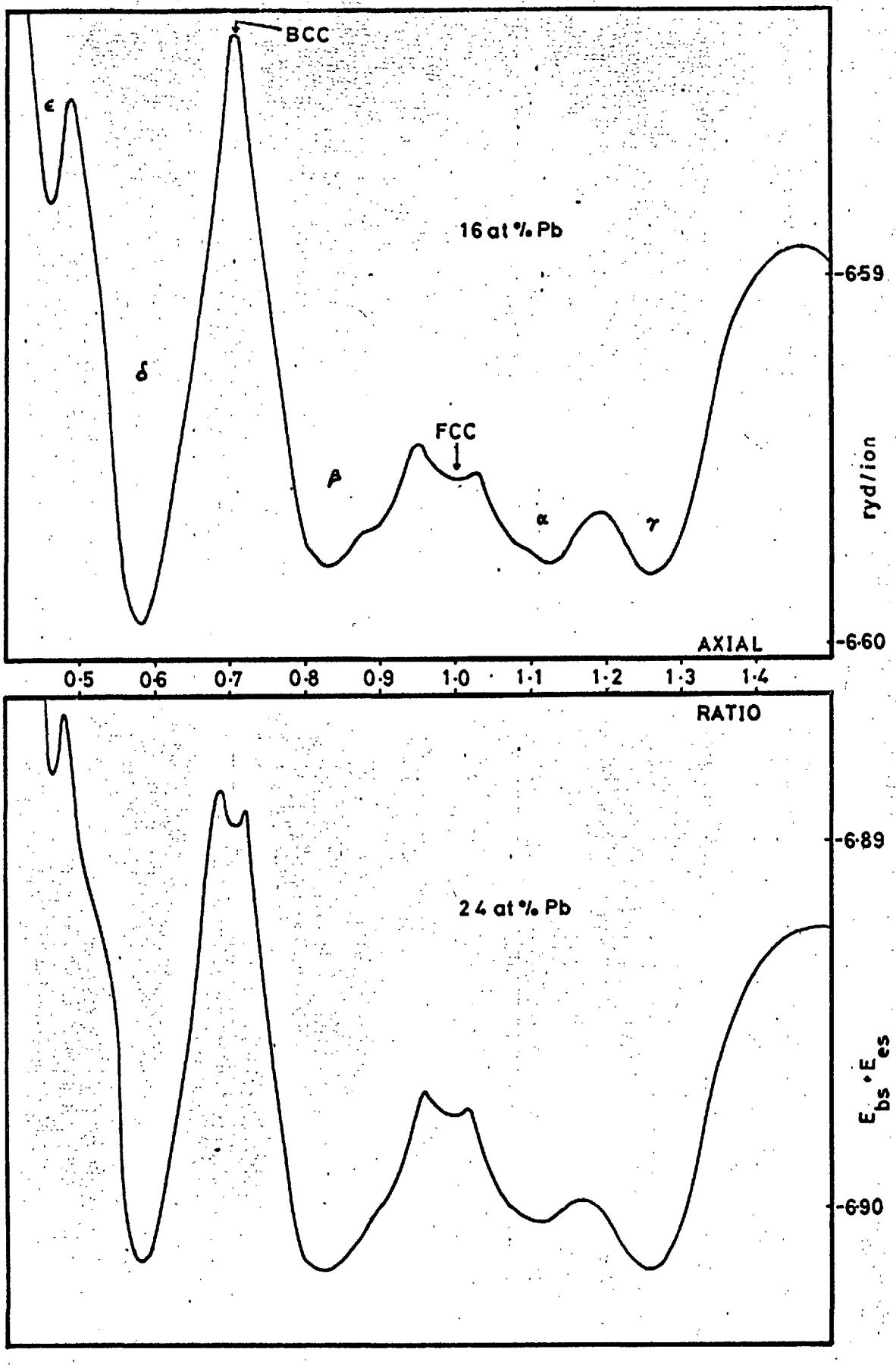

Figure 5.8 Total structural energy in the system In-Pb.

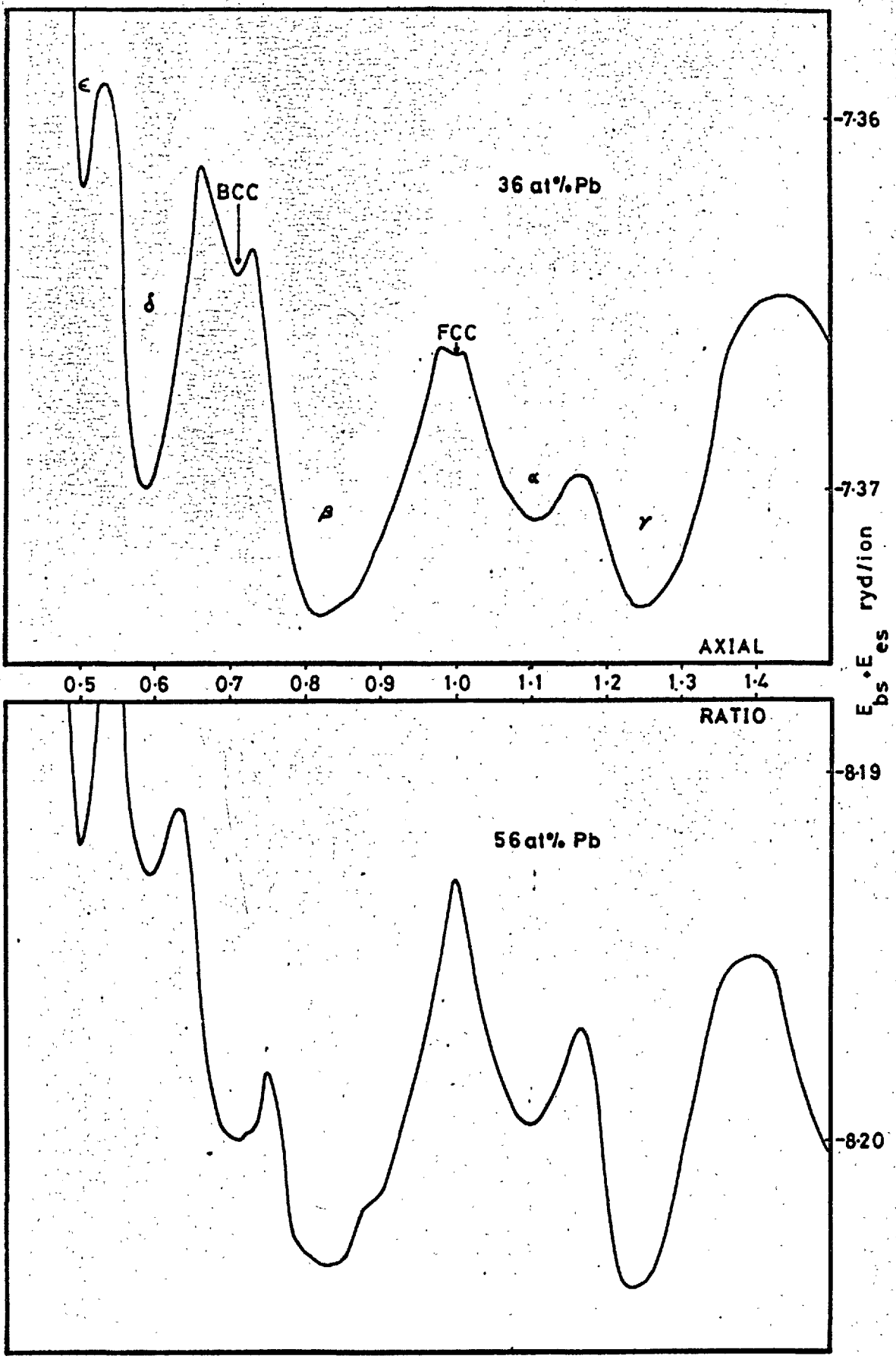

Figure 5.9 Total structural energy in the system In-Pb.

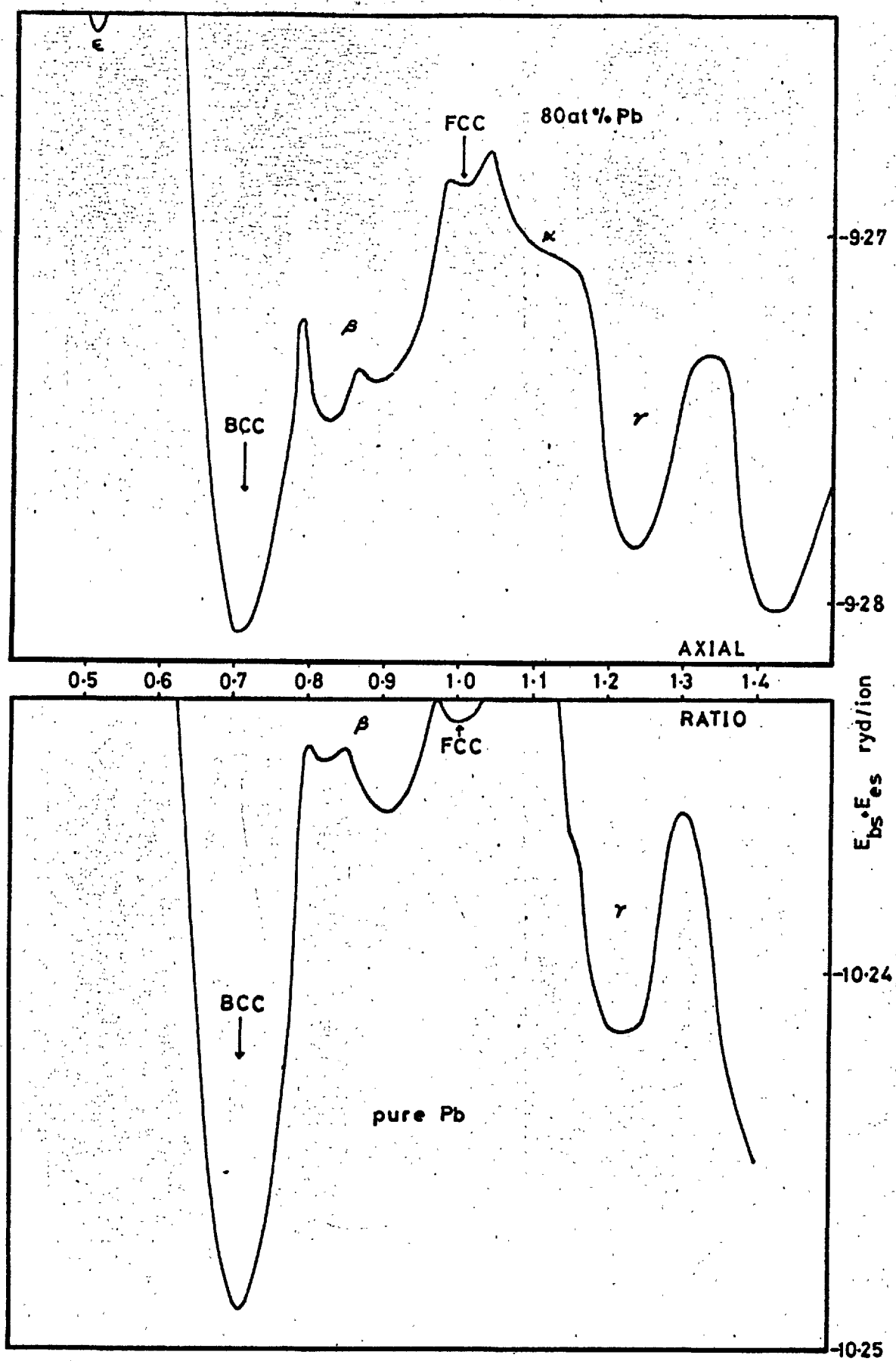

Figure 5.10 Total structural energy in the system In-Pb.

for indium alloys containing 8, 12, 16, 24, 36, 56, 80 and 100 at.% Pb. By a composition of 8 at.% Pb, the energy in the region of the FCTβ structure has degenerated into a double minimum, which has dropped below the FCC minimum, as also has the energy of the hypothetical FCTγ structure, whereas FCTα remains the most stable of the competing structures.

By 16 at.% Pb, however, the energy of the FCTβ structure falls below that of the FCTα structure and hence the energy calculations make sense of the structure change observed in In-Pb at 14 at.% Pb. These $0^{o}K$ calculations, however, indicate that the FCTγ structure should in fact be slightly more stable than FCTβ. If the crude parabolic model of the thermal energy is invoked, however, it can be proposed that the more distorted structure becomes the less favoured when the temperature is increased above $0^{o}K$. Nevertheless, the possible occurrence of the FCTγ structure (on cold working at low temperatures, for example) cannot be ruled out. Further additions of lead, up to about 40 at.% Pb, serve to strengthen the case for the FCTβ structure.

For alloys containing more than 60 at.% Pb the BCC structure appears to become a stronger possibility and at 80 at.% Pb it is apparently the most favoured structure as the energy minima associated with the FCTδ and the FCC structures tend to disappear. The last finding is rather disappointing, since alloys in the In-Pb system become FCC beyond about 32 at.%, this phase being the primary solid solution of indium in lead. Indeed the BCC structure appears to be far the most favoured in pure lead as can be seen from Fig. (5.10) The failure of the pseudopotential method to predict the correct structure for lead may be because an essential assumption of the method, that of the small-core approximation, is invalid for the heavy metals.

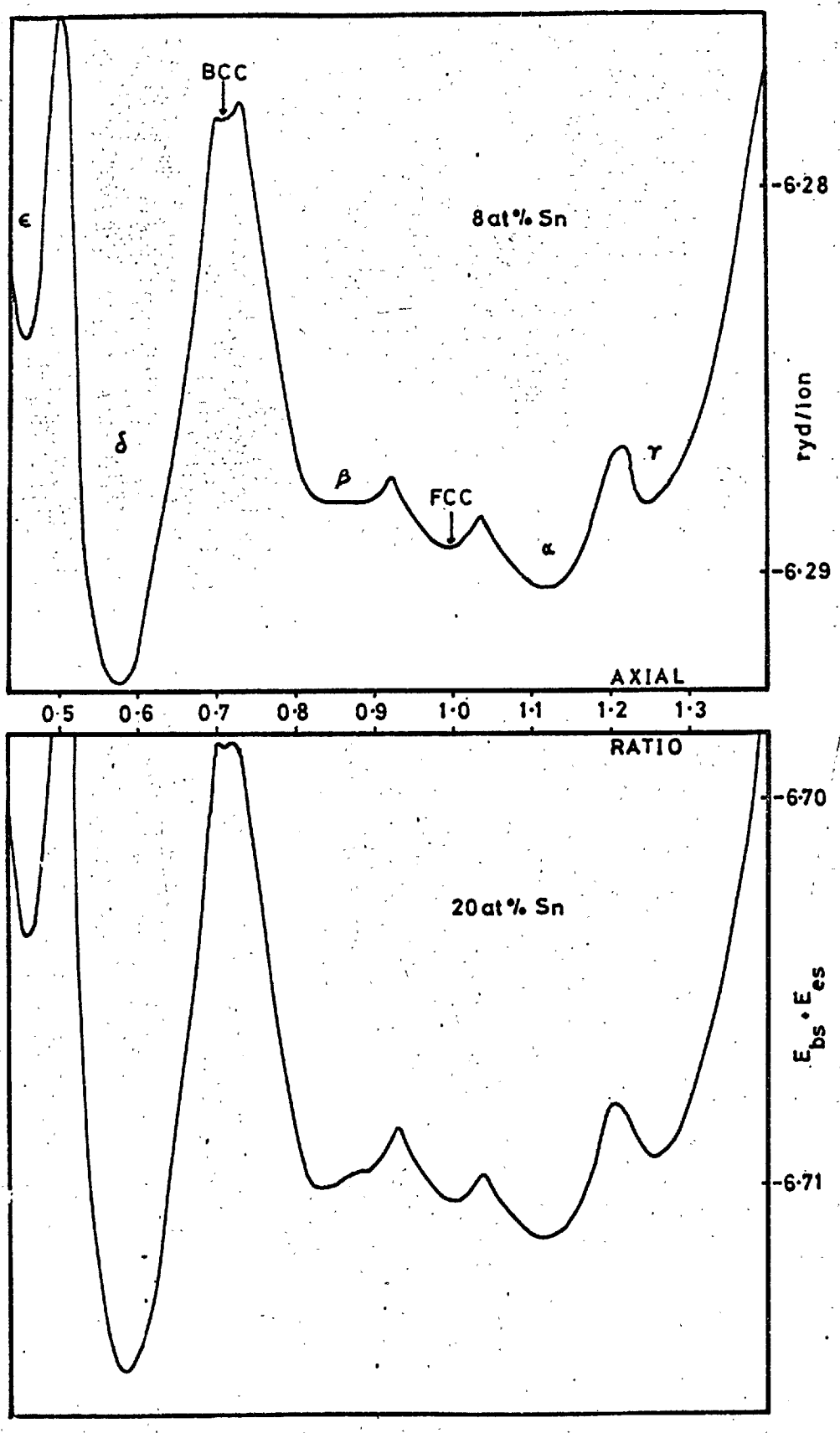

Figure 5.11 Total structural energy in the system In-Sn.

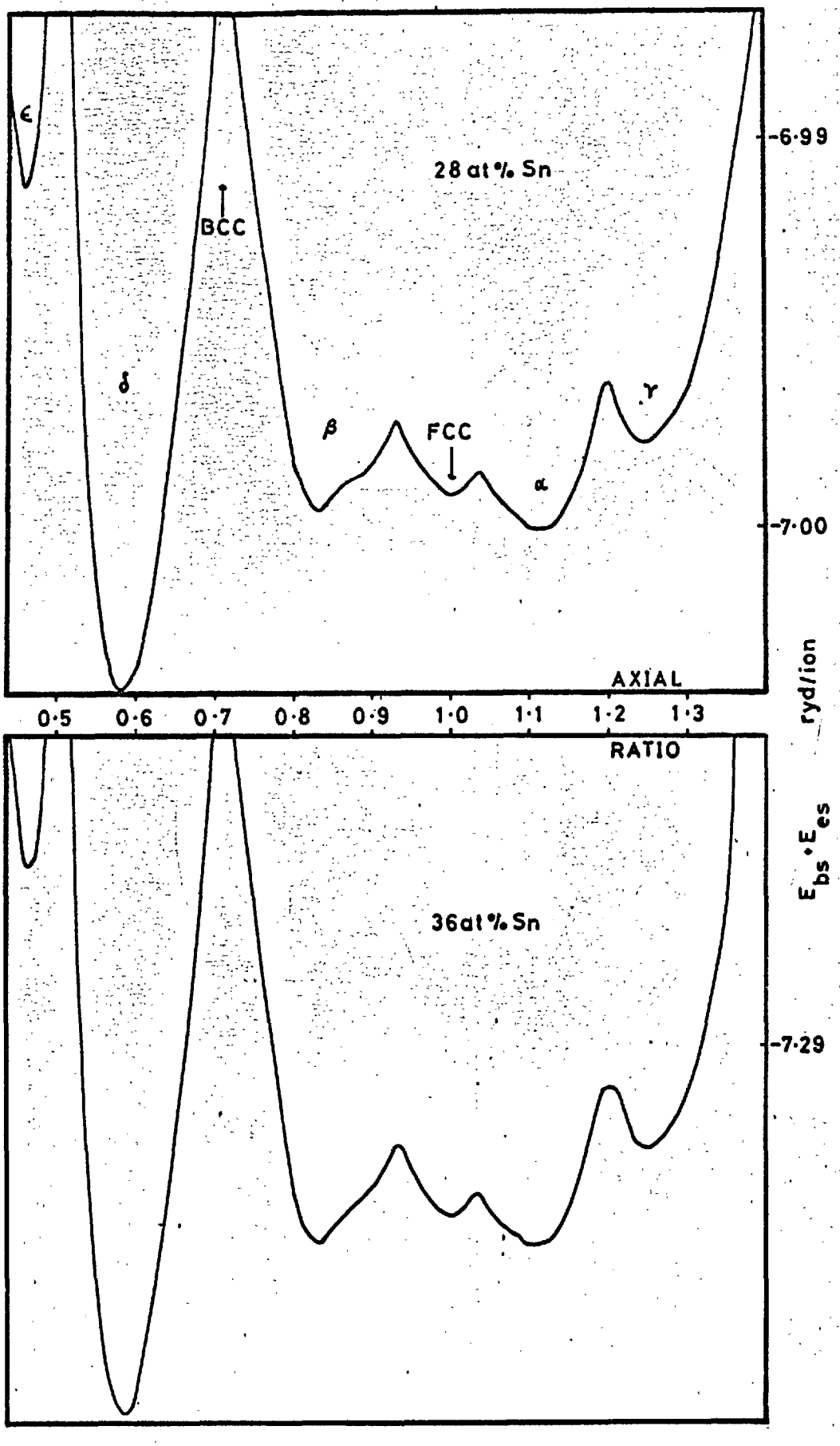

Figure 5.12 Total structural energy in the system In-Sn.

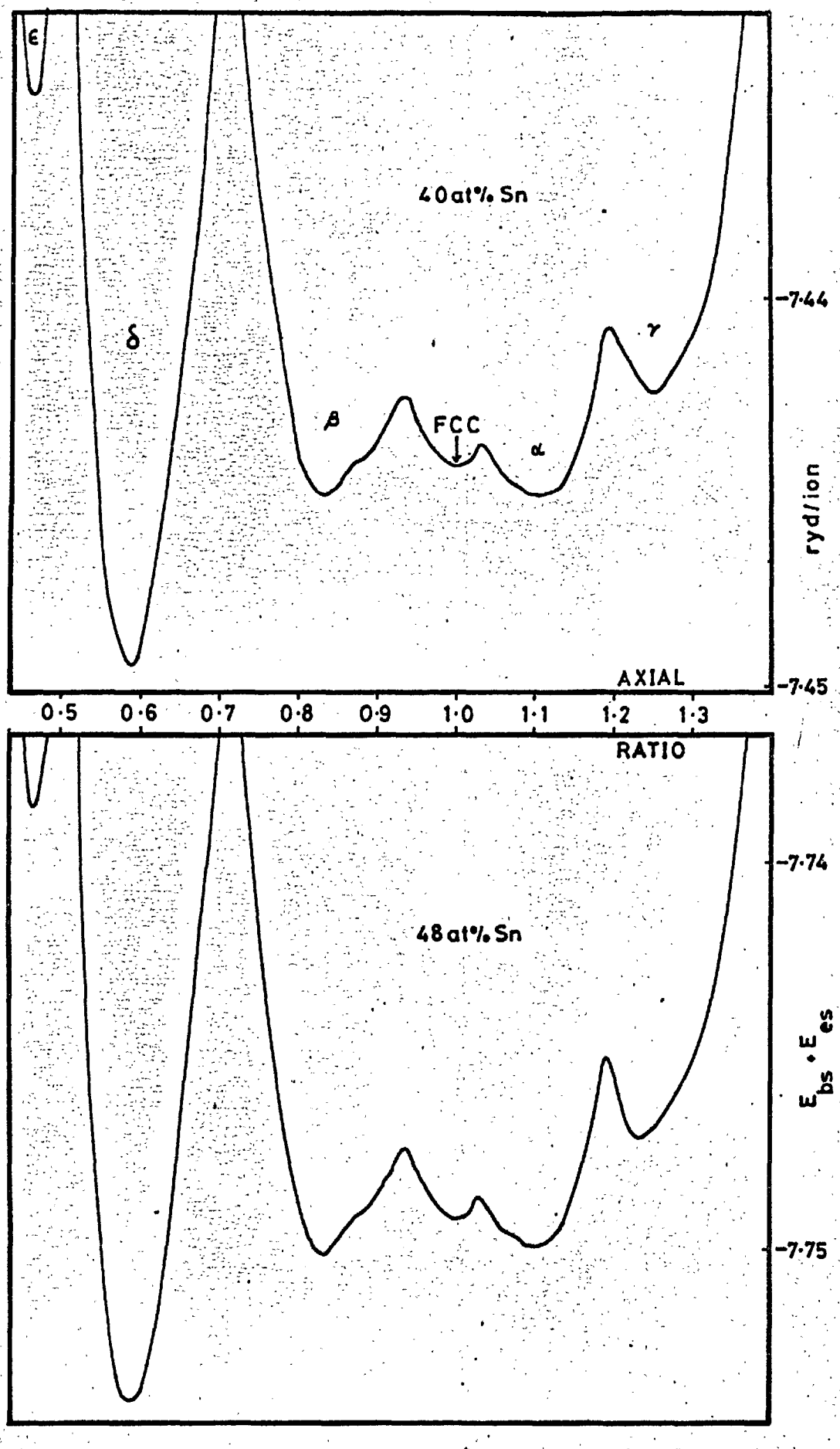

Figure 5.13 Total structural energy in the system In-Sn.

The indium-tin system

The total energy, calculated for various alloys in this system, is plotted as a function of axial ratio in Figs. (5.11) to (5.13). The picture is somewhat similar to that of In-Pb except that the hypothetical FCTγ structure does not play an important part. Furthermore, the FCTα structure remains dominant (apart from the FCTδ structure) to higher electron/atom ratio than in In-Pb. The FCTβ minimum comes down below FCTα at about 40 at.% Sn. The phase change in In-Sn occurs, in practice, at about 13 at.% Sn although there has been some argument (Pearson, 1967) as to the precise structure of the phase labelled β in the phase diagram (Fig. 1.10). Although it has been indexed as an FCTβ type structure, anomalies have been pointed out in the relative intensities of lines in the X-ray diffraction pattern (see Chapter 1).

The indium-mercury system

The total energy computed for this system is shown, as a function of $^{c}/_{a}$, in Figs. (5.14) to (5.16). It is interesting to note that the FCTβ structure vanishes very quickly and, furthermore, the FCTγ also ceases to be significant after only small additions of Hg (<4 at.%) Thus, apart from the FCTδ structure, the position is very much simplified, the only real choice of structure being between FCC and FCTα. This situation is sensible in view of the phase change (see Chapters 1 and 4) at about 7 at.% Hg. In fact the calculations do not show this phase change until about 36at.% Hg. Using the thermal energy parabola this change would take place somewhat earlier (at about 16 at.% Hg). An interesting development, in this system, is a slight degeneracy of the FCC minimum which by 40 at.% Hg has split into two minima corresponding to slight tetragonal distortion. As pointed out in Chapter 4 the present experimental results show a broadening of some of the Bragg profiles in the α_c phase which meant a diffraction pattern could be indexed as slightly tetragonal.

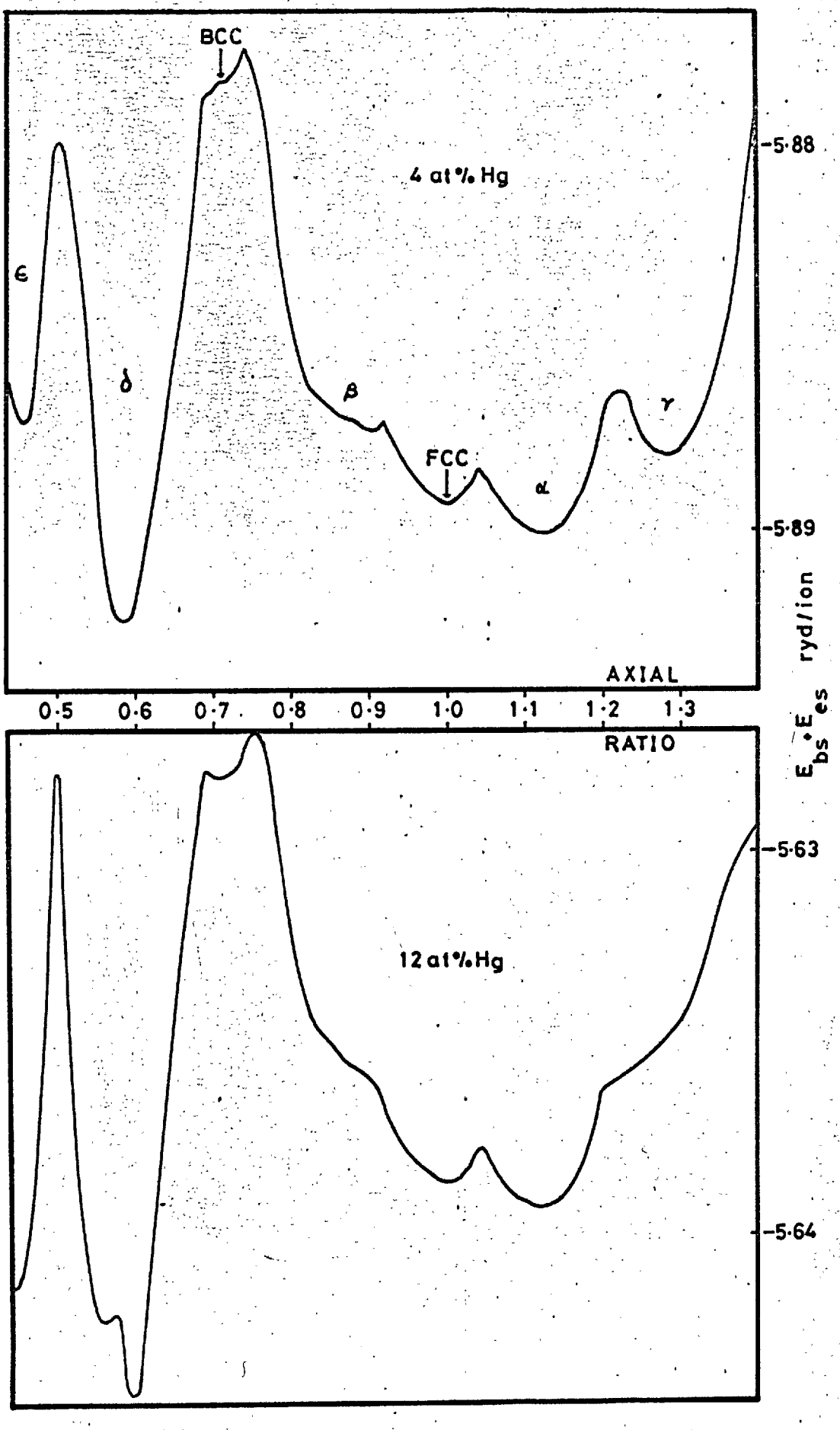

Figure 5.14 Total structural energy in the system In-Hg.

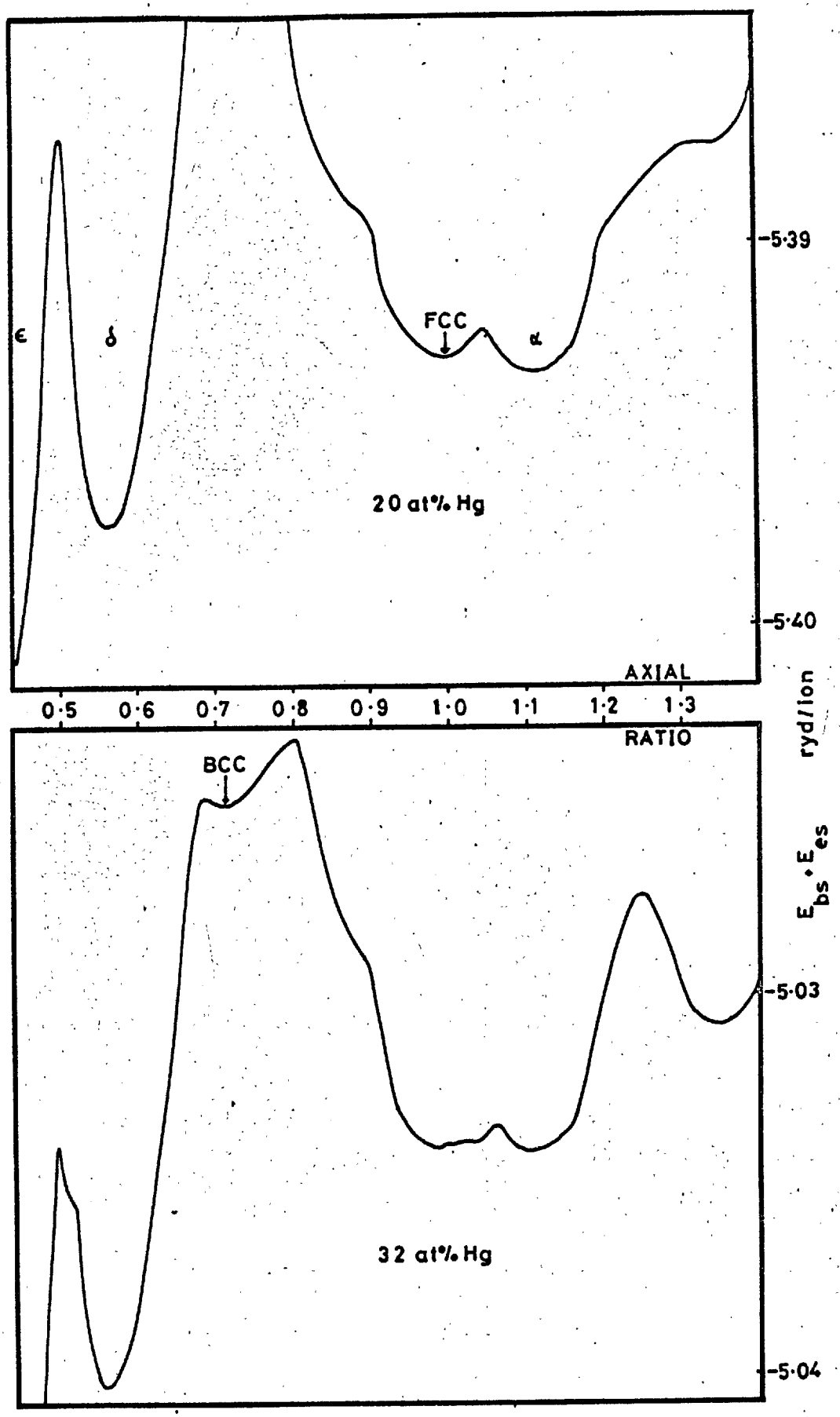

Figure 5.15 Total structural energy in the system In-Hg.

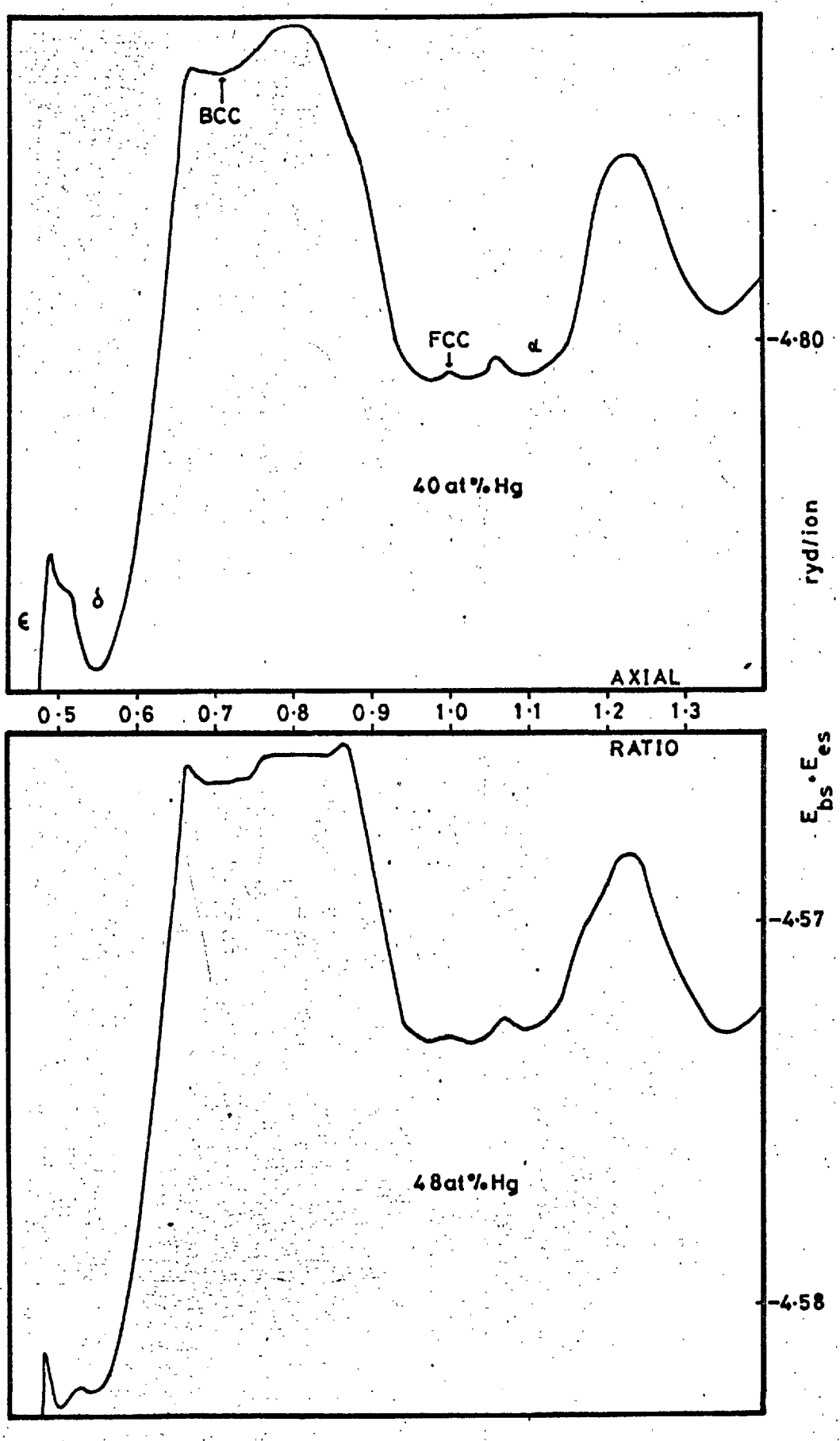

Figure 5.16 Total structural energy in the system In-Hg.

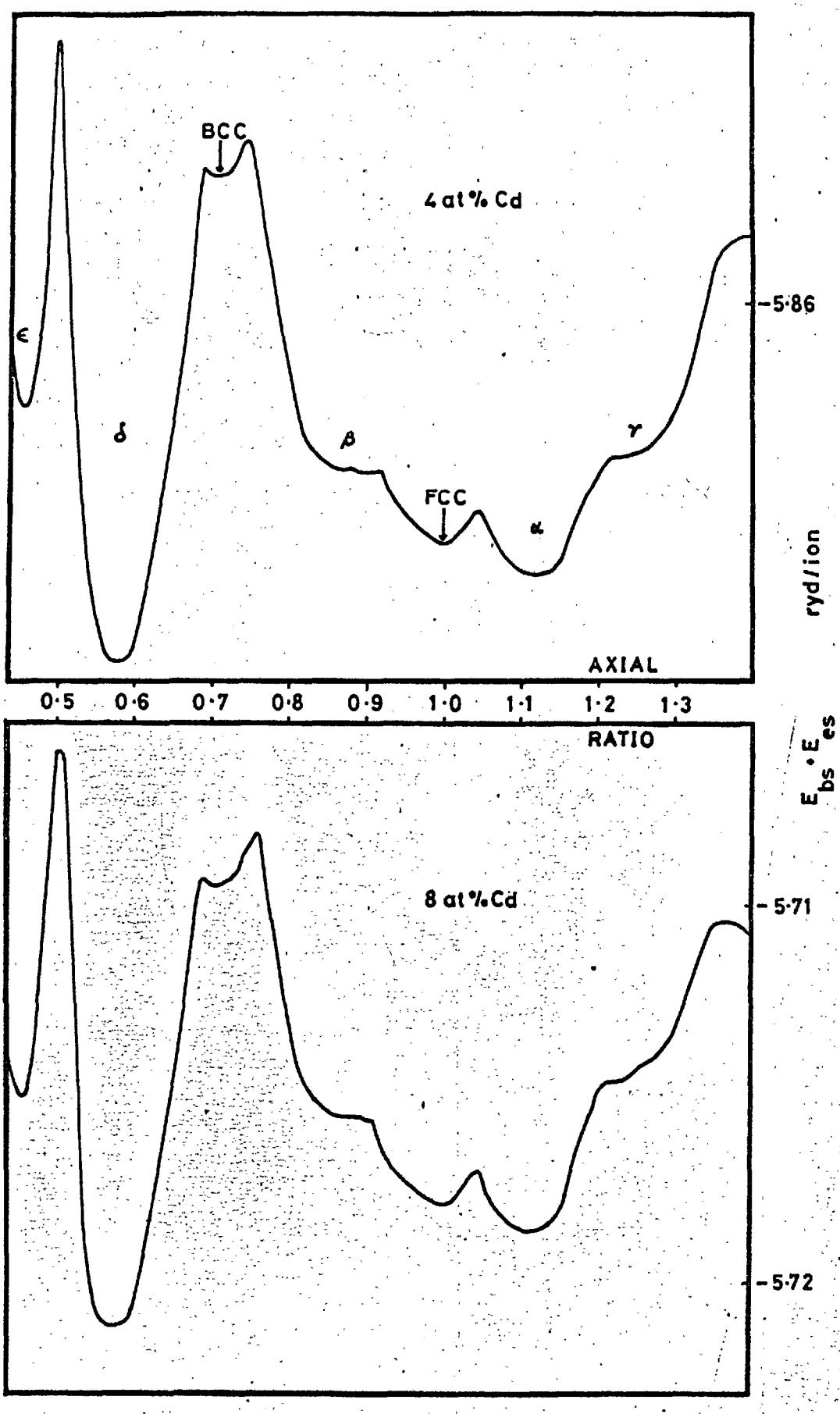

Figure 5.17 Total structural energy in the system In-Cd.

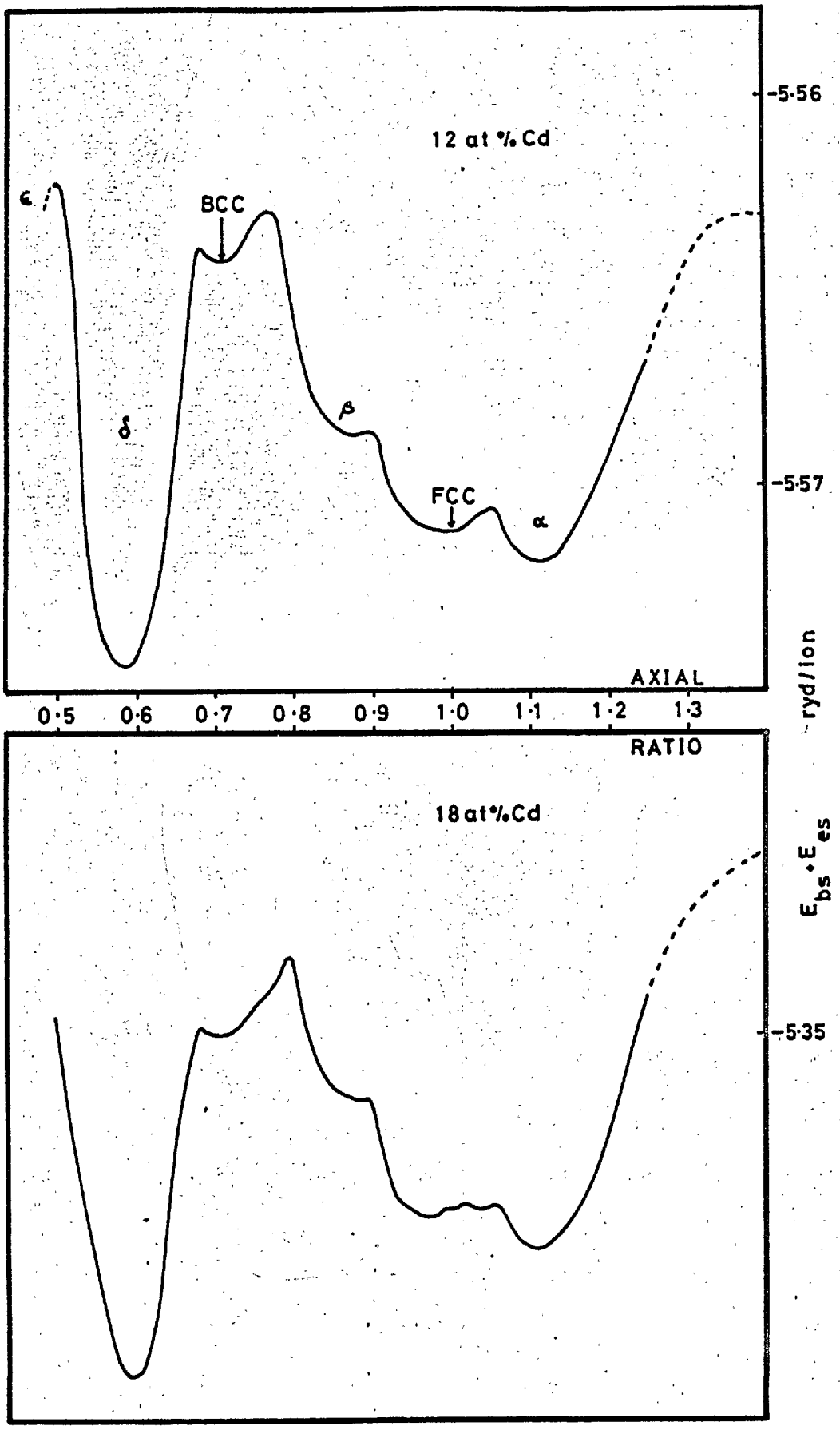

Figure 5.18 Total structural energy in the system In-Cd.

The indium-cadmium system

The calculations for In-Cd alloys are illustrated in Figs. (5.17) and (5.18) and the energy plots are seen to resemble the In-Hg picture. The FCTβ structure does not vanish quite so dramatically but the two dominant structures are again FCC and FCTα. The difference in energy levels between the two structures hardly alters, however, and there is no real indication of the observed FCTα → FCC structure change at about 8 at.% Cd.

The indium-bismuth system

The energies calculated for some alloys in the indium-bismuth system, are plotted as functions of axial ratio in Figs. (5.19) and (5.20). Addition of Bi rapidly changes the energy picture of pure indium. By 8 at.% Bi the FCC structure has vanished as a possibility and the FCTγ structure appears to be the most stable (even the FCTδ minimum has risen above it). Furthermore the FCTβ minimum is below the FCTα. By 20 at.% Bi the only two competitors for the structure are FCTβ and FCTγ and consequently a change of structure ought to be expected in this system whereas none is reported in the literature, or observed in the present experimental investigation. The limit of solid solubility of Bi in In may come before the structural change occurs, but since this limit has not been established with certainty (Hansen, 1958) it is probably worth investigating the In-Bi system at higher Bi compositions than those used here (i.e. higher than 10 at.% Bi).

The indium-lithium system has not been investigated theoretically but the indium-thallium system has been studied, however, since it shows a change of structure from FCTα to FCC which is sensitive to temperature but not related to the electron/atom ratio since In and Tl have the same valence, 3. These pseudopotential calculations were disappointing since, as can be seen from Figs. (5.21) and (5.22), they predict that the FCC structure should become progressively less likely

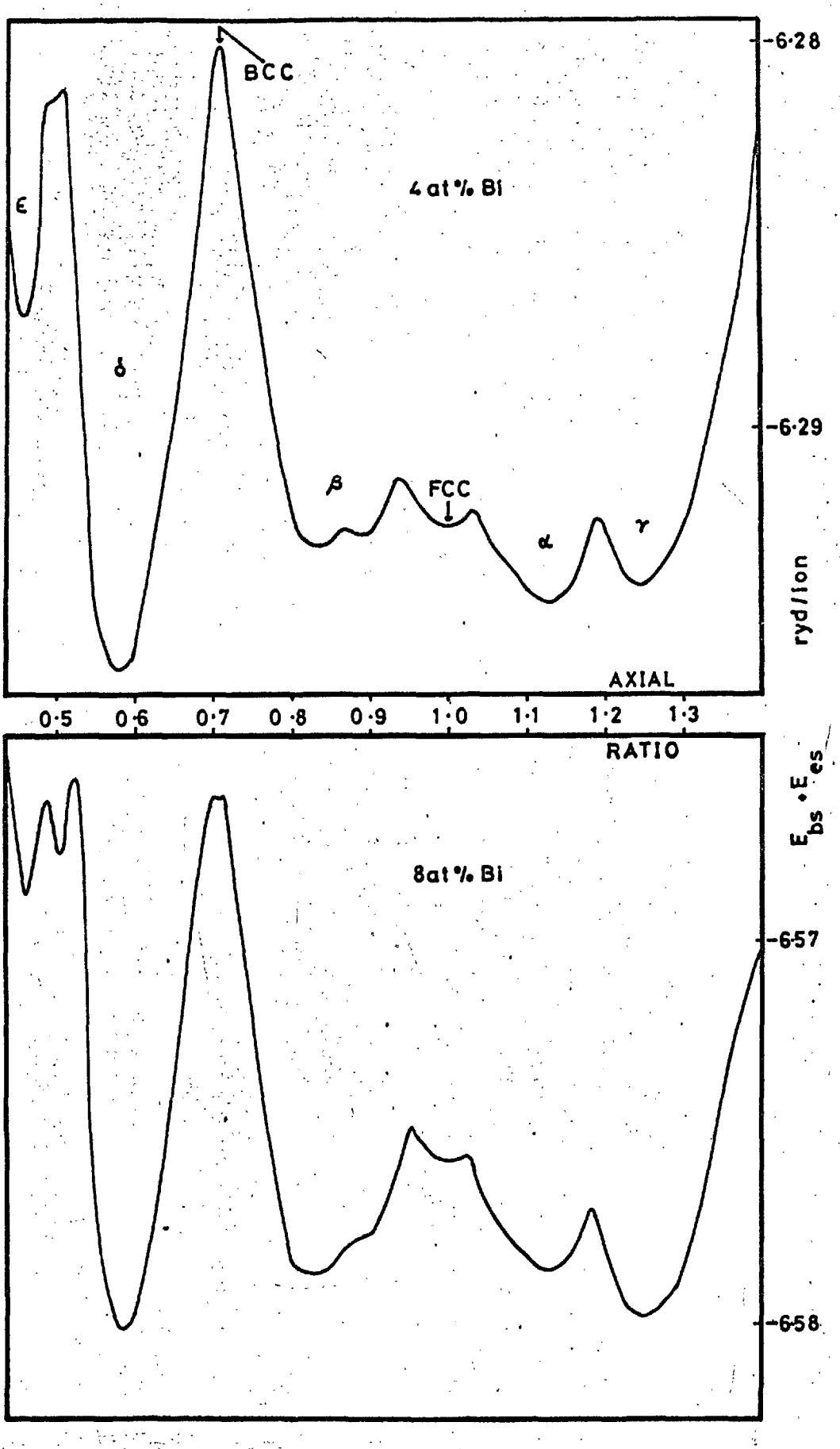

Figure 5.19 Total structural energy in the system In-Bi.

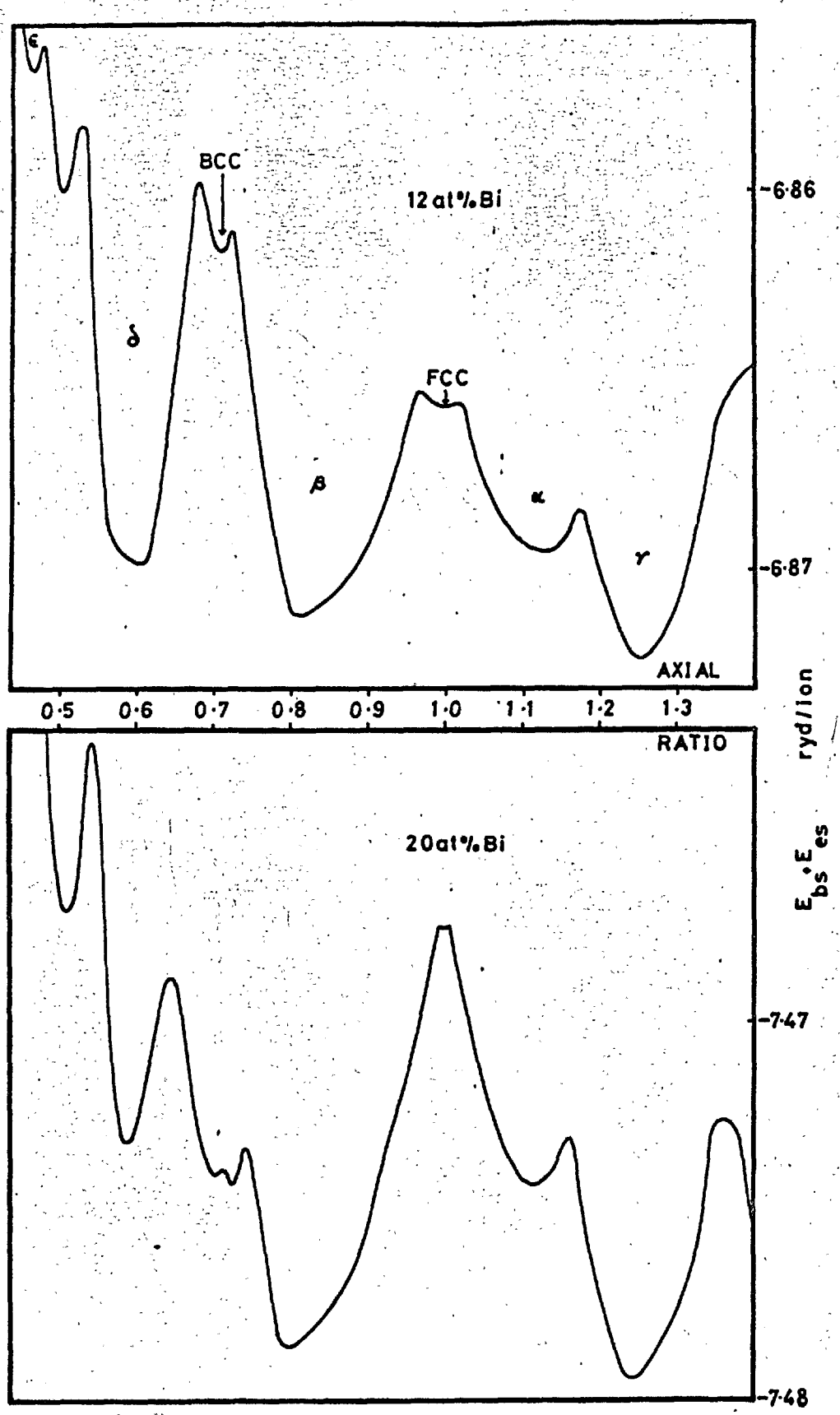

Figure 5.20 Total structural energy in the system In-Bi.

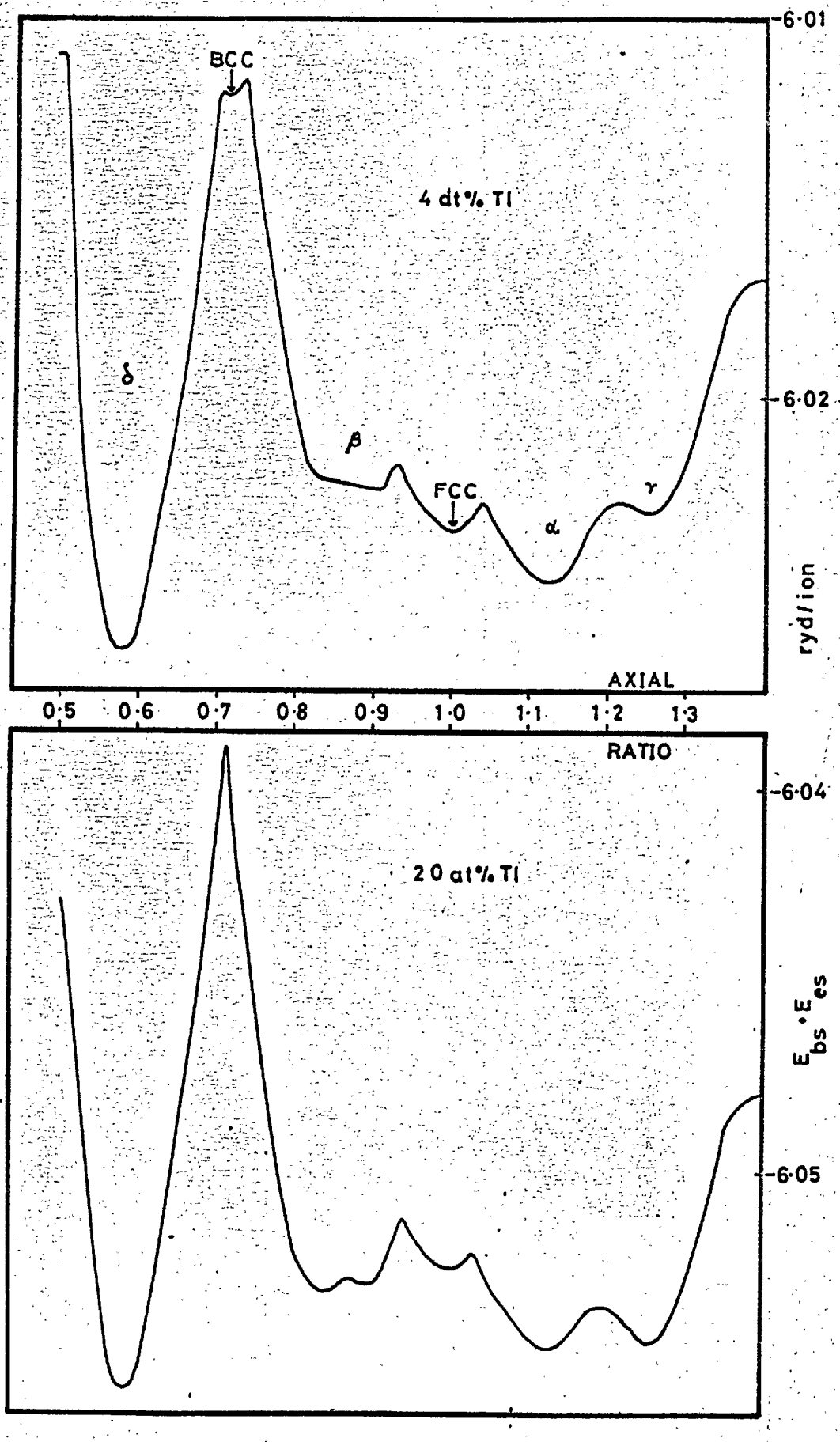

Figure 5.21 Total structural energy in the system In-Tl.

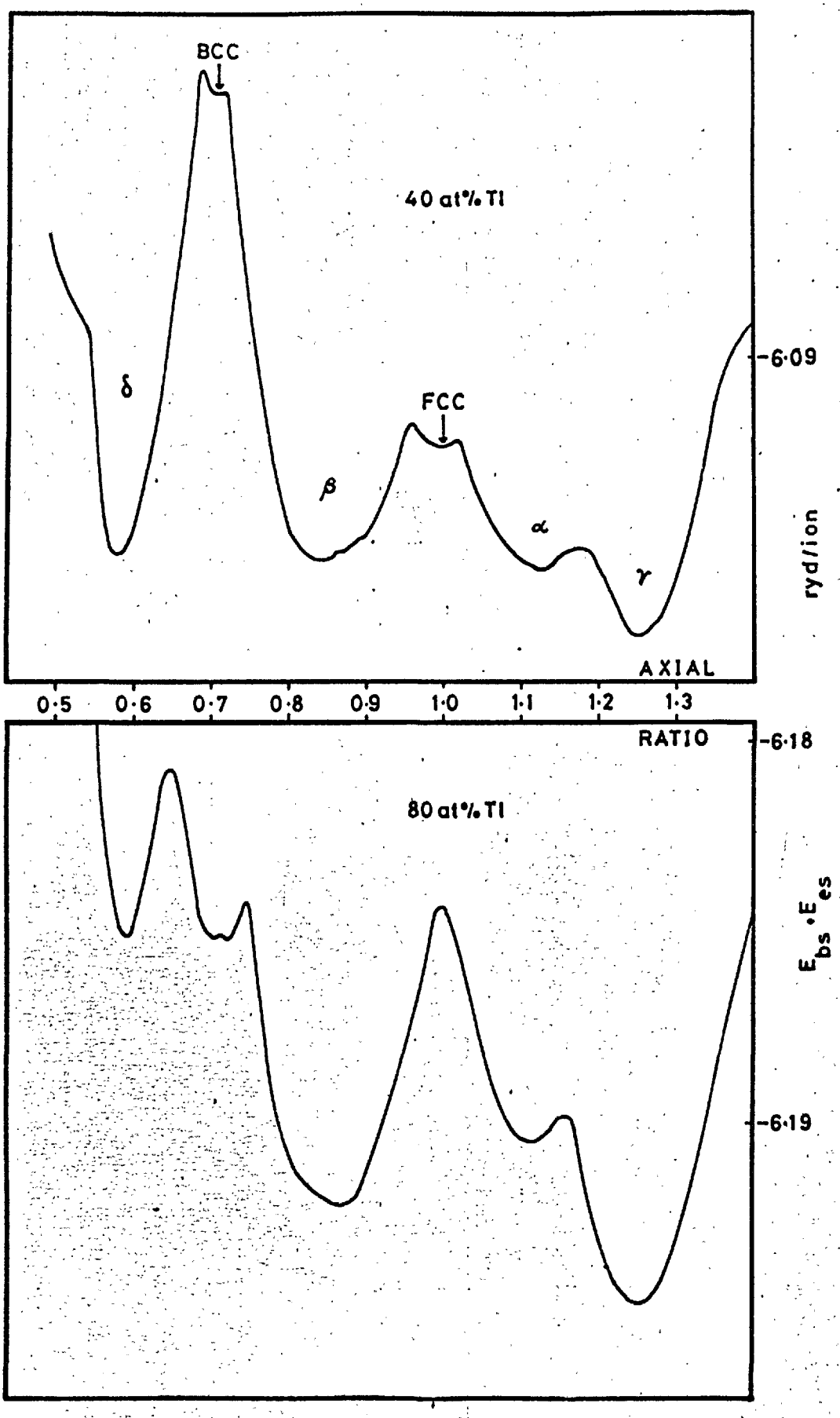

Figure 5.22 Total structural energy in the system In-Tl.

with increasing Tl concentration which is precisely the opposite of the experimental observations. This failure of the pseudopotential method is again, perhaps, due to the invalidity of the small core approximation when applied to the heavy metals such as Pb and Tl.

On the whole, the present application of the pseudopotential method, has been very satisfactory. The theoreticians have reduced the problem of computing band-structure energy to one of arithmetic and accountancy and the problem of electrostatic energy, though in general very complicated, appears to be tractable for simple structures. As a result, with an initial outlay of time spent on developing the programme for the computer, the pseudopotential method could well become a valuable tool for the physical metallurgist interested in the theory of alloy phases.

It is rather intriguing to see what would happen if the energy balance is artificially tipped by scaling down band-structure energy relative to the electrostatic energy. If, for example, it was scaled down by a factor of $1\frac{1}{2}$, then in pure indium, the FCTδ and FCTγ structures would vanish as possibilities and the axial ratio of the FCTα would be reduced to a value nearer the observed value (to c/a = 1.095 compared to the observed 1.085). The structural change from FCTα to FCTβ in In-Pb would occur at 12 at.% Pb, in agreement with experiment and, furthermore, the In-Hg structural change from FCTα to FCC would occur at about 8 at.% Hg (compared with the observed 7 at.% Hg) and the In-Cd structural change would occur at about 6 at.% Cd (compared with the observed 7.5 at.% Cd). This simple alteration in the relative magnitudes of the band-structure and the electrostatic energies will not, however, acoount for the FCC structure observed in In-Tl and In-Pb. Nevertheless in view of the effectiveness of this adjustment for the other systems, there would appear to be good ground for questioning whether the band-structure energy is over-estimated in the pseudopotential theory. An alternative possibility is that the thermal energy (which has not been amenable to estimation) as a function of tetragonal distortion, resembles in functional form the electrostatic energy and hence alters the balance in the total energy.

Wiggles

Neither the pseudopotential method nor the theory of the superconducting transition temperature is sufficiently developed at present to explain the fine details in the lattice parameter or T_c plots. The wiggles in the T_c and lattice parameter plots of the In-Cd alloys and the similar wiggles observed by Merriam in the In-Sn alloy system and the In-Pb system must be explained by qualitative examination of band structure calculations.

As mentioned in Chapter 1 the most reliable evaluation of the band structure of indium, is probably that of Hughes and Shepherd (1969) and this band structure was shown in Fig. (1.6). Since the observed kinks occur at only a few at.% solute it can probably be assumed that the band structure remains roughly rigid, at least for qualitative argument. If 2 at.% Cd is dissolved into indium, the fermi level will drop about 0.05 eV. The electrons will no longer overlap into the third zone at the corners C and the third zone ring of β-arms will break up into four 'sausages'. If the process of joining of the 'sausages' can be likened to the coalescence of liquid droplets then a discontinuous jump in area of the fermi surface is likely to occur. The corresponding discontinuity in energy would result in a discontinuity in the crystal lattice parameters. There is no reason why this should not apply to the cell volume. This interpretation of the kink at 2 at.% Cd is consistent with the findings in a recent paper by Higgins and Kaehn (1969) who analysed the results of T_c measurements under pressure p. The quantity $\partial T_c/\partial p$ may be related to the derivative of the density of states, with respect to energy. This latter quantity alters in a manner characteristic of changes in the fermi surface topology and, in particular, alters rapidly in the region of a 'van Hove' singularity. These singularities correspond to the creation or annihilation of electron or hole spheroids and the creation or annihilation of saddle points in the electron or hole surfaces. The Higgins and Kaehn calculations suggest that an electron saddle point disappears at 0.9 at.% Cd (the observed kink

is at 2 at.% Cd) i.e. the β ring breaks up. The same calculations, however reveal the possibility of an electron-pocket annihilation at 1.6 at.% Cd suggesting that small globules of fermi surface might be left at the corners of the β-ring when it dissociates. It is interesting to note that Hughes and Shepherd (1969) detected a slight swelling in the arms of the β ring at the corners.

When about 8 at.% Sn or Pb is dissolved in indium, the fermi level rises about 0.2 eV. It can be seen from Fig. (1.6) that this is just sufficient to cause overlap into the third zone at the points W i.e. the initiation of the α-arms. The energy discontinuity associated with the nucleation of these electron pockets would manifest itself in discontinuous changes of lattice parameter. It seems clear, therefore, that the explanation of the wiggles in the indium solid solutions, lies in consideration of the third-zone electron surface and not with the fourth zone as was previously thought (Svechkarev, 1964; Russell, 1966).

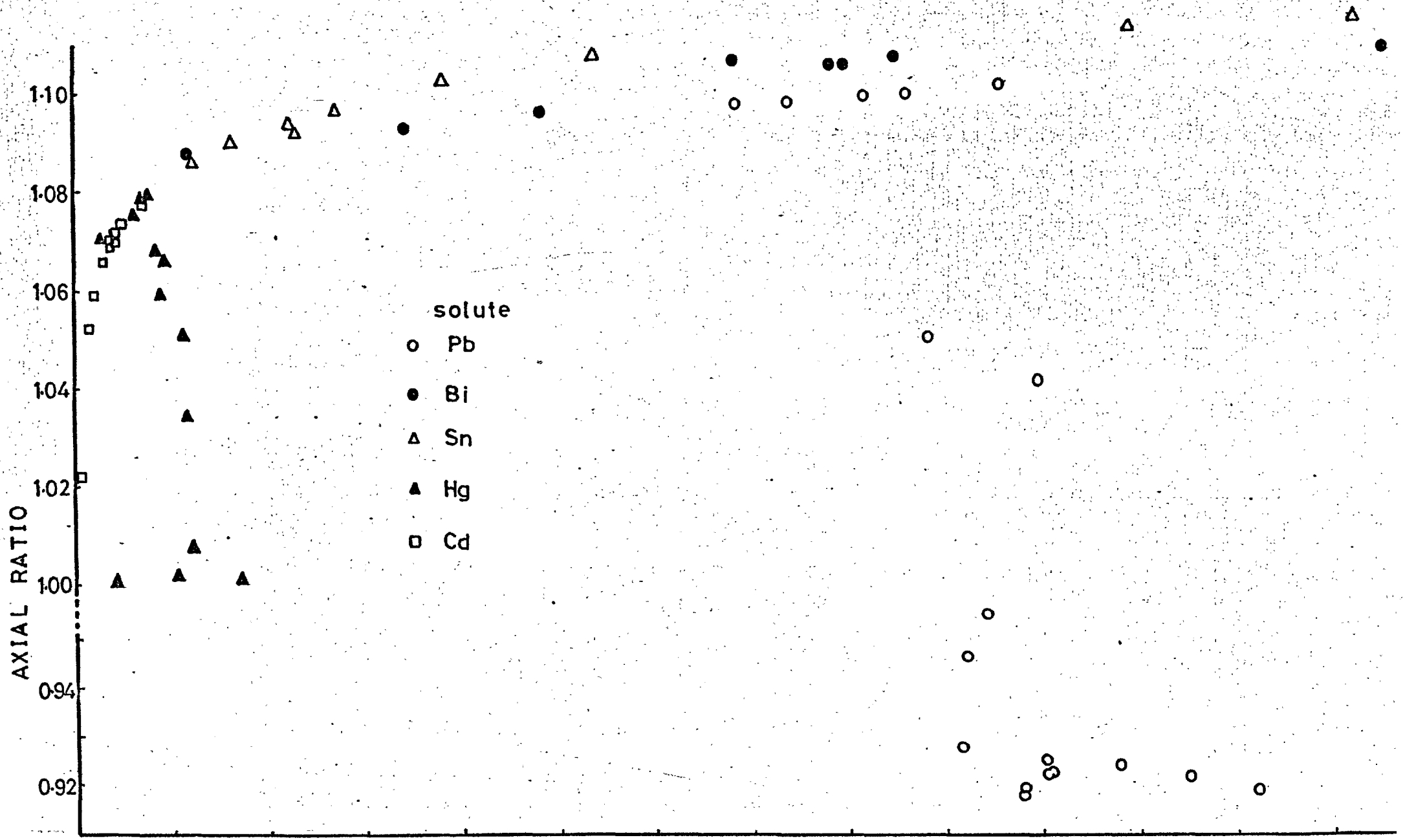

Figure 5.23 A plot of T_c against c/a for the indium alloys.

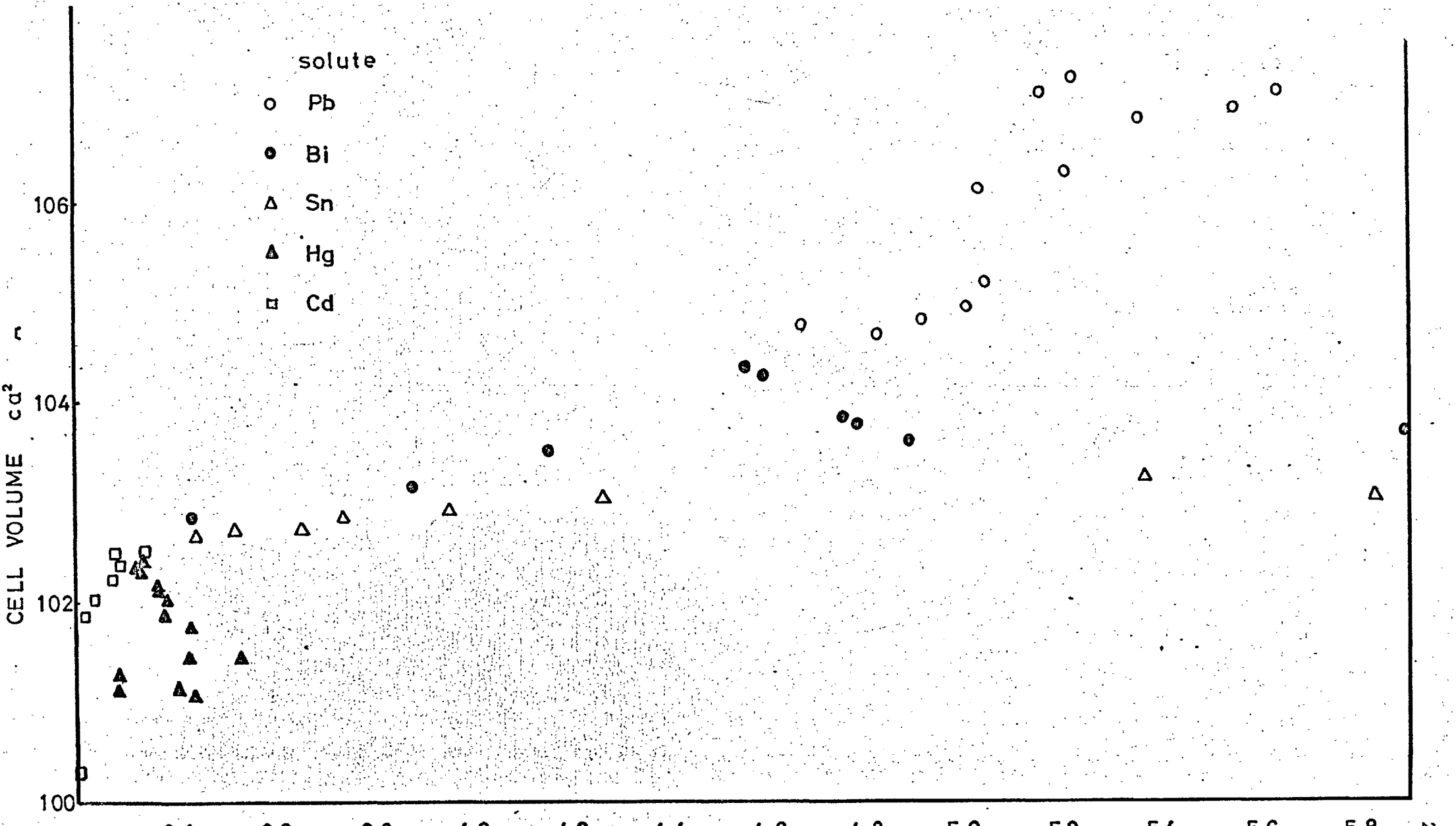

Figure 5.24 A plot of T_c against cell volume, ca^2, for the indium alloys.

5.3 THE TRANSITION TEMPERATURES, T_c

The transition temperature and the lattice parameter data have been collected together and plotted against each other. Figs. (5.23) and (5.24) are plots of T_c against axial ratio and atomic volume respectively. In neither case is a clear-cut functional form observed and it is concluded that no simple correlations can be inferred. This is hardly surprising when it has been seen how delicate is the energy balance that determines the structure, let alone the axial ratio. The transition temperature is no less sensitive to small changes in the pseudopotential or phonon spectrum.

There is, nevertheless, a pattern in the T_c plots as functions of the electron/atom ratio. Addition of higher valence atoms increases T_c whilst addition of lower valence atoms decreases T_c, though less dramatically. It is an intriguing exercise to see if this makes sense in the light of the observed band-structure. The density of states for indium evaluated by Hughes and Shepherd (1969) is shown in Fig. (5.25). Their pseudopotential was used to obtain energy eigenvalues at 8000 points in the Brillouin zone and the density of states histogram appears to consist of about 200 intervals. There are, thus, some 40 points per interval which may just make the fine detail of the density of states, statistically significant. The band structure is assumed to be rigid for small additions of solute and the Debye temperature is taken to be fixed at 109°K. The BCS equation (1.24) has been used here and fitted to the observed T_c of pure indium (3.4°K) by suitable choice of the coupling constant V. The resulting T_c's are plotted as a function of electron/atom ratio in Fig. (5.26). The actual T_c's observed in the present experiments (plus the In-Pb values of Russell, 1966) are plotted for comparison. The theoretical values rise with increasing $^{e}/_{a}$ but drop suddenly between 3.07 and 3.12 $^{e}/_{a}$ and rise again. The observed T_c's also rise, though rather more steeply, and those of In-Pb and In-Sn also drop at the phase boundary. The Hughes-Shepherd pseudopotential may, therefore, be predicting the phase boundary. Towards lower $^{e}/_{a}$ the theoretical T_c values go

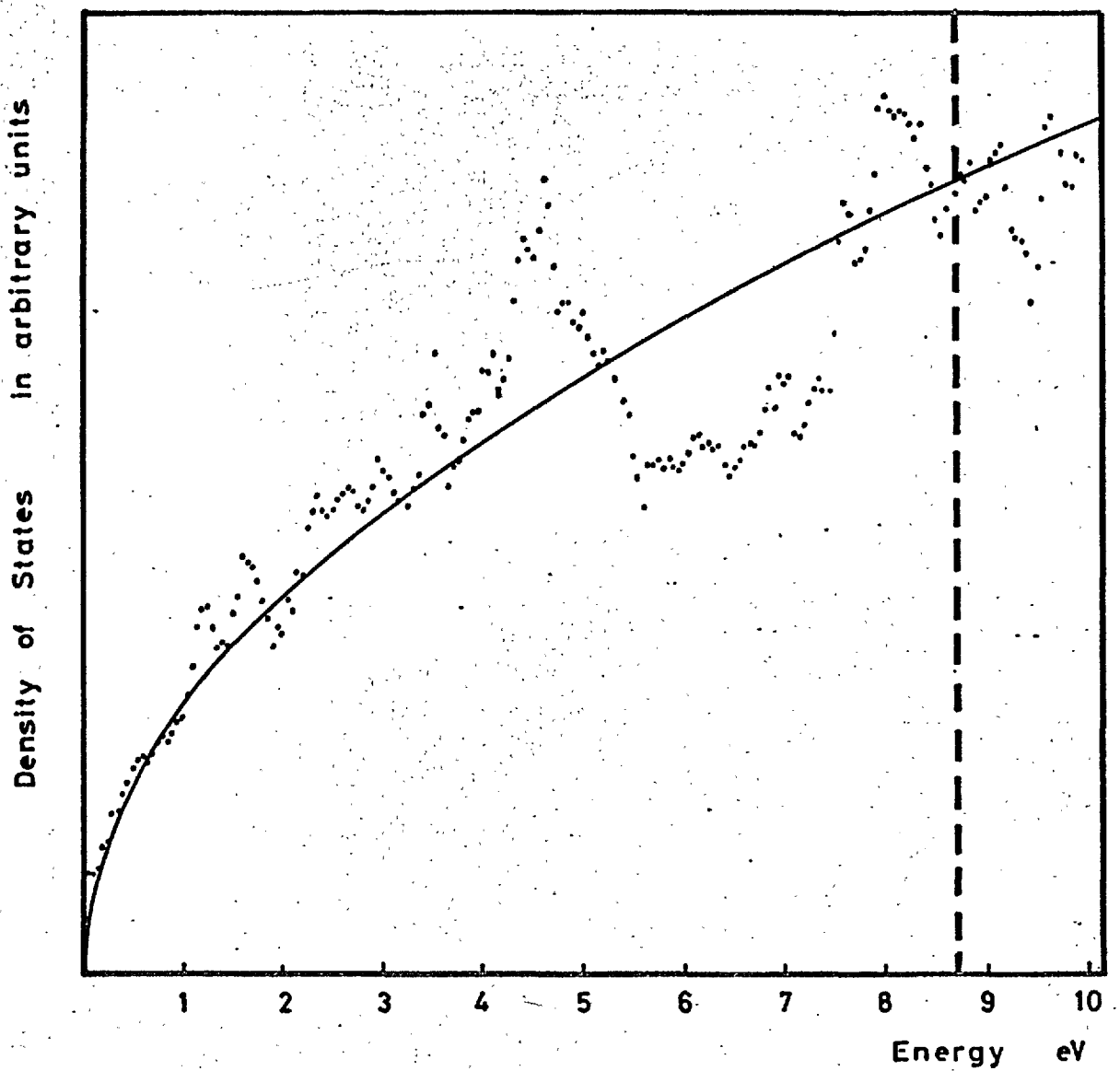

Figure 5.25 The density of states for indium – after Hughes and Shepherd (1969).

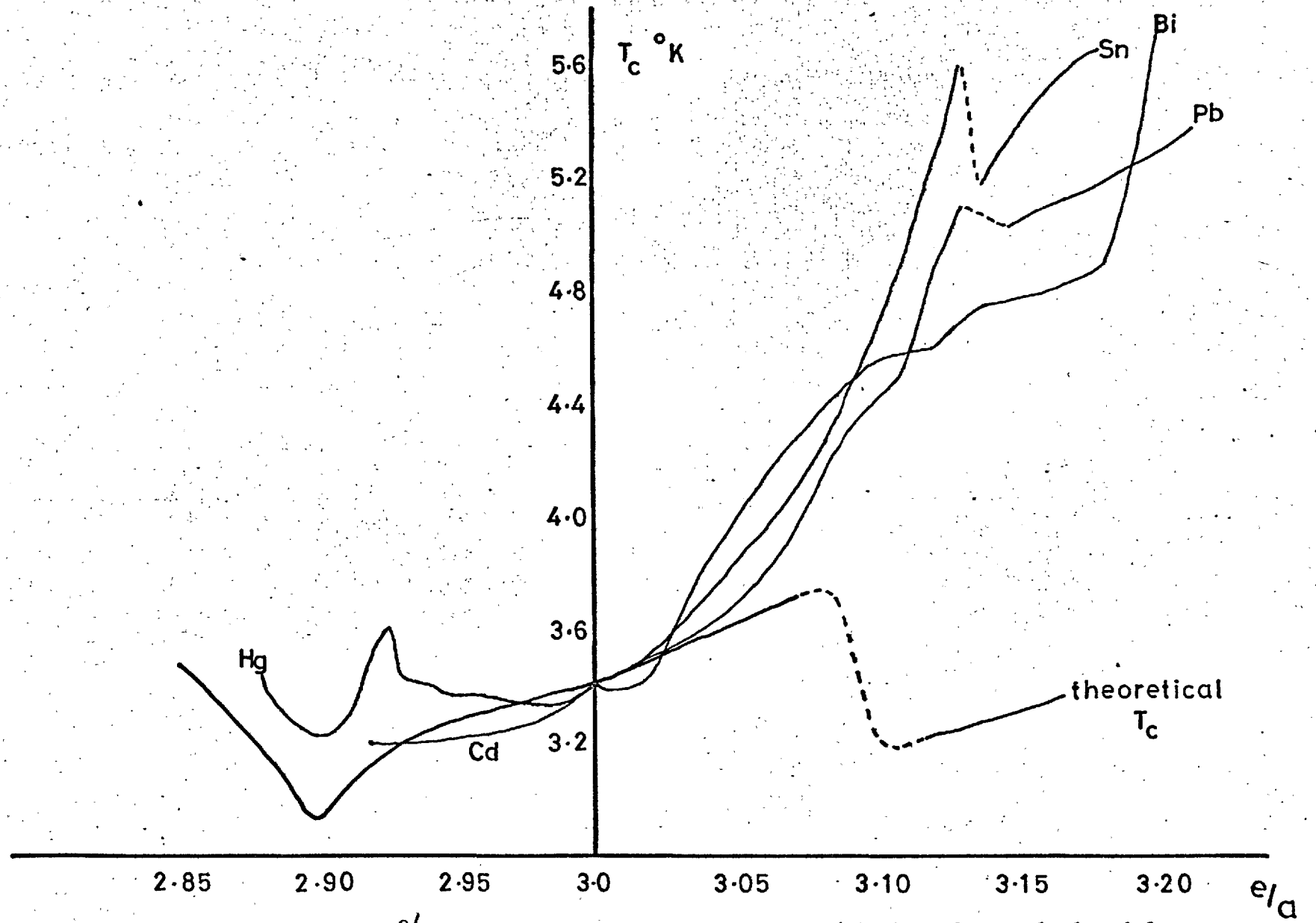

Figure 5.26 T_c as a function of $^{e}/_{a}$ for the indium alloys, compared with the values calculated from the density of states for indium.

through a pronounced dip. The T_c's observed for In-Cd alloys do indeed descend but insufficient alloys have been studied to detect any dip in the region of 10 at.% Cd. The results of Merriam do not cover this region either. The In-Hg values do not follow the theoretical curve very closely at first but do show a dip at precisely the same place.

REFERENCES

Animalu, A.O.E. and Heine, V., (1965), Phil. Mag. 12, 1249.

Atoji, M., Schirber, J.E. and Swenson, C.A., (1959), J. Chem. Phys. 31, 1628.

Barrett, C.S., (1962), Adv. X-ray Anal. 5, 33.

Carr, W.J. Jr., (1961), Phys. Rev. 122, 1437.

Fuchs, K., (1935), Proc. Roy. Soc. A151, 585.

Furukawa, K., (1959), Nature, 184, 1209.

Gamertsfelder, C., (1941), J. Chem. Phys. 9, 450.

Gunnell, B.J., (1970), Private Communication.

Hansen, M., (1958), "The Constitution of Binary Alloys", McGraw-Hill, N.Y.

Harrison, W.A., (1966), "Pseudopotentials in the Theory of Metals", Benjamin, N.Y.

Heine, V. and Weaire, D., (1966), Phys. Rev. 152, 603.

Higgins, R.J. and Kaehn, H.D., (1969), Phys. Rev. 182, 649.

Hughes, A.J. and Shepherd, J.P.G., (1969), J.Phys. C. (P.P.S.), 2, 661.

Inglesfield, J.E., (1969), J. Phys. C. (P.P.S.), 2, 1285.

Inglesfield, J.E., (1970), Thesis, University of Cambridge.

Merriam, M.F., (1966), Phys. Rev. 144, 300.

Pearson, W.B., (1967), "Handbook of Lattice Spacings and Structures of Metals and Alloys", Pergamon, London.

Russell, C.M., (1966), Thesis, Imperial College.

Segmuller, A. and Wincierz, P., (1959), Arch. Eisenh. 30, 577.

Shaw, R.W., and Harrison, W.A., (1967), Phys. Rev. 163, 604.

Svechkarev, I.V., (1965), J.E.T.P., 20, 643.

Ubbelohde, A.R., (1965), "Melting and Crystal Structure", Clarendon, Oxford.

Zener, C., (1947), Phys. Rev. 71, 846.

CHAPTER 6

CHAPTER 6

CONCLUSION

6.1 SUMMARY

1. A modification of a Bragg-Brentano diffractometer enables the rapid change from BB geometry to the fully-focusing Seeman-Bohlin geometry. A unique feature is the dovetail specimen track which gives the operator a considerable choice of angular ranges. In particular, the region (unobtainable on conventional diffractometers) between $162^{\circ}2\theta$ and $172^{\circ}2\theta$, is made available.

2. The instrument, by virtue of the interchangeable geometries, may readily be aligned without reference to a standard substance. This has not been possible with any other SB diffractometer reported.

3. The ability to increase the intensity, without loss of resolution, of a Bragg reflection, by increasing the divergent slit aperture, was demonstrated. The stationary nature of the specimen in the SB mode simplified the use of a cryostat on the instrument. Considerable profile improvement was occasioned when the indium alloys were cooled to $78^{\circ}K$.

4. A complete review was made of all the errors associated with the SB geometry. Many of the SB errors were analysed here for the first time, in particular those due to axial divergence. The availability of the high angle region allowed an experiment to be performed to check the existence of the $\tan^3\theta$ centroid shift due to the Lorentz factor and dispersion.

5. Examination of the error functions suggested the use of two extrapolation functions for elimination of systematic errors. These are presented in tabular form. A least squares programme was also devised which incorporated this elimination in analytic form.

6. A probe was constructed, for the measurement of superconducting transition temperatures by the AC inductance method, the magnetisation and temperature of the specimens being displayed simultaneously on a twin pen chart recorder. The equipment yielded T_c values to $\pm$ 0.01°K and $\pm$ 0.03°K at temperatures below and above 4.2°K respectively.

7. The results of the X-ray diffraction experiments and the T_c measurements, are summarized in Table (6.1). The wiggle, in the axial ratio and the T_c plots in In-Cd, at 2 at.% Cd, which was reported by Merriam (1966), has been confirmed by careful experiment. The kink was also found in the atomic volume plot. The possibility of composition errors has been eliminated by applying internal consistency tests to the results. Taking into consideration the most recently available band-structure data, the wiggle is attributed to the dissociation of the third-zone β-ring into separate arms. Similar kinks observed by Merriam in In-Sn and In-Pb, at about 8 at.% solute are attributed to the initiation of the third-zone α-arms.

8. The Madelung (or Ewald-Fuchs) constant α is evaluated for tetragonal distortions of the FCC structure and the electrostatic energy calculated therefrom. The band-structure energy is calculated using the Heine-Animalu form factors. The total structurally dependent energy is computed for pure indium and a number of its solid solution alloys. The most stable structure for indium, indicated by these pseudopotential calculations, is FCTδ ($^c/_a$ = 0.58) and reasons for this structure not being observed are considered. In particular the observed structure in the liquid state is taken into account in the solidification process. For the region of $^c/_a$

TABLE 6.1

System	Structure	Phase width at.% solute	T_c Variation with solute composition	c/a Variation with solute composition	Remarks
In-Pb	FCT α	0-13.5	steep rise	gradual rise	both T_c and c/a drop discontinuously at 13.5 at.% Pb.
	FCT β	13.5-28	steep rise	remains constant	T_c drops discontinuously at 28 at.% Pb whilst c/a changes at 32 at.% Pb.
	FCC	28-100	slight rise	-	33 at.% Pb may be indexed as slightly tetragonal.
In-Sn	FCTα	0-13.5	steep rise	steep rise	
	FCTβ	135->18	gradual rise	not measured	
In-Hg	FCTα	0-7.5	slight dip followed by steady rise	gradual decline becoming steep	
	FCC	7.5->12	goes through a minimum at 10 at.% Hg	-	11 and 12 at.% Hg samples may be indexed as slightly tetragonal. The atomic volume has a dip between 6 & 8 at.% Hg.
In-Cd	FCTα	0-7.5	gradual decline	gradual decline becoming steep	kink observed in T_c, c/a & ca^2 at 2at.%Cd
In-Bi	FCTα	0->10	steep rise becoming steeper at 9 at.% Bi	rises to 5%, declines & rises again at 8% Bi	very poor quality peaks above 3at.%Bi
In-Li	FCTα	0 - ?	no change for 1-7 at.% Li	similar to T_c	likely Li solubility <1%

TABLE 6.2

SUMMARY OF PSEUDOPOTENTIAL CALCULATIONS

System	Structure	Phase width at.% solute	Comments
In-Pb	FCTα	0 - 16	FCTγ is a strong competitor
	FCTβ	16—	The FCC structure fails to manifest itself. The dominant structure at high Pb composition is BCC.
In-Sn	FCTα	0 - 40	
	FCTβ	40 -	The observed structures beyond FCTβ cannot be represented by an FCT structure
In-Cd	FCTα	0 -	FCC remains a strong possibility but never becomes dominant.
In-Hg	FCTα	0 - 36	
	FCC	36 -	The FCC becomes slightly degenerate being strictly resolvable into two slightly tetragonal structures
In-Bi	FCTα	0 - 8	No FCTβ structure is, in fact, observed up to 10 at.% Bi.
	FCTβ	8 -	
In-Tl	FCTα	0 -	The FCC structure fails to manifest itself.

within ± 0.25 of unity, the three structures FCC, FCTα ($^{c}/_{a} \sim 1.1$) and FCTβ ($^{c}/_{a} \sim 0.9$) are indicated, the most stable of these being FCTα, which makes good sense of the observed structure of pure indium. A fourth possible structure is FCTγ ($^{c}/_{a} \sim 1.25$) whilst the BCC structure (FCT, $^{c}/_{a} = 0.71$), which is predominant when only electrostatic energy is concerned, vanishes when the band structure term for indium is added. The BCC structure is not, in fact, observed in any of the lower composition alloys.

Simple models are considered to obtain an average phonon frequency but these lead to insignificant variations in thermal energy with tetragonal distortion. The tendency towards increasing distortion with decreasing temperature is used to propose a model thermal energy well centred on FCC. This is used qualitatively, in particular to explain why the FCTγ structure might not be observed in the In-Pb system. It is considered that the FCTδ structure might be a possibility for indium and that experiments might be devised to find it.

9. In order to apply the pseudopotential method to various indium based alloys the theory of the electrostatic energy is extended to deal with systems of constituents with different valence. This appears to be the first time calculations on such systems have been performed and the results are summarized in Table (6.2). The success in making sense of the sequences of phases observed in the indium alloys is most encouraging. The failure of the model at higher concentrations in In-Pb and In-Tl is considered to result from the non-applicability of the small-core approximation to these metals.

10. It is observed, with interest, that a scaling down of the band-structure energy gives results very close to experiment.

11. No correlation between T_c and axial ratio or atomic volume, is obvious. No attempt is made to justify the trends in T_c from basic theory. In an attempt, however, to correlate these

trends with the available band-structure data, the individual points on the density-of-states histogram of Hughes and Shepherd (1969) are assumed to have statistical significance. Taking a rigid band-structure and the BCS equation for the transition temperature, values of T_c as a function of electron/atom ratio are calculated. Comparison with observed values is favourable and, furthermore, the Hughes-Shepherd results appear to imply discontinuities in the density of states in the regions of the observed phase boundaries.

6.2 SUGGESTIONS FOR FURTHER WORK

1. The β phase in In-Sn requires further examination in order to establish whether it has the FCTβ structure.

2. T_c measurements in the region of 10 at.% Cd in the In-Cd system, may reveal a dip as in the In-Hg system. This would make an interesting comparison with the T_c values calculated from the Hughes-Shepherd density of states.

3. The determination of T_c across the In-Bi system may prove interesting and help to analyse the phase diagram.

4. Further experiments are needed to establish the limit of solubility of Bi and of Li in In.

5. The pseudopotential calculations may be extended to other systems based on indium e.g. In-Ga, In-Mg. Calculations might also be performed on systems based on other simple metals, in particular on Tl.

6. Indium should be subjected to high pressure or to low temperature cold-working in an attempt to obtain the possible FCTδ structure predicted by the pseudopotential theory.

7. The Allen-Cohen theory for prediction of T_c might be applied to alloys. This would require rather a lot of programming.

REFERENCES

Hughes, A.J. and Shepherd, J.P.G., (1969), J. Phys. C. (P.P.S.), 2, 661.

Merriam, M.F., (1966), Phys. Rev. 144, 300.

Appendix 1

centroid programme

```
      INTEGER L,M,NN(100),NS      ,NP,NQ,I
      READ(5,106)RTN
      READ(5,106)RTP
      READ(5,100)M
C     M=NO. OF PEAKS
C    RTN=SQRT(N)*LAMBDA/2
      DO 50 L=1,M
      WRITE(6,110)L
      READ(5,101)(NM(L))
      NN=NM(L)
      X=0
      TMX=0
      VMX=0
      D=0
      IMX=1
      READ(5,102)(H(I),I=1,NN)
      READ(5,105)TH2,LJ,KL,SS
      SS=SS*0.03125
C     NM(L)=NO. OF PTS TO PEAK L
C    LJ=DISTANCE BETWIXT PEAKS
C     KL=INDEX OF PLANES REDUCED
      E=LJ
      DO 62 MJ=2,3
      LR=1
      NS=NM(L)
      NNN=NM(L)
      J=1
      Z=MJ
      E=E*Z*0.45
      LJ=E
      NP=1
      NQ=1
      NR=1
      X=(H(NS)-H(J))/FLOAT(NS-J)
      DO 30 I=J,NS
      T(I)=H(I)-(H(J)+X*FLOAT(I-J))
   30 CONTINUE
      IF(MJ-2)4,15,4
   15 DO 80 I=1,NS
      IF(T(I)-TMX)80,80,16
   16 TMX=T(I)
      IMX=I
   80 CONTINUE
      VMX=IMX
      AP=TH2+      (VMX-1.0)*SS
      AP=RTP(KL)/SIN(AP*3.14159/360.0)
      WRITE(6,111)AP
    4 R=0
      S=0
      LR=LR+1
      IF(LR-10)31,31,32
   32 WRITE(6,109)G
      GO TO 9
   31 DO 40 I=J,NS
      IF(I-NNN)12,12,21
   21 T(I)=0
   12 R=R+T(I)*FLOAT(I)
      S=S+T(I)
   40 CONTINUE
      G=R/S
      WRITE(6,104)G,J
    5 K=G
      BG=K
      IF(G-BG-0.5)73,74,74
   74 K=K+1
   73 J=K-LJ
      NS=K+LJ
      IF(J)1,1,2
```

Appendix 1

```
    1 J=1
      WRITE(6,112)
    2 IF(K -NP)7,6,7
    7 IF(K -NQ)8,6,8
    8 IF(K -NR)11,6,11
   11 NR=K
      NP=K +1
      NQ=K -1
      GO TO 4
    6 CONTINUE
   14 WRITE(6,103)G,NS    ,NQ,NP,L,NB
    9 TH3=TH2
      TH2=TH2+      (G-1.0)*SS
      TH1=TH2/2.0
      AG=RTN(KL)/SIN(TH1*3.14159/180.0)
      WRITE(6,107)TH2,AG
      IF(D-2.0)49,45,49
   45 TH2=TH3
      NR=1
      GO TO 4
   49 TH2=TH3
   60 D=0




      NS=NN
      NP=1
      NQ=1
      NR=1
       J=1
      LR=1
   62 CONTINUE
      DO 70 I=1,300
      T(I)=0
   70 CONTINUE
   50 CONTINUE
  100 FORMAT(I3)
  101 FORMAT(I3)
  102 FORMAT(21F3.0)
  103 FORMAT(6H  G = ,F8.4,8H  NS =  ,I3,8H  NQ =  ,I3,8H  NP =  ,I3,4
     TL =  ,I3,6H NB=  ,I3)
  104 FORMAT(17H  CGTEMPORARY =  ,F8.4,5H J = ,I3)
  105 FORMAT(F6.3,I3,I1,F2.0)
  106 FORMAT(9F7.6)
  107 FORMAT(8H TH2  = ,F7.3,8H  AG  = ,F8.6///)
  108 FORMAT(5H T = ,8F8.1)
  109 FORMAT(15H  LOOPED G =   ,F8.4)
  110 FORMAT(6H L  = ,I3//////)
  111 FORMAT(8H  AP  = ,F8.6//)
  112 FORMAT(14H J IS NEGATIVE)
      STOP
      END
```

APPENDIX 1

Centroid Programme

Reads in $\frac{\sqrt{(h^2 + k^2 + \ell^2)}\lambda}{2}$ for $\lambda = \lambda_{centroid}$ and $\lambda = \lambda_{peak\,\alpha_1}$

Reads in the intensity H(I) across the profile from low 2θ at intervals of step size SS (in $^{o}2\theta$) from a base angle TH2 (in $^{o}2\theta$). Also reads in LJ as α_1/α_2 doublet separation (in $^{o}2\theta$). Chooses one of two multiples of LJ and assigns LJ to the result.

Draws a straight line from the first intensity readings to the last by computing its slope X. Then subtracts trapezium below this line. Looks for peak valuesTMX of the remaining intensity data T(I) and computes the corresponding lattice parameter AP.

Computes the sum $R = \Sigma\, i\, T_i$ and the sum $S = \Sigma T_i$ across the profile and produces a first centroid $G = R/S$. Selects a point LJ to the left of G and a point LJ to the right of G and a new range of integration (summation) defined by these points. The process iterates until G is in the centre of the range of integration. Repeats process for larger range using the second value of LJ.

GAMA = 15

TH=	20	EPS=	.061958	TH=	25	EPS=	.048849	TH=	30	EPS=	.039433
TH=	35	EPS=	.032182	TH=	40	EPS=	.026436	TH=	45	EPS=	.021768
TH=	50	EPS=	.017873	TH=	55	EPS=	.014598	TH=	60	EPS=	.011906
TH=	65	EPS=	.009680	TH=	70	EPS=	.007801	TH=	75	EPS=	.006173
TH=	80	EPS=	.004726	TH=	85	EPS=	.003407	TH=	90	EPS=	.002173
TH=	95	EPS=	.000989	TH=	100	EPS=	-.000174	TH=	105	EPS=	-.001345
TH=	110	EPS=	-.002554	TH=	115	EPS=	-.003834	TH=	120	EPS=	-.005227
TH=	125	EPS=	-.006787	TH=	130	EPS=	-.008588	TH=	135	EPS=	-.010740
TH=	140	EPS=	-.013411	TH=	145	EPS=	-.016877	TH=	150	EPS=	-.021605
TH=	155	EPS=	-.028457	TH=	160	EPS=	-.039136	TH=	165	EPS=	-.057385
TH=	170	EPS=	-.094051	TH=	175	EPS=	-.203094				

GAMA = 30

TH=	35	EPS=	.029258	TH=	40	EPS=	.025149	TH=	45	EPS=	.021768
TH=	50	EPS=	.018841	TH=	55	EPS=	.016205	TH=	60	EPS=	.013769
TH=	65	EPS=	.011501	TH=	70	EPS=	.009432	TH=	75	EPS=	.007642
TH=	80	EPS=	.006105	TH=	85	EPS=	.004767	TH=	90	EPS=	.003573
TH=	95	EPS=	.002481	TH=	100	EPS=	.001456	TH=	105	EPS=	.000466
TH=	110	EPS=	-.000514	TH=	115	EPS=	-.001513	TH=	120	EPS=	-.002560
TH=	125	EPS=	-.003690	TH=	130	EPS=	-.004949	TH=	135	EPS=	-.006400
TH=	140	EPS=	-.008138	TH=	145	EPS=	-.010311	TH=	150	EPS=	-.013169
TH=	155	EPS=	-.017167	TH=	160	EPS=	-.023237	TH=	165	EPS=	-.033573
TH=	170	EPS=	-.054797	TH=	175	EPS=	-.119956	TH=	180	EPS=	*.847774
TH=											

GAMA = 45

TH=	50	EPS=	.015315	TH=	55	EPS=	.013510	TH=	60	EPS=	.011906
TH=	65	EPS=	.010425	TH=	70	EPS=	.009013	TH=	75	EPS=	.007642
TH=	80	EPS=	.006298	TH=	85	EPS=	.005014	TH=	90	EPS=	.003867
TH=	95	EPS=	.002854	TH=	100	EPS=	.001944	TH=	105	EPS=	.001106
TH=	110	EPS=	.000310	TH=	115	EPS=	-.000470	TH=	120	EPS=	-.001261
TH=	125	EPS=	-.002090	TH=	130	EPS=	-.002989	TH=	135	EPS=	-.004002
TH=	140	EPS=	-.005188	TH=	145	EPS=	-.006639	TH=	150	EPS=	-.008508
TH=	155	EPS=	-.011069	TH=	160	EPS=	-.014871	TH=	165	EPS=	-.021207
TH=	170	EPS=	-.033964	TH=	175	EPS=	-.072640	TH=	180	EPS=	*.687329
TH=											

GAMA = 60

TH=	65	EPS=	.008096	TH=	70	EPS=	.007097	TH=	75	EPS=	.006173
TH=	80	EPS=	.005292	TH=	85	EPS=	.004430	TH=	90	EPS=	.003573
TH=	95	EPS=	.002716	TH=	100	EPS=	.001879	TH=	105	EPS=	.001106
TH=	110	EPS=	.000393	TH=	115	EPS=	-.000281	TH=	120	EPS=	-.000942
TH=	125	EPS=	-.001616	TH=	130	EPS=	-.002330	TH=	135	EPS=	-.003119
TH=	140	EPS=	-.004029	TH=	145	EPS=	-.005127	TH=	150	EPS=	-.006523
TH=	155	EPS=	-.008411	TH=	160	EPS=	-.011180	TH=	165	EPS=	-.015734
TH=	170	EPS=	-.024787	TH=	175	EPS=	-.051922	TH=	180	EPS=	*.514290

GAMA = 75

TH=	80	EPS=	.003399	TH=	85	EPS=	.002765	TH=	90	EPS=	.002173
TH=	95	EPS=	.001601	TH=	100	EPS=	.001035	TH=	105	EPS=	.000466
TH=	110	EPS=	-.000110	TH=	115	EPS=	-.000689	TH=	120	EPS=	-.001261
TH=	125	EPS=	-.001840	TH=	130	EPS=	-.002449	TH=	135	EPS=	-.003119
TH=	140	EPS=	-.003888	TH=	145	EPS=	-.004814	TH=	150	EPS=	-.005989
TH=	155	EPS=	-.007572	TH=	160	EPS=	-.009882	TH=	165	EPS=	-.013661
TH=	170	EPS=	-.021127	TH=	175	EPS=	-.043379	TH=	180	EPS=	*.977821
TH=											

TH = 2θ°

EPS = 2ε

Appendix 2 Axial Divergence <2ε> in °2θ towards low 2θ for two sets of Soller slits Δ = 0.05

GAMA = 90

TH= 95 EPS= -.000490 TH= 100 EPS= -.000932 TH= 105 EPS= -.001345 TH= 110 EPS= -.001745
TH= 115 EPS= -.002146 TH= 120 EPS= -.002560 TH= 125 EPS= -.002994 TH= 130 EPS= -.003463
TH= 135 EPS= -.004002 TH= 140 EPS= -.004651 TH= 145 EPS= -.005464 TH= 150 EPS= -.006523
TH= 155 EPS= -.007978 TH= 160 EPS= -.010126 TH= 165 EPS= -.013661 TH= 170 EPS= -.020662
TH= 175 EPS= -.041529 TH= 180 EPS= *.041786 TH=

2 Soller slits
Δ=0·05

GAMA = 15

TH= 20 EPS= .225058 TH= 25 EPS= .178098 TH= 30 EPS= .138849 TH= 35 EPS= .103697
TH= 40 EPS= .078475 TH= 45 EPS= .061413 TH= 50 EPS= .049313 TH= 55 EPS= .040261
TH= 60 EPS= .033161 TH= 65 EPS= .027364 TH= 70 EPS= .022465 TH= 75 EPS= .018200
TH= 80 EPS= .014386 TH= 85 EPS= .010895 TH= 90 EPS= .007626 TH= 95 EPS= .004503
TH= 100 EPS= .001456 TH= 105 EPS= -.001574 TH= 110 EPS= -.004649 TH= 115 EPS= -.007835
TH= 120 EPS= -.011207 TH= 125 EPS= -.014863 TH= 130 EPS= -.018929 TH= 135 EPS= -.023590
TH= 140 EPS= -.029120 TH= 145 EPS= -.035963 TH= 150 EPS= -.044984 TH= 155 EPS= -.057326
TH= 160 EPS= -.076333 TH= 165 EPS= -.109449 TH= 170 EPS= -.180645 TH= 175 EPS= -.415102
TH= 180 EPS= *.665874 TH=

GAMA = 30

TH= 35 EPS= .089751 TH= 40 EPS= .075942 TH= 45 EPS= .061413 TH= 50 EPS= .045903
TH= 55 EPS= .034125 TH= 60 EPS= .026155 TH= 65 EPS= .020564 TH= 70 EPS= .016435
TH= 75 EPS= .013236 TH= 80 EPS= .010647 TH= 85 EPS= .008472 TH= 90 EPS= .006580
TH= 95 EPS= .004882 TH= 100 EPS= .003315 TH= 105 EPS= .001828 TH= 110 EPS= .000379
TH= 115 EPS= -.001073 TH= 120 EPS= -.002565 TH= 125 EPS= -.004145 TH= 130 EPS= -.005867
TH= 135 EPS= -.007810 TH= 140 EPS= -.010084 TH= 145 EPS= -.012866 TH= 150 EPS= -.016449
TH= 155 EPS= -.021376 TH= 160 EPS= -.028757 TH= 165 EPS= -.041241 TH= 170 EPS= -.066956
TH= 175 EPS= -.147184 TH= 180 EPS= *.151378 TH=

2 Soller slits
Δ =0·1·

GAMA = 45

TH= 50 EPS= .047936 TH= 55 EPS= .041004 TH= 60 EPS= .033161 TH= 65 EPS= .024428
TH= 70 EPS= .017743 TH= 75 EPS= .013236 TH= 80 EPS= .010089 TH= 85 EPS= .007770
TH= 90 EPS= .005971 TH= 95 EPS= .004505 TH= 100 EPS= .003258 TH= 105 EPS= .002152
TH= 110 EPS= .001133 TH= 115 EPS= .000159 TH= 120 EPS= -.000806 TH= 125 EPS= -.001798
TH= 130 EPS= -.002855 TH= 135 EPS= -.004026 TH= 140 EPS= -.005377 TH= 145 EPS= -.007010
TH= 150 EPS= -.009090 TH= 155 EPS= -.011914 TH= 160 EPS= -.016082 TH= 165 EPS= -.023001
TH= 170 EPS= -.036927 TH= 175 EPS= -.079237 TH= 180 EPS= *.392731 TH=

GAMA = 60

TH= 65 EPS= .026634 TH= 70 EPS= .022712 TH= 75 EPS= .018200 TH= 80 EPS= .013133
TH= 85 EPS= .009233 TH= 90 EPS= .006580 TH= 95 EPS= .004700 TH= 100 EPS= .003285
TH= 105 EPS= .002152 TH= 110 EPS= .001193 TH= 115 EPS= .000334 TH= 120 EPS= -.000473
TH= 125 EPS= -.001270 TH= 130 EPS= -.002093 TH= 135 EPS= -.002985 TH= 140 EPS= -.003995
TH= 145 EPS= -.005199 TH= 150 EPS= -.006713 TH= 155 EPS= -.008745 TH= 160 EPS= -.011706
TH= 165 EPS= -.016555 TH= 170 EPS= -.026174 TH= 175 EPS= -.054986 TH= 180 EPS= *.343438

GAMA = 75

TH=	80	EPS=	.011894	TH=	85	EPS=	.009881	TH=	90	EPS=	.007626
TH=	95	EPS=	.005144	TH=	100	EPS=	.003204	TH=	105	EPS=	.001628
TH=	110	EPS=	.000790	TH=	115	EPS=	-.000059	TH=	120	EPS=	-.000806
TH=	125	EPS=	-.001514	TH=	130	EPS=	-.002226	TH=	135	EPS=	-.002965
TH=	140	EPS=	-.003837	TH=	145	EPS=	-.004847	TH=	150	EPS=	-.006112
TH=	155	EPS=	-.007801	TH=	160	EPS=	-.010251	TH=	165	EPS=	-.014239
TH=	170	EPS=	-.022096	TH=	175	EPS=	-.045469	TH=	180	EPS=	*.473634
TH=											

GAMA = 90

TH=	95	EPS=	-.000655	TH=	100	EPS=	-.001165	TH=	105	EPS=	-.001574
TH=	110	EPS=	-.001897	TH=	115	EPS=	-.002211	TH=	120	EPS=	-.002565
TH=	125	EPS=	-.002975	TH=	130	EPS=	-.003455	TH=	135	EPS=	-.004026
TH=	140	EPS=	-.004719	TH=	145	EPS=	-.005587	TH=	150	EPS=	-.006713
TH=	155	EPS=	-.008255	TH=	160	EPS=	-.010521	TH=	165	EPS=	-.014239
TH=	170	EPS=	-.021584	TH=	175	EPS=	-.043439	TH=	180	EPS=	*.535244
TH=											

2 Soller slits

Δ=0·1

GAMA = 15

TH=	20	EPS=	.195779	TH=	25	EPS=	.156878	TH=	30	EPS=	.131039
TH=	35	EPS=	.112195	TH=	40	EPS=	.097266	TH=	45	EPS=	.084540
TH=	50	EPS=	.073624	TH=	55	EPS=	.062372	TH=	60	EPS=	.052867
TH=	65	EPS=	.044460	TH=	70	EPS=	.036960	TH=	75	EPS=	.030171
TH=	80	EPS=	.023926	TH=	85	EPS=	.018084	TH=	90	EPS=	.012527
TH=	95	EPS=	.007153	TH=	100	EPS=	.001869	TH=	105	EPS=	-.003416
TH=	110	EPS=	-.008791	TH=	115	EPS=	-.014360	TH=	120	EPS=	-.020241
TH=	125	EPS=	-.026583	TH=	130	EPS=	-.033585	TH=	135	EPS=	-.041524
TH=	140	EPS=	-.050818	TH=	145	EPS=	-.062121	TH=	150	EPS=	-.076552
TH=	155	EPS=	-.096178	TH=	160	EPS=	-.125285	TH=	165	EPS=	-.174143
TH=	170	EPS=	-.273469	TH=	175	EPS=	-.576809				

GAMA = 30

TH=	35	EPS=	.041118	TH=	40	EPS=	.036135	TH=	45	EPS=	.032094
TH=	50	EPS=	.028601	TH=	55	EPS=	.025398	TH=	60	EPS=	.022321
TH=	65	EPS=	.019267	TH=	70	EPS=	.016270	TH=	75	EPS=	.013543
TH=	80	EPS=	.011117	TH=	85	EPS=	.008945	TH=	90	EPS=	.006971
TH=	95	EPS=	.005142	TH=	100	EPS=	.003411	TH=	105	EPS=	.001739
TH=	110	EPS=	.000087	TH=	115	EPS=	-.001582	TH=	120	EPS=	-.003309
TH=	125	EPS=	-.005143	TH=	130	EPS=	-.007143	TH=	135	EPS=	-.009394
TH=	140	EPS=	-.012018	TH=	145	EPS=	-.015204	TH=	150	EPS=	-.019271
TH=	155	EPS=	-.024799	TH=	160	EPS=	-.032959	TH=	165	EPS=	-.046520
TH=	170	EPS=	-.073860	TH=	175	EPS=	-.156979	TH=	180	EPS=	*.993370
TH=											

GAMA = 45

TH=	50	EPS=	.017691	TH=	55	EPS=	.015950	TH=	60	EPS=	.014384
TH=	65	EPS=	.012904	TH=	70	EPS=	.011446	TH=	75	EPS=	.009967
TH=	80	EPS=	.008441	TH=	85	EPS=	.006909	TH=	90	EPS=	.005496
TH=	95	EPS=	.004224	TH=	100	EPS=	.003068	TH=	105	EPS=	.001995
TH=	110	EPS=	.000973	TH=	115	EPS=	-.000026	TH=	120	EPS=	-.001033
TH=	125	EPS=	-.002080	TH=	130	EPS=	-.003202	TH=	135	EPS=	-.004440
TH=	140	EPS=	-.005886	TH=	145	EPS=	-.007618	TH=	150	EPS=	-.009814
TH=	155	EPS=	-.012776	TH=	160	EPS=	-.017112	TH=	165	EPS=	-.024247
TH=	170	EPS=	-.038469	TH=	175	EPS=	-.081267	TH=	180	EPS=	*.352369
TH=											

1 Soller slit in reflected beam

Δ=0·05

GAMA = 60

TH=	65	EPS=	.008918	TH=	70	EPS=	.008034	TH=	75	EPS=	.007194
TH=	80	EPS=	.006361	TH=	85	EPS=	.005510	TH=	90	EPS=	.004621
TH=	95	EPS=	.003687	TH=	100	EPS=	.002734	TH=	105	EPS=	.001832
TH=	110	EPS=	.000991	TH=	115	EPS=	.000191	TH=	120	EPS=	-.000592
TH=	125	EPS=	-.001386	TH=	130	EPS=	-.002220	TH=	135	EPS=	-.003131
TH=	140	EPS=	-.004170	TH=	145	EPS=	-.005408	TH=	150	EPS=	-.006963
TH=	155	EPS=	-.009043	TH=	160	EPS=	-.012061	TH=	165	EPS=	-.016981
TH=	170	EPS=	-.026693	TH=	175	EPS=	-.055662	TH=	180	EPS=	*.221486

GAMA = 75

TH=	80	EPS=	.003767	TH=	85	EPS=	.003251	TH=	90	EPS=	.002743
TH=	95	EPS=	.002224	TH=	100	EPS=	.001677	TH=	105	EPS=	.001093
TH=	110	EPS=	.000467	TH=	115	EPS=	-.000190	TH=	120	EPS=	-.000850
TH=	125	EPS=	-.001520	TH=	130	EPS=	-.002220	TH=	135	EPS=	-.002981
TH=	140	EPS=	-.003845	TH=	145	EPS=	-.004872	TH=	150	EPS=	-.006159
TH=	155	EPS=	-.007874	TH=	160	EPS=	-.010353	TH=	165	EPS=	-.014376
TH=	170	EPS=	-.022278	TH=	175	EPS=	-.045733				

GAMA = 90

TH=	95	EPS=	-.000327	TH=	100	EPS=	-.000641	TH=	105	EPS=	-.000962
TH=	110	EPS=	-.001306	TH=	115	EPS=	-.001687	TH=	120	EPS=	-.002114
TH=	125	EPS=	-.002593	TH=	130	EPS=	-.003133	TH=	135	EPS=	-.003754
TH=	140	EPS=	-.004491	TH=	145	EPS=	-.005398	TH=	150	EPS=	-.006561
TH=	155	EPS=	-.008136	TH=	160	EPS=	-.010436	TH=	165	EPS=	-.014189
TH=	170	EPS=	-.021574	TH=	175	EPS=	-.043496	TH=	180	EPS=	*.270413
TH=											

Soller slit
in reflected beam
$\Delta = 0.05$

GAMA = 15

TH=	20	EPS=	1.415569	TH=	25	EPS=	.313395	TH=	30	EPS=	.131039
TH=	35	EPS=	.071961	TH=	40	EPS=	.045912	TH=	45	EPS=	.032094
TH=	50	EPS=	.023779	TH=	55	EPS=	.018286	TH=	60	EPS=	.014384
TH=	65	EPS=	.011444	TH=	70	EPS=	.009116	TH=	75	EPS=	.007194
TH=	80	EPS=	.005545	TH=	85	EPS=	.004082	TH=	90	EPS=	.002743
TH=	95	EPS=	.001481	TH=	100	EPS=	.000258	TH=	105	EPS=	-.000962
TH=	110	EPS=	-.002212	TH=	115	EPS=	-.003531	TH=	120	EPS=	-.004965
TH=	125	EPS=	-.006573	TH=	130	EPS=	-.008442	TH=	135	EPS=	-.010698
TH=	140	EPS=	-.013545	TH=	145	EPS=	-.017328	TH=	150	EPS=	-.022675
TH=	155	EPS=	-.030836	TH=	160	EPS=	-.044604	TH=	165	EPS=	-.071327
TH=	170	EPS=	-.135952	TH=	175	EPS=	-.378913				

GAMA = 30

TH=	35	EPS=	.779979	TH=	40	EPS=	.190127	TH=	45	EPS=	.084540
TH=	50	EPS=	.048260	TH=	55	EPS=	.031522	TH=	60	EPS=	.022321
TH=	65	EPS=	.016622	TH=	70	EPS=	.012765	TH=	75	EPS=	.009967
TH=	80	EPS=	.007817	TH=	85	EPS=	.006082	TH=	90	EPS=	.004621
TH=	95	EPS=	.003343	TH=	100	EPS=	.002182	TH=	105	EPS=	.001093
TH=	110	EPS=	.000037	TH=	115	EPS=	-.001020	TH=	120	EPS=	-.002114
TH=	125	EPS=	-.003284	TH=	130	EPS=	-.004580	TH=	135	EPS=	-.006070
TH=	140	EPS=	-.007856	TH=	145	EPS=	-.010100	TH=	150	EPS=	-.013078
TH=	155	EPS=	-.017308	TH=	160	EPS=	-.023861	TH=	165	EPS=	-.035337
TH=	170	EPS=	-.059803	TH=	175	EPS=	-.138654	TH=	180	EPS=	*.968285
TH=											

Soller slit
in incident beam
$\Delta = 0.05$

```
GAMA = 45
TH=  50 EPS=  .477502 TH=  55 EPS=  .118342 TH=  60 EPS=  .052867 TH=  65 EPS=  .030065
TH=  70 EPS=  .019436 TH=  75 EPS=  .013543 TH=  80 EPS=  .009861 TH=  85 EPS=  .007345
TH=  90 EPS=  .005496 TH=  95 EPS=  .004052 TH= 100 EPS=  .002862 TH= 105 EPS=  .001832
TH= 110 EPS=  .000899 TH= 115 EPS=  .000019 TH= 120 EPS= -.000850 TH= 125 EPS= -.001741
TH= 130 EPS= -.002693 TH= 135 EPS= -.003754 TH= 140 EPS= -.004989 TH= 145 EPS= -.006497
TH= 150 EPS= -.008442 TH= 155 EPS= -.011117 TH= 160 EPS= -.015119 TH= 165 EPS= -.021853
TH= 170 EPS= -.035576 TH= 175 EPS= -.077729 TH= 180 EPS= *.347952 TH=
GAMA = 60
TH=  65 EPS=  .278526 TH=  70 EPS=  .068546 TH=  75 EPS=  .030171 TH=  80 EPS=  .016767
TH=  85 EPS=  .010486 TH=  90 EPS=  .006971 TH=  95 EPS=  .004741 TH= 100 EPS=  .003180
TH= 105 EPS=  .001995 TH= 110 EPS=  .001028 TH= 115 EPS=  .000186 TH= 120 EPS= -.000592
TH= 125 EPS= -.001352 TH= 130 EPS= -.002134 TH= 135 EPS= -.002981 TH= 140 EPS= -.003945
TH= 145 EPS= -.005099 TH= 150 EPS= -.006561 TH= 155 EPS= -.008537 TH= 160 EPS= -.011440
TH= 165 EPS= -.016229 TH= 170 EPS= -.025792 TH= 175 EPS= -.054584 TH= 180 EPS= *.220194
GAMA = 75
TH=  80 EPS=  .126620 TH=  85 EPS=  .030067 TH=  90 EPS=  .012527 TH=  95 EPS=  .006379
TH= 100 EPS=  .003445 TH= 105 EPS=  .001739 TH= 110 EPS=  .000588 TH= 115 EPS= -.000291
TH= 120 EPS= -.001033 TH= 125 EPS= -.001720 TH= 130 EPS= -.002404 TH= 135 EPS= -.003131
TH= 140 EPS= -.003951 TH= 145 EPS= -.004927 TH= 150 EPS= -.006159 TH= 155 EPS= -.007815
TH= 160 EPS= -.010232 TH= 165 EPS= -.014189 TH= 170 EPS= -.022020 TH= 175 EPS= -.045398
GAMA = 90
TH=  95 EPS= -.007670 TH= 100 EPS= -.004312 TH= 105 EPS= -.003416 TH= 110 EPS= -.003149
TH= 115 EPS= -.003151 TH= 120 EPS= -.003309 TH= 125 EPS= -.003582 TH= 130 EPS= -.003959
TH= 135 EPS= -.004448 TH= 140 EPS= -.005074 TH= 145 EPS= -.005885 TH= 150 EPS= -.006963
TH= 155 EPS= -.008461 TH= 160 EPS= -.010690 TH= 165 EPS= -.014376 TH= 170 EPS= -.021698
TH= 175 EPS= -.043557 TH= 180 EPS= *.270413 TH=
```

Soller slit in incident beam $\Delta = 0.05$

Axial Divergence Error $\langle 2\epsilon \rangle$ in °2θ towards low 2θ No Soller slits

```
GAMA = 15.

2TH =  20 2EPS = 2.076835 2TH =  25 2EPS = 0.607186 2TH =  30 2EPS = 0.317931 2TH =  35 2EPS = 0.207449
2TH =  40 2EPS = 0.152700 2TH =  45 2EPS = 0.116371 2TH =  50 2EPS = 0.093039 2TH =  55 2EPS = 0.075948
2TH =  60 2EPS = 0.062660 2TH =  65 2EPS = 0.051921 2TH =  70 2EPS = 0.042856 2TH =  75 2EPS = 0.034936
2TH =  80 2EPS = 0.027969 2TH =  85 2EPS = 0.021564 2TH =  90 2EPS = 0.015591 2TH =  95 2EPS = 0.009908
2TH = 100 2EPS = 0.004396 2TH = 105 2EPS = -.001044 2TH = 110 2EPS = -.006520 2TH = 115 2EPS = -.012134
2TH = 120 2EPS = -.018009 2TH = 125 2EPS = -.024268 2TH = 130 2EPS = -.031114 2TH = 135 2EPS = -.038790
2TH = 140 2EPS = -.047664 2TH = 145 2EPS = -.058509 2TH = 150 2EPS = -.071687 2TH = 155 2EPS = -.089572
2TH = 160 2EPS = -.115646 2TH = 165 2EPS = -.158964 2TH = 170 2EPS = -.243538 2TH = 175 2EPS = -.540693
```

2TH = 2θ 2EPS = $\langle 2\epsilon \rangle$

GAMA = 30.

2TH = 35 2EPS = 0.911097 2TH = 40 2EPS = 0.242466 2TH = 45 2EPS = 0.116371 2TH = 50 2EPS = 0.070794
2TH = 55 2EPS = 0.048745 2TH = 60 2EPS = 0.036005 2TH = 65 2EPS = 0.027790 2TH = 70 2EPS = 0.022014
2TH = 75 2EPS = 0.017680 2TH = 80 2EPS = 0.014253 2TH = 85 2EPS = 0.011425 2TH = 90 2EPS = 0.009001
2TH = 95 2EPS = 0.006855 2TH = 100 2EPS = 0.004896 2TH = 105 2EPS = 0.003058 2TH = 110 2EPS = 0.001286
2TH = 115 2EPS = -.000497 2TH = 120 2EPS = -.002250 2TH = 125 2EPS = -.004114 2TH = 130 2EPS = -.006121
2TH = 135 2EPS = -.008355 2TH = 140 2EPS = -.010935 2TH = 145 2EPS = -.014047 2TH = 150 2EPS = -.018003
2TH = 155 2EPS = -.023375 2TH = 160 2EPS = -.031331 2TH = 165 2EPS = -.044683 2TH = 170 2EPS = -.072079
2TH = 175 2EPS = -.157677 2TH = 180 2EPS = *-5875.289104 2TH =

GAMA = 45.

2TH = 50 2EPS = 0.519650 2TH = 55 2EPS = 0.134719 2TH = 60 2EPS = 0.062686 2TH = 65 2EPS = 0.036955
2TH = 70 2EPS = 0.024600 2TH = 75 2EPS = 0.017680 2TH = 80 2EPS = 0.013222 2TH = 85 2EPS = 0.010115
2TH = 90 2EPS = 0.007795 2TH = 95 2EPS = 0.005960 2TH = 100 2EPS = 0.004434 2TH = 105 2EPS = 0.003108
2TH = 110 2EPS = 0.001908 2TH = 115 2EPS = 0.000779 2TH = 120 2EPS = -.000323 2TH = 125 2EPS = -.001439
2TH = 130 2EPS = -.002616 2TH = 135 2EPS = -.003898 2TH = 140 2EPS = -.005363 2TH = 145 2EPS = -.007114
2TH = 150 2EPS = -.009324 2TH = 155 2EPS = -.012303 2TH = 160 2EPS = -.016672 2TH = 165 2EPS = -.023896
2TH = 170 2EPS = -.038400 2TH = 175 2EPS = -.082457 2TH = 180 2EPS = *-2937.649656 2TH =

GAMA = 60.

2TH = 65 2EPS = 0.298671 2TH = 70 2EPS = 0.076520 2TH = 75 2EPS = 0.034986 2TH = 80 2EPS = 0.020154
2TH = 85 2EPS = 0.013094 2TH = 90 2EPS = 0.009001 2TH = 95 2EPS = 0.006385 2TH = 100 2EPS = 0.004530
2TH = 105 2EPS = 0.003108 2TH = 110 2EPS = 0.001943 2TH = 115 2EPS = 0.000930 2TH = 120 2EPS = 0.000000
2TH = 125 2EPS = -.000859 2TH = 130 2EPS = -.001812 2TH = 135 2EPS = -.002785 2TH = 140 2EPS = -.003873
2TH = 145 2EPS = -.005156 2TH = 150 2EPS = -.006751 2TH = 155 2EPS = -.008877 2TH = 160 2EPS = -.011958
2TH = 165 2EPS = -.016963 2TH = 170 2EPS = -.026924 2TH = 175 2EPS = -.056659 2TH = 180 2EPS = *-1958.43

GAMA = 75.

2TH = 80 2EPS = 0.138260 2TH = 85 2EPS = 0.035001 2TH = 90 2EPS = 0.015591 2TH = 95 2EPS = 0.008563
2TH = 100 2EPS = 0.005111 2TH = 105 2EPS = 0.003058 2TH = 110 2EPS = 0.001654 2TH = 115 2EPS = 0.000530
2TH = 120 2EPS = -.000345 2TH = 125 2EPS = -.001145 2TH = 130 2EPS = -.001949 2TH = 135 2EPS = -.002785
2TH = 140 2EPS = -.003767 2TH = 145 2EPS = -.004783 2TH = 150 2EPS = -.006116 2TH = 155 2EPS = -.007882
2TH = 160 2EPS = -.010465 2TH = 165 2EPS = -.014546 2TH = 170 2EPS = -.022639 2TH = 175 2EPS = -.046671

GAMA = 90.

2TH = 95 2EPS = -.000360 2TH = 100 2EPS = -.000687 2TH = 105 2EPS = -.001044 2TH = 110 2EPS = -.001419
2TH = 115 2EPS = -.001817 2TH = 120 2EPS = -.002250 2TH = 125 2EPS = -.002729 2TH = 130 2EPS = -.003271
2TH = 135 2EPS = -.003896 2TH = 140 2EPS = -.004645 2TH = 145 2EPS = -.005566 2TH = 150 2EPS = -.006751
2TH = 155 2EPS = -.008359 2TH = 160 2EPS = -.010709 2TH = 165 2EPS = -.014546 2TH = 170 2EPS = -.022104
2TH = 175 2EPS = -.044569 2TH = 180 2EPS = *-1468.826777 2TH =

No Soller slits

S-B Extrapolation Function for Absorption when $\mu t \to \infty$

$$\frac{1 + \cos 2\theta}{\sin \gamma + (\sin 2\theta - \gamma)}$$

$\mu t \to \infty$ FUNCTION FOR GAMMA=90

θ	0.0	0.1	0.2	0.3	0.4	0.5	0.6	0.7	0.8	0.9
50	.704	.699	.694	.689	.684	.680	.675	.670	.665	.660
51	.656	.651	.646	.642	.637	.633	.628	.624	.619	.615
52	.610	.606	.602	.597	.593	.589	.585	.580	.576	.572
53	.568	.564	.560	.556	.552	.548	.544	.540	.536	.532
54	.528	.524	.520	.516	.513	.509	.505	.501	.498	.494
55	.490	.487	.483	.479	.476	.472	.469	.465	.462	.458
56	.455	.452	.448	.445	.441	.438	.435	.431	.428	.425
57	.422	.419	.415	.412	.409	.406	.403	.400	.397	.394
58	.390	.387	.384	.381	.378	.376	.373	.370	.367	.364
59	.361	.358	.355	.353	.350	.347	.344	.341	.339	.336
60	.333	.331	.328	.325	.323	.320	.318	.315	.312	.310
61	.307	.305	.302	.300	.297	.295	.292	.290	.288	.285
62	.283	.280	.278	.276	.273	.271	.269	.266	.264	.262
63	.260	.257	.255	.253	.251	.249	.246	.244	.242	.240
64	.238	.236	.234	.232	.230	.228	.225	.223	.221	.219
65	.217	.215	.214	.212	.210	.208	.206	.204	.202	.200
66	.198	.196	.195	.193	.191	.189	.187	.185	.184	.182
67	.180	.178	.177	.175	.173	.172	.170	.168	.167	.165
68	.163	.162	.160	.158	.157	.155	.154	.152	.150	.149
69	.147	.146	.144	.143	.141	.140	.138	.137	.135	.134
70	.132	.131	.130	.128	.127	.125	.124	.123	.121	.120
71	.119	.117	.116	.115	.113	.112	.111	.109	.108	.107
72	.106	.104	.103	.102	.101	.099	.098	.097	.096	.095
73	.093	.092	.091	.090	.089	.088	.087	.086	.084	.083
74	.082	.081	.080	.079	.078	.077	.076	.075	.074	.073
75	.072	.071	.070	.069	.068	.067	.066	.065	.064	.063
76	.062	.061	.060	.059	.059	.058	.057	.056	.055	.054
77	.053	.052	.052	.051	.050	.049	.048	.048	.047	.046
78	.045	.044	.044	.043	.042	.041	.041	.040	.039	.038
79	.038	.037	.036	.036	.035	.034	.034	.033	.032	.032

$\mu t \to \infty$ FUNCTION FOR GAMMA=90

θ	0.0	0.1	0.2	0.3	0.4	0.5	0.6	0.7	0.8	0.9
80	.031	.030	.030	.029	.029	.028	.027	.027	.026	.026
81	.025	.025	.024	.023	.023	.022	.022	.021	.021	.020
82	.020	.019	.019	.018	.018	.017	.017	.016	.016	.016
83	.015	.015	.014	.014	.013	.013	.013	.012	.012	.011
84	.011	.011	.010	.010	.010	.009	.009	.009	.008	.008
85	.008	.007	.007	.007	.006	.006	.006	.006	.005	.005
86	.005	.005	.004	.004	.004	.004	.004	.003	.003	.003
87	.003	.003	.002	.002	.002	.002	.002	.002	.001	.001
88	.001	.001	.001	.001	.001	.001	.001	.001	.000	.000
89	.000	.000	.000	.000	.000	.000	.000	.000	.000	.000

$\mu t \to \infty$ FUNCTION FOR GAMMA=75

θ	0.0	0.1	0.2	0.3	0.4	0.5	0.6	0.7	0.8	0.9
40	1.114	1.108	1.101	1.094	1.087	1.080	1.074	1.067	1.060	1.054
41	1.047	1.041	1.034	1.028	1.022	1.015	1.009	1.003	.996	.990
42	.984	.978	.972	.966	.960	.954	.948	.942	.936	.931
43	.925	.919	.913	.908	.902	.896	.891	.885	.880	.874
44	.869	.864	.858	.853	.848	.842	.837	.832	.827	.822
45	.816	.811	.806	.801	.796	.791	.786	.782	.777	.772
46	.767	.762	.757	.753	.748	.743	.739	.734	.729	.725
47	.720	.716	.711	.707	.702	.698	.694	.689	.685	.680
48	.676	.672	.668	.663	.659	.655	.651	.647	.643	.639
49	.635	.630	.626	.622	.618	.615	.611	.607	.603	.599
50	.595	.591	.588	.584	.580	.576	.573	.569	.565	.561
51	.558	.554	.551	.547	.543	.540	.536	.533	.529	.526
52	.523	.519	.516	.512	.509	.506	.502	.499	.496	.492
53	.489	.486	.483	.479	.476	.473	.470	.467	.464	.461
54	.457	.454	.451	.448	.445	.442	.439	.436	.433	.430
55	.427	.424	.422	.419	.416	.413	.410	.407	.404	.402
56	.399	.396	.393	.391	.388	.385	.383	.380	.377	.375
57	.372	.369	.367	.364	.361	.359	.356	.354	.351	.349
58	.346	.344	.341	.339	.336	.334	.332	.329	.327	.324
59	.322	.320	.317	.315	.313	.310	.308	.306	.303	.301
60	.299	.297	.294	.292	.290	.288	.286	.283	.281	.279
61	.277	.275	.273	.271	.269	.266	.264	.262	.260	.258
62	.256	.254	.252	.250	.248	.246	.244	.242	.240	.238
63	.236	.235	.233	.231	.229	.227	.225	.223	.221	.220
64	.218	.216	.214	.212	.211	.209	.207	.205	.204	.202

$\mu t \to \infty$ FUNCTION FOR GAMMA=60°

θ	0.0	0.1	0.2	0.3	0.4	0.5	0.6	0.7	0.8	0.9
45	.732	.728	.724	.720	.716	.711	.707	.703	.699	.695
46	.691	.687	.683	.680	.676	.672	.668	.664	.660	.656
47	.653	.649	.645	.641	.638	.634	.630	.627	.623	.620
48	.616	.612	.609	.605	.602	.598	.595	.591	.588	.584
49	.581	.578	.574	.571	.567	.564	.561	.558	.554	.551
50	.548	.544	.541	.538	.535	.532	.528	.525	.522	.519
51	.516	.513	.510	.507	.504	.501	.498	.495	.492	.489
52	.486	.483	.480	.477	.474	.471	.468	.465	.463	.460
53	.457	.454	.451	.449	.446	.443	.440	.438	.435	.432
54	.429	.427	.424	.421	.419	.416	.414	.411	.408	.406
55	.403	.401	.398	.396	.393	.390	.388	.385	.383	.381
56	.378	.376	.373	.371	.368	.366	.364	.361	.359	.357
57	.354	.352	.350	.347	.345	.343	.340	.338	.336	.334
58	.331	.329	.327	.325	.322	.320	.318	.316	.314	.312
59	.310	.307	.305	.303	.301	.299	.297	.295	.293	.291
60	.289	.287	.285	.283	.281	.279	.277	.275	.273	.271
61	.269	.267	.265	.263	.261	.259	.257	.255	.254	.252
62	.250	.248	.246	.244	.242	.241	.239	.237	.235	.233
63	.232	.230	.228	.226	.225	.223	.221	.219	.218	.216
64	.214	.213	.211	.209	.208	.206	.204	.203	.201	.199
65	.198	.196	.195	.193	.191	.190	.188	.187	.185	.184
66	.182	.181	.179	.178	.176	.175	.173	.172	.170	.169
67	.167	.166	.164	.163	.161	.160	.158	.157	.156	.154
68	.153	.151	.150	.149	.147	.146	.145	.143	.142	.141
69	.139	.138	.137	.135	.134	.133	.131	.130	.129	.128
70	.126	.125	.124	.123	.121	.120	.119	.118	.117	.115
71	.114	.113	.112	.111	.110	.108	.107	.106	.105	.104
72	.103	.102	.100	.099	.098	.097	.096	.095	.094	.093
73	.092	.091	.090	.089	.088	.087	.085	.084	.083	.082
74	.081	.080	.079	.078	.078	.077	.076	.075	.074	.073
75	.072	.071	.070	.069	.068	.067	.066	.065	.065	.064
76	.063	.062	.061	.060	.059	.058	.058	.057	.056	.055
77	.054	.053	.053	.052	.051	.050	.050	.049	.048	.047
78	.046	.046	.045	.044	.043	.043	.042	.041	.041	.040
79	.039	.039	.038	.037	.036	.036	.035	.035	.034	.033
80	.033	.032	.031	.031	.030	.029	.029	.028	.028	.027
81	.027	.026	.025	.025	.024	.024	.023	.023	.022	.022
82	.021	.021	.020	.020	.019	.019	.018	.018	.017	.017
83	.016	.016	.015	.015	.014	.014	.014	.013	.013	.012
84	.012	.012	.011	.011	.011	.010	.010	.009	.009	.009

$\mu t \to \infty$ FUNCTION FOR GAMMA=75

θ	0.0	0.1	0.2	0.3	0.4	0.5	0.6	0.7	0.8	0.9
65	.200	.198	.197	.195	.193	.192	.190	.188	.187	.185
66	.183	.182	.180	.178	.177	.175	.174	.172	.171	.169
67	.167	.166	.164	.163	.161	.160	.158	.157	.155	.154
68	.152	.151	.150	.148	.147	.145	.144	.142	.141	.140
69	.138	.137	.136	.134	.133	.132	.130	.129	.128	.126
70	.125	.124	.122	.121	.120	.119	.117	.116	.115	.114
71	.112	.111	.110	.109	.108	.106	.105	.104	.103	.102
72	.101	.099	.098	.097	.096	.095	.094	.093	.092	.091
73	.089	.088	.087	.086	.085	.084	.083	.082	.081	.080
74	.079	.078	.077	.076	.075	.074	.073	.072	.071	.070
75	.069	.068	.067	.067	.066	.065	.064	.063	.062	.061
76	.060	.059	.059	.058	.057	.056	.055	.054	.054	.053
77	.052	.051	.050	.050	.049	.048	.047	.047	.046	.045
78	.044	.044	.043	.042	.041	.041	.040	.039	.039	.038
79	.037	.037	.036	.035	.035	.034	.033	.033	.032	.031
80	.031	.030	.030	.029	.028	.028	.027	.027	.026	.025
81	.025	.024	.024	.023	.023	.022	.022	.021	.021	.020
82	.020	.019	.019	.018	.018	.017	.017	.016	.016	.016
83	.015	.015	.014	.014	.013	.013	.013	.012	.012	.011
84	.011	.011	.010	.010	.010	.009	.009	.009	.008	.008
85	.008	.007	.007	.007	.007	.006	.006	.006	.005	.005
86	.005	.005	.004	.004	.004	.004	.004	.003	.003	.003
87	.003	.003	.002	.002	.002	.002	.002	.002	.002	.001
88	.001	.001	.001	.001	.001	.001	.001	.001	.000	.000
89	.000	.000	.000	.000	.000	.000	.000	.000	.000	.000

$\mu t \to \infty$ FUNCTION FOR GAMMA=60

θ	0.0	0.1	0.2	0.3	0.4	0.5	0.6	0.7	0.8	0.9
35	1.291	1.283	1.276	1.269	1.261	1.254	1.247	1.240	1.233	1.226
36	1.219	1.212	1.205	1.198	1.191	1.185	1.178	1.171	1.165	1.158
37	1.151	1.145	1.138	1.132	1.125	1.119	1.113	1.106	1.100	1.094
38	1.088	1.082	1.076	1.069	1.063	1.057	1.051	1.046	1.040	1.034
39	1.028	1.022	1.016	1.011	1.005	.999	.994	.988	.983	.977
40	.972	.966	.961	.955	.950	.944	.939	.934	.929	.923
41	.918	.913	.908	.903	.898	.893	.888	.883	.878	.873
42	.868	.863	.858	.853	.848	.844	.839	.834	.829	.825
43	.820	.815	.811	.806	.802	.797	.793	.788	.784	.779
44	.775	.771	.766	.762	.758	.753	.749	.745	.740	.736

$\mu t \to \infty$ FUNCTION FOR GAMMA=60

θ	0.0	0.1	0.2	0.3	0.4	0.5	0.6	0.7	0.8	0.9
85	.008	.008	.008	.007	.007	.007	.007	.006	.006	.006
86	.005	.005	.005	.005	.004	.004	.004	.004	.003	.003
87	.003	.003	.003	.003	.002	.002	.002	.002	.002	.002
88	.001	.001	.001	.001	.001	.001	.001	.001	.001	.000
89	.000	.000	.000	.000	.000	.000	.000	.000	.000	.000

$\mu t \to \infty$ FUNCTION FOR GAMMA=45

θ	0.0	0.1	0.2	0.3	0.4	0.5	0.6	0.7	0.8	0.9
25	2.068	2.056	2.044	2.032	2.019	2.007	1.996	1.984	1.972	1.960
26	1.949	1.938	1.926	1.915	1.904	1.893	1.882	1.871	1.860	1.849
27	1.839	1.828	1.818	1.807	1.797	1.787	1.776	1.766	1.756	1.746
28	1.736	1.727	1.717	1.707	1.698	1.688	1.679	1.669	1.660	1.651
29	1.641	1.632	1.623	1.614	1.605	1.596	1.588	1.579	1.570	1.561
30	1.553	1.544	1.536	1.528	1.519	1.511	1.503	1.494	1.486	1.478
31	1.470	1.462	1.454	1.446	1.439	1.431	1.423	1.416	1.408	1.400
32	1.393	1.385	1.378	1.371	1.363	1.356	1.349	1.342	1.334	1.327
33	1.320	1.313	1.306	1.299	1.293	1.286	1.279	1.272	1.265	1.259
34	1.252	1.246	1.239	1.232	1.226	1.220	1.213	1.207	1.200	1.194
35	1.188	1.182	1.176	1.169	1.163	1.157	1.151	1.145	1.139	1.133
36	1.127	1.122	1.116	1.110	1.104	1.098	1.093	1.087	1.081	1.076
37	1.070	1.065	1.059	1.054	1.048	1.043	1.037	1.032	1.027	1.021
38	1.016	1.011	1.006	1.001	.995	.990	.985	.980	.975	.970
39	.965	.960	.955	.950	.945	.940	.936	.931	.926	.921
40	.916	.912	.907	.902	.898	.893	.888	.884	.879	.875
41	.870	.866	.861	.857	.853	.848	.844	.839	.835	.831
42	.826	.822	.818	.814	.810	.805	.801	.797	.793	.789
43	.785	.781	.777	.773	.769	.765	.761	.757	.753	.749
44	.745	.741	.737	.733	.730	.726	.722	.718	.715	.711
45	.707	.703	.700	.696	.692	.689	.685	.682	.678	.674
46	.671	.667	.664	.660	.657	.653	.650	.647	.643	.640
47	.636	.633	.630	.626	.623	.620	.616	.613	.610	.607
48	.603	.600	.597	.594	.591	.587	.584	.581	.578	.575
49	.572	.569	.566	.562	.559	.556	.553	.550	.547	.544
50	.541	.538	.536	.533	.530	.527	.524	.521	.518	.515
51	.512	.510	.507	.504	.501	.498	.496	.493	.490	.487
52	.485	.482	.479	.477	.474	.471	.468	.466	.463	.461
53	.458	.455	.453	.450	.448	.445	.442	.440	.437	.435
54	.432	.430	.427	.425	.422	.420	.418	.415	.413	.410

$\mu t \to \infty$ FUNCTION FOR GAMMA=45

θ	0.0	0.1	0.2	0.3	0.4	0.5	0.6	0.7	0.8	0.9
55	.408	.405	.403	.401	.398	.396	.394	.391	.389	.387
56	.384	.382	.380	.377	.375	.373	.371	.368	.366	.364
57	.362	.359	.357	.355	.353	.351	.348	.346	.344	.342
58	.340	.338	.336	.333	.331	.329	.327	.325	.323	.321
59	.319	.317	.315	.313	.311	.309	.307	.305	.303	.301
60	.299	.297	.295	.293	.291	.289	.287	.285	.283	.281
61	.280	.278	.276	.274	.272	.270	.268	.267	.265	.263
62	.261	.259	.257	.256	.254	.252	.250	.248	.247	.245
63	.243	.241	.240	.238	.236	.235	.233	.231	.229	.228
64	.226	.224	.223	.221	.219	.218	.216	.215	.213	.211
65	.210	.208	.207	.205	.203	.202	.200	.199	.197	.196
66	.194	.192	.191	.189	.188	.186	.185	.183	.182	.180
67	.179	.177	.176	.174	.173	.172	.170	.169	.167	.166
68	.164	.163	.162	.160	.159	.157	.156	.155	.153	.152
69	.151	.149	.148	.147	.145	.144	.143	.141	.140	.139
70	.137	.136	.135	.134	.132	.131	.130	.128	.127	.126
71	.125	.123	.122	.121	.120	.119	.117	.116	.115	.114
72	.113	.112	.110	.109	.108	.107	.106	.105	.103	.102
73	.101	.100	.099	.098	.097	.096	.095	.094	.092	.091
74	.090	.089	.088	.087	.086	.085	.084	.083	.082	.081
75	.080	.079	.078	.077	.076	.075	.074	.073	.072	.071
76	.070	.069	.068	.068	.067	.066	.065	.064	.063	.062
77	.061	.060	.059	.059	.058	.057	.056	.055	.054	.054
78	.053	.052	.051	.050	.049	.049	.048	.047	.046	.046
79	.045	.044	.043	.042	.042	.041	.040	.040	.039	.038
80	.037	.037	.036	.035	.035	.034	.033	.033	.032	.031
81	.031	.030	.029	.029	.028	.027	.027	.026	.026	.025
82	.024	.024	.023	.023	.022	.022	.021	.021	.020	.020
83	.019	.018	.018	.017	.017	.016	.016	.016	.015	.015
84	.014	.014	.013	.013	.012	.012	.012	.011	.011	.010
85	.010	.010	.009	.009	.008	.008	.008	.007	.007	.007
86	.006	.006	.006	.006	.005	.005	.005	.004	.004	.004
87	.004	.003	.003	.003	.003	.003	.002	.002	.002	.002
88	.002	.002	.001	.001	.001	.001	.001	.001	.001	.001
89	.000	.000	.000	.000	.000	.000	.000	.000	.000	.000

$\mu t \to \infty$ FUNCTION FOR GAMMA=30

θ	0.0	0.1	0.2	0.3	0.4	0.5	0.6	0.7	0.8	0.9
20	2.622	2.605	2.589	2.572	2.556	2.540	2.524	2.509	2.493	2.478
21	2.462	2.447	2.432	2.417	2.403	2.388	2.374	2.360	2.345	2.331
22	2.317	2.304	2.290	2.276	2.263	2.250	2.236	2.223	2.210	2.198
23	2.185	2.172	2.160	2.147	2.135	2.123	2.111	2.099	2.087	2.075
24	2.063	2.052	2.040	2.029	2.017	2.006	1.995	1.984	1.973	1.962
25	1.951	1.940	1.930	1.919	1.909	1.898	1.888	1.878	1.867	1.857
26	1.847	1.837	1.827	1.818	1.808	1.798	1.789	1.779	1.770	1.760
27	1.751	1.742	1.733	1.724	1.715	1.706	1.697	1.688	1.679	1.670
28	1.662	1.653	1.644	1.636	1.628	1.619	1.611	1.603	1.594	1.586
29	1.578	1.570	1.562	1.554	1.546	1.538	1.531	1.523	1.515	1.508
30	1.500	1.492	1.485	1.478	1.470	1.463	1.456	1.448	1.441	1.434
31	1.427	1.420	1.413	1.406	1.399	1.392	1.385	1.378	1.371	1.365
32	1.358	1.351	1.345	1.338	1.332	1.325	1.319	1.312	1.306	1.300
33	1.293	1.287	1.281	1.275	1.268	1.262	1.256	1.250	1.244	1.238
34	1.232	1.226	1.220	1.214	1.209	1.203	1.197	1.191	1.186	1.180
35	1.174	1.169	1.163	1.158	1.152	1.147	1.141	1.136	1.130	1.125
36	1.120	1.114	1.109	1.104	1.099	1.093	1.088	1.083	1.078	1.073
37	1.068	1.063	1.058	1.053	1.048	1.043	1.038	1.033	1.028	1.023
38	1.019	1.014	1.009	1.004	.999	.995	.990	.985	.981	.976
39	.972	.967	.963	.958	.954	.949	.945	.940	.936	.931
40	.927	.923	.918	.914	.910	.905	.901	.897	.893	.889
41	.884	.880	.876	.872	.868	.864	.860	.856	.852	.848
42	.844	.840	.836	.832	.828	.824	.820	.816	.813	.809
43	.805	.801	.797	.794	.790	.786	.782	.779	.775	.771
44	.768	.764	.760	.757	.753	.750	.746	.743	.739	.736
45	.732	.729	.725	.722	.718	.715	.711	.708	.705	.701
46	.698	.695	.691	.688	.685	.681	.678	.675	.671	.668
47	.665	.662	.659	.655	.652	.649	.646	.643	.640	.637
48	.633	.630	.627	.624	.621	.618	.615	.612	.609	.606
49	.603	.600	.597	.594	.591	.588	.586	.583	.580	.577
50	.574	.571	.568	.565	.563	.560	.557	.554	.551	.549
51	.546	.543	.540	.538	.535	.532	.530	.527	.524	.521
52	.519	.516	.513	.511	.508	.506	.503	.500	.498	.495
53	.493	.490	.488	.485	.482	.480	.477	.475	.472	.470
54	.467	.465	.463	.460	.458	.455	.453	.450	.448	.446
55	.443	.441	.438	.436	.434	.431	.429	.427	.424	.422
56	.420	.417	.415	.413	.410	.408	.406	.404	.401	.399
57	.397	.395	.393	.390	.388	.386	.384	.382	.379	.377
58	.375	.373	.371	.369	.366	.364	.362	.360	.358	.356
59	.354	.352	.350	.348	.346	.343	.341	.339	.337	.335

$\mu t \to \infty$ FUNCTION FOR GAMMA=30

θ	0.0	0.1	0.2	0.3	0.4	0.5	0.6	0.7	0.8	0.9
60	.333	.331	.329	.327	.325	.323	.321	.319	.317	.315
61	.314	.312	.310	.308	.306	.304	.302	.300	.298	.296
62	.294	.292	.291	.289	.287	.285	.283	.281	.279	.278
63	.276	.274	.272	.270	.269	.267	.265	.263	.261	.260
64	.258	.256	.254	.253	.251	.249	.247	.246	.244	.242
65	.241	.239	.237	.235	.234	.232	.230	.229	.227	.225
66	.224	.222	.221	.219	.217	.216	.214	.212	.211	.209
67	.208	.206	.205	.203	.201	.200	.198	.197	.195	.194
68	.192	.191	.189	.187	.186	.184	.183	.181	.180	.178
69	.177	.176	.174	.173	.171	.170	.168	.167	.165	.164
70	.163	.161	.160	.158	.157	.155	.154	.153	.151	.150
71	.149	.147	.146	.144	.143	.142	.140	.139	.138	.136
72	.135	.134	.132	.131	.130	.129	.127	.126	.125	.123
73	.122	.121	.120	.118	.117	.116	.115	.114	.112	.111
74	.110	.109	.107	.106	.105	.104	.103	.102	.100	.099
75	.098	.097	.096	.095	.094	.092	.091	.090	.089	.088
76	.087	.086	.085	.084	.082	.081	.080	.079	.078	.077
77	.076	.075	.074	.073	.072	.071	.070	.069	.068	.067
78	.066	.065	.064	.063	.062	.061	.060	.059	.058	.057
79	.057	.056	.055	.054	.053	.052	.051	.050	.049	.048
80	.048	.047	.046	.045	.044	.043	.043	.042	.041	.040
81	.039	.039	.038	.037	.036	.035	.035	.034	.033	.032
82	.032	.031	.030	.030	.029	.028	.028	.027	.026	.026
83	.025	.024	.024	.023	.022	.022	.021	.020	.020	.019
84	.019	.018	.018	.017	.016	.016	.015	.015	.014	.014
85	.013	.013	.012	.012	.011	.011	.010	.010	.010	.009
86	.009	.008	.008	.008	.007	.007	.006	.006	.006	.005
87	.005	.005	.004	.004	.004	.004	.003	.003	.003	.003
88	.002	.002	.002	.002	.001	.001	.001	.001	.001	.001
89	.001	.000	.000	.000	.000	.000	.000	.000	.000	.000

$\mu t \to \infty$ FUNCTION FOR GAMMA=15

θ	0.0	0.1	0.2	0.3	0.4	0.5	0.6	0.7	0.8	0.9
10	5.606	5.547	5.489	5.432	5.376	5.322	5.268	5.215	5.163	5.112
11	5.062	5.013	4.965	4.918	4.871	4.825	4.781	4.736	4.693	4.650
12	4.608	4.567	4.526	4.486	4.447	4.408	4.370	4.332	4.295	4.259
13	4.223	4.188	4.153	4.119	4.085	4.052	4.019	3.986	3.955	3.923
14	3.892	3.862	3.832	3.802	3.773	3.744	3.715	3.687	3.659	3.632
15	3.605	3.578	3.552	3.526	3.500	3.475	3.450	3.425	3.401	3.377
16	3.353	3.329	3.306	3.283	3.260	3.238	3.216	3.194	3.172	3.151
17	3.130	3.109	3.088	3.068	3.048	3.028	3.008	2.988	2.969	2.950
18	2.931	2.912	2.894	2.876	2.857	2.840	2.822	2.804	2.787	2.770
19	2.753	2.736	2.719	2.703	2.686	2.670	2.654	2.638	2.623	2.607
20	2.592	2.576	2.561	2.546	2.532	2.517	2.502	2.488	2.474	2.459
21	2.445	2.432	2.418	2.404	2.391	2.377	2.364	2.351	2.338	2.325
22	2.312	2.299	2.287	2.274	2.262	2.250	2.238	2.225	2.214	2.202
23	2.190	2.178	2.167	2.155	2.144	2.133	2.121	2.110	2.099	2.088
24	2.077	2.067	2.056	2.045	2.035	2.024	2.014	2.004	1.994	1.984
25	1.974	1.964	1.954	1.944	1.934	1.925	1.915	1.905	1.896	1.887
26	1.877	1.868	1.859	1.850	1.841	1.832	1.823	1.814	1.805	1.796
27	1.788	1.779	1.771	1.762	1.754	1.745	1.737	1.729	1.721	1.712
28	1.704	1.696	1.688	1.680	1.672	1.665	1.657	1.649	1.641	1.634
29	1.626	1.619	1.611	1.604	1.596	1.589	1.582	1.574	1.567	1.560
30	1.553	1.546	1.539	1.532	1.525	1.518	1.511	1.504	1.497	1.491
31	1.484	1.477	1.471	1.464	1.458	1.451	1.445	1.438	1.432	1.425
32	1.419	1.413	1.407	1.400	1.394	1.388	1.382	1.376	1.370	1.364
33	1.358	1.352	1.346	1.340	1.334	1.329	1.323	1.317	1.311	1.306
34	1.300	1.294	1.289	1.283	1.278	1.272	1.267	1.261	1.256	1.250
35	1.245	1.240	1.234	1.229	1.224	1.219	1.213	1.208	1.203	1.198
36	1.193	1.188	1.183	1.178	1.173	1.168	1.163	1.158	1.153	1.148
37	1.143	1.138	1.133	1.129	1.124	1.119	1.114	1.110	1.105	1.100
38	1.096	1.091	1.087	1.082	1.077	1.073	1.068	1.064	1.059	1.055
39	1.051	1.046	1.042	1.037	1.033	1.029	1.024	1.020	1.016	1.012
40	1.007	1.003	.999	.995	.991	.986	.982	.978	.974	.970
41	.966	.962	.958	.954	.950	.946	.942	.938	.934	.930
42	.926	.922	.919	.915	.911	.907	.903	.900	.896	.892
43	.888	.885	.881	.877	.873	.870	.866	.863	.859	.855
44	.852	.848	.845	.841	.837	.834	.830	.827	.823	.820
45	.816	.813	.810	.806	.803	.799	.796	.793	.789	.786
46	.783	.779	.776	.773	.769	.766	.763	.760	.756	.753
47	.750	.747	.744	.740	.737	.734	.731	.728	.725	.721
48	.718	.715	.712	.709	.706	.703	.700	.697	.694	.691
49	.688	.685	.682	.679	.676	.673	.670	.667	.664	.661

$\mu t \to \infty$ FUNCTION FOR GAMMA=15

θ	0.0	0.1	0.2	0.3	0.4	0.5	0.6	0.7	0.8	0.9
50	.658	.656	.653	.650	.647	.644	.641	.638	.636	.633
51	.630	.627	.624	.622	.619	.616	.613	.610	.608	.605
52	.602	.600	.597	.594	.591	.589	.586	.583	.581	.578
53	.576	.573	.570	.568	.565	.562	.560	.557	.555	.552
54	.550	.547	.544	.542	.539	.537	.534	.532	.529	.527
55	.524	.522	.519	.517	.514	.512	.509	.507	.505	.502
56	.500	.497	.495	.493	.490	.488	.485	.483	.481	.478
57	.476	.474	.471	.469	.467	.464	.462	.460	.457	.455
58	.453	.450	.448	.446	.444	.441	.439	.437	.435	.432
59	.430	.428	.426	.424	.421	.419	.417	.415	.413	.410
60	.408	.406	.404	.402	.400	.397	.395	.393	.391	.389
61	.387	.385	.383	.381	.378	.376	.374	.372	.370	.368
62	.366	.364	.362	.360	.358	.356	.354	.352	.350	.348
63	.346	.344	.342	.340	.338	.336	.334	.332	.330	.328
64	.326	.324	.322	.320	.318	.316	.314	.312	.310	.308
65	.307	.305	.303	.301	.299	.297	.295	.293	.291	.290
66	.288	.286	.284	.282	.280	.279	.277	.275	.273	.271
67	.269	.268	.266	.264	.262	.260	.259	.257	.255	.253
68	.251	.250	.248	.246	.244	.243	.241	.239	.237	.236
69	.234	.232	.231	.229	.227	.225	.224	.222	.220	.219
70	.217	.215	.214	.212	.210	.209	.207	.205	.204	.202
71	.200	.199	.197	.196	.194	.192	.191	.189	.188	.186
72	.184	.183	.181	.180	.178	.176	.175	.173	.172	.170
73	.169	.167	.166	.164	.163	.161	.159	.158	.156	.155
74	.153	.152	.150	.149	.148	.146	.145	.143	.142	.140
75	.139	.137	.136	.134	.133	.131	.130	.129	.127	.126
76	.124	.123	.122	.120	.119	.117	.116	.115	.113	.112
77	.111	.109	.108	.107	.105	.104	.103	.101	.100	.099
78	.097	.096	.095	.093	.092	.091	.090	.088	.087	.086
79	.085	.083	.082	.081	.080	.078	.077	.076	.075	.074
80	.072	.071	.070	.069	.068	.067	.065	.064	.063	.062
81	.061	.060	.059	.058	.056	.055	.054	.053	.052	.051
82	.050	.049	.048	.047	.046	.045	.044	.043	.042	.041
83	.040	.039	.038	.037	.036	.035	.034	.033	.032	.032
84	.031	.030	.029	.028	.027	.026	.026	.025	.024	.023
85	.022	.022	.021	.020	.019	.018	.018	.017	.016	.016
86	.015	.014	.014	.013	.012	.012	.011	.011	.010	.009
87	.009	.008	.008	.007	.007	.006	.006	.005	.005	.005
88	.004	.004	.003	.003	.003	.002	.002	.002	.002	.001
89	.001	.001	.001	.001	.000	.000	.000	.000	.000	.000

S-B Extrapolation Function for Specimen Curvature and Displacement for Thin Transparent Specimens with $\mu t \to 0$

$$\frac{1 + \cos 2\theta}{\sin \gamma \cdot \sin(2\theta - \gamma)}$$

$\mu t \to 0$ FUNCTION FOR GAMMA=90

θ	0.0	0.1	0.2	0.3	0.4	0.5	0.6	0.7	0.8	0.9
50	4.759	4.647	4.540	4.436	4.337	4.241	4.148	4.059	3.973	3.890
51	3.810	3.732	3.657	3.584	3.514	3.445	3.379	3.315	3.253	3.192
52	3.134	3.077	3.021	2.967	2.915	2.864	2.814	2.766	2.719	2.673
53	2.628	2.584	2.542	2.500	2.460	2.420	2.382	2.344	2.307	2.271
54	2.236	2.202	2.168	2.135	2.103	2.072	2.041	2.011	1.981	1.952
55	1.924	1.896	1.869	1.842	1.816	1.790	1.765	1.741	1.716	1.693
56	1.669	1.647	1.624	1.602	1.581	1.559	1.538	1.518	1.498	1.478
57	1.459	1.439	1.421	1.402	1.384	1.366	1.349	1.331	1.314	1.298
58	1.281	1.265	1.249	1.233	1.218	1.203	1.188	1.173	1.158	1.144
59	1.130	1.116	1.103	1.089	1.076	1.063	1.050	1.037	1.025	1.012
60	1.000	.988	.976	.964	.953	.942	.930	.919	.908	.898
61	.887	.877	.866	.856	.846	.836	.826	.817	.807	.798
62	.788	.779	.770	.761	.752	.743	.735	.726	.718	.710
63	.701	.693	.685	.677	.669	.662	.654	.646	.639	.632
64	.624	.617	.610	.603	.596	.589	.582	.575	.569	.562
65	.556	.549	.543	.537	.530	.524	.518	.512	.506	.500
66	.494	.489	.483	.477	.472	.466	.461	.455	.450	.445
67	.440	.434	.429	.424	.419	.414	.409	.404	.400	.395
68	.390	.386	.381	.376	.372	.367	.363	.359	.354	.350
69	.346	.341	.337	.333	.329	.325	.321	.317	.313	.309
70	.305	.302	.298	.294	.290	.287	.283	.280	.276	.272
71	.269	.266	.262	.259	.255	.252	.249	.246	.242	.239
72	.236	.233	.230	.227	.224	.221	.218	.215	.212	.209
73	.206	.203	.201	.198	.195	.192	.190	.187	.184	.182
74	.179	.177	.174	.172	.169	.167	.164	.162	.159	.157
75	.155	.152	.150	.148	.146	.143	.141	.139	.137	.135
76	.133	.130	.128	.126	.124	.122	.120	.118	.116	.115
77	.113	.111	.109	.107	.105	.103	.102	.100	.098	.096
78	.095	.093	.091	.090	.088	.086	.085	.083	.082	.080
79	.079	.077	.076	.074	.073	.071	.070	.068	.067	.066

$\mu t \to 0$ FUNCTION FOR GAMMA=90

θ	0.0	0.1	0.2	0.3	0.4	0.5	0.6	0.7	0.8	0.9
80	.064	.063	.062	.060	.059	.058	.056	.055	.054	.053
81	.051	.050	.049	.048	.047	.046	.045	.043	.042	.041
82	.040	.039	.038	.037	.036	.035	.034	.033	.032	.032
83	.031	.030	.029	.028	.027	.026	.025	.025	.024	.023
84	.022	.022	.021	.020	.019	.019	.018	.017	.017	.016
85	.015	.015	.014	.014	.013	.012	.012	.011	.011	.010
86	.010	.009	.009	.008	.008	.008	.007	.007	.006	.006
87	.006	.005	.005	.004	.004	.004	.004	.003	.003	.003
88	.002	.002	.002	.002	.002	.001	.001	.001	.001	.001
89	.001	.000	.000	.000	.000	.000	.000	.000	.000	.000

$\mu t \to 0$ FUNCTION FOR GAMMA=75

θ	0.0	0.1	0.2	0.3	0.4	0.5	0.6	0.7	0.8	0.9
40	13.94	13.37	12.84	12.34	11.88	11.45	11.05	10.68	10.32	9.99
41	9.677	9.381	9.101	8.836	8.584	8.345	8.118	7.901	7.695	7.498
42	7.310	7.130	6.957	6.792	6.634	6.482	6.335	6.195	6.060	5.930
43	5.804	5.683	5.567	5.454	5.345	5.240	5.138	5.040	4.945	4.852
44	4.763	4.676	4.592	4.510	4.431	4.354	4.279	4.207	4.136	4.067
45	4.000	3.935	3.871	3.809	3.749	3.690	3.633	3.577	3.523	3.469
46	3.417	3.367	3.317	3.269	3.221	3.175	3.130	3.085	3.042	3.000
47	2.958	2.917	2.878	2.839	2.801	2.763	2.726	2.691	2.655	2.621
48	2.587	2.554	2.521	2.489	2.458	2.427	2.397	2.367	2.338	2.309
49	2.281	2.253	2.226	2.199	2.173	2.147	2.122	2.097	2.072	2.048
50	2.024	2.001	1.978	1.955	1.933	1.911	1.889	1.868	1.847	1.827
51	1.806	1.786	1.767	1.747	1.728	1.709	1.691	1.672	1.654	1.636
52	1.619	1.602	1.584	1.568	1.551	1.535	1.519	1.503	1.487	1.471
53	1.456	1.441	1.426	1.411	1.397	1.382	1.368	1.354	1.341	1.327
54	1.313	1.300	1.287	1.274	1.261	1.249	1.236	1.224	1.212	1.200
55	1.188	1.176	1.164	1.153	1.141	1.130	1.119	1.108	1.097	1.086
56	1.076	1.065	1.055	1.045	1.035	1.025	1.015	1.005	.995	.985
57	.976	.967	.957	.948	.939	.930	.921	.912	.903	.895
58	.886	.878	.869	.861	.853	.845	.837	.829	.821	.813
59	.805	.798	.790	.783	.775	.768	.761	.753	.746	.739
60	.732	.725	.718	.711	.705	.698	.691	.685	.678	.672
61	.665	.659	.653	.647	.640	.634	.628	.622	.616	.611
62	.605	.599	.593	.587	.582	.576	.571	.565	.560	.554
63	.549	.544	.539	.533	.528	.523	.518	.513	.508	.503
64	.498	.493	.489	.484	.479	.474	.470	.465	.461	.456

$\mu t \to 0$ FUNCTION FOR GAMMA=75

θ	0.0	0.1	0.2	0.3	0.4	0.5	0.6	0.7	0.8	0.9
65	.451	.447	.443	.438	.434	.430	.425	.421	.417	.413
66	.408	.404	.400	.396	.392	.388	.384	.380	.376	.373
67	.369	.365	.361	.358	.354	.350	.346	.343	.339	.336
68	.332	.329	.325	.322	.318	.315	.312	.308	.305	.302
69	.298	.295	.292	.289	.286	.283	.279	.276	.273	.270
70	.267	.264	.261	.258	.255	.253	.250	.247	.244	.241
71	.238	.236	.233	.230	.228	.225	.222	.220	.217	.214
72	.212	.209	.207	.204	.202	.199	.197	.194	.192	.190
73	.187	.185	.183	.180	.178	.176	.173	.171	.169	.167
74	.165	.162	.160	.158	.156	.154	.152	.150	.148	.146
75	.144	.142	.140	.138	.136	.134	.132	.130	.128	.126
76	.124	.123	.121	.119	.117	.115	.114	.112	.110	.108
77	.107	.105	.103	.102	.100	.098	.097	.095	.094	.092
78	.091	.089	.088	.086	.085	.083	.082	.080	.079	.077
79	.076	.075	.073	.072	.070	.069	.068	.067	.065	.064
80	.063	.061	.060	.059	.058	.057	.055	.054	.053	.052
81	.051	.050	.049	.047	.046	.045	.044	.043	.042	.041
82	.040	.039	.038	.037	.036	.035	.034	.033	.033	.032
83	.031	.030	.029	.028	.027	.027	.026	.025	.024	.023
84	.023	.022	.021	.020	.020	.019	.018	.018	.017	.016
85	.016	.015	.015	.014	.013	.013	.012	.012	.011	.011
86	.010	.010	.009	.009	.008	.008	.007	.007	.007	.006
87	.006	.005	.005	.005	.004	.004	.004	.003	.003	.003
88	.003	.002	.002	.002	.002	.001	.001	.001	.001	.001
89	.001	.001	.000	.000	.000	.000	.000	.000	.000	.000

$\mu t \to 0$ FUNCTION FOR GAMMA=60

θ	0.0	0.1	0.2	0.3	0.4	0.5	0.6	0.7	0.8	0.9
35	8.924	8.729	8.542	8.362	8.189	8.022	7.861	7.705	7.555	7.410
36	7.270	7.134	7.003	6.876	6.753	6.634	6.518	6.406	6.297	6.191
37	6.089	5.989	5.892	5.797	5.706	5.616	5.529	5.444	5.362	5.281
38	5.203	5.126	5.051	4.979	4.907	4.838	4.770	4.704	4.639	4.576
39	4.514	4.453	4.394	4.336	4.279	4.223	4.169	4.116	4.064	4.012
40	3.962	3.913	3.865	3.818	3.772	3.726	3.682	3.638	3.595	3.553
41	3.511	3.471	3.431	3.392	3.353	3.315	3.278	3.242	3.206	3.170
42	3.136	3.102	3.068	3.035	3.002	2.970	2.939	2.908	2.877	2.847
43	2.818	2.789	2.760	2.732	2.704	2.677	2.650	2.623	2.597	2.571
44	2.545	2.520	2.496	2.471	2.447	2.423	2.400	2.377	2.354	2.332

$\mu t \to 0$ FUNCTION FOR GAMMA=60

θ	0.0	0.1	0.2	0.3	0.4	0.5	0.6	0.7	0.8	0.9
45	2.309	2.288	2.266	2.245	2.224	2.203	2.182	2.162	2.142	2.122
46	2.103	2.084	2.065	2.046	2.027	2.009	1.991	1.973	1.956	1.938
47	1.921	1.904	1.887	1.870	1.854	1.838	1.822	1.806	1.790	1.775
48	1.759	1.744	1.729	1.714	1.699	1.685	1.670	1.656	1.642	1.628
49	1.615	1.601	1.587	1.574	1.561	1.548	1.535	1.522	1.509	1.497
50	1.484	1.472	1.460	1.448	1.436	1.424	1.413	1.401	1.389	1.378
51	1.367	1.356	1.345	1.334	1.323	1.312	1.302	1.291	1.281	1.270
52	1.260	1.250	1.240	1.230	1.220	1.210	1.201	1.191	1.182	1.172
53	1.163	1.154	1.144	1.135	1.126	1.117	1.108	1.100	1.091	1.082
54	1.074	1.065	1.057	1.048	1.040	1.032	1.024	1.016	1.008	1.000
55	.992	.984	.976	.969	.961	.953	.946	.938	.931	.924
56	.916	.909	.902	.895	.888	.881	.874	.867	.860	.853
57	.847	.840	.833	.827	.820	.814	.807	.801	.795	.788
58	.782	.776	.770	.764	.758	.752	.746	.740	.734	.728
59	.722	.717	.711	.705	.700	.694	.688	.683	.677	.672
60	.667	.661	.656	.651	.645	.640	.635	.630	.625	.620
61	.615	.610	.605	.600	.595	.590	.585	.581	.576	.571
62	.566	.562	.557	.552	.548	.543	.539	.534	.530	.525
63	.521	.517	.512	.508	.504	.499	.495	.491	.487	.483
64	.479	.475	.471	.466	.462	.458	.455	.451	.447	.443
65	.439	.435	.431	.428	.424	.420	.416	.413	.409	.405
66	.402	.398	.395	.391	.387	.384	.380	.377	.374	.370
67	.367	.363	.360	.357	.353	.350	.347	.344	.340	.337
68	.334	.331	.328	.325	.321	.318	.315	.312	.309	.306
69	.303	.300	.297	.294	.291	.289	.286	.283	.280	.277
70	.274	.272	.269	.266	.263	.261	.258	.255	.252	.250
71	.247	.245	.242	.239	.237	.234	.232	.229	.227	.224
72	.222	.219	.217	.214	.212	.210	.207	.205	.203	.200
73	.198	.196	.193	.191	.189	.187	.184	.182	.180	.178
74	.176	.173	.171	.169	.167	.165	.163	.161	.159	.157
75	.155	.153	.151	.149	.147	.145	.143	.141	.139	.137
76	.135	.133	.132	.130	.128	.126	.124	.122	.121	.119
77	.117	.115	.114	.112	.110	.109	.107	.105	.104	.102
78	.100	.099	.097	.096	.094	.092	.091	.089	.088	.086
79	.085	.083	.082	.081	.079	.078	.076	.075	.073	.072
80	.071	.069	.068	.067	.065	.064	.063	.062	.060	.059
81	.058	.057	.055	.054	.053	.052	.051	.049	.048	.047
82	.046	.045	.044	.043	.042	.041	.040	.039	.038	.037
83	.036	.035	.034	.033	.032	.031	.030	.029	.028	.027
84	.027	.026	.025	.024	.023	.022	.022	.021	.020	.019

$\mu t \to 0$ FUNCTION FOR GAMMA=60

θ	0.0	0.1	0.2	0.3	0.4	0.5	0.6	0.7	0.8	0.9
85	.019	.018	.017	.017	.016	.015	.015	.014	.013	.013
86	.012	.012	.011	.010	.010	.009	.009	.008	.008	.007
87	.007	.006	.006	.006	.005	.005	.004	.004	.004	.003
88	.003	.003	.003	.002	.002	.002	.002	.001	.001	.001
89	.001	.001	.001	.000	.000	.000	.000	.000	.000	.000

$\mu t \to 0$ FUNCTION FOR GAMMA=45

θ	0.0	0.1	0.2	0.3	0.4	0.5	0.6	0.7	0.8	0.9
25	26.66	25.59	24.61	23.69	22.84	22.04	21.30	20.60	19.95	19.33
26	18.75	18.20	17.68	17.19	16.72	16.28	15.85	15.45	15.07	14.70
27	14.35	14.02	13.70	13.39	13.10	12.82	12.54	12.28	12.03	11.79
28	11.56	11.33	11.11	10.90	10.70	10.51	10.32	10.13	9.96	9.78
29	9.618	9.457	9.300	9.148	9.000	8.857	8.717	8.581	8.449	8.321
30	8.196	8.074	7.956	7.840	7.728	7.618	7.511	7.407	7.305	7.205
31	7.108	7.013	6.920	6.830	6.741	6.654	6.569	6.486	6.405	6.326
32	6.248	6.172	6.097	6.024	5.953	5.882	5.814	5.746	5.680	5.615
33	5.551	5.489	5.428	5.367	5.308	5.250	5.193	5.137	5.082	5.028
34	4.975	4.923	4.872	4.821	4.772	4.723	4.675	4.628	4.581	4.536
35	4.491	4.447	4.403	4.360	4.318	4.276	4.235	4.195	4.155	4.116
36	4.078	4.040	4.002	3.965	3.929	3.893	3.858	3.823	3.788	3.755
37	3.721	3.688	3.656	3.623	3.592	3.560	3.530	3.499	3.469	3.439
38	3.410	3.381	3.353	3.324	3.297	3.269	3.242	3.215	3.189	3.162
39	3.136	3.111	3.086	3.061	3.036	3.012	2.987	2.964	2.940	2.917
40	2.894	2.871	2.848	2.826	2.804	2.782	2.761	2.740	2.718	2.698
41	2.677	2.657	2.636	2.616	2.597	2.577	2.558	2.538	2.519	2.501
42	2.482	2.464	2.445	2.427	2.410	2.392	2.374	2.357	2.340	2.323
43	2.306	2.289	2.273	2.256	2.240	2.224	2.208	2.192	2.177	2.161
44	2.146	2.131	2.116	2.101	2.086	2.071	2.057	2.042	2.028	2.014
45	2.000	1.986	1.972	1.959	1.945	1.932	1.918	1.905	1.892	1.879
46	1.866	1.853	1.841	1.828	1.816	1.803	1.791	1.779	1.767	1.755
47	1.743	1.731	1.720	1.708	1.697	1.685	1.674	1.663	1.652	1.641
48	1.630	1.619	1.608	1.597	1.587	1.576	1.565	1.555	1.545	1.535
49	1.524	1.514	1.504	1.494	1.484	1.475	1.465	1.455	1.446	1.436
50	1.427	1.417	1.408	1.399	1.389	1.380	1.371	1.362	1.353	1.344
51	1.336	1.327	1.318	1.310	1.301	1.292	1.284	1.276	1.267	1.259
52	1.251	1.243	1.234	1.226	1.218	1.210	1.202	1.195	1.187	1.179
53	1.171	1.164	1.156	1.148	1.141	1.133	1.126	1.119	1.111	1.104
54	1.097	1.090	1.082	1.075	1.068	1.061	1.054	1.047	1.040	1.034

$\mu t \to 0$ FUNCTION FOR GAMMA=45

θ	0.0	0.1	0.2	0.3	0.4	0.5	0.6	0.7	0.8	0.9
55	1.027	1.020	1.013	1.007	1.000	.993	.987	.980	.974	.967
56	.961	.954	.948	.942	.936	.929	.923	.917	.911	.905
57	.899	.893	.887	.881	.875	.869	.863	.857	.852	.846
58	.840	.834	.829	.823	.817	.812	.806	.801	.795	.790
59	.785	.779	.774	.769	.763	.758	.753	.748	.742	.737
60	.732	.727	.722	.717	.712	.707	.702	.697	.692	.687
61	.682	.677	.673	.668	.663	.658	.654	.649	.644	.640
62	.635	.630	.626	.621	.617	.612	.608	.603	.599	.595
63	.590	.586	.582	.577	.573	.569	.564	.560	.556	.552
64	.548	.543	.539	.535	.531	.527	.523	.519	.515	.511
65	.507	.503	.499	.495	.491	.488	.484	.480	.476	.472
66	.469	.465	.461	.457	.454	.450	.446	.443	.439	.435
67	.432	.428	.425	.421	.418	.414	.411	.407	.404	.400
68	.397	.394	.390	.387	.383	.380	.377	.374	.370	.367
69	.364	.361	.357	.354	.351	.348	.345	.341	.338	.335
70	.332	.329	.326	.323	.320	.317	.314	.311	.308	.305
71	.302	.299	.296	.293	.290	.288	.285	.282	.279	.276
72	.273	.271	.268	.265	.262	.260	.257	.254	.252	.249
73	.246	.244	.241	.238	.236	.233	.231	.228	.226	.223
74	.221	.218	.216	.213	.211	.208	.206	.203	.201	.199
75	.196	.194	.191	.189	.187	.184	.182	.180	.178	.175
76	.173	.171	.169	.166	.164	.162	.160	.158	.156	.153
77	.151	.149	.147	.145	.143	.141	.139	.137	.135	.133
78	.131	.129	.127	.125	.123	.121	.119	.117	.116	.114
79	.112	.110	.108	.106	.105	.103	.101	.099	.098	.096
80	.094	.092	.091	.089	.087	.086	.084	.082	.081	.079
81	.078	.076	.075	.073	.071	.070	.068	.067	.066	.064
82	.063	.061	.060	.058	.057	.056	.054	.053	.052	.050
83	.049	.048	.046	.045	.044	.043	.042	.040	.039	.038
84	.037	.036	.035	.033	.032	.031	.030	.029	.028	.027
85	.026	.025	.024	.023	.022	.022	.021	.020	.019	.018
86	.017	.016	.016	.015	.014	.013	.013	.012	.011	.011
87	.010	.009	.009	.008	.008	.007	.006	.006	.005	.005
88	.005	.004	.004	.003	.003	.003	.002	.002	.002	.001
89	.001	.001	.001	.001	.000	.000	.000	.000	.000	.000

$\mu t \to 0$ FUNCTION FOR GAMMA=30

θ	0.0	0.1	0.2	0.3	0.4	0.5	0.6	0.7	0.8	0.9
20	20.34	19.92	19.52	19.13	18.75	18.39	18.04	17.71	17.38	17.07
21	16.77	16.48	16.19	15.92	15.65	15.39	15.14	14.90	14.66	14.44
22	14.21	14.00	13.79	13.58	13.39	13.19	13.00	12.82	12.64	12.47
23	12.30	12.13	11.97	11.81	11.66	11.51	11.36	11.22	11.07	10.94
24	10.80	10.67	10.54	10.42	10.29	10.17	10.06	9.94	9.83	9.72
25	9.606	9.500	9.395	9.292	9.192	9.093	8.996	8.901	8.808	8.716
26	8.626	8.538	8.451	8.365	8.281	8.199	8.118	8.038	7.960	7.883
27	7.807	7.733	7.660	7.588	7.517	7.447	7.378	7.310	7.244	7.178
28	7.114	7.050	6.987	6.926	6.865	6.805	6.746	6.687	6.630	6.573
29	6.518	6.463	6.408	6.355	6.302	6.250	6.199	6.148	6.098	6.049
30	6.000	5.952	5.905	5.858	5.811	5.766	5.721	5.676	5.632	5.589
31	5.546	5.504	5.462	5.420	5.380	5.339	5.299	5.260	5.221	5.183
32	5.144	5.107	5.070	5.033	4.996	4.961	4.925	4.890	4.855	4.821
33	4.787	4.753	4.720	4.687	4.654	4.622	4.590	4.558	4.527	4.496
34	4.465	4.435	4.405	4.375	4.346	4.317	4.288	4.260	4.231	4.203
35	4.176	4.148	4.121	4.094	4.067	4.041	4.015	3.989	3.963	3.938
36	3.913	3.888	3.863	3.838	3.814	3.790	3.766	3.742	3.719	3.696
37	3.673	3.650	3.627	3.605	3.583	3.560	3.539	3.517	3.495	3.474
38	3.453	3.432	3.411	3.391	3.370	3.350	3.330	3.310	3.290	3.270
39	3.251	3.231	3.212	3.193	3.174	3.156	3.137	3.119	3.100	3.082
40	3.064	3.046	3.029	3.011	2.993	2.976	2.959	2.942	2.925	2.908
41	2.891	2.875	2.858	2.842	2.826	2.809	2.793	2.778	2.762	2.746
42	2.731	2.715	2.700	2.685	2.669	2.654	2.639	2.625	2.610	2.595
43	2.581	2.566	2.552	2.538	2.524	2.510	2.496	2.482	2.468	2.454
44	2.441	2.427	2.414	2.400	2.387	2.374	2.361	2.348	2.335	2.322
45	2.309	2.297	2.284	2.272	2.259	2.247	2.235	2.222	2.210	2.198
46	2.186	2.174	2.162	2.151	2.139	2.127	2.116	2.104	2.093	2.081
47	2.070	2.059	2.048	2.036	2.025	2.014	2.004	1.993	1.982	1.971
48	1.960	1.950	1.939	1.929	1.918	1.908	1.898	1.887	1.877	1.867
49	1.857	1.847	1.837	1.827	1.817	1.807	1.797	1.788	1.778	1.768
50	1.759	1.749	1.740	1.730	1.721	1.712	1.702	1.693	1.684	1.675
51	1.666	1.657	1.648	1.639	1.630	1.621	1.612	1.603	1.595	1.586
52	1.577	1.569	1.560	1.552	1.543	1.535	1.526	1.518	1.510	1.501
53	1.493	1.485	1.477	1.469	1.461	1.452	1.444	1.437	1.429	1.421
54	1.413	1.405	1.397	1.389	1.382	1.374	1.366	1.359	1.351	1.344
55	1.336	1.329	1.321	1.314	1.307	1.299	1.292	1.285	1.277	1.270
56	1.263	1.256	1.249	1.242	1.235	1.228	1.221	1.214	1.207	1.200
57	1.193	1.186	1.179	1.173	1.166	1.159	1.152	1.146	1.139	1.133
58	1.126	1.119	1.113	1.106	1.100	1.094	1.087	1.081	1.074	1.068
59	1.062	1.055	1.049	1.043	1.037	1.031	1.024	1.018	1.012	1.006

$\mu t \to 0$ FUNCTION FOR GAMMA=30

θ	0.0	0.1	0.2	0.3	0.4	0.5	0.6	0.7	0.8	0.9
60	1.000	.994	.988	.982	.976	.970	.964	.958	.952	.947
61	.941	.935	.929	.923	.918	.912	.906	.901	.895	.889
62	.884	.878	.873	.867	.862	.856	.851	.845	.840	.834
63	.829	.824	.818	.813	.808	.802	.797	.792	.787	.781
64	.776	.771	.766	.761	.756	.751	.746	.740	.735	.730
65	.725	.720	.716	.711	.706	.701	.696	.691	.686	.681
66	.677	.672	.667	.662	.657	.653	.648	.643	.639	.634
67	.629	.625	.620	.616	.611	.606	.602	.597	.593	.588
68	.584	.579	.575	.571	.566	.562	.557	.553	.549	.544
69	.540	.536	.532	.527	.523	.519	.515	.510	.506	.502
70	.498	.494	.490	.486	.481	.477	.473	.469	.465	.461
71	.457	.453	.449	.445	.441	.438	.434	.430	.426	.422
72	.418	.414	.410	.407	.403	.399	.395	.392	.388	.384
73	.380	.377	.373	.369	.366	.362	.359	.355	.351	.348
74	.344	.341	.337	.334	.330	.327	.323	.320	.316	.313
75	.309	.306	.303	.299	.296	.293	.289	.286	.283	.279
76	.276	.273	.270	.266	.263	.260	.257	.254	.250	.247
77	.244	.241	.238	.235	.232	.229	.226	.223	.220	.217
78	.214	.211	.208	.205	.202	.199	.196	.193	.190	.188
79	.185	.182	.179	.176	.174	.171	.168	.165	.163	.160
80	.157	.155	.152	.150	.147	.144	.142	.139	.137	.134
81	.132	.129	.127	.124	.122	.119	.117	.115	.112	.110
82	.108	.105	.103	.101	.099	.096	.094	.092	.090	.088
83	.086	.083	.081	.079	.077	.075	.073	.071	.069	.067
84	.065	.063	.062	.060	.058	.056	.054	.052	.051	.049
85	.047	.046	.044	.042	.041	.039	.038	.036	.035	.033
86	.032	.030	.029	.027	.026	.025	.023	.022	.021	.020
87	.019	.018	.016	.015	.014	.013	.012	.011	.010	.010
88	.009	.008	.007	.006	.006	.005	.004	.004	.003	.003
89	.002	.002	.001	.001	.001	.001	.000	.000	.000	.000

$\mu t \to 0$ FUNCTION FOR GAMMA=15

θ	0.0	0.1	0.2	0.3	0.4	0.5	0.6	0.7	0.8	0.9
10	85.99	82.64	79.54	76.66	73.97	71.47	69.13	66.93	64.87	62.93
11	61.10	59.37	57.73	56.18	54.71	53.32	51.99	50.72	49.52	48.36
12	47.26	46.21	45.20	44.23	43.31	42.42	41.56	40.74	39.95	39.18
13	38.45	37.74	37.06	36.40	35.76	35.14	34.54	33.97	33.41	32.87
14	32.34	31.83	31.34	30.86	30.39	29.94	29.50	29.07	28.66	28.25
15	27.86	27.47	27.10	26.73	26.38	26.03	25.69	25.36	25.04	24.73
16	24.42	24.12	23.83	23.54	23.26	22.99	22.72	22.46	22.20	21.95
17	21.71	21.47	21.23	21.00	20.77	20.55	20.33	20.12	19.91	19.71
18	19.50	19.31	19.11	18.92	18.73	18.55	18.37	18.19	18.02	17.85
19	17.68	17.52	17.35	17.19	17.04	16.88	16.73	16.58	16.43	16.29
20	16.15	16.01	15.87	15.73	15.60	15.47	15.34	15.21	15.08	14.96
21	14.84	14.71	14.60	14.48	14.36	14.25	14.14	14.03	13.92	13.81
22	13.70	13.60	13.49	13.39	13.29	13.19	13.09	13.00	12.90	12.81
23	12.71	12.62	12.53	12.44	12.35	12.26	12.18	12.09	12.01	11.92
24	11.84	11.76	11.68	11.60	11.52	11.44	11.37	11.29	11.21	11.14
25	11.07	10.99	10.92	10.85	10.78	10.71	10.64	10.57	10.51	10.44
26	10.37	10.31	10.24	10.18	10.12	10.05	9.99	9.93	9.87	9.81
27	9.748	9.689	9.631	9.573	9.515	9.459	9.402	9.347	9.291	9.237
28	9.183	9.129	9.076	9.023	8.971	8.919	8.868	8.817	8.767	8.717
29	8.667	8.618	8.570	8.522	8.474	8.427	8.380	8.333	8.287	8.241
30	8.196	8.151	8.107	8.062	8.019	7.975	7.932	7.889	7.847	7.805
31	7.763	7.722	7.681	7.640	7.600	7.559	7.520	7.480	7.441	7.402
32	7.364	7.325	7.287	7.250	7.212	7.175	7.138	7.102	7.066	7.030
33	6.994	6.958	6.923	6.888	6.853	6.819	6.785	6.751	6.717	6.683
34	6.650	6.617	6.584	6.552	6.519	6.487	6.455	6.424	6.392	6.361
35	6.330	6.299	6.268	6.238	6.208	6.178	6.148	6.118	6.089	6.060
36	6.031	6.002	5.973	5.945	5.916	5.888	5.860	5.832	5.805	5.777
37	5.750	5.723	5.696	5.669	5.643	5.616	5.590	5.564	5.538	5.512
38	5.486	5.461	5.435	5.410	5.385	5.360	5.336	5.311	5.286	5.262
39	5.238	5.214	5.190	5.166	5.143	5.119	5.096	5.072	5.049	5.026
40	5.003	4.981	4.958	4.936	4.913	4.891	4.869	4.847	4.825	4.803
41	4.782	4.760	4.739	4.717	4.696	4.675	4.654	4.633	4.612	4.592
42	4.571	4.551	4.530	4.510	4.490	4.470	4.450	4.430	4.411	4.391
43	4.371	4.352	4.333	4.313	4.294	4.275	4.256	4.237	4.219	4.200
44	4.181	4.163	4.144	4.126	4.108	4.090	4.071	4.053	4.036	4.018
45	4.000	3.982	3.965	3.947	3.930	3.912	3.895	3.878	3.861	3.844
46	3.827	3.810	3.793	3.777	3.760	3.743	3.727	3.710	3.694	3.678
47	3.661	3.645	3.629	3.613	3.597	3.581	3.566	3.550	3.534	3.519
48	3.503	3.487	3.472	3.457	3.441	3.426	3.411	3.396	3.381	3.366
49	3.351	3.336	3.321	3.307	3.292	3.277	3.263	3.248	3.234	3.219

$\mu t \to 0$ FUNCTION FOR GAMMA=15

θ	0.0	0.1	0.2	0.3	0.4	0.5	0.6	0.7	0.8	0.9
50	3.205	3.191	3.176	3.162	3.148	3.134	3.120	3.106	3.092	3.078
51	3.065	3.051	3.037	3.024	3.010	2.996	2.983	2.969	2.956	2.943
52	2.929	2.916	2.903	2.890	2.877	2.864	2.851	2.838	2.825	2.812
53	2.799	2.786	2.774	2.761	2.748	2.736	2.723	2.711	2.698	2.686
54	2.673	2.661	2.649	2.637	2.624	2.612	2.600	2.588	2.576	2.564
55	2.552	2.540	2.528	2.516	2.505	2.493	2.481	2.469	2.458	2.446
56	2.434	2.423	2.411	2.400	2.389	2.377	2.366	2.355	2.343	2.332
57	2.321	2.310	2.298	2.287	2.276	2.265	2.254	2.243	2.232	2.221
58	2.211	2.200	2.189	2.178	2.167	2.157	2.146	2.135	2.125	2.114
59	2.104	2.093	2.083	2.072	2.062	2.051	2.041	2.031	2.021	2.010
60	2.000	1.990	1.980	1.969	1.959	1.949	1.939	1.929	1.919	1.909
61	1.899	1.889	1.879	1.870	1.860	1.850	1.840	1.830	1.821	1.811
62	1.801	1.792	1.782	1.772	1.763	1.753	1.744	1.734	1.725	1.715
63	1.706	1.697	1.687	1.678	1.669	1.659	1.650	1.641	1.632	1.622
64	1.613	1.604	1.595	1.586	1.577	1.568	1.559	1.550	1.541	1.532
65	1.523	1.514	1.505	1.496	1.487	1.479	1.470	1.461	1.452	1.443
66	1.435	1.426	1.417	1.409	1.400	1.392	1.383	1.374	1.366	1.357
67	1.349	1.340	1.332	1.324	1.315	1.307	1.298	1.290	1.282	1.273
68	1.265	1.257	1.249	1.240	1.232	1.224	1.216	1.208	1.200	1.191
69	1.183	1.175	1.167	1.159	1.151	1.143	1.135	1.127	1.119	1.111
70	1.104	1.096	1.088	1.080	1.072	1.064	1.057	1.049	1.041	1.033
71	1.026	1.018	1.010	1.003	.995	.987	.980	.972	.965	.957
72	.950	.942	.935	.927	.920	.912	.905	.897	.890	.883
73	.875	.868	.861	.853	.846	.839	.832	.824	.817	.810
74	.803	.796	.788	.781	.774	.767	.760	.753	.746	.739
75	.732	.725	.718	.711	.704	.697	.690	.684	.677	.670
76	.663	.656	.650	.643	.636	.629	.623	.616	.609	.603
77	.596	.589	.583	.576	.570	.563	.557	.550	.544	.537
78	.531	.524	.518	.512	.505	.499	.493	.486	.480	.474
79	.467	.461	.455	.449	.443	.437	.430	.424	.418	.412
80	.406	.400	.394	.388	.382	.376	.371	.365	.359	.353
81	.347	.341	.336	.330	.324	.319	.313	.307	.302	.296
82	.291	.285	.280	.274	.269	.263	.258	.253	.247	.242
83	.237	.232	.226	.221	.216	.211	.206	.201	.196	.191
84	.186	.181	.176	.171	.167	.162	.157	.153	.148	.143
85	.139	.134	.130	.126	.121	.117	.113	.109	.104	.100
86	.096	.092	.088	.084	.081	.077	.073	.070	.066	.062
87	.059	.056	.052	.049	.046	.043	.040	.037	.034	.032
88	.029	.026	.024	.022	.019	.017	.015	.013	.011	.010
89	.008	.007	.005	.004	.003	.002	.001	.001	.000	.000

Appendix 4

Programme for the calculation of lattice parameters

```
      REAL TTH(40),TH(40),SGTH(40),YO(40),YA(40),H(40),K(40),L(40),
     1H1(40),K1(40),L1(40),H2(40),K2(40),L2(40),LAM(3),DIFF(40),W(40),
     OMM(40),HO(40),KO(40),LO(40),YAO(40),YA1(40),YA2(40),R(40),UA(40),
     UUC(40),UD(40)
      INTEGER NM(40)
      LAM(1)=1.54051
      LAM(2)=1.54433
      LAM(3)=1.54178
      R(1)=1.0
      R(2)=(LAM(1)/LAM(2))**2
      R(3)=(LAM(1)/LAM(3))**2
      DO 50 J=1,30
      READ(5,100)NOP,SPEC
      WRITE(6,117)SPEC
      SCR=0.7
      NQ=NOP
      WRITE(6,116)J
      NP=0
      READ(5,91)(TTH(I),MM(I),SGTH(I),H(I),K(I),L(I),H1(I),K1(I),L1(I),
     TH2(I),K2(I),L2(I),NM(I),I=1,NOP)
C     NOP=NO. OF PEAKS
C     SGTH=ASSIGNED VARIANCE OF MEASUREMENTS
C     NM=1,2 FOR ALPHA 1,2
      READ(5,102)C1,A1
      GM=45.0*3.14159/180.0
C     GM=GAMMA IN RADS
      DO 10 I=1,NOP
      TTH(I)=TTH(I)+MM(I)*0.0125
      WRITE(6,112)TH(I)
      TH(I)=TTH(I)*3.14159/360.0
      TTH(I)=TH(I)*2.0                          TTH=2θ
      NI=NM(I)
      YO(I)= SIN(TH(I))**2*R(NI)
   10 CONTINUE
C     YO=OBSERVED VALUE OF SIN(TH)**2
      AU=(LAM(1)/(2.0*A1))**2
      CU=(LAM(1)/(2.0*C1))**2
      DU=0
C     CU,AU,DU = UPPER CASE C,A,D
    3 NP=NP+1
      IF(NP-6)4,4,50
    4 WRITE(6,104)NP
      NN=NOP-3
      PA=0
      PC=0
      PD=0
      QA=0
      QC=0
      QD=0
      RC=0
      RD=0
      SA=0
      SD=0
      SUMN2=0
      SUMN=0
      DO 20 I=1,NOP
```

```
      YA(I)=AU*(H(I)**2+K(I)**2)+CU*L(I)**2+(DU*SIN(TTH(I))**2)/(SIN(GM)
     *U*SIN(TTH(I)-GM))
      YA1(I)=AU*(H1(I)**2+K1(I)**2)+CU*L1(I)**2+(DU*SIN(TTH(I))**2)/(SIN
     *T(GM)*SIN(TTH(I)-GM))
      YA2(I)=AU*(H2(I)**2+K2(I)**2)+CU*L2(I)**2+(DU*SIN(TTH(I))**2)/(SIN
     *T(GM)*SIN(TTH(I)-GM))
C     YA(I)=APPROX VALUE OF SINTH)**2
      DIFF(I)=2.0*SIN(TTH(I))*(2.0*COS(TTH(I))-SIN(TTH(I))*COS(TTH(I)-GM
     *I)/SIN(TTH(I)-GM))/(SIN(TTH(I)-GM)*SIN(GM))
      DIFF(I)=DIFF(I)*DU-SIN(TTH(I))
C     DIFF=DF/DTH
      W(I)=1.0/(SGTH(I)*DIFF(I)**2)
      SGF=SGN/U(I)
      IF(NP-1)8,8,19
   19 Z=(YO(I)-YA(I))**2
      Z1=(YO(I)-YA1(I))**2
      Z2=(YO(I)-YA2(I))**2
      IF(Z-Z1)1,2,17
    1 IF(Z-Z2)5,5,7
    2 IF(Z-Z2)8,8,18
    5 IF(Z-SGF*SCR)8,8,9
   17 IF(Z1-Z2)13,16,7
   13 IF(Z1-SGF*SCR)16,16,9
   16 HO(I)=H1(I)
      KO(I)=K1(I)
      LO(I)=L1(I)
      YAO(I)=YA1(I)
      H1(I)=H(I)
      K1(I)=K(I)
      L1(I)=L(I)
      YA1(I)=YA(I)
      H(I)=HO(I)
      K(I)=KO(I)
      L(I)=LO(I)
      YA(I)=YAO(I)
      GO TO 8
    7 IF(Z2-SGF*SCR)18,18,9
   18 HO(I)=H2(I)
      KO(I)=K2(I)
      LO(I)=L2(I)
      YAO(I)=YA2(I)
      H2(I)=H(I)
      K2(I)=K(I)
      L2(I)=L(I)
      YA2(I)=YA(I)
      H(I)=HO(I)
      K(I)=KO(I)
      L(I)=LO(I)
      YA(I)=YAO(I)
      GO TO 8
    9 WRITE(6,103)I
      NN=NN-1
      NQ=NN+3
      GO TO 20
    8 IF(NP.EQ.6)WRITE(6,105)H(I),K(I),L(I)
      SUMN2=SUMN2+(YO(I)-YA(I))**2*W(I)
      UA(I)=H(I)**2+K(I)**2
      UC(I)=L(I)**2
      UD(I)=(SIN(TTH(I))**2)/(SIN(TTH(I)-GM)*SIN(GM))
      PA=PA+(YO(I)-YA(I))*W(I)*UA(I)
      PC=PC+(YO(I)-YA(I))*W(I)*UC(I)
      PD=PD+(YO(I)-YA(I))*W(I)*UD(I)
      QA=QA+W(I)*UA(I)**2
      QC=QC+W(I)*UA(I)*UC(I)
      QD=QD+W(I)*UA(I)*UD(I)
      RC=RC+W(I)*UC(I)**2
      RD=RD+W(I)*UC(I)*UD(I)
      SD=SD+W(I)*UD(I)**2
```

YA(I)= y_i (approx.)

DIFF(I)= $\frac{\partial F_i}{\partial \theta_i}$

←Choosing best (h,k,l)

←Evaluation of $D_T(ij)$

```
   20 CONTINUE
      RA=QC
      SC=RD
      SA=QD
      DETA=PA*RC*SD+QC*RD*PD+QD*PC*SC-PA*RD*SC-QC*PC*SD-QD*RC*PD
      DETC=QA*PC*SD+PA*RD*SA+QD*RA*PD-QA*RD*PD-PA*RA*SD-QD*PC*SA
      DETD=QA*RC*PD+QC*PC*SA+PA*RA*SC-QA*PC*SC-QC*RA*PD-PA*RC*SA
      DETT=QA*RC*SD+QC*RD*SA+QD*RA*SC-QA*RD*SC-QC*RA*SD-QD*RC*SA
      E=DETA/DETT
      F=DETC/DETT
      G=DETD/DETT
      AU=AU+E
      CU=CU+F
      DU=DU+G
      CL=SQRT(LAM(1)**2/(4.0*CU))
      AL=SQRT(LAM(1)**2/(4.0*AU))
C     AL,CL     =LOWER CASE A,C
      COVA=CL/AL
      VOL=CL*AL**2
      VARAU=(RC*SD-RD**2)*SUMN2      /(DETT*FLOAT(NN))
      VARCU=(QA*SD-QD**2)*SUMN2      /(DETT*FLOAT(NN))
      VARDU=(QA*RC-QC**2)*SUMN2      /(DETT*FLOAT(NN))
      VARAL=((LAM(1)/4.0)**2/AU**3)*VARAU
      VARCL=((LAM(1)/4.0)**2/CU**3)*VARCU
      IF(NP-1)21,21,22
   21 SGN=SUMN2      /(FLOAT(NN))
   22 SGAL=SQRT(VARAL)
      SGCL=SQRT(VARCL)
      SGDU=SQRT(VARDU)
      VRCOA=VARCL/(AL**2)+(CL**2*VARAL/AL**4)
      SGCOA=SQRT(VRCOA)
      VRVOL=4.0*(CL*AL)**2*VARAL+AL**4*VARCL
      SGVOL=SQRT(VRVOL)
      WRITE(6,110)AL,CL,COVA,DU,SGAL,SGCL,SGCOA,SGDU,VOL,SGVOL
      IF(NQ.GE.NOP-1)SCR=SCR/2.0
   23 GO TO 3
   50 CONTINUE
  100 FORMAT(I3,A77)
   91 FORMAT(3(F6.3,F3.2,F2.0,9F1.0,I1))
  102 FORMAT(2F5.4)
  103 FORMAT(16H SCRAP LINE I = ,I2)
  104 FORMAT(20H ITERATIVE RUN NO.  ,I2)
  105 FORMAT(5H H = ,F2.0,5H K = ,F2.0,5H L = ,F2.0)
  106 FORMAT(10H  Z=Z1     )
  107 FORMAT(10H Z=Z1=Z2   )
  108 FORMAT(10H  Z1=Z2    )
  109 FORMAT(10H  Z=Z2     )
  110 FORMAT(6H AL = ,F8.6,6H CL = ,F8.6,7H C/A = ,F8.6,6H DU = ,F8.6/8H
     T SGAL = ,F8.6,8H SGCL = ,F8.6,9H SGCOA = ,F8.6,8H SGDU = ,F8.6/7H
     TVOL = ,F12.6,9H SGVOL = ,F9.6)
  111 FORMAT(5H Z = ,F8.6,6H Z1 = ,F8.6,6H Z2 = ,F8.6)
  112 FORMAT(8H TTH =  ,F8.4)
  113 FORMAT(5H E = ,F8.6,5H F = ,F8.6,5H G = ,F8.6)
  114 FORMAT(6H AU = ,F8.6,6H CU = ,F8.6)
  115 FORMAT(5H P = ,F10.5)
  116 FORMAT(5H J = ,I3)
  117 FORMAT(A77)
      STOP
      END
```

Evaluation of determinants

COVA= c/a

Variance of results

Appendix 5

Evaluation of Madelung constant

```
      REALK(20),H(20),P(20),COFA(30),MU,Z(20),LAM
      PI=3.14159
      A=-0.877857
      READ(5,101)(H(I),K(I),P(I),Z(I),I=1,20)
C     MULTIPLICITY    Z P
      DO 60 I=40,160
      COVA=FLOAT(I)*0.01
      WRITE(6,105)COVA
      LAM=0
C     B=0 ISLT.    B=1 ISLTO                    ∑° when Z=1
      DO 50 J=1,20                        LAM =
      B=Z(J)                                   ∑• when Z=0
      MU=SQRT(H(J)**2+K(J)**2)
      IF(B)1,1,2
    1 LAM=LAM+P(J)/(MU*(EXP(PI*MU*COVA)-1.0))
      GO TO 50
    2 LAM=LAM-P(J)/(MU*(EXP(PI*MU*COVA)+1.0))
   50 CONTINUE
    6 ALPH=(1.5*PI**2*COVA)**(1.0/3.0)*(A+COVA/6.0+LAM*2.0/PI)
      WRITE(6,103)ALPH
   60 CONTINUE
  100 FORMAT(10F6.5)
  101 FORMAT(2F1.0,F2.0,F1.0)
  102 FORMAT(7H LAM = ,F8.6)
  103 FORMAT(8H ALPH = ,F8.6)
  104 FORMAT(5H A = ,F8.6)
  105 FORMAT(7H C/A = ,F7.5)
      STOP
      END
```

Appendix 6

Evaluation of the total energy of the indium alloys

```
      REAL          H(132),K(132),L(132),U(132),KF,DIF1(50),DIF2(50),DIF3
     T(50),COVA(70)
      COMMON  COMP,FQ(50),VQ1(60),VQ2(60),C,A,ALPH(70),J,EES,V2,PI,EL,V
      PI=3.14159
      EL=4.8025
      MCA=65
      V1=104.49
      V1=V1/(0.52915)**3
      V2=107.57
      V2=V2/(0.52915)**3
      READ(5,105)(COVA(I),I=1,MCA)
      READ(5,101)(H(I),K(I),L(I),U(I),I=1,36)
      READ(5,111)(ALPH(I),I=1,MCA)
      READ(5,110)VQ1
      READ(5,110)VQ2
      DO 80 M=32,80,4
      WRITE(6,108)M
      COMP=FLOAT(M)*0.01
      V=(1.0-COMP)*V1+COMP*V2
      CALL FFN
      LB=1
      DO 60 J=LB,MCA
      WRITE(6,107)COVA(J)
      EBS=0
      CALL  UES
      A=(V/COVA(J))**(1.0/3.0)
      C=A*COVA(J)
      AS=A*A
      CS=C*C
      DO 50 I=1,36
      Q=(H(I)**2+K(I)**2)/AS+L(I)**2/CS
      Q=2.0*PI*SQRT(Q)
      X=Q/0.125
      NE=X
   14 IF(NE-45)10,21,21
   21 WRITE(6,103)I,EBS
      GO TO 59
   10 B=X-FLOAT(NE)
      FQQ=FQ(NE)+B*(FQ(NE+1)-FQ(NE))
      EBS=EBS+FQQ*U(I)
   15 IF(I-25)16,1,16
   16 IF(I-30)12,1,12
    1 WRITE(6,103)I,EBS
   12 CONTINUE
   50 CONTINUE
   59 ETOT=EBS+EES
      WRITE(6,112)ETOT
   60 CONTINUE
   80 CONTINUE
  101 FORMAT(36F2.0)
  102 FORMAT(2F7.6)
  103 FORMAT(5H I = ,I3,7H EBS = ,F8.5)
  105 FORMAT(24F3.2)
  107 FORMAT(//7H C/A = ,F5.3//)
  108 FORMAT(///25H ----------------------/18H SN COMPOSITION = ,I3,8H
     T PERCENT)
  110 FORMAT(10F6.5)
  111 FORMAT(9F8.6)
  112 FORMAT(/16H TOTAL ENERGY = ,F10.7)
      STOP
      END
```

```
      SUBROUTINE FFN
      REAL KF,KS,MS,VQ(50)
      COMMON COMP,FQ(50),VQ1(60),VQ2(60),C,A,ALPH(70),J,EES,V2,PI,EL,V
      MS=9.1066
      HB=6.624/(2.0*PI)
      Z1=3.0
      Z2=4.0
      ALF1=0.1186
      ALF2=0.0822
      ZAV=(1.0-COMP)*Z1+COMP*Z2
      ALPHA=(1.0-COMP)*ALF1+COMP*ALF2
      KF=(12.0*ZAV*PI**2/V)**(1.0/3.0)
      KS=SQRT(2.0*KF/PI)
      WRITE(6,105)KF,KS
      B=(MS*EL**2*0.0052915)/(2.0*PI*KF*HB**2)
      D=0.52915*1.601864*13.60353*V/(32.0*PI*EL**2)
      DO 50 I=1,50
      VQ(I)=(1.0-COMP)*VQ1(I)+COMP*VQ2(I)
      Q=I
      Q=Q*0.125
      ETA=Q/(2.0*KF)
      IF(ETA-1.0)1,2,1
    2 EPS=1.0+B/ETA**2
      GO TO 3
    1 EPS=1.0+B*((1.0-ETA**2)*ALOG(ABS ((1.0+ETA)/(1.0-ETA)))/(2.0*ETA)*
     T1.0)/ETA**2
    3 CONTINUE
      EPS2=1.0+(1.0+ALPHA)*(1.0-(Q**2/2.0)/(Q**2+KF**2+KS**2))*(EPS-1.0)
      GQ=-D*Q**2*VQ(I)**2*(EPS-1.0)*EPS2
      FQ(I)=GQ
   50 CONTINUE
  105 FORMAT(6H KF = ,F7.5,6H KS = ,F7.5)
      RETURN
      END
```

```
      SUBROUTINE UES
      COMMON COMP,FQ(50),VQ1(60),VQ2(60),C,A,ALPH(70),J,EES,V2,PI,EL,V
      Z1=3.3558
      Z2=4.3288
C     Z1=Z* FOR INDIUM
C     Z2=Z* FOR SECOND ELEMENT
      OMEGA=V/4.0
      R=(3.0*OMEGA/(4.0*PI))**(1.0/3.0)*0.52915
      ZAV =(1.0-COMP)*Z1 +COMP*Z2
      ZAVS=ZAV**2
C     ZAVS = MEAN VALENCE SQUARED
      EES= ZAVS*EL **2*ALPH(J)/(2.0*R)
      EES=EES/(1.601864*13.60353)
      WRITE(6,102)ALPH(J),EES
  102 FORMAT(8H ALPH = ,F9.6,7H EES = ,F8.6)
      RETURN
      END
```